Modeling Macro- and Micro-Scale Turbulent Mixing and Chemistry in Engine Exhaust Plumes

Suresh Menon
School of Aerospace Engineering
Georgia Institute of Technology
Atlanta, Georgia 30332-0150
404-894-9126
404-894-2760 (Fax)
suresh.menon@aerospace.gatech.edu

Final Report
Under Grant NAG 1-1631

Submitted to
National Aeronautics and Space Administration
Langley Research Center
Hampton, VA

October 10, 1998

Executive Summary

Simulation of turbulent mixing and chemical processes in the near-field plume and plume-vortex regimes has been successfully carried out recently using a reduced gas phase kinetics mechanism which substantially decreased the computational cost. A detailed mechanism including gas phase HOx, NOx, and SOx chemistry between the aircraft exhaust and the ambient air in near-field aircraft plumes is compiled. A reduced mechanism capturing the major chemical pathways is developed. Predictions by the reduced mechanism are found to be in good agreement with those by the detailed mechanism. With the reduced chemistry, the computer CPU time is saved by a factor of more than 3.5 for the near-field plume modeling. Distributions of major chemical species are obtained and analyzed. The computed sensitivities of major species with respect to reaction step are deduced for identification of the dominant gas phase kinetic reaction pathways in the jet plume.

Both the near field plume and the plume-vortex regimes were investigated using advanced mixing models. In the near field, a stand -alone mixing model was used to investigate the impact of turbulent mixing on the micro- and macro-scale mixing processes using a reduced reaction kinetics model. The plume-vortex regime was simulated using a large-eddy simulation model. Vortex plume behind Boeing 737 and 747 aircraft was simulated along with relevant kinetics. Many features of the computed flow field show reasonable agreement with data. The entrainment of the engine plumes into the wing tip vortices and also the partial detrainment of the plume were numerically captured. The impact of fluid mechanics on the chemical processes was also studied. Results show that there are significant differences between spatial and temporal simulations especially in the predicted SO_3 concentrations. This has important implications for the prediction of sulfuric acid aerosols in the wake and many partly explain the discrepancy between past numerical studies (that employed parabolic or temporal approximations) and the measured data.

Finally to address the major uncertainty in the near-field plume modeling related to the plume processing of sulfur compounds and advanced model was developed to evaluate its impact on the chemical processes in the near wake. A comprehensive aerosol model is developed and it is coupled with chemical kinetics and the axisymmetric turbulent jet flow models. The integrated model is used to simulate microphysical processes in the near-field jet plume, including sulfuric acid and water binary homogeneous nucleation, coagulation, non-equilibrium heteromolecular condensation, and sulfur-induced soot activation. The formation and evolution of aerosols are computed and analyzed. The computed results show that a large number of ultra-fine (0.3--0.6 nm in radius) volatile $H_2SO_4 - H_2O$ embryos are generated in the near-field plume. These embryos further grow in size by self coagulation and condensation. Soot particles can be activated by both heterogeneous nucleation and scavenging of $H_2SO_4 - H_2O$ aerosols. These activated soot particles can serve as water condensation nuclei for contrail formation. Conditions under which ice contrails can form behind aircrafts are studied. The sensitivities of the threshold temperature for contrail formation with respect to aircraft propulsion efficiency, relative humidity, and ambient pressure are evaluated. The computed aerosol properties for different extent of fuel sulfur conversion to S(VI) (SO_3 and H_2SO_4) in engine are examined and the results are found to be sensitive to this conversion fraction.

1. PROBLEM DESCRIPTION

The projected increase in future aviation especially in heavy traffic flight corridors has the potential for causing a major upper atmospheric perturbation. Recent research has focused on the potential impact on the upper troposphere and on the lower stratosphere due to exhaust emission from the proposed fleet of supersonic high-speed civil transport (HSCT) and/or advanced subsonic transport (AST) operating in the transatlantic and Pacific rim flight corridors (e.g., Brasseur et al., 1990, Beck et al., 1992; Stolarski and Wesoky, 1995; Friedl, 1997). Emissions from individual aircraft are initially highly localized in the engine plume wake and rapidly disperses in the far wake. However, the chemical processes in the hot species-rich plume may lead to changes on the global scale if it causes marked changes in the far field exhaust composition. This concern, especially as related to the potential deployment of HSCT and/or AST fleets, has led to many investigations focusing on the near field (characterized as the exhaust plume and plume-wing-tip vortex interaction regimes) chemical processes. Gas phase chemical processes due to NO_x, HO_x and SOx species and heterogeneous kinetics due to exhaust aerosols and soot particles in the plume are being studied (Fahey et al., 1995a, 1995b; Brown et al., 1996a, b; Weisenstein et al., 1993). Both measurements and numerical studies in the near field indicate potentially significant impact on the atmosphere depending upon the significance of both homogeneous and heterogeneous kinetics. In particular, conversion of emitted NO_x to inactive forms of nitrogen, plume processing of sulfur and formation of ice in the plume have been the focus of many recent investigations (Friedl, 1997).

The net effect of NO_x emission on ozone is known to be reduced if some of it is converted to its less reactive form (via the hydrolysis of N_2O_5 to HNO_3). Near-field modeling studies (Miake-Lye et al., 1993, 1994; Quackenbush et al., 1993) and measurements (Fahey et al., 1995a) indicate that relatively small amounts of NO_y is deposited in the form of nitrous and nitric acid with the bulk remaining in the form of NO_x. Thus, both data and measurements suggest that there is only a minimal conversion of emitted NO_x into other species in the near field plume. On the other hand, the sulfur compounds in the near field plume are known to be significantly affected by the chemical processes. Recent calculations (Miake-Lye et al., 1994, Brown et al., 1996a, d) and experimental observations (Fahey et al., 1995b; Karcher and Fahey, 1997) suggest that many small aerosol particles are formed when H_2SO_4(v) undergoes binary homogeneous nucleation with water. The number of these particles is estimated to be orders of magnitude larger than the emitted soot particles. Calculations (Miake-Lye et al., 1994) suggests that the nucleation process is much more likely than heterogeneous condensation of H_2SO_4 on soot particles. The resulting increase in overall aerosol surface area in the plume has the potential for changing the exhaust composition in the far field wake and thereby, impacting the global dynamics.

The major uncertainty is in the modeling of soot and aerosol particles in the plume. For example, measurements (Fahey et al., 1995b) suggests that around 10% of the fuel sulfur is converted to sulfates whereas models (Brown et al., 1996a, c) predict only around 1-2 %. This discrepancy has been the focus of recent studies (e.g., Brown et al., 1996a-d; Schumann et al., 1996; Karcher and Fahey, 1997) and is of fundamental interest since the formation of large number of aerosol particles in the plume may lead to significant global effects in the long term. For reliable estimates, physical processes that involve gas-particle condensation, homogeneous binary nucleation of $H_2SO_4 - H_2O$ aerosols, condensation of $H_2SO_4 - H_2O$ on soot particles, aerosol coagulation and soot

agglomeration, etc., all must be modeled. Although most of these processes have been modeled in the past, either separately or together, the coupling of these processes along with the gas phase kinetics in a fluid dynamic solver has been difficult primarily due to the computational cost. Both condensation aerosols and coagulation of aerosols require that the number density and size distribution of the particles be determined as a function of space and time (due to their dependence on the local composition and thermodynamic state). The computational cost to track all the aerosol sizes is excessive even for 2D steady state calculations (although, recently Brown et al., 1996a, d have begun doing some calculations). Evaluating aerosol dynamics in an unsteady reacting environment by using LES is impossible at present. Unsteady mixing effects on aerosol dynamics may be important since condensation and coagulation processes could be modified if aerosol or soot particles are entrained in local vortical structures containing large concentrations of key species (e.g., OH, SO_3, H_2O). Reliable predictions of plume processing of sulfur may require taking all these issues into account.

The exorbitant cost of computing the details of aerosol dynamics appears to be the main stumbling block in the study of heterogeneous kinetics in the near-field plume. However, if the models used for condensation and coagulation can be reformulated so that a significant reduction in computational cost is achieved without causing a major loss of accuracy, then it would be feasible to address these processes within the context of even an unsteady simulation of the near-field. The advantages of a computationally efficient model for aerosol dynamics are obvious. In the present study, both homogeneous and heterogeneous kinetics modeling issues have been addressed with the view for application in large-scale 3D simulation methodology such as large-eddy simulations.

This report summarizes the results obtained in this study. Most of the details are given in the papers attached as Appendices. Here we briefly summarize the pertinent results.

2. SUMMARY OF RESULTS

Many past studies (Miake-Lye et al., 1993; 1994; Quackenbush et al., 1996; Brown et al., 1996a) of the near field plume have employed a variant of the standard plume code (SPF-II) called UNIWAKE. This code is a space-marching, parabolized solver and employs the standard $k-\varepsilon$ turbulence model to obtain the steady state field. The computational efficiency of this code is achieved by using a parabolic (2D) approach and by modeling all chemical and fluid dynamic processes in the steady state limit. As a result, physical time dependent processes that govern mixing and combustion processes such as molecular diffusion, large-scale entrainment and small-scale turbulent mixing are ignored (or modeled using eddy viscosity/diffusivity models). Thus, the importance (if any) of the unsteady processes on the chemical processing in the plume could not be addressed using this type of code.

To determine the impact of the time-dependent processes on plume dynamics, a study was undertaken under this NASA AEAP program. Since computations that resolve the unsteady processes are extremely expensive, new cost-effective methodologies had to be developed and incorporated for this study.

The project had four primary objectives:

(1) to develop and validate reduced chemical kinetics models for near-field studies
(2) to evaluate micro- and macro-scale mixing effects in the plume regime
(3) to investigate the effects of mixing on chemical processes in the plume-vortex regime
(4) to investigate reduced (computationally efficient) models for heterogeneous kinetics

We have achieved all of the above noted objectives and have obtained new insight into the fluid dynamic and chemical processes occurring in the near field. The investigation to develop reduced heterogeneous models is currently underway. However, the complexity of the heterogeneous processes that must be included, the lack of detailed data for comparison and the computational cost of doing baseline (i.e., conventional discrete-nodal/sectional method) simulations has delayed the development effort. Currently, we are including aerosol models into our codes and we expect to get some results before the end of the current project. However, discrete-nodal/sectional method is computationally too expensive for general purpose studies. To develop computationally efficient aerosol dynamics models, we have identified two methodologies that show potential for application within fluid dynamic solvers. However, the various issues that must be addressed cannot be completed under the current program. In the following, we briefly summarize the key results of the current research. More details are given in Menon and Chen (1995), Menon and Wu (1998) Wu and Menon (1998a, 1998b), Wang and Chen (1997).

2. 1 Reduced Kinetics Development

Reduced reaction kinetics are modified chemical reaction models that mimic accurately all the critical features of a full (or detailed) reaction set. An obvious advantage of reduced kinetics is that it provides a computationally affordable set of key species that can be used in unsteady models and in large-eddy simulations (LES). Gas-phase mechanisms appropriate for the engine exhaust plume in the upper troposphere and lower stratosphere were compiled from literature. A 25-species, 47 reaction set used earlier for the HSCT (Miake-Lye et al., 1993; Brown et al., 1996) was reduced to a 8-species, 16 reaction set. Note that this approach does not just neglect the other reactions and species. Rather, it modifies the reaction rates in the reduced set using sensitivity analysis so that the resolved species production/destruction time scales reflect the impact of the neglected species (which are assumed to be in quasi-equilibrium).

The dominant oxidation kinetic pathways are identified through sensitivity analysis of major species with respect to gas phase reaction steps. The spatial distributions of major chemical species in the near-field jet plume are computed and analyzed. The reduced mechanism is developed which captures the major chemical pathways in the near-field jet plume. Results obtained with the reduced chemistry show good agreement with those predicted by the detailed chemistry. However, using the reduced chemistry has cut down computer CPU time by a factor of more than 3.5 for the near-field simulation. Results also show that the reduced mechanism captures the major pathways responsible for ozone destruction very accurately and also predicts accurately all the species that were included in the reduced set (Menon and Chen, 1995; Wang and Chen, 1997).

2. 2 Turbulent Mixing and Chemical Processes in the Plume Regime

The potential impact of engine exhaust gas on ambient ozone has been studied using several numerical models with differ in their treatments of the mixing process between the exhaust gas and the ambient air. These models include Perfectly-Stirred Reactor (PSR), transient Well-Mixed Reactor (WMR), Partially-Stirred-Reactor (PaSR), joint scalar Probability Density Function (PDF) and the Linear-Eddy Mixing (LEM) models. The last two methods, i.e., **PDF** and **LEM** (developed during this study for near-field plume studies) are *time dependent* simulation methods that incorporate effects of both micro- and macro-scale mixing. The PDF model is similar to the standard plume model in terms of the fluid dynamics but it incorporates a Monte-Carlo stochastic

simulation for the joint scalar pdf. This allows proper incorporation of the effects of turbulence on the chemical process. However, only the LEM approach includes micro-scale mixing using physically consistent turbulent scaling rules and incorporates, in addition, the effects of molecular diffusion. The results for an exhaust plume of a typical HSCT aircraft (Menon and Wu, 1998) showed that compared to predictions based on models that do not include small-scale mixing and/or molecular diffusion effects, 30% less O_3 and 15% less NO_x are depleted in the near field of the plume. This suggests that local unmixedness can have an inhibiting effect on ozone depletion in the near-field plume. Inclusion of the formation of condensed nitric acid on soot particles showed that 15% of the available NO_x is converted into its inactive form but has negligible effect on O_3 concentration. Competition between the gas phase H_2SO_4 formation and the H_2SO_4 condensation on soot particles for the available SO_3 in the plume was found to depend partly on the mixing process. Results (see Menon and Wu, 1998) show that for the single plume case, the LEM results are quite similar to the earlier models that ignored or modeled in an ad hoc manner, the mixing processes. This suggests that the macro (large) scale entrainment process (included in various models) dominate the mixing process. However, as shown in Wang and Chen (1997) and Menon and Wu (1997) there are significant differences in the local details of the radical (OH, SO_2, SO_3) distribution that is likely to impact the heterogeneous kinetics related to sulfuric acid. Effects of unsteady mixing on the aerosol and soot related chemical processes remains unresolved at this time. Future study will address this particular issue.

2.3 LES of Reacting Plume-Vortex Interactions

The development of the reduced reaction mechanism provided a computationally affordable model for LES. LES is probably the only method available to study unsteady mixing and chemical processes during plume-vortex interaction. In LES, all scales larger than the grid are resolved using a time- and space-accurate scheme and only the small scales are modeled. We have developed a new localized dynamic subgrid model for the subgrid kinetic energy to close the LES equations. Using this approach with a 15-species reduced gas phase reaction mechanism (and the heterogeneous kinetics involving nitric and sulfuric acid condensation on soot particles) a series of calculations were carried out to determine (a) the dynamics of fluid mixing and entrainment of the engine exhaust into the wing tip vortex, (b) the impact of mixing on the kinetics in the plume-vortex stage, and, (c) the capability of temporal versus spatial LES to capture the entrainment and the chemical processes.

The 3D LES was carried out using both temporal and spatial methods. In temporal simulation, periodic boundary conditions are used in the streamwise direction and the simulation captures a region of plume-vortex evolving in time which corresponds spatially (via a velocity transformation) to a location that moves (with increasing time) in the downstream direction. An advantage of this approach is that simulations can be used to study the long time (far downstream) evolution of the plume-vortex interaction. This approach is always used in the far field wake break up regimes (e.g., Lewellen and Lewellen, 1997) and in global modeling. However, temporal simulations cannot capture the inflow-outflow effects which may be important in the initial stages of the interaction between the engine exhaust plume and the wingtip vortices. Of particular interest here is the process of entrainment and detrainment (whereby portion of the plume is not entrained into the vortex, as observed in flight). To investigate these issues, two simulations using identical resolution and conditions were carried out using temporal and spatial methods. For the latter method, proper inflow turbulence and non-reflective outflow conditions were implemented. Reduced kinetics including the heterogeneous

processes were studied for an initial period (approximately 6-8 seconds) of the plume-vortex interaction phase. Although these simulations are quite expensive, using an optimized massively parallel code, a spatial LES using 1.2 million grid points and with 15 reacting species takes approximately 2000 single-processor hours on a SGI Origin 2000 to simulate 5 flow-through times. This CPU requirement is not considered exorbitant considering the availability of fast parallel systems.

Results show that the entrainment of the plume into the vortex in both the Boeing 737 and 747 cases are qualitatively similar to the LIDAR measurements. Results also showed that for the 747 case, a portion of the engine plume is not entrained into the vortex and if fact, appears to split away (a form of detrainment similar to that observed earlier in flight). To evaluate the effect of modeling strategy on the mixing process temporal (as is typically used by most researchers) and true spatial evaluation were simulated under otherwise identical conditions. Although both temporal and spatial LES look similar there are significant differences in the entrainment process and in the actual distribution of typical species. The breakup of the plumes into two pieces (one that is entrained and another that is left behind) is seen to occur more readily in the spatial case. More importantly, estimated of the mass of NO and SO_3 entrained into the vortex core show that the temporal simulation overpredicts the entrainment of NO by nearly 25% by 4 seconds while under predicting entrained SO_3 by nearly 25%. Since SO_3 is formed due to gas phase reactions and subsequently plays a major role in the formation of sulfuric acid aerosols as well as in the formation of condensed sulfuric acid on soot particles, this result has some significant implication when dealing with heterogeneous effects.

In summary, unsteady mixing and gas phase kinetics have been incorporated into two different types of fluid dynamic solvers in the plume regime: the PDF and LEM methods. Inclusion of aerosol dynamics into these codes using the discrete-sectional method is currently underway. The plume-vortex interaction regime has been addressed using dynamic subgrid model based LES. Inclusion of gas phase kinetics and simple heterogeneous processes have been successfully carried out. Details of the mixing and chemical processes have been extracted from these simulations and results point to the importance of dealing with inflow/outflow processes when simulating the initial process of plume-vortex interaction. The computational cost has been made reasonable using an optimized parallel version of the 3D code.

2.4 Aerosol and Soot Dynamics Modeling in the Plume Regime

A detailed chemical mechanism between aircraft exhaust and ambient air in near-field jet plumes was earlier developed and compiled. To further extend the chemistry capability, a comprehensive aerosol model is developed to simulate micro physical processes including sulfuric acid and water binary homogeneous nucleation, aerosol coagulation, non-equilibrium heteromolecular condensation, and sulfur-induced soot activation as water condensation nuclei. These micro physical processes are coupled with gas-phase chemistry and used to study axisymmetric turbulent jet flow.

The modeling results indicate that a large number of subnanometer-sized volatile $H_2SO_4 - H_2O$ embryos are generated in the near-field plume. These embryos grow in size by condensation in the early jet regime and by self coagulation later. Soot particles can be activated into water condensation nuclei in the jet plume for possible contrail formation through both heterogeneous nucleation and scavenging of volatile $H_2SO_4 - H_2O$ aerosols.

The gas phase conversion of SO_2 to H_2SO_4 is controlled by OH driven oxidation and it is limited to less than 1%. However, the amount of H_2SO_4 produced will increase via fast reaction of SO_3 with H_2O directly if SO_3 emission due to fuel sulfur oxidation to SO_3 in the engine is considered. Higher levels of H_2SO_4 in turn result in more sulfate aerosol embryos formed in the early jet stage, and also enhance condensation of $H_2SO_4$and H_2O onto the sulfate aerosols in this regime.

Consequently, SO_3 emission from the engine nozzle exit increases the cumulative number density and surface area density of volatile sulfate aerosols. SO_3 emission also promotes chemical activation of soot particles with enhanced acid coating. This suggests the need for measurements of the partitioning of sulfur species (SO_2 and SO_3) at the exhaust exit.

The threshold condition for ice contrail formation behind an aircraft depends on the ambient pressure, the ambient relative humidity, the overall propulsion efficiency of the aircraft, and the fuel properties such as the fuel hydrogen mass fraction and the specific combustion heat. Higher values of ambient relative humidity or pressure facilitate contrail formation. The threshold temperature is found sensitive to the overall propulsion efficiency of the aircraft. The prediction of particle and species distribution in the near-field plume can serve as input for the follow-on larger-scale model. The present work also provides an estimate of the aerosol surface area density for subsequent evaluation of heterogeneous oxidation mechanisms in the wake.

3. PUBLICATIONS/PRESENTATIONS UNDER THIS GRANT

Menon, S. and Chen, J.-Y. (1995) "A Numerical Study of Mixing and Chemical Processes during Interactions between an Aircraft's Engine Jet Plume and its Wingtip Vortices," NASA Conference on The Atmospheric Effects of Aviation, April 23-29, 1995, Virginia Beach, Virginia.

Menon, S. and Wu, J. (1997a) "Large-Eddy Simulations of Interaction between Engine Exhaust Plume and Aircraft Wingtip Vortices," NASA Conference on The Atmospheric Effects of Aviation, Virginia Beach, VA, March 10-14, 1997.

Menon, S. and Wu, J. (1998) "Effects of Micro- and Macro-scale Turbulent Mixing on the Chemical Processes in Engine Exhaust Plumes," *J. Applied Meteorology*, Vol. 37, pp. 639-654, 1998.

Wu, J. and Menon, S. (1998a) "Numerical Studies of Near-Field Plume-Vortex Interactions," AIAA Paper No. 98-2902, 29th AIAA Fluid Dynamics Conference, June 15-18, Albuquerque, NM.

Wu, J. and Menon, S. (1998b) "Large-Eddy Simulations of Near field Plume-Vortex Interactions," *J. Geophysics Research* (submitted).

Wang, Z. and Chen, J.-Y. (1997) "Numerical Modeling of Mixing and Chemistry in Near-Field Engine Exhaust Plumes," *J. Geophys. Res..*, 102, 12871-12883.

References

Beck, J., Reeves, C., de Leeuw, F., and Penkett, S. (1992) "The Effect of Aircraft Emissions on Tropospheric Ozone in the Northern Hemisphere, "Atm. *Env.*, 26A, 17-19.

Brasseur, G. P., Granier, C., and Walters, S. (1990) "Future Changes in Stratospheric Ozone and the Role of Heterogeneous Chemistry, "Nature, 348, 626-628.

Brown, R. C., Miake-Lye, R. C., Anderson, M. R., Kolb, C. E., and Resch, T. J. (1996a) "Aerosol Dynamics in Near Field Aircraft Plumes," *J. Geophys. Res.*, 101, 22,939-22,953.

Brown, R. C., Miake-Lye, M. R., Anderson, M. R., and Kolb, C. E., (1996b) "Effect of Aircraft Exhaust Sulfur Emissions on Near Field Plume Aerosol, "Geophys. *Res. Lett.*, 24, 3607-3610.

Brown, R. C., Anderson, M. R., Miake-Lye, R. C., Kolb, C. E., Sorokin, A. A., and Buriko, Y. Y. (1996c) "Aircraft Exhaust Sulfur Emissions," *Geo. Phys. Lett.*, 23, 3603-3606.

Brown, R. C., Miake-Lye, R. C., Anderson, M. R. and Kolb, C. E. (1996d) "Aircraft Sulfur Emissions and the Formation of Visible Contrails," *Geophys. Res. Letts.*

Fahey, D. W., et al. (1995a) "In situ Observations in Aircraft Exhaust Plume in the Lower Stratosphere at Mid Latitudes," *J. Geophys. Res.*, 100, 3065-3074.

Fahey, D. W., et al., (1995b) "Emission Measurements of the Concorde Supersonic Aircraft in the Lower Stratosphere, "Science, 270, 70-74.

Ford, I. J., Hayman, G. D., and Kingdon, R. D. (1996) "Plume and Aerosol Modeling for the POLINAT Project, Final Report," in Pollution from Aircraft Emissions in the North Altantic Flight Corridor (POLNAT) Report.

Friedl, R. R. (1997) "Atmospheric Effects of Subsonic Aircraft: Interim Assessment Report of the Advanced Subsonic Technology Program". NASA RP 1400.

Karcher, B. and Fahey, D. W., (1997) "The Role of Sulfur Emission in Volatile Particle Formation in Jet Aircraft Exhaust Plumes, "Geophys. *Res. Lett.*, 24, 389-392.

Lewellen, D. C. and Lewellen, W. S. (1997) "Large-Eddy Simulation of the Vortex-Pair Breakup in Aircraft Wakes, "AIAA *J.*, 34, 2337-2345.

Menon, S. and Chen, J.-Y. (1995) "A Numerical Study of Mixing and Chemical Processes during Interactions between an Aircraft's Engine Jet Plume and its Wingtip Vortices," NASA Conference on The Atmospheric Effects of Aviation, April 23-29, 1995, Virginia Beach, Virginia.

Menon, S. and Wu, J. (1997a) "Large-Eddy Simulations of Interaction between Engine Exhaust Plume and Aircraft Wingtip Vortices," NASA Conference on The Atmospheric Effects of Aviation, Virginia Beach, VA, March 10-14, 1997.

Menon, S. and Wu, J. (1998) "Effects of Micro- and Macro-scale Turbulent Mixing on the Chemical Processes in Engine Exhaust Plumes," *J. Applied Meteorology*, Vol. 37, pp. 639-654, 1998.

Miake-Lye, R. C., Martinez-Sanchez, M., Brown, R. C., Kolb, C. E. (1993) "Plume and Wake Dynamics, Mixing, and Chemistry behind a High Speed Civil Transport Aircraft," *J. Aircraft*, 30, 467-479.

Miake-Lye, R. C., Martinez-Sanchez, M., Brown, R. C., and Kolb, C. E. (1994) "Calculations of condensation and chemistry in an aircraft contrail," Proceedings of Impact of Emissions from Aircraft and Spacecraft upon the Atmosphere, an International Scientific Colloquium, Cologne, Germany, April 18-20, 1994, U. Schumann and D. Wurzzel, Editors, 106-112.

Quackenbush, T. R., Teske, M. E., and Bilanin, A. J. (1993) "Computation of Wake/exhaust mixing downstream of advanced transport aircraft," AIAA Paper No. 93-2944.

Quackenbush, T. R.., Teske, M. E.. and Bilanin, A. J.. (1996) "Dynamics of Exhaust Plume Entrainment in Aircraft Vortex Wakes," AIAA paper No. 96-0747.

Seinfeld, J. H., (1986) "Atmospheric Chemistry and Physics of Air Pollution," Wiley, New York, 1986.

Schumann, U. et al. (1996) "In situ observation of Particles in Jet Aircraft Exhausts and Contrails for different sulfur-containing Fuels," *J. Geophys. Res.*, 101, 6853-6869.

Wang, Z. and Chen, J.-Y. (1997) "Numerical Modeling of Mixing and Chemistry in Near-Field Engine Exhaust Plumes," *J. Geophys. Res..*, 102, 12871-12883.

Weisenstein, D. K., Ko, M. K. W., Rodriguez, J. M., and Sze, N. D. (1993) "Impact of Heterogeneous Chemistry on Model Calculated Ozone changes due to High Speed Civil Transport Aircraft, "Geophys. *Lett.*, 18, 1991-1994.

Wu, J. and Menon, S. (1998a) "Numerical Studies of Near-Field Plume-Vortex Interactions," AIAA Paper No. 98-2902, 29th AIAA Fluid Dynamics Conference, June 15-18, Albuquerque, NM.

Wu, J. and Menon, S. (1998b) "Large-Eddy Simulations of Near field Plume-Vortex Interactions," *J. Geophysics Research* (submitted).

Effects of Micro- and Macroscale Turbulent Mixing on the Chemical Processes in Engine Exhaust Plumes

S. MENON AND J. WU

School of Aerospace Engineering, Georgia Institute of Technology, Atlanta, Georgia

(Manuscript received 28 April 1997, in final form 19 November 1997)

ABSTRACT

Turbulent mixing and chemical reactions in the near field of an engine exhaust jet plume have been investigated using a mixing model that explicitly incorporates both large- and small-scale turbulent mixing and the molecular diffusion effects. A reduced reaction mechanism that accurately reproduces results of a detailed mechanism for the lower stratosphere was used to simulate the exhaust plume dynamics of a typical high-speed civil transport aircraft. This study shows that, compared to predictions based on models that do not include small-scale mixing and/or molecular diffusion effects, 30% less O_3 and 15% less NO_x are depleted in the near field of the plume. This suggests that the lack of local mixing can have an inhibiting effect on ozone depletion in the near-field plume. Inclusion of heterogeneous kinetics involving the formation of nitric and sulfuric acid due to water condensation on soot particles showed that 15% of the available NO_x is converted into its inactive form but has a negligible effect on O_3 concentration. This method also provides appropriate conditions for the plume–vortex interaction stage where more complex chemistry, including heterogeneous kinetics, is likely to take place.

1. Introduction

The projected increase in future aviation, especially in heavily trafficked flight corridors, has the potential for causing a major upper-atmospheric perturbation. Recent research has focused on the potential impact on the upper troposphere and on the lower stratosphere due to exhaust emissions from the proposed fleets of supersonic high-speed civil transport (HSCT) and/or advanced subsonic transport (AST) operating in the transatlantic and Pacific rim flight corridors (e.g., Brasseur et al. 1990; Beck et al. 1992; Stolarski and Wesoky 1995; Friedl 1997). Emissions from individual aircraft are initially highly localized in the engine plume wake and rapidly dispersed in the far wake. However, the chemical processes in the hot species-rich plume may lead to changes on a global scale if this causes marked changes in the far-field exhaust composition. This concern, especially as related to the potential deployment of HSCT and/or AST fleets, has led to many investigations focusing on the near-field (characterized as the exhaust plume and plume–wing tip vortex interaction regimes) chemical processes. Gas phase chemical processes due to NO_x (NO, NO_2), HO_x (OH, HO_2, H_2O_2), and SO_x (SO, SO_2, SO_3, HSO_3, H_2SO_3) species and heterogeneous kinetics due to exhaust aerosols and soot particles in the plume are being studied (Fahey et al. 1995a,b; Brown et al. 1996a,b; Weisenstein et al. 1996). Both measurements and numerical studies in the near field indicate a potentially significant impact on the atmosphere, depending upon the significance of both homogeneous and heterogeneous kinetics. In particular, the conversion of emitted NO_x to inactive forms of nitrogen and the impact of plume processing of sulfur due to the formation of a large number of aerosol particles in the plume have been the focus of many recent investigations (Friedl 1997; Stolarski et al. 1995; WMO 1995).

The net effect of NO_x emissions on ozone is known to be reduced if some of it is converted to its less reactive form (via the hydrolysis of N_2O_5 to HNO_3). Near-field modeling studies (Miake-Lye et al. 1993, 1994; Quackenbush et al. 1993) and measurements (Fahey et al. 1995a) indicate that relatively small amounts of NO_x are deposited in the form of nitrous and nitric acid, with the bulk remaining in the form of NO_x. Thus, both data and measurements suggest that there is only a minimal conversion of emitted NO_x into other species in the near-field plume. On the other hand, the sulfur compounds in the near-field plume are known to be significantly affected by the chemical processes. Recent calculations (Brown et al. 1996a,b) and experimental observations (Fahey et al. 1995b; Karcher and Fahey 1997) suggest that many small particles are formed in the plume via binary homogeneous nucleation of sulfuric acid with water. This increase in the overall aerosol surface area in the plume has the potential for changing the exhaust composition in the far-field wake.

Corresponding author address: Prof. S. Menon, School of Aerospace Engineering, Georgia Institute of Technology, Atlanta, GA 30332-0150.
E-mail: menon@falcon.ae.gatech.edu

Many past studies (Miake-Lye et al. 1993, 1994; Brown et al. 1996a) of the near-field plume have employed the standard plume code, SPF-II (Dash et al. 1990). SPF-II is a space-marching, axisymmetric solver and employs the standard $k - \varepsilon$ turbulence model to obtain the steady-state field. The computational efficiency of this code is achieved by using an axisymmetric approach and by modeling all chemical and fluid dynamic processes in the steady-state limit. Farther downstream, the evolution of the plume and its interaction with the wingtip vortices are modeled using codes such as UNIWAKE (Quackenbush et al. 1993, 1996) which uses the output from the SPF-II calculation of the plume as inflow conditions. UNIWAKE is a 3D unsteady, parabolized Navier–Stokes solver that incorporates the effect of turbulence using the second-order Reynolds stress closure. Detailed gas phase kinetics have been studied using this code. However, since all turbulent scales are modeled by the closure (in both SPF-II and UNIWAKE codes), many physical time-dependent processes that govern mixing and combustion processes (such as molecular diffusion and small-scale turbulent mixing) are ignored (or modeled) in these codes. To include the time-dependent physics, methods such as large-eddy simulations (LES) can be employed. Although LES has been successfully used in the far field with limited (i.e., one-step chemistry) or no chemistry modeling (e.g., Sykes et al. 1992; Lewellen and Lewellen 1996), this approach is not practical for the near-field studies due to the computational cost (orders of magnitude larger than the parabolized methods) since a large number of species must be simulated along with the fluid dynamics. It would be computationally feasible if a nonreacting LES flow field was used as a representative fluid dynamic snapshot and the chemical reactions were simulated assuming no temporal dependence between the fluid motion and the chemical processes. However, this approach would not resolve the importance (if any) of the unsteady mixing processes on the chemical processing in the plume. In addition, decoupled LES would not allow for proper transport of the various species and would result in potentially incorrect estimation of the chemical effect. Due to these factors, it appears that no study has been reported on the effects of unsteady turbulent mixing in the near-field plume dynamics to date.

This paper describes an innovative simulation methodology that allows proper characterization of the effect of small-scale mixing processes on the chemical processes. Inclusion of microscale mixing (missing in the earlier plume studies) should result in a physically consistent simulation model and should provide a more accurate estimate of the radical (e.g., OH, NO_x, CO, SO_x) reactions that are highly dependent upon the mixing process. The model described in this paper allows incorporation of detailed kinetics (if warranted) without making the computational cost unduly exorbitant. The key innovative feature of this approach is that the microscale mixing processes (diffusion and turbulent stirring) are explicitly simulated at their characteristic timescales. Thus, turbulence–chemistry interaction evolves in a consistent manner and its effects on the scalar fields are obtained by statistically averaging over the period of simulation. This is in contrast to steady-state methods where all time-dependent processes are modeled.

The domain simulated in this study extends from the engine nozzle exit to a point where the plume begins to interact with the wingtip vortex. This domain spans a distance of about 1 km and simulates the plume for about 1–2 s. Although this spatial and temporal extent is very small relative to the overall scales for plume evolution, this near-field region has been identified as the region where significant chemical processing occurs (Brown et al. 1996a). The engine exhaust conditions are chosen for a representative HSCT aircraft flying at an altitude of 18 km along with appropriate ambient conditions (Brown et al. 1996a; Miake-Lye et al. 1993). Both homogeneous and heterogeneous kinetics in the near-field plume are investigated. Gas phase kinetics involving HO_x, NO_x, and SO_x reactions are simulated using a reduced reaction mechanism that significantly reduces the computational cost without losing any accuracy in the prediction of the important species. Condensation of water on emitted soot particles and heterogeneous kinetics resulting in condensed HNO_3 and H_2SO_4 formation on the surface of condensed solid water are investigated in this study. More detailed heterogeneous kinetics related to soot adsorption, homogeneous binary nucleation of sulfur particles, volatile H_2O–H_2SO_4 condensation on aerosol particles, and aerosol coagulation (Brown et al. 1996a) are deferred for a later study.

The unsteady mixing model demonstrated here is expected to provide a more accrurate estimate of chemical processing in the species-rich plume when compared to SPF-II. Thus, the outflow (time-averaged data) from this model can provide a more accurate inflow condition for the regime where the plume interacts with the wingtip vortices. UNIWAKE calculations or LES of this regime can employ this data. Currently, LES in the plume–vortex regime is using this initialization approach (Menon and Wu 1997).

2. Turbulent mixing models

In this study, the predictions using the new mixing model are compared to the predictions made using other well-known mixing models. These models are described below.

a. Perfectly stirred reactor/well-mixed reactor (PSR/WMR)

This model is also sometimes called the "continuously stirred" reactor or "box" model (e.g., Kee et al. 1989; Karcher 1995; Danilin et al. 1994) and is the most commonly used model (in one variation or other) in aircraft plume studies. In this model, there is a continuous mass flow in and out of a constant volume reactor. Within this

reactor, the scalar fields are assumed perfectly mixed so that the rate of chemical processes is controlled by the kinetics of the reaction mechanism and not by the mixing process. The key parameter for the calculation is the residence time in the reactor that determines the final reacted state of the initially specified scalar fields. These models cannot account for turbulent mixing by both the large and the small scales and, therefore, cannot be used to study turbulence effects. On the other hand, due to its computational efficiency, PSR/WMR codes can be used to investigate detailed multispecies reaction mechanisms very quickly and to evaluate reduced kinetics. The mathematical and computational aspects of this modeling approach are given in numerous past studies (e.g., Kee et al. 1989; Danilin et al. 1994) and, therefore, are omitted for brevity.

b. *Probability density function (PDF) simulation method*

In this approach, the joint scalar PDF for the scalar fields is solved by a transport equation using the Monte Carlo technique. The mean flow is modeled by the Reynolds stress closure with a downstream marching algorithm (Wang and Chen 1997) as in the standard plume codes (e.g., SPF-II). Although turbulence effects are explicitly included in the direct estimation (i.e., without any modeling) of the chemical source term, the turbulent mixing is included using an ad hoc model and molecular diffusion is ignored. This approach was used extensively earlier (Menon and Chen 1995; Wang and Chen 1997) to evaluate chemical kinetics. In this paper, we will compare predictions using the new mixing model against the PDF predictions.

c. *The linear-eddy model (LEM) for scalar mixing*

This model explicitly treats three physical processes: 1) large-scale turbulent entrainment, 2) small-scale turbulent mixing, and 3) reaction–diffusion at the small scales as independent processes that occur at their characteristic times. In the following, a brief overview of these processes are given. Subsequently, in section 2d, more details pertaining to the actual implementation for exhaust plume simulations are provided to identify the new and innovative features of this modeling approach.

In LEM, the scalar reaction–diffusion equations are solved on a 1D domain (and hence, called linear eddy) using an explicit finite-difference scheme on a high-resolution grid so that all the length scales (e.g., from the integral scale L to the Kolmogorov scale η) are resolved. Thus, the reaction–diffusion evolution is considered exact and requires no closure. Although this evolution is simulated in 1D, this domain is not a physically fixed spatial domain. Rather, this domain represents an instantaneous statistical slice of the 3D turbulent field at the chosen location. In the present formulation, this slice is correlated (in a statistical sense) to the radial extent of the exhaust plume, and the "mean" radial scalar field at a given axial location is obtained by statistically averaging many realizations of the 1D slice. The axial evolution of the exhaust plume is simulated by convecting this 1D slice downstream using appropriate conservation of mass and momentum.

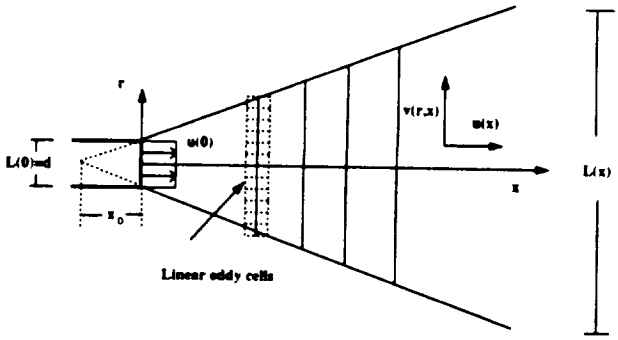

FIG. 1. Schematic of the computational domain.

Simultaneous to (but independent of) the reaction–diffusion simulation, turbulent mixing by the eddies in the flow field is implemented using a stochastic Monte Carlo simulation. This simulation models the effect of turbulent eddies on the scalar field and is captured in the model as a rearrangement of the scalar gradients using a mapping process. This mapping process (described in section 2d) occurs at discrete intervals and can be physically correlated to the action of a turbulent eddy on the scalar field. The eddy size, the eddy location, and the mapping frequency (i.e., the turbulent mixing timescale) are all determined using inertial range scaling as applicable to full 3D turbulence. Thus, even though the present model is 1D, the effects of the high Reynolds number 3D turbulence is included. It is this particular feature that makes the present approach capable of capturing realistic 3D turbulence effects on the reaction–diffusion processes within a 1D formulation.

The ability of this model to capture realistic, high Reynolds number flow features in reacting shear layers, mixing layers, and jets has been reported in numerous studies in the past (e.g., Kerstein 1987, 1989, 1990; Menon et al. 1994). However, to study the engine exhaust plumes new features had to be developed and incorporated. These new features are described in the following section.

d. *Application of LEM for jet plume studies*

Figure 1 shows a schematic of an exhaust jet plume and the discretization used in the 1D radial LEM model. To incorporate the axial spreading, we assume that the exhaust plume is reasonably approximated by a round free jet. Therefore, the well-known round-jet similarity scaling law (Landau and Lifshitz 1959) is used to approximate jet spreading. The resulting decrease of the mean jet velocity with the axial distance is given as

$$\frac{u(0)}{u(x)} = c\left(\frac{x - x_0}{d}\right), \tag{1}$$

where $u(0)$ is the axial jet velocity at the nozzle exit, d is the nozzle diameter, and x_0 is the virtual origin of the jet (see Fig. 1). The value of the spreading rate $c = 0.11$ is estimated from experimental data for a free jet. However, when there is a coflowing air (as in real cases of the engine exhaust of a flying aircraft), the jet spreading rate is decreased. This can be included by changing the value of c. In Eq. (1), x_0/d is set equal to -5 so that the mean flow similarity is satisfied for all $x > 0$. A constraint of the present study is that within the turbulent zone, the radial variation of the mean axial velocity $u(x, r)$ is neglected and, thus, $u(x)$ is given by Eq. (1) for the entire jet plume. However, the turbulent mixing process is radially dependent and is included in this formulation. The axial evolution of the radial line is related to the computational time t according to the relation $dx/dt = u(x)$, where x is the axial location.

1) Molecular diffusion

The small-scale molecular diffusion effects are obtained by numerically solving the reaction–diffusion equation:

$$\frac{\partial Y_k}{\partial t} = \frac{\dot{w}_k W_k}{\rho} - \frac{1}{\rho r}\frac{\partial}{\partial r}(\rho r Y_k V_k), \tag{2}$$

within the 1D radial domain. Here, Y_k, W_k, V_k, and $\dot{w}_k$ are, respectively, the kth species mass fraction, molecular weight, diffusion velocity, and molar production rate. Also, ρ is the mixture density, and the kth species diffusion velocity is determined using Fick's law of diffusion: $V_k = -(D_k^m/X_k)\partial X_k/\partial r$, where X_k and D_k^m are, respectively, the kth species mole fraction and diffusion coefficients. The diffusion coefficients and the molar production rates for each species are obtained from the general-purpose CHEMKIN library (e.g., Kee et al. 1989). Thus, differential diffusion effects are also included.

The coordinate r in Eq. (2) is the local radial coordinate that is discretized into cells of equal size Δr (see Fig. 1). The cell size is chosen to resolve the effects of all turbulent eddies present in the flow, and the domain is prescribed as $|r| < L(x)$, where $L(x)$ is the integral length scale defined as $L(x) = c(x - x_0)$. This relation for $L(x)$ allows inclusion of the spreading rate in the model without actually modeling the free jet. Thus, for example, the increase in the jet volume (due to large-scale entrainment) as a function of axial distance (which increases the local integral length scale) is included explicitly into the model. In contrast, in the PDF method, although the jet spreading rate can be enforced, the resulting mixing process cannot be physically implemented since mixing is modeled using an ad hoc model.

The reaction–diffusion equation (2) is solved using a second-order, finite difference scheme (a sixth-order scheme was also used; however, since all length scales are resolved in the 1D domain, it was determined that the computationally efficient, second-order scheme was sufficient) and time integrated at the local time step using a second-order scheme. For stability, the time step is determined by the minimum of the diffusion and chemical time steps.

Note that in Eq. (2) the convection terms in the conventional species equations (i.e., the terms $u_i\partial Y_k/\partial x_i$) are not included because turbulent transport by the velocity field is explicitly included as a distinct (and independent) mechanism, as described below.

2) Turbulent convection

The effect of turbulent stirring (or convection) is represented by stochastic mixing events that interrupt the deterministic solution of the reaction–diffusion equations. Each mixing event (incorporated as a mapping process) is interpreted as the action of a single eddy on the scalar field. *Three* random quantities must be specified before implementing the mapping or rearrangement event: 1) the segment (or eddy) size, 2) the location of the event, and 3) the frequency of the event. The eddy size, ℓ, is determined randomly from a distribution (or PDF) of eddy sizes, $f(\ell)$ $\eta \le \ell \le L$. The event location is randomly chosen within the 1D domain using another distribution function, and the event rate (or time) is determined using an analogy between fluid dispersion and turbulent diffusivity (Kerstein 1987, 1989). Detailed discussions of these parameters have been reported elsewhere (Kerstein 1989; Menon et al. 1994). However, new modifications were needed for plume studies and are described below.

The eddy size ℓ is chosen randomly from a power-law distribution $f(\ell)$ within the range $\eta < \ell < L_m(x; r)$, where $L_m(x; r)$ is the largest eddy at the radial location r. The PDF $f(\ell)$ is determined from inertial range scaling rules (see Kerstein 1989, for detailed analysis):

$$f(\ell) = \frac{5}{3L_m(x; r)}\frac{1}{[(L_m(x; r)/\eta)^{5/3} - 1]}\left(\frac{\ell}{L_m(x; r)}\right)^{-8/3}, \tag{3}$$

in terms of $L_m(x; r)$. The local eddy size $L_m(x; r)$ is related to $L(x)$ by the relation

$$L_m(x; r) = \begin{cases} L(x), & |r| < L(x)/2, \\ 2[L(x) - |r|], & |r| \ge L(x)/2. \end{cases} \tag{4}$$

Equation (4) ensures that the eddies taking part in the mixing processes are not larger than the integral scale and that the chosen eddies physically reside in the jet shear layer. These requirements are consistent with experimental observations of large-scale entrainment and small-scale turbulent mixing in jet flows. As noted earlier, this information cannot be incorporated in the PSR/WMR or PDF models.

Once the eddy size is chosen, the effect of this eddy

TABLE 1. Detailed gas phase reaction mechanisms for stratosphere (Miake-Lye et al. 1993). The mechanism contains 24 species.

No.	Reactions	A (cm^3 molecule^{-1} s^{-1})	n	E/R (K)
		O_x reactions		
1	$O + O_2 + M \Rightarrow O_3 + M$	3.00×10^{-34}	−2.3	0
2	$O + O_3 \Rightarrow O_2 + O_2$	8.00×10^{-12}	0.0	2060
3	$H + O_2 + M \Rightarrow HO_2 + M$	5.20×10^{-32}	−1.6	0
4	$H + O_3 \Rightarrow OH + O_2$	1.40×10^{-10}	0	470
5	$HO_2 + H \Rightarrow OH + OH$	7.30×10^{-11}	0	0
6	$HO_2 + H \Rightarrow H_2O + O$	1.60×10^{-12}	0	0
7	$HO_2 + H \Rightarrow H_2 + O_2$	6.50×10^{-12}	0	0
8	$OH + O \Rightarrow H + O_2$	2.20×10^{-11}	0	−120
9	$HO_2 + O \Rightarrow OH + O_2$	3.00×10^{-11}	0	−200
10	$H_2O_2 + O \Rightarrow OH + HO_2$	1.40×10^{-12}	0	2000
11	$OH + HO_2 \Rightarrow H_2O + O_2$	4.80×10^{-11}	0	−250
12	$OH + O_3 \Rightarrow HO_2 + O_2$	1.60×10^{-12}	0	940
13	$OH + OH \Rightarrow H_2O + O$	1.60×10^{-12}	0	940
14	$OH + OH + M \Rightarrow H_2O_2 + M$	6.60×10^{-31}	−0.8	0
15	$OH + H_2O_2 \Rightarrow H_2O + HO_2$	2.90×10^{-12}	0	160
16	$OH + H2 \Rightarrow H_2O + H$	5.50×10^{-12}	0	2000
17	$HO_2 + HO_2 \Rightarrow H_2O_2 + O_2$	2.30×10^{-13}	0	−600
18	$HO_2 + O_3 \Rightarrow OH + 2O_2$	1.10×10^{-14}	0	500
		NO_x reactions		
19	$N + O_2 \Rightarrow NO + O$	1.50×10^{-11}	0	3600
20	$N + NO \Rightarrow N_2 + O$	3.40×10^{-11}	0	0
21	$NO + O + M \Rightarrow NO_2 + M$	4.70×10^{-28}	−1.5	0
22	$NO_2 + O \Rightarrow NO + O_2$	6.50×10^{-12}	0	−120
23	$NO_2 + O + M \Rightarrow NO_3 + M$	8.10×10^{-27}	−2	0
24	$NO_3 + O \Rightarrow NO_2 + O_2$	1.00×10^{-11}	0	0
25	$H + NO_2 \Rightarrow OH + NO$	4.00×10^{-10}	0	340
26	$NO + O_3 \Rightarrow NO_2 + O_2$	2.00×10^{-12}	0	1400
27	$NO + HO_2 \Rightarrow NO_2 + OH$	3.70×10^{-12}	0	−250
28	$NO + NO_3 \Rightarrow NO_2 + NO_2$	1.50×10^{-11}	0	−170
29	$OH + NO + M \Rightarrow HONO + M$	1.90×10^{-24}	−2.6	0
30	$OH + NO_2 + M \Rightarrow HNO_3 + M$	2.20×10^{-22}	−3.2	0
31	$OH + HONO \Rightarrow H_2O + NO_2$	1.80×10^{-11}	0	390
32	$OH + HNO_3 \Rightarrow H_2O + NO_3$	7.20×10^{-15}	0	−785
33	$NO_2 + O_3 \Rightarrow NO_3 + O_2$	1.20×10^{-13}	0	2450
34	$NO_2 + NO_3 + M \Rightarrow N_2O_5 + M$	1.00×10^{-20}	−3.9	0
35	$N_2O_5 + M \Rightarrow NO_2 + NO_3 + M$	1.70×10^{-8}	−4.4	11 080
36	$HO_2 + NO_3 \Rightarrow OH + NO_2 + O_2$	2.50×10^{-12}	0	0
37	$HO_2 + NO_3 \Rightarrow HNO3 + O_2$	1.90×10^{-12}	0	0
38	$OH + NO_3 \Rightarrow HO_2 + NO_2$	2.30×10^{-11}	0	0
		SO_x and CO_x reactions		
39	$SO + O_2 \Rightarrow SO_2 + O$	2.60×10^{-13}	0	2400
40	$SO + O_3 \Rightarrow SO_2 + O_2$	3.60×10^{-12}	0	1100
41	$SO + NO_2 \Rightarrow SO_2 + NO$	1.40×10^{-11}	0	0
42	$HSO_3 + O_2 \Rightarrow HO_2 + SO_3$	1.30×10^{-12}	0	330
43	$SO_2 + OH + M \Rightarrow HSO_3 + M$	4.50×10^{-23}	−3.3	0
44	$SO + OH \Rightarrow SO_2 + H$	8.60×10^{-11}	0	0
45	$SO_3 + H_2O \Rightarrow H_2SO_4$	1.20×10^{-15}	0	0
46	$CO + OH \Rightarrow CO_2 + H$	1.60×10^{-13}	0	0

on the scalar field is implemented as a stochastic rearrangement event called *block inversion* (Kerstein 1987) that mimics the effect of turbulent stirring on the scalar field. Given the eddy size ℓ from $f(\ell)$, the block inversion process involves first, locating randomly the center of the eddy within the radial line, and second, selecting the scalar field(s) $Y_k(r, t)$ in an interval $(r_0 - \ell/2, r_0 + \ell/2)$ and replacing it with the scalar fields $Y_k(2r_0 - r, t)$. Physically, inversion results in an instantaneous 180° rotation of the scalar fields contained in the eddy. Although this instantaneous mapping is an artifact of the model (since turbulent eddies take finite time to transport the scalars), past studies (Kerstein 1987, 1989) have shown that this discrete mapping does not cause significant errors since it occurs at the local mixing time, and a multitude of these mappings is ensemble averaged to obtain the statistically "mean" field. Molecular Fickian diffusion subsequently smoothens the sharp scalar gradients caused by these inversion events. In this manner, both diffusion and stirring play competitive and collaborative roles during the mixing process. Since all the length scales are resolved, no special care is needed during the diffusion step to deal with the sharp scalar gradients caused by the turbulent stirring. In an axisymmetric plume the cell volume must increase with radial

TABLE 2. Reduced gas phase reaction mechanism for stratosphere (Wang and Chen 1997). The mechanism contains 14 species.

No.	Reaction mechanism
(I)	$3O_2 = 2O_3$
(II)	$2OH + O_3 = 2O_2 + H_2O$
(III)	$2OH = O_2 + H_2$
(IV)	$2O_2 + NO = NO_2 + O_3$
(V)	$OH + NO = HONO$
(VI)	$OH + NO_2 = HNO3$
(VII)	$2O_2 + SO_2 = O_3 + SO_3$
(VIII)	$SO_3 + H_2O = H_2SO_4$
(IX)	$O_3 + CO = O_2 + CO_2$

Reduced reaction rates

$\omega_I = \omega1 + \omega3 + \omega14 - \omega18 + \omega22 + \omega23 + \omega25 - \omega26 - \omega27 - \omega28 + \omega32 - \omega36 - \omega37 + \omega41$
$\omega_{II} = \omega6 + \omega11 + \omega13 + \omega15 + \omega16 + \omega31 + \omega32$
$\omega_{III} = \omega7 - \omega16$
$\omega_{IV} = \omega21 - \omega22 - \omega25 + \omega26 + \omega27 + \omega28 + \omega31 - \omega41$
$\omega_V = \omega29 - \omega31$
$\omega_{VI} = \omega30 - \omega32 + \omega37$
$\omega_{VII} = \omega42$
$\omega_{VIII} = \omega45$
$\omega_{IX} = \omega46$

distance even though a constant cell size is used to facilitate the mapping process. Thus, a direct implementation of the mapping would cause mass conservation errors. Therefore, to conserve mass each mapping from a cell "a" with volume V_a containing a scalar Y_a to a cell "b" with volume V_b containing the scalar Y_b, the new (denoted by the superscript n) mapped scalar value Y_b^n becomes

$$Y_b^n = \frac{(\rho_a Y_a - \rho_b Y_b)V_a + \rho_b Y_b V_b}{(\rho_a - \rho_b)V_a + \rho_b V_b}. \quad (5)$$

Here, ρ_a and ρ_b are, respectively, the mass density in cells "a" and "b." This mapping conserves the scalar fields even when the cells have different volumes.

The second element of the turbulent stirring process requires locating the turbulent eddy within the local 1D domain. The location of the block is determined randomly from a distribution function:

$$G(|r_0|) = \left[\frac{|r_0|}{L(x)}\right]^{1/2}, \qquad 0 \le |r_0| \le L(x). \quad (6)$$

Finally, the frequency of the stirring event λ [or the timescale for the mapping, $\tau_{stir} = (\lambda L)^{-1}$] is determined based on inertial range scaling laws [details are given in Kerstein (1987) and Menon et al. (1994) and, therefore, omitted here for brevity]:

$$\lambda = \frac{v}{L(x)^3}\left[\frac{L(x)}{\eta}\right]^{4/3}\frac{(L(x)/\eta)^{5/3} - 1}{1 - (\eta/L(x))^{4/3}}. \quad (7)$$

3) DILATION PROCESS

The x dependence of the axial component u of the mean velocity implies a mean flow and a radial spreading due to entrainment. These features have to be included to capture the global dynamics of the jet. Using mass conservation, the radial mean motion can be determined from the continuity equation:

$$\frac{v}{r} + \frac{\partial v}{\partial r} = -\frac{\partial u}{\partial x}. \quad (8)$$

Since $u = u(x)$, Eq. (8) implies $v = -(r/2)\partial u/\partial x$. To incorporate the effect of the radial motion within the 1D formulation, the radial grid is stretched at a rate prescribed by Eq. (8) without changing the scalar value at each cell. Stretching is implemented deterministically by means of dilation events at regular time intervals. By incorporating radial flow, the algorithm conserves total scalar flux corresponding to the quantity $\pi u(x) \int_{-\infty}^{\infty} |r|\rho Y_i(x, r)\, dr$ in the simulation.

e. Chemical reaction mechanisms

The study of atmospheric chemistry within the mixing zone requires incorporation of many species and their associated chemical reactions. Depending upon the altitude, ambient and engine exhaust conditions as well as both gas phase and heterogeneous chemical processes have to be included. Although detailed kinetics can be simulated using the LEM approach, the computational cost can be quite significant. Therefore, using sensitivity analysis (Menon and Chen 1995; Wang and Chen 1997), a detailed mechanism (used earlier by Miake-Lye et al. 1993) of 24 species, 46 reactions for the lower stratosphere was reduced to a 14 species, 9 reactions mechanism. Tables 1 and 2 show, respectively, the detailed and the reduced mechanisms. Reduction of the reaction set is achieved by an implicit assumption that some of the species are under quasi-equilibrium. However, the accuracy of the reduced kinetics has been verified by using WMR and PDF calculations (Menon and Chen 1995; Wang and Chen 1997). Since the reduced chemistry is computationally very efficient, it has been employed for the present studies.

Heterogeneous chemical processes in the near-field exhaust plume can significantly modify chemical processing in the plume. Processes such as homogeneous binary nucleation, soot adsorption, condensation on aerosols, and aerosol coagulation will be incorporated in a later study. Here, using simplified reactions occurring on solid condensed water (on soot particles), the effect of the following heterogeneous reactions on the gas phase species distribution (in particular, NO_x, SO_3, H_2SO_4) has been studied:

$$N_2O_5 + H_2O(c) \rightarrow 2HNO_3(c)$$

and

$$SO_3 + H_2O(c) \rightarrow H_2SO_4(c). \quad (9)$$

Here, (c) indicates the condensed (solid) state. Condensation of water on soot particles is possible because the

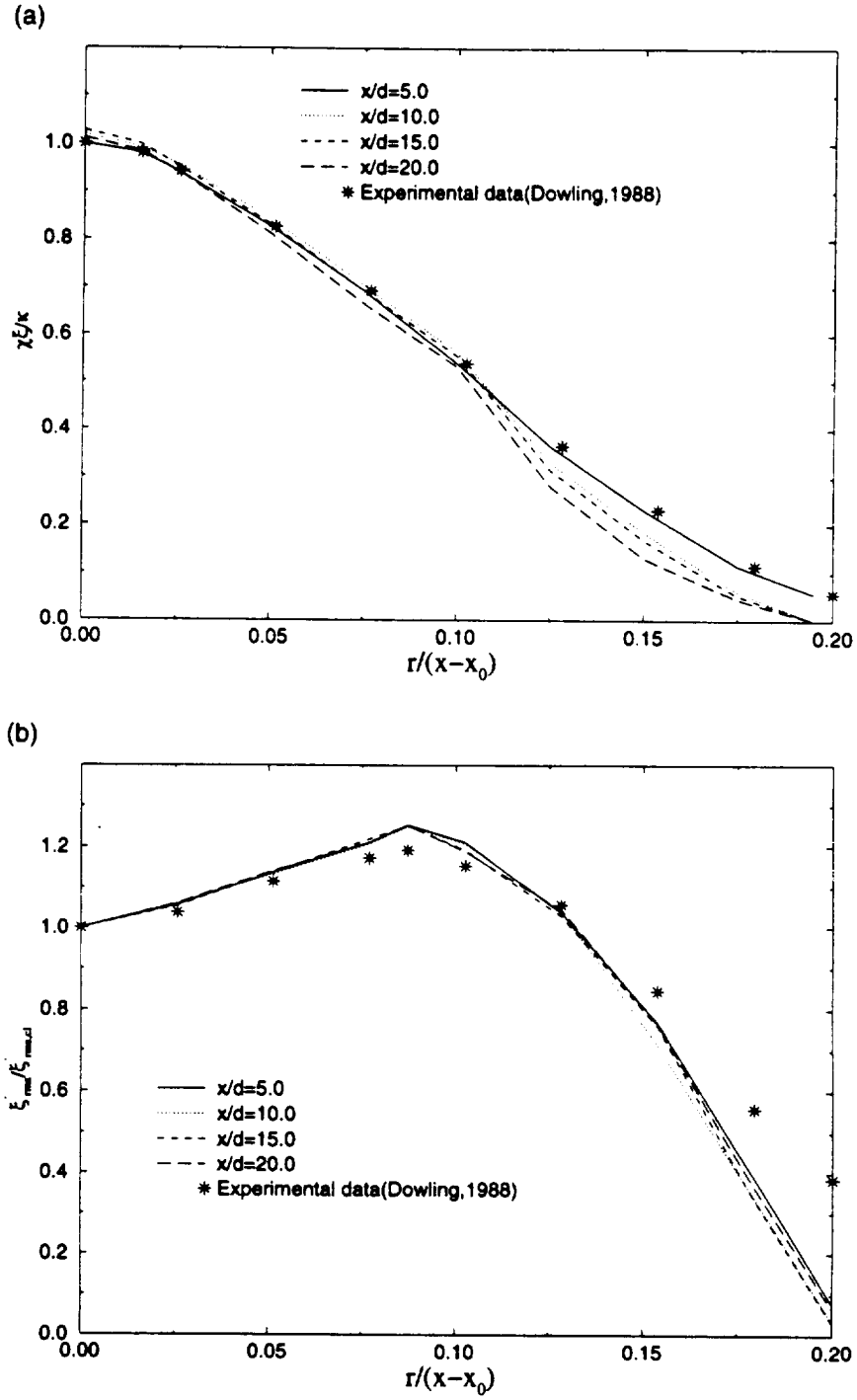

FIG. 2. (a) Variation of the scaled mean mixture fraction $\chi\zeta/\kappa$ in the radial direction. (b) Variation of normalized rms fluctuation of mixture fraction $\zeta'_{rms}/\zeta'_{rms,cl}$ in the radial direction.

temperature of the plume drops rapidly due to turbulent mixing of the exhaust plume with the ambient air (which is at a temperature of around 215 K). The reactions are assumed to occur immediately after the gas species is absorbed into the solid water. Thus, the heterogeneous reaction rates are proportional to the surface area of the condensed water and the flux of gas species N_2O_5 and SO_3 toward the condensed water surface. Once formed, both nitric and sulfuric acid remain in the solid state. Thus, evaporation of the condensed nitric acid is not covered in this study. A sticking coefficient (which accounts for the fact that a collision between the gas mol-

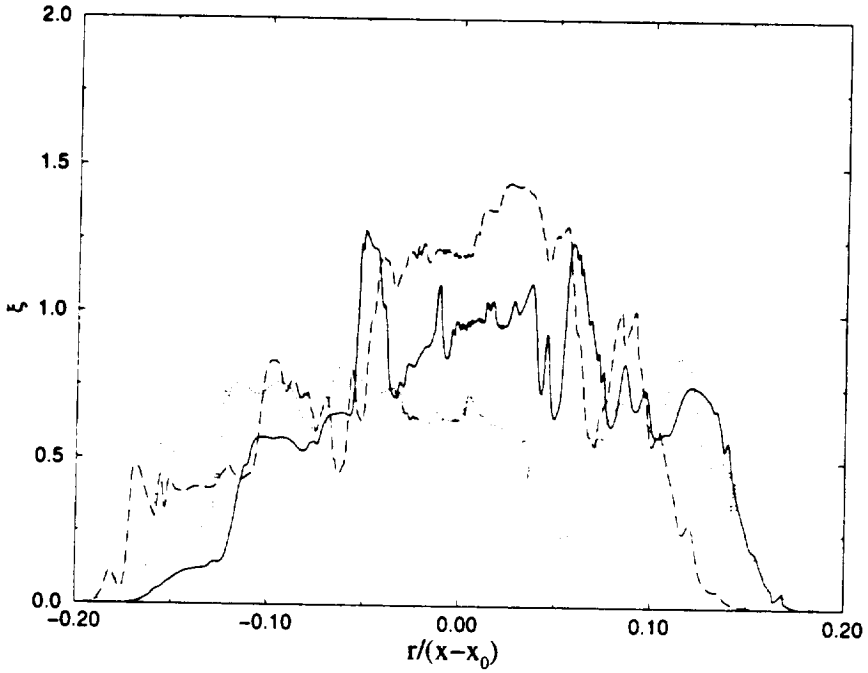

FIG. 3. Simulated instantaneous radial profiles of scaled mixture fraction $\chi\zeta/\kappa$ at $\chi = 25$ for air (Sc = 0.7) at $Re_{\kappa t} = 5000$. The curves show three different realizations of the scaled mixture fraction.

TABLE 3. Initial conditions for the near-field plume calculations for the HSCT (Brown et al. 1996a).

	HSCT	
	Exhaust flow condition	Ambient condition
Temperature (K)	561	205.2
Velocity (m s^{-1})	620(450)	0.0
Pressure (atm)	0.0573	0.0573
Mole fraction		
CO	2.4×10^{-5}	20×10^{-8}
CO_2	3.2×10^{-2}	3.5×10^{-4}
H	1.0×10^{-7}	2.8×10^{-21}
O	1.6×10^{-7}	3.1×10^{-13}
H_2	1.0×10^{-6}	5.2×10^{-7}
O_2	0.159	0.2098
OH	1.0×10^{-5}	2.8×10^{-13}
HO_2	9.9×10^{-8}	3.3×10^{-13}
H_2O_2	2.4×10^{-8}	2.1×10^{-12}
H_2O	3.0×10^{-2}	4.8×10^{-6}
N_2	0.779	0.789
NO	4.3×10^{-5}	5.9×10^{-11}
NO_2	4.8×10^{-6}	4.3×10^{-10}
HNO_3	0.0	3.3×10^{-9}
SO	0.0	0.0
SO_2	6.9×10^{-6}	0.0
SO_3	0.0	0.0
HSO_3	0.0	0.0
H_2SO_4	0.0	0.0
O_3	0.0	2.5×10^{-6}

ecule and condensed solid water may or may not result in the capture of the gas molecule) of 0.1 is used to represent the probability of gas being absorbed in solid water after hitting the surface (Fukuta and Walter 1970). The flux of gas species to the surface is determined using gas kinetic theory. To model the droplet surface area and water condensed on active nuclei, the active nuclei distribution is divided into a number of groups. In each group, the nuclei are assumed to have the same radius. Based on experimental data for typical engine gas exhaust (Miake-Lye et al. 1994; Brown et al. 1996a), a lognormal soot distribution is assumed. Water condensation is modeled by a kinetic process of aerosol droplet growth on preexisting nuclei particles and is based on a model developed by Fukuta and Walter (1970) for droplet growth by vapor diffusion.

In the current implementation, all particles are assumed to travel with the mean fluid velocity, and diffusion between particles is ignored. These simplifications are not necessary but are invoked here for computational expediency. The soot particle size distribution is divided into 11 groups. Thus, there are 11 more equations to solve with the source terms given by the kinetic model. This is equivalent to having 11 more species in every computational cell but, unlike the gas species, these 11 groups only take part in the turbulent stirring and dilation processes.

3. Numerical implementation

The numerical implementation of LEM is relatively straightforward. For computational purposes, the radial

TABLE 4. Comparison of predicted mole fractions of NO and NO_2 along the jet centerline.

	61 m	306 m	613 m	1128 m
NO (Brown et al. 1996a)	2.87×10^{-5}	1.74×10^{-6}	8.06×10^{-7}	4.59×10^{-7}
NO (spreading rate 0.011, present)	7.82×10^{-6}	1.41×10^{-6}	7.85×10^{-7}	4.13×10^{-7}
NO (spreading rate 0.055, present)	7.77×10^{-6}	1.77×10^{-6}	8.92×10^{-7}	4.46×10^{-7}
NO (spreading rate 0.11, present)	4.75×10^{-6}	1.48×10^{-6}	8.83×10^{-7}	4.43×10^{-7}
NO (Wang and Chen 1997)	—	3.0×10^{-6}	1.6×10^{-6}	—
NO_2 (Brown et al. 1996a)	3.47×10^{-6}	2.53×10^{-7}	1.24×10^{-7}	7.79×10^{-8}
NO_2 (spreading rate 0.011, present)	8.39×10^{-7}	1.68×10^{-7}	1.00×10^{-7}	5.77×10^{-8}
NO_2 (spreading rate 0.055, present)	8.71×10^{-7}	2.13×10^{-7}	1.15×10^{-7}	6.30×10^{-8}
NO_2 (spreading rate 0.11, present)	5.28×10^{-7}	1.79×10^{-7}	1.13×10^{-7}	6.19×10^{-8}
NO_2 (Wang and Chen 1997)	—	3.1×10^{-7}	1.8×10^{-7}	—

domain $-L(x) \le r \le L(x)$ is discretized into cells small enough to resolve the smallest eddy in the domain. Since the range of eddies $\eta < \ell < L(x)$ varies with the Reynolds number, the resolution must be fine enough so that grid effects are negligible for the entire domain of interest. For example, at $x/d = 10$ a resolution of 2000 cells was sufficient to resolve all the local scales, while at $x/d = 1000$ a resolution of 20 000 cells was required. Although this resolution requirement appears excessive, due to the 1D nature of the simulation model, the entire plume with 16 species can be simulated on a workstation (SGI Power Indigo) in about 12 h.

On the 1D domain, the reaction–diffusion equations are solved deterministically at the (stability based) time step. The reaction–diffusion evolution is interrupted by the turbulent stirring process that occurs at a time interval based on the event frequency [Eq. (7)]. The mean flow advection is then implemented using the dilation process to obtain the v velocity and the stretched grid at the next downstream location. Reaction–diffusion and turbulent stirring continues at the new axial location. This process is continued until the downstream outflow boundary is reached.

The main advantage of this method is that with proper choices of the inflow and ambient conditions, the evolution of the scalar fields (with and without chemical reactions) in the jet plume can be obtained as a function of radial location and time, that is, $Y_k = Y_k(r, t)$. Then the time domain is transformed to an axial location to obtain the spatial scalar field, $Y_k = Y_k(x, r)$. The spatially resolved statistics of the fluctuating scalar fields are obtained by averaging a large number (greater than 50) of realizations (using different initial random seeds) of the jet plume.

4. Results and discussion

To validate the present formulation, simulations of free jets were first carried out. The effects of changing the Reynolds number and the Schmidt number were investigated and compared to experimental data. Simulations for Re = 5000 and 20 000 and for Sc = 0.7 (corresponding to air) and Sc = 600 (corresponding to liquid) were carried out using the mixture fraction approach. Thus, the reaction–diffusion equation [Eq. (3)] was replaced by a single equation for the mixture fraction: $\partial\xi/\partial t = D\partial^2\xi/\partial r^2$. Here, $\xi(x, r)$ is the mixture fraction and D is the diffusion coefficient.

Since the jet is evolving in the self-similar regime, the mixture fraction field should also show self-similarity. This is demonstrated in Fig. 2a, which shows the mean mixture fraction radial profiles in the similarity form $\xi(x, r) = kg(\eta)/\chi$ at various axial locations plotted as a function of the scaled radial coordinate $\eta = r/(x - x_0)$. Here, $g(\eta)$ is the similarity form of the mixture fraction and $\chi = (x - x_0)/d$. The figure shows that self-similarity is achieved in the present calculation and that the result is consistent with experimental data (Dowling 1988). The radial profile of root-mean-square (rms) fluctuation of mixture fraction, shown in Fig. 2b, also exhibits self-similarity as expected. The occurrence of the peak rms fluctuation, where the slope of the mean profile is greatest, is a general feature in free jets and has been reproduced by the present model. The model predictions

TABLE 5. Comparison of predicted temperature and species mole fractions at a fixed axial location.

306 m	Brown et al. (1996a)	Present study with molecular diffusion	Present study without molecular diffusion	Present study with molecular diffusion and heterogeneous reaction
Temp	229.7 K	213.9 K	213.9 K	217.2 K
OH	1.54×10^{-9}	1.06×10^{-10}	0.87×10^{-10}	1.29×10^{-10}
NO	1.74×10^{-6}	1.77×10^{-6}	1.04×10^{-6}	1.39×10^{-6}
NO_2	2.53×10^{-7}	2.13×10^{-7}	1.24×10^{-7}	1.67×10^{-7}
HNO_3	3.98×10^{-8}	2.80×10^{-8}	2.62×10^{-8}	3.70×10^{-8}
SO_2	3.05×10^{-7}	2.37×10^{-7}	2.30×10^{-7}	3.18×10^{-7}
SO_3	1.02×10^{-9}	1.01×10^{-10}	0.96×10^{-10}	0.29×10^{-10}
H_2SO_4	3.19×10^{-9}	5.76×10^{-9}	5.70×10^{-9}	1.22×10^{-9}

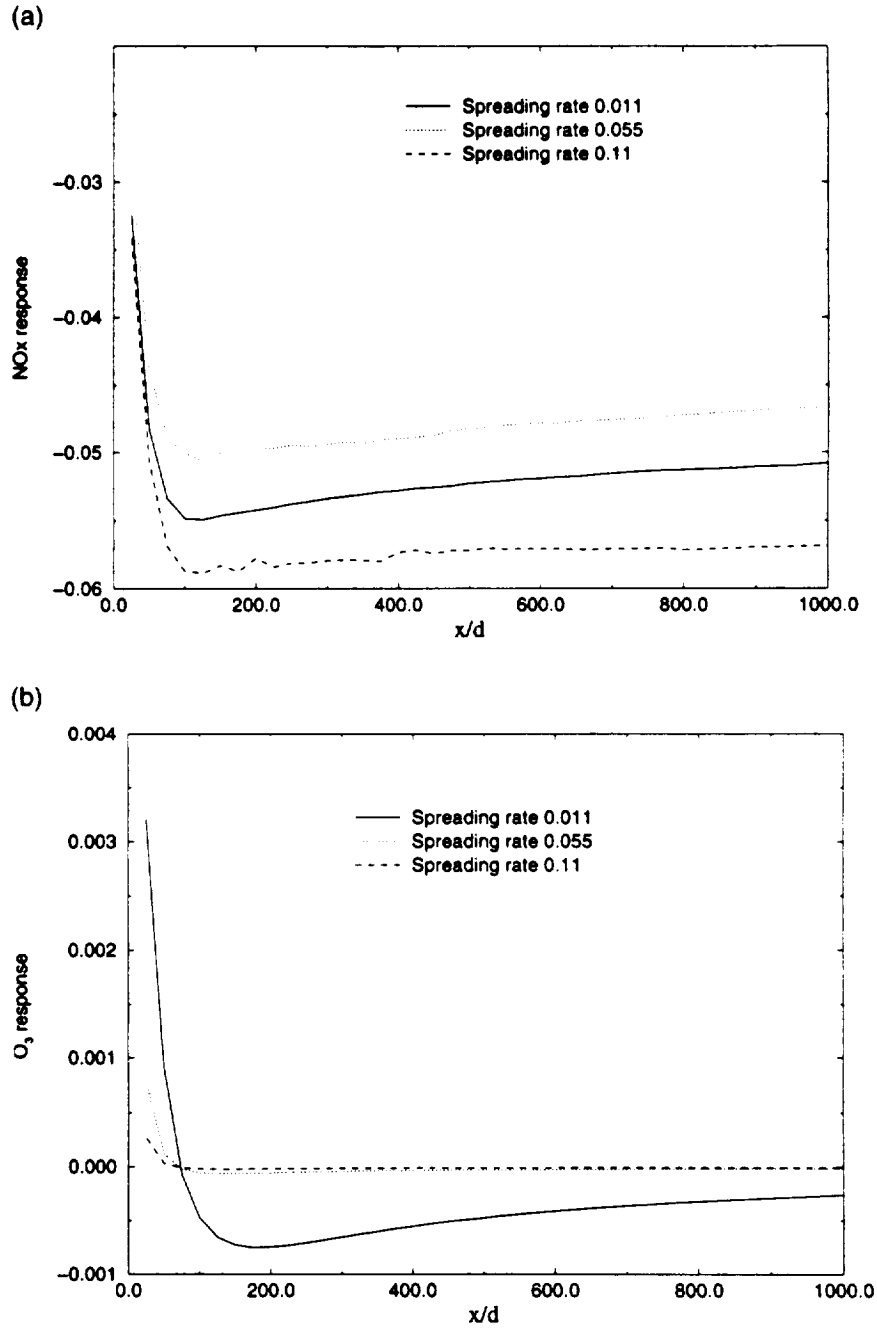

FIG. 4. (a) Axial NO_x response variation with spreading rate for an initial jet exit speed of 620 m s^{-1}. (b) Axial O_3 response variation with spreading rate for an initial jet exit speed of 620 m s^{-1}. (c) The O_3 depletion along the exhaust centerline (radially integrated).

deviate from the data near the edges of the jet. This is due to the intermittency (in the experiments) that was not included in the present formulation.

Three different realizations of the scalar field are shown in Fig. 3 for Re = 5000, Sc = 0.7, and at a location of $\chi = (x - x_0)/d = 25$. This is quite consistent with the experimental observations of Dahm and Dimotakis (1987). The scalar mixture fraction fluctuates about a constant scalar level near the centerline with a relatively sharp drop at the boundaries of the shear layer. This behavior is seen both in water shear layers (Sc = 600) and in air shear layers (Cruyningen et al. 1989).

The LEM approach was then implemented to study aircraft jet plumes. Simulations were carried out for representative conditions for the HSCT and are summarized

(c)

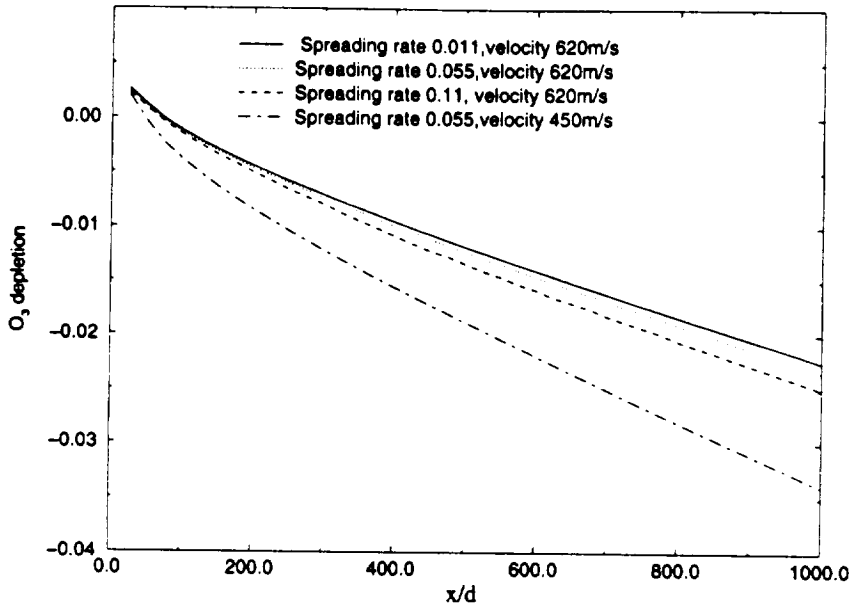

FIG. 4. (*Continued*)

in Table 3. To include the effects of the ambient flow surrounding the jet (which is not included in the present formulation but would effectively decrease the spreading rate), the spreading rate parameter c and the jet exit velocity were varied. The domain simulated was a region from the engine exit to 1000 jet diameters downstream. For a reference initial jet diameter of 1.2 m, this implies a domain of 1.2 km. Although this is an appropriate region for the near-field plume study (Quackenbush et al. 1993; Brown et al. 1996a), it should be noted that by the end of this domain, the engine exhaust plume could be entrained into the wingtip vortex. The plume–vortex interaction is not included in this study. However, the present simulation provides an appropriate boundary condition for the full 3D simulation of the plume–vortex interaction process (Menon and Wu 1997).

Several quantities describing the depletion of NO_x and O_3, such as the responses of NO, NO_2, O_3, and NO_x (sum of NO and NO_2) and the depletion of O_3 with respect to the initial NO_x, have been computed for all the simulations. However, only representative results are shown here. The species response is defined as

$$R_i = \frac{m_i(t) - m_{i,\text{total}}}{m_{i,\text{total}}}, \tag{10}$$

where $m_i(t)$ is the mass flux of species i evaluated over the cross section of the jet at a certain time that then corresponds to a certain downstream location of the jet. Also, $m_{i,\text{total}}$ is the sum of the mass flux of the ith species originating from the nozzle exit, $m_{i,\text{nozzle}}$, and the mass flux entrained into the jet, $m_{i,\text{entrained}}$. A response $R_i = 0$ implies no change of the total amount of the species. Negative or positive responses correspond to destruction or creation of the ith species, respectively. The depletion of O_3 is defined relative to the amount of NO_x originating from the nozzle exit, m_{NO_x}, and is given as $[O_3]_{\text{depletion}} = [m_{O_3}(t) - m_{O,\text{entrained}}]/m_{NO_x}$. By definition, this quantity is always negative and gives an estimate of the amount of O_3 destroyed by NO_x in the jet plume.

Species concentrations along the axis of the jet plume at different locations are compared to the results from Brown et al. (1996a) and Wang and Chen (1997) in Tables 4 and 5. The results for NO and NO_2 show reasonable agreement after $x/d > 250$ (greater than 300 m) with earlier calculations. The differences in the near field, that is, $x/d < 50$ (61 m), may be due to the nonsimilar initial evolution of the jet immediately downstream of the engine exit plane. This feature is not captured since the present scaling requires jet similarity. The spreading rate does not have much effect on the axial species concentrations of NO and NO_2 because the initial NO and NO_2 are the same and no ambient NO and NO_2 are entrained. Although the spreading rate does show some effect on the data in the very near field, by $x/d > 500$ (greater than 600 m), its effect has diminished considerably.

Some results for other radicals are also shown in Table 5. Only limited comparison was possible with other model predictions and, therefore, no major conclusions can be made at this time. However, it is evident that inclusion of molecular diffusion and heterogeneous kinetics does have an impact on the OH radical and sulfuric acid concentrations. The changes in OH concentration have an impact on ozone depletion, as discussed below. The decrease in the gas phase H_2SO_4 formation

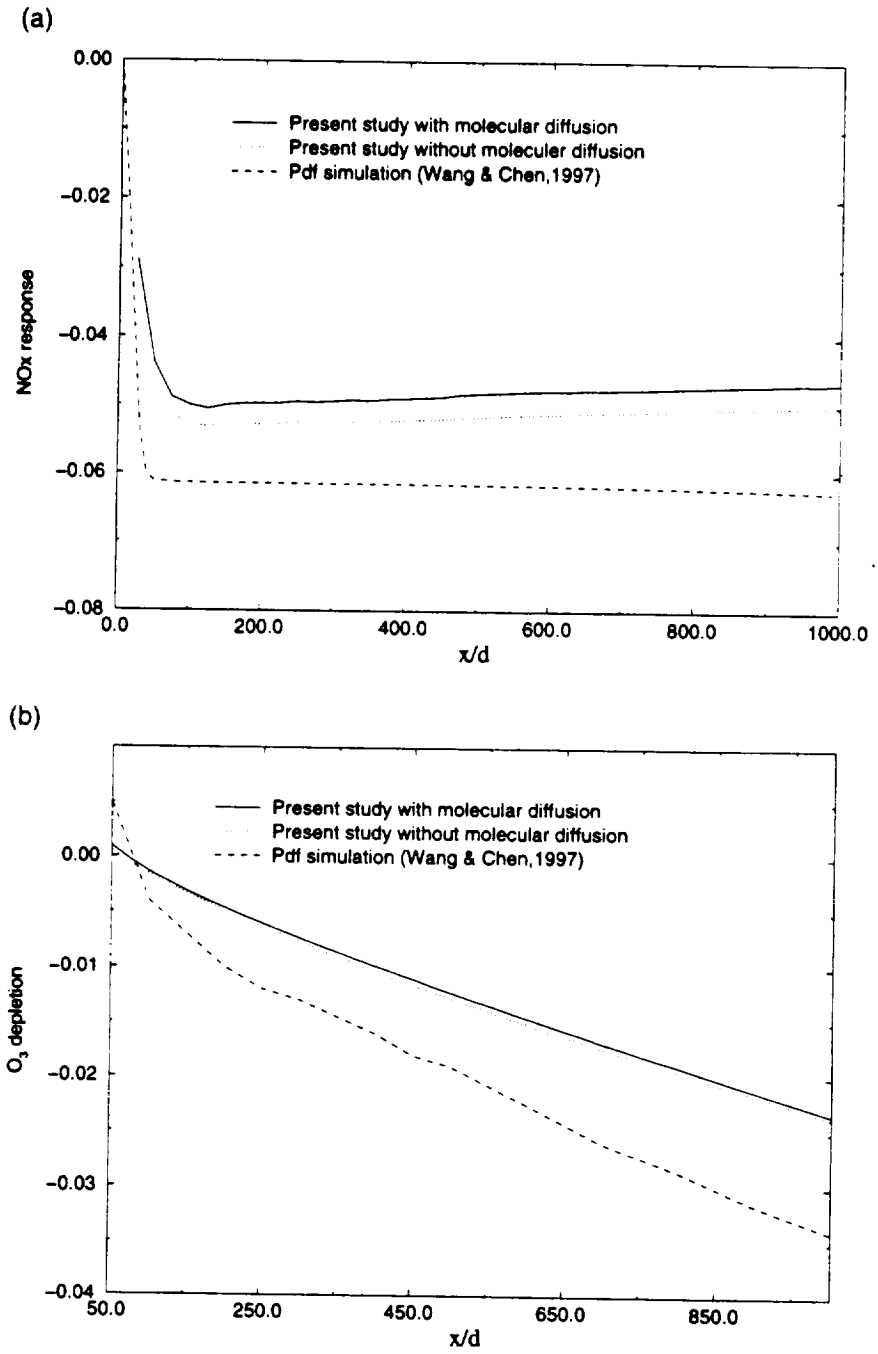

FIG. 5. (a) Comparison of axial variation of NO_x response predicted by the present LEM simulation and PDF simulation (Wang and Chen 1997). (b) Comparison of axial variation of O_3 depletion predicted by the present LEM simulation and PDF simulation (Wang and Chen 1997).

is due to the heterogeneous conversion of SO_3 to the condensed form of H_2SO_4 on soot particles.

Figure 4a shows the NO_x response in the jet plume. Initially, the NO_x response has a sudden drop (a 5%–6% decrease) and then reaches an almost constant value. Notice that the response does not increase consistently with decrease in spreading rate. This can be shown to be related to the competition between various reaction mechanisms as the ozone concentration changes (decreases with decrease in spreading rate). The reasons for the initial sudden drop are the reaction (R1), $NO + O_3 = NO_2 + O_2$, due to entrainment of O_3 from ambient air, and the reaction of converting NO_2 to nitric acid (R2), $NO_2 + OH + M = HNO_3 + M$. Initially, the concentration of NO is much larger than NO_2, and the destruction rate of NO depends on the concentration of

O_3 entrained from the ambient air (R1). Since the ozone entrainment increases with spreading rate, it can cause an effective decrease in OH (via reactions 11, 12, and 18; see Table 1). This will decrease the conversion of NO_2 to nitric acid (R2), thereby decreasing the destruction of NO_x. However, if the ozone concentration increases above a certain level, R1 dominates, leading to a large production of NO_2 that is then converted to nitric acid by R2. The competition between these reaction pathways leads to the NO_x variation with spreading rate. It is seen in all cases that, after around $x/d = 100$, the depletion of NO is balanced by the creation of NO_2.

Figure 4b shows the corresponding O_3 response. Initially, the O_3 response also drops from a positive to a negative value and then tends to almost zero. The spreading rate has an effect on the O_3 response with the largest O_3 response corresponding to the smallest spreading rate. This is reasonable since the spreading rate controls the entrainment of O_3. The initial drop is due to the initial rapid entrainment of O_3, which allows the reaction $NO + O_3 = NO_2 + O_2$ to deplete O_3. The initial variation in the O_3 response is due to the differences in the O_3 entrained (which increases with spreading rate) and the depletion of O_3 (which depends on the NO_x from the engine and the temperature). Thus, for the lowest spreading rate (smallest amount of O_3 entrained), the reactions between O_3 and NO_x are very effective in depleting O_3 since very little mixing occurs (which results in high temperature and high NO_x concentration). However, when the spreading rate is increased and more ozone is entrained, the increased mixing in the jet enhances the dilution of NO_x concentration and the temperature also decreases. As a result, the ozone response is very small. Further downstream, although O_3 entrainment linearly increases with the distance, the radicals from the engine have been almost exhausted and results in almost negligible depletion of O_3.

Figure 4c shows the ozone depletion as a function of spreading rate and initial jet velocity. In all cases, ozone is depleted by around 2%–3% in the jet plume. Increase in the spreading rate (for a fixed jet velocity) slightly increases ozone depletion. There is, however, a much stronger dependence on the jet velocity with more ozone depleted when the jet velocity is reduced. This is understandable since reducing the jet velocity implies reduced convective motion (increased large-eddy turnover time). This allows more time for the local reaction–diffusion and the turbulent mixing processes to complete before downstream convection occurs.

A comparison between the present results and the PDF jet simulation by Wang and Chen (1997) was carried out for a fixed spreading rate of $c = 0.055$ and an initial jet velocity of 620 m s^{-1}. Figures 5a and 5b show, respectively, the NO_x response and ozone depletion predicted by the two methods. Although the same trend is seen, this study shows a reduced NO_x response and a reduced ozone depletion in the jet plume. Around 15% less NO_x and 30% less O_3 are depleted when microscale turbulent mixing and molecular diffusion effects are included. Earlier, comparisons between WMR and PDF predictions were carried out (Wang and Chen 1997). Results showed that a similar decrease in depletion occurs even when mixing was modeled (using an ad hoc mixing timescale model). However, the overall response was not very high. The WMR and PDF methods predicted, respectively, a 6% and a 5% decrease in NO_x in the plume while the present results suggest an even smaller decrease: approximately 4%. Thus, it appears that taking into account the local turbulent mixing and diffusion timescales results in a reduction in NO_x depletion. A similar result for ozone depletion is shown in Fig. 5b and indicates that the inclusion of local mixing effects result in an overall O_3 response of around 0.25%, compared to around 0.35% as predicted by the PDF method.

To determine the importance of molecular diffusion (and differential diffusion), a simulation was carried out by suppressing molecular diffusion but allowing the small-scale turbulent stirring to occur unchanged. This result, also shown in Fig. 5, suggests that accounting for turbulent mixing at all the spatial and temporal small scales has a much larger impact than including molecular diffusion.

When heterogeneous reactions are included, NO_x is transformed to its relatively stable form in the reservoir specie nitric acid. This increases the destruction rate of NO_x (by around 15%), as shown in Fig. 6a (some results for other radicals are shown in Table 5). Note that most of the NO_x destruction occurs within the first 100 jet diameters, and after that remains almost constant. Destruction of O_3 (not shown) is also decreased, although at a less significant level than NO_x destruction because there is less NO_x. However, since O_3 is also destroyed by radicals such as OH and HO_2, the final O_3 response is almost unchanged when heterogeneous reactions are included. This result further emphasizes the importance of properly estimating the concentration of other radicals such as OH and HO_2.

The competition between the gas phase H_2SO_4 and the condensed phase H_2SO_4 formation reactions for the available SO_3 was also studied. Figure 6b shows the centerline SO_3 concentration for these cases. The SO_3 concentration is significantly decreased when the gas phase H_2SO_4 formation reaction is included. Adding the heterogeneous process of H_2SO_4 condensation on soot particles causes a further decrease in the SO_3 concentration. This behavior is reflected in the gas phase H_2SO_4 centerline mass fractions for these two cases, as shown in Fig. 6c. When condensed H_2SO_4 is formed, the gas phase H_2SO_4 concentration is significantly decreased since a substantial amount of SO_3 is lost from the gas phase to the condensed phase reaction. Note that this study did not address the other heterogeneous processes related to sulfur particles in the plume. Thus, these results are likely to be modified when binary homogenous nucleation and other aerosol-related kinetics are includ-

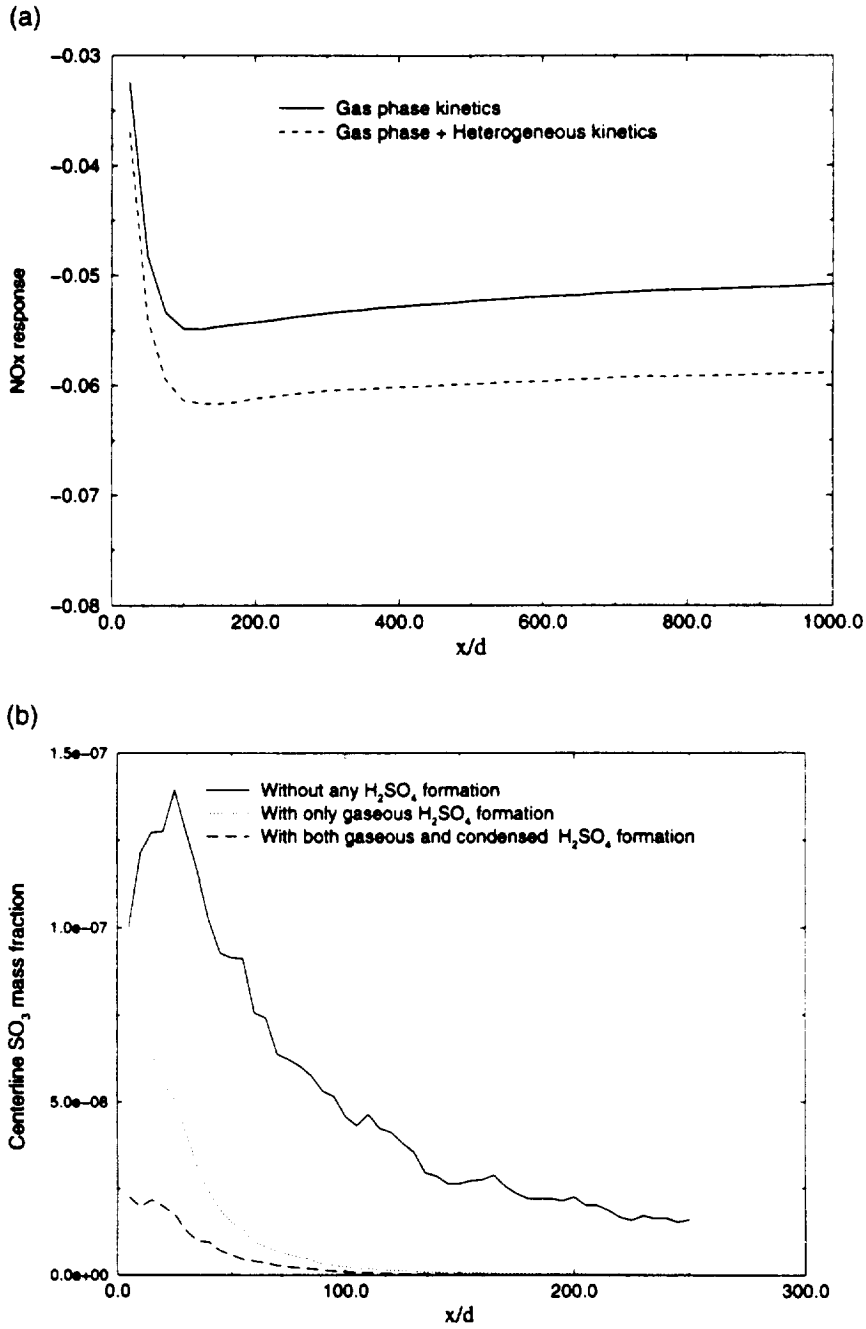

FIG. 6. (a) Effect of heterogeneous kinetics on the NO_x response in the exhaust plume. (b) Centerline variation of SO_3 with and without sulfuric acid formation. (c) Centerline variation of H_2SO_4.

ed. Extension of this model to factor in these heterogeneous processes is currently under way.

5. Conclusions

In this study, fluid mixing and chemical reactions in the near field of an engine exhaust jet plume were investigated using a mixing model that explicitly incorporates the large-scale mixing process as entrainment events and stochastically simulates small-scale turbulent mixing and molecular diffusion effects. A reduced reaction mechanism that accurately reproduces results of a detailed mechanism for the lower-stratosphere chemistry was used to simulate the exhaust plume dynamics of a typical HSCT aircraft.

This study shows that, compared to predictions based

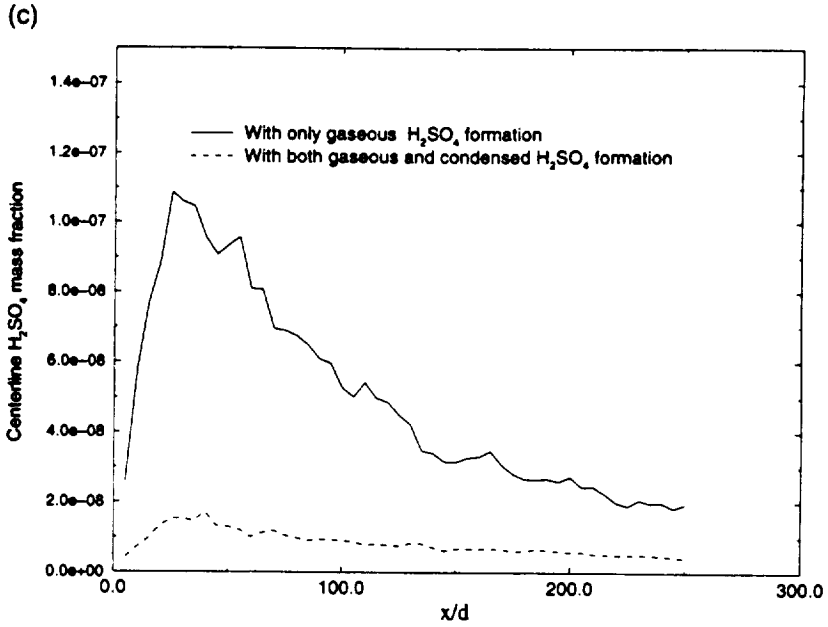

FIG. 6. (*Continued*)

on models that do not include small-scale mixing and/or molecular diffusion effects, 30% less O_3 and 15% less NO_x are depleted in the near field of the plume. This suggests that the effects of the local lack of mixing have an inhibiting effect on ozone depletion in the near-field plume. Inclusion of heterogeneous kinetics involving formation of condensed nitric and sulfuric acid on water condensed on soot particles showed that 15% of the available NO_x is converted into its inactive form but has negligible effects on O_3 concentration. The predictions are also shown to be dependent on the availability of other radicals such as OH. Although these results are in reasonable agreement with other predictions using less sophisticated (or no) mixing models, the importance of the small-scale mixing and diffusion processes on the near-field plume dynamics can only be addressed using a physically consistent simulation model. The development of this model offers such a capability. The impact of small-scale mixing on homogeneous nucleation of sulfuric acid aerosol particles has not yet been addressed but is currently being incorporated and will be reported soon. Another possible role of this model is to provide appropriate conditions for the plume–wingtip vortex interaction phase that immediately follows the plume stage. More complex chemistry, especially heterogeneous kinetics that occur in this stage, depends critically on the chemical state of the plume during the interaction phase. Accurate estimate of the species concentrations and aerosol particle distribution at the end of the plume stage will allow a more accurate evaluation of the plume–vortex dynamics. To evaluate this capability, simulations are currently under way (Menon and Wu 1997) of the plume–vortex interaction phase using data from this study. These results will be reported in the future.

Acknowledgments. This work was supported by NASA/Langley Research Center monitored by Dr. William Grose. The authors acknowledge the constructive comments by the anonymous reviewers.

REFERENCES

Beck, J., C. Reeves, F. de Leeuw, and S. Penkett, 1992: The effect of aircraft emissions on tropospheric ozone in the Northern Hemisphere. *Atmos. Environ.*, **26A,** 17–19.

Brasseur, G. P., C. Granier, and S. Walters, 1990: Future changes in stratospheric ozone and the role of heterogeneous chemistry. *Nature,* **348,** 626–628.

Brown, R. C., R. C. Miake-Lye, M. R. Anderson, C. E. Kolb, and T. J. Resch, 1996a: Aerosol dynamics in near field aircraft plumes. *J. Geophys. Res.*, **101,** 22 939–22 953.

——, ——, ——, and ——, 1996b: Effect of aircraft exhaust sulfur emissions on near field plume aerosol. *Geophys. Res. Lett.*, **24,** 3607–3610.

Cruyningen, I., A. Lozano, and R. K. Hanson, 1989: Interpretation of planar laser induced fluorescence flow field images. *Proc. ASME Winter Conf.*, San Francisco, CA, American Society of Mechanical Engineering, 109–114.

Dahm, W. J. A., and P. E. Dimotakis, 1987: Measurements of entrainment and mixing in turbulent jets. *AIAA J.*, **25,** 1216–1223.

Danilin, M. Y., A. Ebel, H. Elbern, and H. Petry, 1994: Evolution of the concentration of trace species in an aircraft plume: Trajectory study. *J. Geophys. Res.*, **99,** 18 951–18 972.

Dash, S. M., H. S. Pergament, D. E. Wolf, N. Sinha, M. W. Taylor, and M. E. Vaughn Jr., 1990: The JANNAF standardized plume flow field code version II (SPF-II), Vols. I and II. Tech. Rep. TR-CR-RD SS 90-4, U.S. Army Missile Command, Huntsville, AL, 108 pp.

Dowling, D. R., 1988: Mixing in gas phase turbulent jets. Ph.D. Thesis, California Institute of Technology, 241 pp.

Fahey, D. W., and Coauthors, 1995a: In situ observations in aircraft exhaust plume in the lower stratosphere at mid latitudes. *J. Geophys. Res.*, **100,** 3065–3074.

——, and Coauthors, 1995b: Emission measurements of the Concorde supersonic aircraft in the lower stratosphere. *Science*, **270,** 70–74.

Friedl, R. R., 1997: Atmospheric effects of subsonic aircraft: Interim assessment report of the advanced subsonic technology program. NASA RP 1400, NASA/Goddard Space Flight Center, Greenbelt, MD, 143 pp.

Fukuta, N., and L. A. Walter, 1970: Kinetics of hydrometer or growth from a vapor-spherical model. *J. Atmos. Sci.*, **27,** 1160–1172.

Karcher, B., 1995: A trajectory box model for aircraft exhaust plumes. *J. Geophys. Res.*, **100,** 18 835–18 844.

——, and D. W. Fahey, 1997: The role of sulfur emission in volatile particle formation in jet aircraft exhaust plumes. *Geophys. Res. Lett.*, **24,** 389–392.

Kee, R. J., F. M. Rupley, and J. A. Miller, 1989: CHEMKIN II: A FORTRAN chemical kinetics package for modeling well-stirred reactors. Sandia National Laboratories Rep. SAND 89-8009B, Sandia National Laboratory, Livermore, CA, 54 pp.

Kerstein, A. R., 1987: Linear-eddy model of turbulent scalar transport and mixing. *Comb. Sci. Technol.*, **60,** 391–421.

——, 1989: Linear-eddy modeling of turbulent transport. II: Application to shear layer mixing. *Comb. Sci. Technol.*, **75,** 397–413.

——, 1990: Linear-eddy modeling of turbulent transport. Part 3: Mixing and differential molecular diffusion in round jets. *J. Fluid Mech.*, **216,** 411–435.

Landau, L. D., and E. M. Lifshitz, 1959: Turbulence. *Fluid Mechanics*, Pergamon Press, 130–134.

Lewellen, D. C., and W. S. Lewellen, 1996: Large-eddy simulation of the vortex-pair breakup in aircraft wakes. *AIAA J.*, **34,** 2337–2345.

Menon, S., and J.-Y. Chen, 1995: A numerical study of mixing and chemical processes during interactions between an aircraft's engine jet plume and its wingtip vortices. *NASA Conf. on the Atmospheric Effects on Aviation*, Virginia Beach, VA, National Aeronautics and Space Administration.

——, and J. Wu, 1997: Large-eddy simulations of interaction between engine exhaust plume and aircraft wingtip vortices. *NASA Conf. on the Atmospheric Effects of Aviation*, Virginia Beach, VA, National Aeronautics and Space Administration.

——, P. McMurtry, A. R. Kerstein, and J.-Y. Chen, 1994: A mixing model to predict NO_x production in hydrogen–air turbulent jet flames. *J. Propul. Power*, **10,** 161–168.

Miake-Lye, R. C., M. Martinez-Sanchez, R. C. Brown, and C. E. Kolb, 1993: Plume and wake dynamics, mixing, and chemistry behind a high speed civil transport aircraft. *J. Aircraft*, **30,** 467–479.

——, ——, ——, and ——, 1994: Calculations of condensation and chemistry in an aircraft contrail. *Proc. Impact of Emissions from Aircraft and Spacecraft upon the Atmosphere, an Int. Scientific Colloquium*, Cologne, Germany, National Aeronautics and Space Administration, 106–112.

Quackenbush, T. R., M. E. Teske, and A. J. Bilanin, 1993: Computation of wake/exhaust mixing downstream of advanced transport aircraft. AIAA Paper 93-2944, 15 pp.

——, ——, and ——, 1996: Dynamics of exhaust plume entrainment in aircraft vortex wakes. AIAA Paper 96-0747, 34 pp.

Stolarski, R. S., and H. L. Wesoky, 1995: The atmospheric effects of stratosphere aircrafts: A fourth program report. NASA Ref. Publ. 1359, National Aeronautics and Space Administration, Washington, DC, 236 pp.

——, and Coauthors, 1995: Scientific assessment of atmospheric effects of stratospheric aircraft. NASA Ref. Publ. 1381, National Aeronautics and Space Administration, Washington, DC, 64 pp.

Sykes, R. I., D. S. Henn, and S. F. Parker, 1992: Large-eddy simulation of a turbulent reacting plume. *Atmos. Environ.*, **26A,** 2565–2574.

Wang, Z., and J.-Y. Chen, 1997: Numerical modeling of mixing and chemistry in near-field engine exhaust plumes. *J. Geophys. Res.*, **102,** 12 871–12 883.

Weisenstein, D. K., M. K. W. Ko, N. D. Sze, and J. M. Rodriguez, 1996: Potential impact of SO_2 emissions from stratospheric aircraft on ozone. *Geophys. Lett.*, **23,** 161–164.

WMO, 1995: Scientific assessment of ozone depletion. World Meteor. Org. Global Ozone Research and Monitoring Project Rep. 37, 502.

JOURNAL OF GEOPHYSICAL RESEARCH, VOL. 102, NO. D11, PAGES 12,871-12,883, JUNE 20, 1997

Modeling of microscale turbulence and chemistry interaction in near-field aircraft plumes

Z. Wang and J.-Y. Chen

Department of Mechanical Engineering, University of California, Berkeley

Abstract. The potential impact of aircraft exhaust gas on entrained ambient air in the stratosphere has been studied by using several numerical models to manifest the importance of mixing processes occurring at different scales. These models include perfectly stirred reactor (PSR), transient well-mixed reactor (WMR), partially stirred reactor (PaSR), and joint scalar probability density function (PDF) simulation for the near-field jet exhaust. Sensitivities of major species to chemical reactions are presented to illustrate the chemical transformation in the near-field jet regime. An accurate reduced chemical mechanism that captures major reaction pathways has been systematically developed and tested. The predicted results with the reduced mechanism are found in good agreement with those from the detailed mechanism, but the computing time is decreased by a factor of 3. The effect of microscale turbulent mixing and chemistry interaction on species evolution is studied, and its impact is found most noticeable in the near field where the timescale of chemistry for highly reactive radicals, such as OH and HO_2, is comparable or faster compared with that of microscale mixing. When microscale mixing is included, the predicted H_2SO_4 level increases at locations where sulfate aerosol formation may be important in the near field.

Introduction

Engine emissions from the rapidly growing subsonic aircrafts and the planned high-flying supersonic aircrafts may significantly alter concentrations of ozone, water vapor, and aerosol in upper atmosphere and may lead to climate changes. In particular, potential ozone depletion caused by aircraft emissions in the stratosphere is of great concern. Consequently, the impact of emissions from the planned supersonic commercial aircrafts on atmospheric chemistry needs to be assessed as thoroughly as possible. Currently, several major research efforts are undertaken within NASA's High-Speed Research Program (HSRP) to address various issues related to the effects of a fleet of high-speed civil transport (HSCT) flights on the stratospheric chemistry. Research tasks on similar subjects for the growing subsonic aircrafts are also being conducted within NASA's Advanced Subsonic Technology Program (ASTP). A review of these studies [*Stolarski and Wesoky*, 1995] clearly demonstrates the complexity of the problems and the associated uncertainties. Numerical calculations on near-field jet plume [*Miake-Lye et al.*, 1993a, b; *Kärcher*, 1994, 1996; *Anderson et al.*, 1996; *Brown et al.*, 1996] and experiments in the wake [*Arnold et al.*, 1992; *Fahey et al.*, 1995] have been implemented to quantify levels of major gas phase species and exhaust aerosols. Although the near-field jet regime lasts only a few seconds, major conversion of gas phase NO_x and SO_x into HNO_3 and H_2SO_4 driven by hydroxyl radical occurs in the near field. Nucleation of sulfate aerosol particles and their possible interaction with active soot particles are believed to occur primarily in this regime. Modeling of near-field jet is considered an important task to provide proper initial conditions of NO_x and aerosol contents for the subsequent study on chemistry and microphysics in the intermediate vortex interaction and far-away dispersion regimes. One area that lacks fundamental understanding is the relative importance of microscale turbulence and chemistry interaction in the near-field aircraft plume and its influence on chemical kinetics when combined with large-scale entrainment process.

Since the fluid mechanics becomes complicated in the region where the exhaust jet plume and wing vortex begin to interact, large-eddy simulations may be necessary for exploring the role of wing vortex on mixing process. The consequential impact of wing vortex on chemical kinetics can be studied provided that simplified chemistry is available for describing the key reaction paths. In addition, aerosol dynamics, e.g., binary nucleation of sulfuric acid and water vapor, condensation, coagulation, are considered important processes in the near-field plume. Inclusion of these processes, while taking into account the interaction between microscale turbulence and chemistry, would demand substantial computing time. The main objectives of this study are to identify and characterize the distribution of key species in the near-field plume regime, to develop an accurate reduced chemical mechanism for gas phase chemical reactions, and to explore the impact of microscale mixing on the chemistry in the exhaust plume.

Numerical Models

Table 1 lists the major features of various numerical models that are used to assess the relative importance of mixing processes at different scales on the evolution of plume chemistry in the near field of exhaust plume. The macroscale mixing process refers to turbulent convection and stirring across the jet plume. The dominant role of macroscale mixing is to bring fluids from different parts of flow over a distance much

Paper number 97JD00900.
0148-0227/97/97JD-00900$09.00

Table 1. Features of Various Numerical Models for Modeling Jet Plume Chemistry

Model Assumptions	PSR	WMR	PaSR	PDF Jet With Each Cell Well Mixed	PDF Jet With Modified Curl's Mixing Model For Each Cell
Microscale well mixed	yes	yes	no	yes	no
Macroscale well mixed	yes	yes	yes	no	no
Transient effect	no	yes	yes	yes	yes

PSR, perfectly stirred reactor; WMR, well-mixed reactor; PaSR, partially stirred reactor; PDF, probability density function. Microscale well mixed means micromixing time is much smaller than the chemistry time, so microscale turbulence effect is ignored. Macroscale well mixed means macroscale turbulent diffusion time is much smaller than the residence time, so properties are spatially uniform (homogeneous). It is assumed that in PSR and PaSR, there is a stirrer which makes the reactor homogeneous and either well mixed or not well mixed in microscale. WMR is similar to a Lagrangian box model, and PDF jet with each cell well mixed is equivalent to the standard plume flow field code [*Dash et al.*, 1990] and *Kärcher*'s [1996] 2-D jet model.

larger than the scale of molecular diffusion and to create substantially large interfacial areas among fluids. The microscale mixing refers to the turbulent diffusion process occurring at the microscale which is strongly enhanced by macroscale mixing. Only after fluids are well mixed at the microscale will chemical reactions take place. The resolution of numerical simulation for the mixing process is limited by the grid size which is usually much larger than the scale of molecular diffusion. Consequently, modeling of turbulence and mixing process for fluids within grid cells is necessary. A microscale well-mixed state can be assumed when the turbulent mixing within a grid cell is faster than chemical kinetics.

If the mixing processes at both macroscale and microscale are assumed infinitely fast, the jet plume can be modeled by the well-mixed reactor (WMR) which is similar to the Lagrangian box model [e.g., *Miake-Lye et al.*, 1993b; *Karol et al.*, 1994; *Kärcher*, 1995]. A perfectly stirred reactor (PSR) is a simplified version of WMR as it computes only steady state solutions of chemical kinetics for a mixture of different fluids brought together into the reactor for a period of residence time. PSR calculations facilitate detailed sensitivity analysis which is useful for identifying the major chemical reaction pathways.

When the fast mixing assumption at the microscale is relaxed, a partially stirred reactor (PaSR) is developed to include the effect of microscale mixing. The unmixed nature is described by the joint scalar probability density function (PDF) for reactive species. To account for the interaction of fluid dynamics and chemistry that causes non-uniform fluid compositions inside the jet plume, two-dimensional modeling of jet is necessary to resolve the spatial distribution. For instance, the standard plume flow (SPF-II) field model developed by *Dash et al.* [1990] can be used to model jet development with the assumption of fast microscale mixing within grid cells. To explore the potential impact on chemical kinetics due to microscale mixing, the joint scalar PDF is used to describe the unmixed nature of fluids within each grid cell. The PDF jet model will be computed with/without microscale mixing models to provide information on the relative importance of microscale turbulent mixing and its interaction with chemical kinetics. Described below are details of these numerical models.

Perfectly Stirred Reactor (PSR) Model

The perfectly stirred reactor (PSR) is a homogeneous reactor which has a continuous mass flow in/out of the reactor as shown in Figure 1 [*Glarborg et al.*, 1986]. When the fluids enter the reactor, it is assumed that the fluids are perfectly mixed with the existing fluids in the reactor immediately. This assumption is justified when the characteristic time of turbulent mixing in both macroscale and microscale is much smaller than that of chemistry, so the rate of chemical process is controlled solely by chemical kinetics. Turbulence effects are not accounted for in this model because of the assumption of infinitely fast mixing. Detailed chemical kinetics can be studied by using mean thermochemical properties.

The conservation equation for reactive species at the steady state is given by

$$\dot{m}(Y_k - Y_k^*) - \dot{\omega}_k W_k V = 0, \tag{1}$$

and the corresponding energy equation is described by

$$\dot{m}\sum_{k=1}^{K}(Y_k h_k - Y_k^* h_k^*) + Q = 0. \tag{2}$$

In these two equations, Y_k is the mass fraction of the kth species (there are K species); W_k is the molecular weight of the kth species; V is the reactor volume; $\dot{m}$ is the mass flow rate through the reactor; ω_k is the molar production rate of kth species per unit volume by chemical reactions; h_k is the specific enthalpy of the kth species; and Q is the reactor heat loss. The superscript asterisk indicates the inlet conditions. The characteristic flow time is residence time $\tau = \rho V / \dot{m}$. A hybrid Newton/time-integration algorithm is used to solve for the solution, and details of the numerical method are described by *Glarborg et al.* [1986]. PSR is used in the current

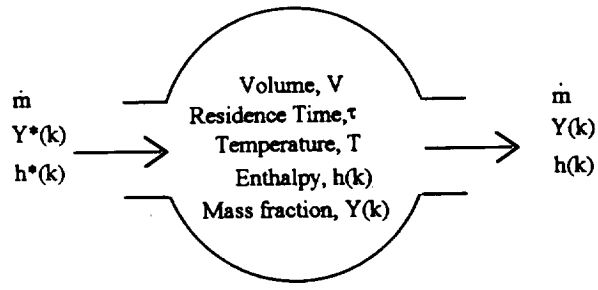

Figure 1. Schematic of perfectly stirred reactor (PSR) showing the characteristics of the reactor, where $\dot{m}$ is the mass flow rate, k denotes species k, and superscript asterisk indicates the inlet condition. The key parameter is the residence time $\tau = \rho V / \dot{m}$.

study primarily for developing reduced chemistry and for identifying controlling steps in O_3 and NO_x chemistry through sensitivity analysis. To assess different treatments for the mixing processes occurring in the near field of the jet plume, we have used more sophisticated numerical models described below.

Transient Well-Mixed Reactor (WMR) Model

The transient WMR model facilitates study of the time evolution of chemical kinetics for engine exhaust gas subject to injection of ambient air. A schematic diagram for the WMR is sketched in Figure 2. Similar to the PSR, a global residence time can be defined as

$$\tau_R = \frac{M_R}{\dot{m}_a}, \tag{3}$$

where M_R is the mass of gas inside the reactor, and $\dot{m}_a$ is mass entrainment rate. Using τ_R as a parameter, conservation equations of mass, species, and energy can be written as

$$\frac{dM_R}{dt} = \frac{M_R}{\tau_R}, \tag{4}$$

$$\frac{dY_{Rj}}{dt} = \frac{1}{\tau_R}(Y_{a,j} - Y_{R,j}) + \frac{\dot{\omega}_{Rj}}{\rho_R}\cdot W_j, \quad j = 1,\cdots,N \tag{5}$$

$$\frac{dT_R}{dt} = \frac{1}{\bar{c}_{pR}\tau_R}\left[\sum_{j=1}^{N}(h_{a,j} - h_{R,j})Y_{a,j}\right] - \sum_{j=1}^{N}\frac{\dot{\omega}_{Rj}h_{Rj}W_j}{\rho_R\bar{c}_{PR}} - \frac{\dot{Q}_{loss}}{\bar{c}_{PR}M_R}, \tag{6}$$

where the subscript R represents quantities inside the reactor and those entrained are denoted by the subscript a. The WMR is applied to study the chemical kinetics of the engine exhaust gas that is continuously mixed with ambient air. For constant temperature cases the WMR model is similar to the Lagrangian box model [*Miake-Lye et al.*, 1993b; *Karol et al.*, 1994; *Kärcher*, 1995] when the following relation is used to bridge the two models:

$$\frac{\dot{m}_a}{M_R} = \frac{K(t)}{A}, \tag{7}$$

where A is the cross-section area of a plume and $K(t)$ is the growth rate of the plume cross-section area in a Lagrangian box model equation

$$\frac{dn_i}{dt} = P_i - L_i - \frac{K(t)}{A}(n_i - n_i^a) + R_i, \tag{8}$$

where n_i, n_i^a are the species concentrations inside the box and the air, respectively; P_i and L_i are the production and destruction rate by chemical reactions; R_i is the source or sink due to other mechanisms. In the WMR model reported here, the air injection rate is determined from the mass entrainment rate into the jet estimated by the PDF jet plume model to be discussed in the later session.

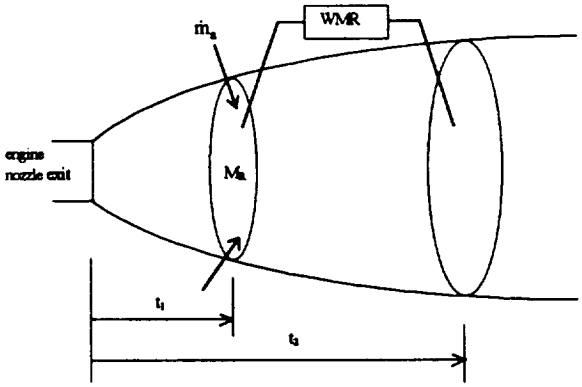

Figure 2. Schematic diagram of a transient well-stirred reactor (WMR) showing ambient air entrained into the reactor with a rate of $\dot{m}_a$, where M_R is the mass of gas in the reactor, and it increases with time.

Partially Stirred Reactor (PaSR) Model

When the characteristic time of turbulent microscale mixing is not fast compared to that of chemical reaction, the impact of microscale mixing may become important. In the current PaSR model, the mean properties are assumed to be spatially homogeneous (well mixed in macroscale turbulence) but not completely mixed at the molecular level. Compared to WMR, the effect of microscale mixing is included in PaSR, so the scalar distribution inside a reactor needs to be modeled to manifest the micromixing process. The joint scalar probability density function (PDF) is used to describe the distribution of scalars, and therefore it contains information about the mixing state. The time evolution equation for the joint PDF for the PaSR has been derived by *Chen* [1996] as

$$\begin{aligned}\frac{\partial \tilde{P}_\phi(\psi,t)}{\partial t} &= -\sum_{\alpha=1}^{k}\frac{\partial}{\partial \psi_\alpha}\left[S_\alpha(\psi)\tilde{P}_\phi(\psi,t)\right] \\ &\quad + \frac{1}{\tau_R}[\tilde{P}_{\phi,inlet}(\psi) - \tilde{P}_\phi(\psi,t)] \\ &\quad - \sum_{\alpha=1,\beta=1}^{k}\frac{\partial^2}{\partial\psi_\alpha\partial\psi_\beta}[<\varepsilon_{\alpha\beta}\,|\,\phi=\psi>\tilde{P}_\phi(\psi,t)],\end{aligned} \tag{9}$$

where the mean residence time is defined as $\tau_R = M_R/\dot{m}_a$, scalar ϕ represents the set of species mass fractions and enthalpy, ψ is the set of independent variables corresponding to the dependent scalar variables ϕ, $P_\phi(\psi,t)$ is the joint PDF of ϕ, a tilde denotes the density-weighted average, $\varepsilon_{\alpha\beta}$ is the scalar dissipation rate given by $\varepsilon_{\alpha\beta} = \Gamma\nabla\phi_\alpha\cdot\nabla\phi_\beta$ where Γ is molecular diffusivity, $<\varepsilon_{\alpha\beta}|\,\phi=\psi>$ represents the average scalar dissipation rate conditioned on a certain set of scalars, and S_α is the chemical source term for scalar ϕ_α. The first two terms on the right-hand side represent the effects of chemical reaction and the throughflow on the joint scalar PDF, respectively. Both of these terms can be calculated directly and do not need modeling. The last term stands for the effect of microscale mixing on the PDF which requires closure approximations. PaSR includes chemical kinetics and the additional interactions with microscale turbulence under the assumption of homogenous flow (no macroscale turbulence) and further ignoring velocity fluctuations. The simplicity of this model permits us to carry out simulations with detailed chemistry without significant computing burdens. More importantly, PaSR can be viewed as a single representative grid cell embedded in a large computation scheme. Therefore PaSR is an ideal test bed for exploring the influence of the microscale mixing on chemical kinetics, for evaluating the performances of reduced chemistry, and for assessing current and emerging mixing models.

In this study, the effect of microscale mixing on the PDF is modeled by the modified Curl's mixing model [*Janika et al.*, 1979],

$$-\sum_{\alpha=1,\beta=1}^{k}\frac{\partial^2}{\partial\psi_\alpha\partial\psi_\beta}[<\varepsilon_{\alpha\beta}\mid\phi=\psi>\tilde{P}_\phi(\psi,t)] = \frac{1}{\tau_{mix}}\left\{\iint_{\psi'\psi''}\tilde{P}_\phi(\psi',t)\tilde{P}_\phi(\psi'',t)H(\psi',\psi''\mid\psi)d\psi'd\psi''-\tilde{P}_\phi(\psi,t)\right\}, \quad (10)$$

where H is the transitional probability defined as

$$H(\psi',\psi''\mid\psi)=\frac{1}{\mid\psi''-\psi'\mid}\quad\text{for }\psi\in[\psi',\psi'']$$
$$=0\qquad\text{elsewise.} \quad (11)$$

The amount of mixing is modeled through a characteristic mixing time which is related to the turbulence timescale for micromixing, $\tau_{mix}=\tilde{k}/\tilde{\varepsilon}$, where k is turbulence kinetic energy and $\tilde{\varepsilon}$ is turbulence dissipation rate. Because of the multidimensional nature of equation (9), Monte Carlo technique is used to solve the PDF evolution equation. In the context of simulating jet plume using a PaSR, the air injection rate, similar to that in the WMR, is needed, and its value is estimated from the PDF jet plume model described next.

Probability Density Function (PDF) Simulation for Near-Field Jet Exhaust

A proper treatment of the interaction between turbulence and chemical kinetics is important to the predictions of ozone and NO_x changes in the engine exhaust gas. The standard plume flow (SPF-II) field model by *Dash et al.* [1990] assumes that the gas inside each computational cell is perfectly mixed. The microscale mixing effect is therefore neglected in the SPF-II code, and its impact on chemical kinetics has not been assessed. To account for the microscale mixing, the joint scalar PDF is solved for by the following transport equation [*Pope*, 1985] using the Monte Carlo technique,

$$\overline{\rho u_k}\frac{\partial\tilde{P}_\phi(\psi;\vec{x},t)}{\partial x_k}=-\sum_{\alpha=1}^{k}\frac{\partial}{\partial\psi_\alpha}\left[\overline{\rho}S_\alpha(\psi)\tilde{P}_\phi(\psi;\vec{x},t)\right] - \frac{\partial}{\partial x_k}[\overline{\rho}<u_k''\mid\phi=\psi>\tilde{P}_{\vec{\phi}}(\psi;\vec{x},t)] - \sum_{\alpha=1,\beta=1}^{k}\frac{\partial}{\partial\psi_\alpha\partial\psi_\beta}[\overline{\rho}<\varepsilon_{\alpha\beta}\mid\phi=\psi>\tilde{P}_\phi(\psi;\vec{x},t)] \quad (12)$$

where the turbulent transport term can be modeled by a gradient diffusion model using the turbulence time and fluctuating velocities from the Reynolds stress model,

$$<u_\alpha''\mid\phi=\psi>\tilde{P}_\phi=-C_S\frac{\tilde{k}}{\tilde{\varepsilon}}\tilde{u_\alpha''u_\beta''}\frac{\partial\tilde{P}_\phi(\psi)}{\partial x_\beta} \quad (13)$$

where C_s is an adjustable constant (= 0.25 in jet flows), $u_k''=u_k-\tilde{u}_k$ is the density-weighted velocity fluctuation, and $<u_k''\mid\phi=\psi>$ is the average fluctuation conditioned on a certain set of scalars. The flow field is solved by a Reynolds stress turbulence closure model, which directly solves the modeled transport equations for Reynolds stress, with a marching downstream algorithm, and the details can be found in the works of *Chen et al.* [1987, 1989]. The modified Curl's mixing model (equation (10)) was used to simulate the effect of microscale mixing process.

The PDF numerical model was validated by comparing computed results without the effect of microscale mixing with those obtained from the SPF-II code by *Brown et al.* [1996] using the same mechanism and initial conditions for a HSCT case. The computed centerline mean concentrations of NO_x, NO_y, SO_2, and H_2SO_4 are found in good agreement despite many differences in the numerical models. In addition, both models predict the NO_x/NO_y ratio in excess of 80% in accord with the measurements by *Fahey et al.* [1995] from the NASA ER-2 high-altitude aircraft. Furthermore, we com-

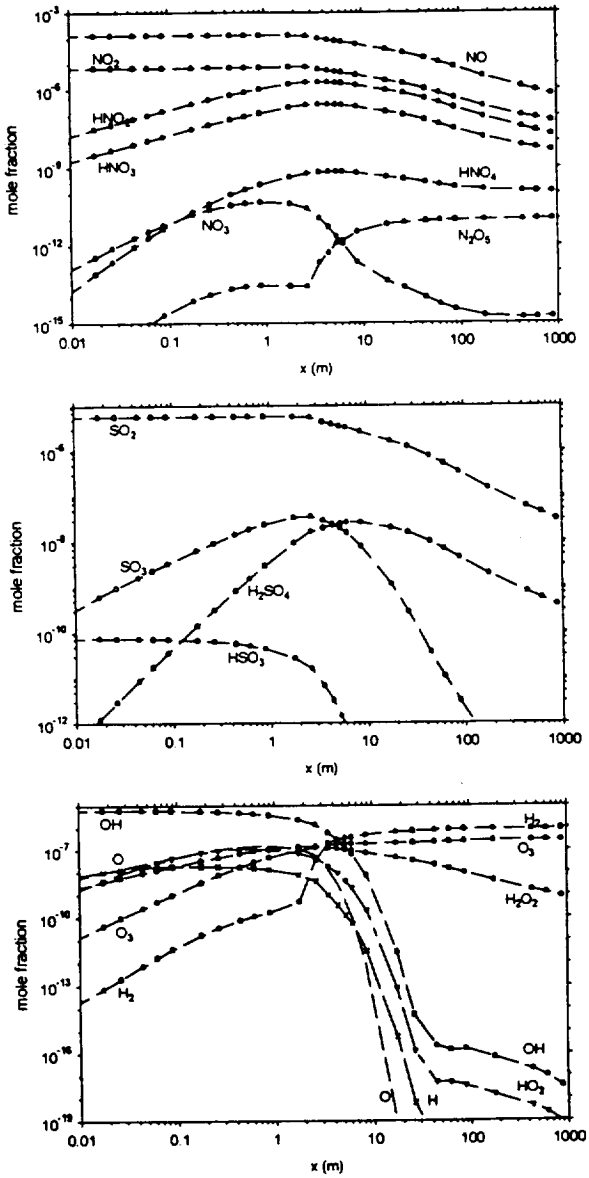

Figure 3. Centerline mole fractions of major nitrogen, sulfur, and hydrogen species for B747 jet engine. They compare well with *Kärcher*'s [1996] results (not shown).

pared our predicted results with *Kärcher's* [1996] B747 case using the same chemical mechanism and initial conditions. Figure 3 presents our predicted centerline mole fractions for NO_x, HO_x, and SO_x, which agree with Kärcher's numerical results (not shown).

Chemical Reaction Mechanisms

Detailed Gas Phase Mechanism

Tables 2a and 2b list a detailed gas phase mechanism containing 24 species with 60 elementary reaction steps. It includes reactions of species O_x, HO_x, NO_x, SO_x, and CO_x that are important in the near-filed jet plume in the stratosphere. The reaction rates are basically taken from data presented by *Kärcher* [1996], which cover reaction rates below 1000 K and most of which represent linear or nonlinear fits to a large number of the data by National Institute of Standards and Technology (NIST) or are extensions to higher or lower temperatures. Rate constants for the reaction of HNO_2 with H and O (reactions (28) and (29)) are taken from data by *Tsang et al.* [1991].

Table 2a. Gas Phase Reaction Mechanism: Binary Reactions

	Reaction	Rate Constant (cm^3 $molecule^{-1}$ s^{-1})
(R1)	$O + O_3 \rightarrow 2O_2$	$1.21 \times 10^{-11} \exp(-2125/T)$
(R2)	$H + O_3 \rightarrow OH + O_2$	$1.15 \times 10^{-10} \exp(-436/T)$
(R3)	$H + OH \rightarrow O + H_2$	$8.10 \times 10^{-21} T^{2.8} \exp(1950/T)$
(R4)	$H + HO_2 \rightarrow 2OH$	$2.8 \times 10^{-10} \exp(-440/T)$
(R5)	$H + HO_2 \rightarrow H_2 + O_2$	$6.9 \times 10^{-11} \exp(-636.9/T)$
(R6)	$H + HO_2 \rightarrow O + H_2O$	$2.80 \times 10^{-12} T^{0.44} \exp(-677.9/T)$
(R7)	$OH + O \rightarrow H + O_2$	$1.83 \times 10^{-11} \exp(173.3/T)$
(R8)	$OH + O_3 \rightarrow HO_2 + O_2$	$1.9 \times 10^{-12} \exp(-1000/T)$
(R9)	$OH + H_2 \rightarrow H + H_2O$	$1.11 \times 10^{-16} T^{1.84} \exp(-1589/T)$
(R10)	$OH + OH \rightarrow O + H_2O$	$8.34 \times 10^{-17} T^{1.54} \exp(355.7/T)$
(R11)	$OH + HO_2 \rightarrow O_2 + H_2O$	$5.09 \times 10^{-11} \exp(72.6/T)$
(R12)	$OH + H_2O_2 \rightarrow HO_2 + H_2O$	$2.13 \times 10^{-13} T^{0.47} \exp(-179.8/T)$
(R13)	$HO_2 + O \rightarrow OH + O_2$	$2.71 \times 10^{-11} \exp(-224/T)$
(R14)	$HO_2 + O_3 \rightarrow OH + 2O_2$	$1.4 \times 10^{-14} \exp(-600/T)$
(R15)	$HO_2 + HO_2 \rightarrow H_2O_2 + O_2$	$2.2 \times 10^{-13} \exp(600/T)$
(R16)	$H_2O_2 + O \rightarrow OH + HO_2$	$2.33 \times 10^{-11} \exp(-2814/T)$
(R17)	$H_2O_2 + H \rightarrow OH + H_2O$	$1.7 \times 10^{-11} \exp(-1800/T)$
(R18)	$H_2O_2 + H \rightarrow HO_2 + H_2$	$1.77 \times 10^{-11} \exp(-2890/T)$
(R19)	$NO + O_3 \rightarrow NO_2 + O_2$	$2.14 \times 10^{-12} \exp(-1408/T)$
(R20)	$NO + HO_2 \rightarrow OH + NO_2$	$3.7 \times 10^{-12} \exp(240/T)$
(R21)	$NO + NO_3 \rightarrow 2NO_2$	$1.8 \times 10^{-11} \exp(110/T)$
(R22)	$NO_2 + O \rightarrow NO + O_2$	$6.5 \times 10^{-12} \exp(120/T)$
(R23)	$NO_2 + O_3 \rightarrow NO_3 + O_2$	$1.2 \times 10^{-13} \exp(-2450/T)$
(R24)	$NO_2 + H \rightarrow OH + NO$	1.4×10^{-10}
(R25)	$NO_2 + NO_3 \rightarrow NO + NO_2 + O_2$	$1.91 \times 10^{-13} \exp(-1696/T)$
(R26)	$NO_3 + O \rightarrow NO_2 + O_2$	1.0×10^{-11}
(R27)	$NO_3 + OH \rightarrow HO_2 + NO_2$	2.3×10^{-11}
(R28)	$HNO_2 + O \rightarrow OH + NO_2$	$2.0 \times 10^{-11} \exp(-3000/T)$
(R29)	$HNO_2 + H \rightarrow NO_2 + H_2$	$2.0 \times 10^{-11} \exp(-3700/T)$
(R30)	$HNO_2 + OH \rightarrow NO_2 + H_2O$	$1.8 \times 10^{-11} \exp(-390/T)$
(R31)	$HNO_3 + O \rightarrow OH + NO_3$	3.0×10^{-17}
(R32)	$HNO_3 + OH \rightarrow NO_3 + H_2O$	$4.02 \times 10^{-14} \exp(317.7/T)$
(R33)	$SO + O_2 \rightarrow O + SO_2$	$1.55 \times 10^{-13} \exp(-2288/T)$
(R34)	$SO + O_3 \rightarrow SO_2 + O_2$	$4.3 \times 10^{-12} \exp(-1148/T)$
(R35)	$SO + OH \rightarrow H + SO_2$	8.59×10^{-11}
(R36)	$SO + NO_2 \rightarrow NO + SO_2$	1.4×10^{-11}
(R37)	$SO_2 + O_3 \rightarrow O_2 + SO_3$	$3.0 \times 10^{-12} \exp(-7000/T)$
(R38)	$SO_3 + O \rightarrow O_2 + SO_2$	$3.17 \times 10^{-12} \exp(-4455/T)$
(R39)	$SO_3 + H_2O \rightarrow H_2SO_4$	1.2×10^{-15}
(R40)	$HSO_3 + O_2 \rightarrow HO_2 + SO_3$	$1.23 \times 10^{-12} \exp(-316.8/T)$
(R41)	$CO + OH \rightarrow H + CO_2$	$4.44 \times 10^{-16} T^{0.98} \exp(94/T)$

Reduced Reaction Mechanism

In the intermediate regime of the wake the jet plume was entrained into the wing tip vortex. To model the impact of the wing vortex on ozone in this region, large eddy simulations (LES) may be required in order to model the vortex properly. Solving the flow field by LES would demand significant computer time, making it impossible to incorporate a detailed chemical mechanism. A reduced mechanism capable of describing the key chemical reactions is necessary. A reduced chemistry is feasible if certain intermediate species reach the quasi-steady state when their production rates are nearly equal to their consumption rates. Consequently, the concentration of a quasi-steady state can be expressed in terms of major species. We identify a species in the quasi-steady state when it satisfies the criterion

$$X_k \cdot \frac{|\dot{\omega}_k^p - \dot{\omega}_k^c|}{\max(|\dot{\omega}_k^p|, |\dot{\omega}_k^c|)} \ll 1 \qquad (14)$$

where $\dot{\omega}_k^p$ and $\dot{\omega}_k^c$ are the production and consumption rates of species k, and X_k is the mole fraction of species k. Because of the rapid temperature changes in the near field of jet plume, a species that does not satisfy the steady state criterion in the near field may reach the steady state in the far field. One may construct different reduced mechanisms suitable for different jet regimes.

Development of reduced chemistry has been carried out using the PSR with a computer-assisted reduced mechanism code [*Herr et al.*, 1993] for the near field of the jet plume where large temperature changes take place. Assuming quasi-steady state for H, HO_2, H_2O_2, SO, H_2, HSO_3, NO_3, N_2O_5, and O (9 species out of a total of 24 species), we obtained the following eight-step reduced mechanism,

(G-R1) $O_3 + SO_2 = O_2 + SO_3$
(G-R2) $O_3 + SO_3 = 2O_2 + SO_2$
(G-R3) $O_3 + 2OH = H_2O + O_3$
(G-R4) $NO + O_3 = O_2 + NO_2$
(G-R5) $O_2 + NO + HNO_3 + SO_2 = OH + 2NO_2 + SO_3$
(G-R6) $O_2 + SO_2 + HNO_2 = OH + NO_2 + SO_3$
(G-R7) $H_2O + SO_3 = H_2SO_4$
(G-R8) $O_3 + CO = O_2 + CO_2$

The rates for the global reactions are expressed in terms of the elementary reaction rates as

$$\omega_{G\text{-}R1} = \omega_1 + \omega_5 + \omega_7 + \omega_{11} + \omega_{13} + \omega_{14} + \omega_{15} + \omega_{22} + \omega_{25} + \omega_{26} - \omega_{33} + \omega_{37} + \omega_{42} - \omega_{45} + \omega_{49} + \omega_{58}$$

$$\omega_{G\text{-}R2} = \omega_3 - \omega_4 + \omega_8 + \omega_{10} - \omega_{13} - \omega_{16} - \omega_{17} - \omega_{20} + \omega_{25} + \omega_{27} + \omega_{29} + \omega_{30} + \omega_{32} - \omega_{42} - \omega_{43} - \omega_{44} + \omega_{48} - \omega_{50} - \omega_{51} - \omega_{52} - \omega_{53} + \omega_{56} + \omega_{57} - \omega_{58} - \omega_{60}$$

$$\omega_{G\text{-}R3} = \omega_6 + \omega_9 + \omega_{10} + \omega_{11} + \omega_{12} + \omega_{17} + \omega_{30} + \omega_{32} + \omega_{47}$$

$$\omega_{G\text{-}R4} = \omega_{19} + \omega_{20} - \omega_{22} + \omega_{23} - \omega_{24} - 2\omega_{25} - \omega_{26} - \omega_{27} - \omega_{36} + \omega_{50} + \omega_{51} + \omega_{52} + \omega_{53} - \omega_{56} - \omega_{57}$$

$$\omega_{G\text{-}R5} = \omega_{21} - \omega_{23} + \omega_{25} + \omega_{26} + \omega_{27} - \omega_{52} - \omega_{53} + \omega_{57}$$

$$\omega_{G\text{-}R6} = \omega_{28} + \omega_{29} + \omega_{30} - \omega_{51} + \omega_{56}$$

$$\omega_{G\text{-}R7} = \omega_{39}$$

$$\omega_{G\text{-}R8} = \omega_{41} + \omega_{60}$$

Table 2b. Gas Phase Reaction Mechanism: Three-Body Combination and Thermal Decombination Reactions

	Reaction	Low-Pressure Limit k_0	High-Pressure Limit k_∞
(R42)	$O + O \xrightarrow{M} O_2$	$5.2 \times 10^{-35} \exp(900/T)$	———
(R43)	$O + O_2 \xrightarrow{M} O_3$	$5.51 \times 10^{-31} T^{-1.3} \exp(152.6/T)$	$4.2 \times 10^{-12} \exp(-183/T)$
(R44)	$H + O \xrightarrow{M} OH$	$1.30 \times 10^{-29} T^{-1}$	———
(R45)	$H + O_2 \xrightarrow{M} HO_2$	$1.05 \times 10^{-30} T^{-0.7} \exp(144.2/T)$	7.5×10^{-11}
(R46)	$H + H \xrightarrow{M} H_2$	$1.28 \times 10^{-29} T^{-1.13} \exp(-100.6/T)$	$2.9 \times 10^{-10} \exp(5821/T)$
(R47)	$H + OH \xrightarrow{M} H_2O$	$1.54 \times 10^{-28} T^{-1.21} \exp(295.3/T)$	$2.69 \times 10^{-10} \exp(-75/T)$
(R48)	$OH + OH \xrightarrow{M} H_2O_2$	$6.58 \times 10^{-29} T^{-0.8}$	1.5×10^{-11}
(R49)	$HO_2 + HO_2 \xrightarrow{M} H_2O_2 + O_2$	$1.9 \times 10^{-33} \exp(980/T)$	$2.2 \times 10^{-13} \exp(600/T)$
(R50)	$NO + O \xrightarrow{M} NO_2$	$9.09 \times 10^{-28} T^{-1.6}$	$5.43 \times 10^{-12} T^{0.3}$
(R51)	$NO + OH \xrightarrow{M} HNO_2$	$1.91 \times 10^{-26} T^{-1.9} \exp(164.8/T)$	$5.1 \times 10^{-12} \exp(159.8/T)$
(R52)	$NO_2 + O \xrightarrow{M} NO_3$	$6.21 \times 0^{-23} T^{-3.22} \exp(-570.5/T)$	$2.65 \times 10^{-11} \exp(-25.78/T)$
(R53)	$NO_2 + OH \xrightarrow{M} HNO_3$	$3.50 \times 10^{-16} T^{-5.2} \exp(-840/T)$	$1.84 \times 10^{-12} \exp(587.2/T)$
(R54)	$NO_2 + NO_3 \xrightarrow{M} N_2O_5$	$6.98 \times 10^{-22} T^{-3.4}$	$6.40 \times 10^{-13} T^{0.2}$
(R55)	$N_2O_5 \xrightarrow{M} NO_2 + NO_3$	$1.5 \times 10^{-6} \exp(-9104/T)$	$5.9 \times 10^{11} \exp(-9370/T)$
(R56)	$HNO_2 \xrightarrow{M} OH + NO$	$5.00 \times 10^{6} T^{-3.8} \exp(-25340/T)$	$1.20 \times 10^{19} T^{-1.23} \exp(-25010/T)$
(R57)	$HNO_3 \xrightarrow{M} OH + NO_2$	$1.2 \times 10^{-6} \exp(-22270/T)$	$2.14 \times 10^{15} \exp(-24270/T)$
(R58)	$SO_2 + O \xrightarrow{M} SO_3$	$1.49 \times 10^{-32} \exp(-601/T)$	1.19×10^{-9}
(R59)	$SO_2 + OH \xrightarrow{M} HSO_3$	$1.97 \times 10^{-32} \exp(867.3/T)$	2.0×10^{-12}
(R60)	$CO + O \xrightarrow{M} CO_2$	$2.49 \times 10^{-33} \exp(-1550/T)$	$2.66 \times 10^{-14} \exp(-1459/T)$

The effective second-order reaction rate constant is [*Demore et al.*, 1992]

$$k(M,T) = \left(\frac{k_0(T)[M]}{1+(k_0(T)[M]/k_\infty(T))}\right) 0.6^{\{1+[\log_{10}(k_0(T)[M]/k_\infty(T))]^2\}^{-1}}$$

For third-order low-pressure and second-order high-pressure limits, the units are cm^6 $molecule^{-2}$ s^{-1} and cm^3 $molecule^{-1}$ s^{-1}, respectively. For second-order low-pressure and first-order high-pressure limits, the units are cm^3 s^{-1} and s^{-1}, respectively.

Although the species in the quasi-steady state do not appear explicitly in the global reactions, their kinetics effects are included in the elementary reaction rates. The concentrations of quasi-steady state species are computed by iteration using the following expressions:

$$[HSO_3] = \frac{k_{59}[OH][SO_2]}{k_{40}[O_2]};$$

$$[NO_3] = \frac{A}{k_{26}[O] + k_{25}[NO_2] + k_{27}[OH] + k_{54}[NO_2] + k_{21}[NO]},$$

$$A = k_{31}[O][HNO_3] + k_{55}[N_2O_5] + k_{52}[O][NO_2] + k_{23}[NO_2][O_3] + k_{32}[OH][HNO_3];$$

$$[H] = \frac{B}{C},$$

$$B = k_{35}[OH][SO] + k_7[OH][O] + k_9[OH][H_2] + k_{41}[OH][CO],$$

$$C = k_{46}[H] + k_3[OH] + k_{44}[O][M] + k_{18}[H_2O_2] + k_{29}[HNO_2] + k_{17}[H_2O_2] + k_6[HO_2] + k_5[HO_2] + k_{47}[OH] + k_4[HO_2] + k_2[O_3] + k_{24}[NO_2] + k_{45}[O_2];$$

$$[O] = \frac{k_{33}[O_2][SO] + k_3[H][OH] + k_6[H][HO_2] + k_{10}[OH][OH]}{D},$$

$$D = k_{b,33}[SO_2] + k_{38}[SO_3] + k_{44}[H][M] + k_{42}[O][M] + k_{16}[H_2O_2] + k_{60}[CO] + k_{31}[HNO_3] + k_{28}[HNO_2] + k_{26}[NO_3] + k_{13}[HO_2] + k_{58}[SO_2] + k_1[O_3] + k_7[OH] + k_{52}[NO_2] + k_{50}[NO] + k_{22}[NO_2] + k_{43}[O_2];$$

$$[SO] = \frac{k_{b,33}[O][SO_2]}{k_{34}[O_3] + k_{35}[OH] + k_{36}[NO_2] + k_{33}[O_2]};$$

$$[H_2] = \frac{E}{k_9[OH]};$$

$$E = k_{46}[H][H] + k_3[H][OH] + k_{18}[H][H_2O_2] + k_{29}[H][HNO_2] + k_5[H][HO_2],$$

$$[H_2O_2] = \frac{k_{49}[HO_2][HO_2] + k_{15}[HO_2][HO_2] + k_{48}[OH][OH]}{k_{18}[H] + k_{16}[O] + k_{17}[H] + k_{12}[OH]},$$

$$[HO_2] = \frac{F}{G},$$

$$F = k_{18}[H][H_2O_2] + k_{16}[O][H_2O_2] + k_{27}[OH][NO_3] + k_{12}[OH][H_2O_2] + k_8[OH][O_3] + k_{40}[O_2][HSO_3] + k_{45}[H][O_2],$$

$$G = k_6[H] + k_5[H] + k_4[H] + k_{13}[O] + k_{49}[HO_2] + k_{15}[HO_2] + k_{14}[O_3] + k_{11}[OH] + k_{20}[NO];$$

$$[N_2O_5] = \frac{k_{54}[NO_2][NO_3]}{k_{55}}.$$

Results and Discussions

Results are presented for a Mach 2.4 HSCT flight flying at 18 km and N85. The initial exhaust and ambient conditions are taken from *Brown et al.* [1996]. A jet exit radius of 0.93 m [*Kärcher*, 1994] is used in the simulations.

Sensitivity Information and Key Reaction Paths

Sensitivity information is useful for identifying the controlling chemical steps responsible for the creation/destruction of a certain species. The sensitivity coefficients are displayed as

$$\beta_{ik} = \frac{A_i}{X_k}\frac{\partial X_k}{\partial A_i} \tag{15}$$

where β_{ik} is the sensitivity for change in the mole fraction of the kth species, X_k, due to a small change in temperature-independent prefactor, A_i, of the ith reaction rate $k_i = A_i T^n \exp(-E_a/T)$. We used the ratio (mole base) between the free-stream (ambient air) and the exhaust gas from the engine to describe the different mixtures. A large free-stream/exhaust ratio corresponds to a mixture highly diluted with ambient air. The PSR model has been used to assess the degree of changes in ozone and NO_x in the engine exhaust gas when it is perfectly mixed with a certain amount of ambient air over residence times up to 100 s. Figure 4 presents a set of sample sensitivity data of NO versus residence time for four free-stream/exhaust ratios at 0.1, 1, 10, and 100. As seen from the plots, both reaction (19) $NO + O_3 \rightarrow NO_2 + O_2$ and reaction (51) $NO + OH + M \rightarrow HNO_2 + M$ are responsible for depleting NO. When there is a large amount of air mixed with the exhaust gas, reaction (19) becomes the dominant step in converting NO into NO_2. Since reactions (53) $OH + NO_2 + M \rightarrow HNO_3 + M$ and (30) $HNO_3 + OH \rightarrow H_2O + NO_3$ are competing with reaction (51) for OH, increasing their rates will reduce the effectiveness of reaction (51) in converting NO into HNO_2. Consequently, reactions (53) and (30) have positive sensitivity values. However, the importance of reactions (53) and (30) diminishes as more air is mixed with the exhaust gas since OH concentration becomes small compared to O_3 in mixtures with high free-stream/exhaust ratios.

Next we examine the sensitivity information for NO_2 as presented in Figure 5. As revealed in the sensitivity data, reaction (53) $OH + NO_2 + M \rightarrow HNO_3 + M$ is the major channel for converting NO_2 into a more stable species HNO_3. Consequently reaction (53) has a negative sensitivity for all mixtures. The sensitivity data also show that NO_2 is produced via reaction of NO with O_3 through reaction (19) and via reaction of OH and HNO_2 through reaction (30). Reaction (30) becomes less important for mixtures with high free-stream/exhaust ratios. Reaction (19) becomes the dominant route for NO_2 production for mixtures with large free-stream/exhaust ratios as more O_3 is present in the system. Reaction (51) has positive sensitivity with respective to NO_2 as it produces HNO_2 which then forms NO_2 via reaction (30). Figure 6 shows the sensitivity information of O_3 over all mixtures. As expected, reaction (19) $NO + O_3 \rightarrow NO_2 + O_2$ is the most important step in controlling O_3. For mixtures with low free-stream/exhaust ratios, O_3 is produced via reaction (43) $O + O_2 + M \rightarrow O_3 + M$, and NO_2 is converted to NO via reaction (22) $NO_2 + O \rightarrow NO + O_2$. When free-stream air is increased, the importance of these two reactions diminishes due to the consumption of the O radical.

Evaluation of Reduced Chemistry

First, PSR is used for evaluating performances of the eight-step reduced by comparing concentrations of NO, NO_2, and O_3 over a wide range of free-stream/exhaust ratios for residence times from 0.01 s to 100 s. In all cases, excellent agreement is found between the results obtained with the detailed mechanism and those with the reduced chemistry. Figure 7 presents sample comparisons showing almost identical results when reduced chemistry is used; however, the computing time is decreased by a factor of 3.

Second, to assess the transient responses of reduced chemistry to time-varying mixing with ambient air, WMR simulations were performed with air injection rates estimated on the basis of the PDF jet simulations. As described above, the WMR simulations are similar to the commonly used Lagrangian box model except that the temperature is not prescribed but is solved for directly using the energy equation. Figure 8 presents the time evolution of major nitrogen, sulfur, and oxygen species for the engine jet exhaust over the first 2 seconds after the exhaust nozzle, showing excellent agreement. To further evaluate the performance of reduced chemistry with the micromixing effect, the PaSR model is computed with identical conditions as those in the WMR model, and the results are presented in Figure 9. Consistent with the comparisons observed in the WMR calculations, the performance of the reduced chemistry remains quite satisfactory in spite of the fact that a wider range of mixtures have been computed since the reactor is not well mixed.

Third, Monte Carlo PDF jet simulations have been performed and Figure 10 presents the predicted centerline temperature evolution obtained with the effects of microscale mixing. The computed temperature is seen to decreases rapidly in the near field, manifesting fast entrainment of cool ambient air. Figure 11 presents the centerline mole fractions of major nitrogen, sulfur, and oxygen species evolution obtained with the detailed mechanism and the eight-step reduced chemistry. It shows good agreement except for O_3 at the early jet stage. This is due to the steady state assumption for the O radical which does not achieve steady state at early jet stage where it contributes to the production of O_3 through $O + O_2 + M \rightarrow O_3 + M$.

Impact of Microscale Mixing on Chemical Kinetics

A parametric study of the influence of various mixing processes on predicted chemistry has been carried out with the models listed in Table 1. To quantify the impact of different mixing processes on NO_x, HNO_3, and O_3 in the jet plume, we

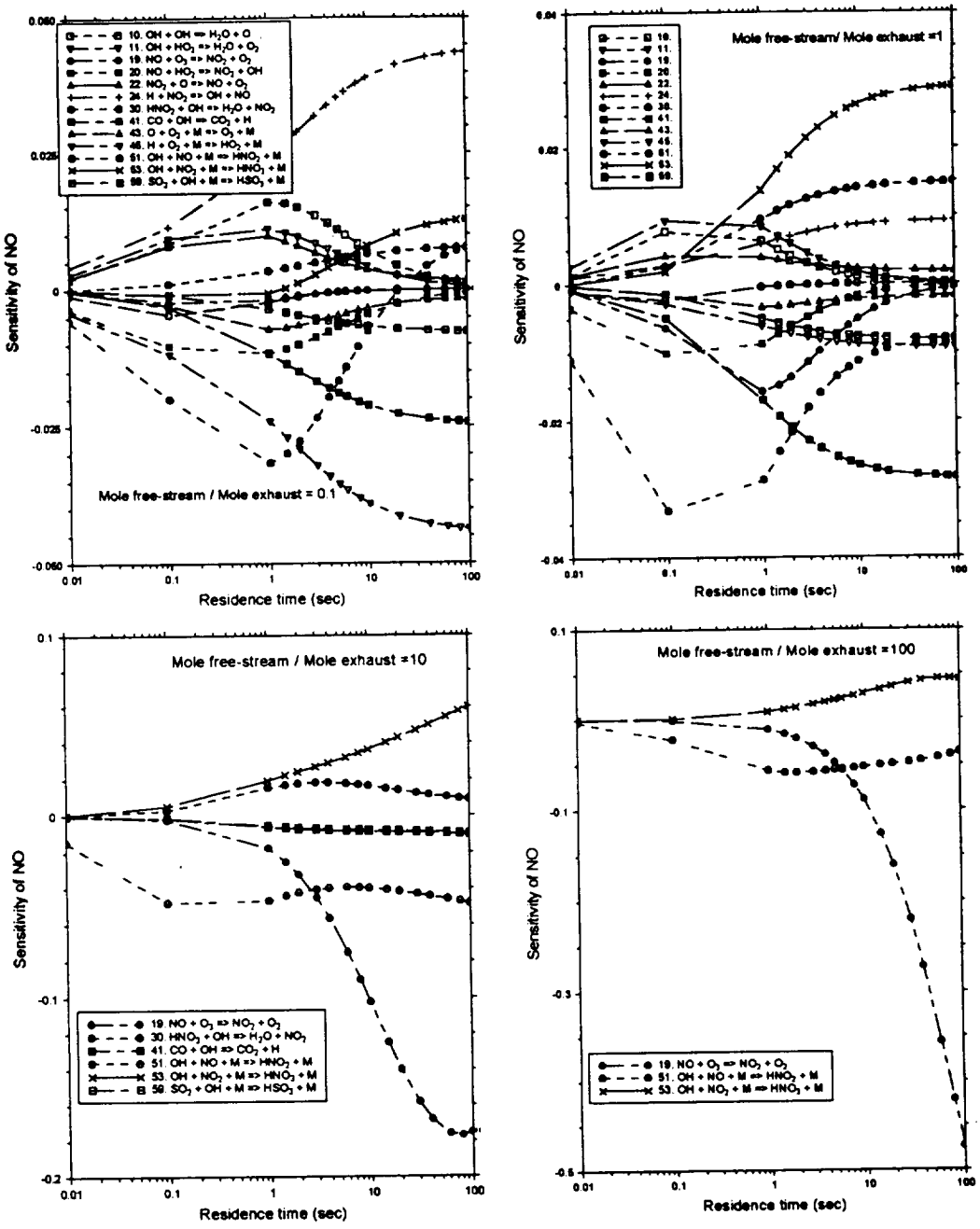

Figure 4. PSR model predictions of sensitivity of NO species to elementary steps at free-stream and exhaust mole ratios of 0.1, 1, 10, and 100.

examine the species response normalized by NO_x flux at the nozzle exit. Because of the small amount of NO_x entrained into the exhaust plume the total NO_x mass flux remains nearly constant. The normalized species response is defined as

$$\text{normalized species response} = \frac{m_i(t) - m_{i,\text{total}}(t)}{m_{\text{NOx}}}, \qquad (16)$$

where $m_i(t)$ is the mass flux of species i evaluated over the cross section of the jet at a certain downstream location, and $m_{i,\text{total}}$ is the sum of the mass flux of a certain species originated from the nozzle exit and the mass flux entrained into the jet, that is, $m_{i,\text{total}}(t) = m_{i,\text{exhaust}} + m_{i,\text{entrained}}(t)$. A species response value of zero indicates that the total amount of species is conserved. Negative or positive species responses correspond, respectively, to destruction or creation of species due to chemical reactions. According to convention, the mass of NO_x is reported as the equivalent mass of NO_2, which is expressed as $m_{\text{NOx}} = m_{\text{NO}_2} + W_{\text{NO}_2}/W_{\text{NO}} m_{\text{NO}}$, where W is the molecular weight of a species.

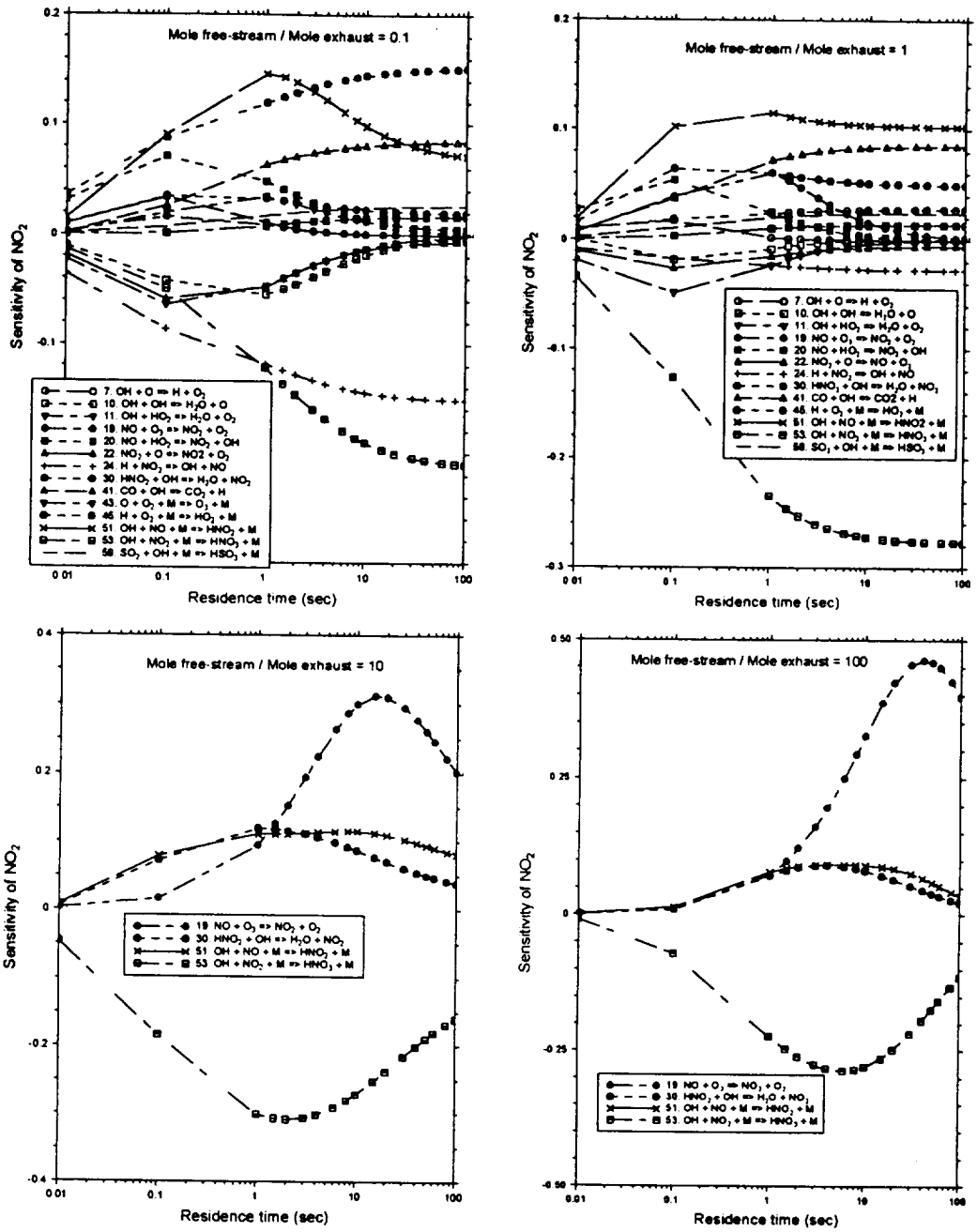

Figure 5. PSR model predictions of sensitivity of NO_2 species to elementary steps at free-stream and exhaust ratios of 0.1, 1, 10, and 100.

Figure 12 presents the predicted NO_x, HNO_3, and O_3 responses obtained with various numerical models. As seen from the NO_x and HNO_3 responses, rapid conversion of NO and NO_2 into HNO_3 occurs in the near field due to reactions of $OH + NO_2 + M \rightarrow HNO_3 + M$ and $NO + O_3 \rightarrow NO_2 + O_2$. After 0.5 s, the NO_x response remains nearly constant, indicating negligible changes in total NO_x due to chemical reactions. The HNO_3 response is directly correlated with the NO_x response as its production is via the reaction between OH and NO_2. The O_3 response shows that a small amount of O_3 is produced via reaction $O + O_2 + M \rightarrow O_3 + M$ at early jet stage, leading to a peak O_3 response at about 0.05 s (~70 m from nozzle exit plane). After the peak, entrainment process becomes important, and the O_3 response starts to decrease due to the dominant destruction reaction $NO + O_3 \rightarrow NO_2 + O_2$ as more O_3 is entrained. The predicted O_3 depletion per unit mass of NO_x increases roughly linearly with time or roughly with downstream distance. The constant destruction of O_3 per unit mass of NO_x exhaust is expected as NO_x plays the catalytic role in consuming O_3.

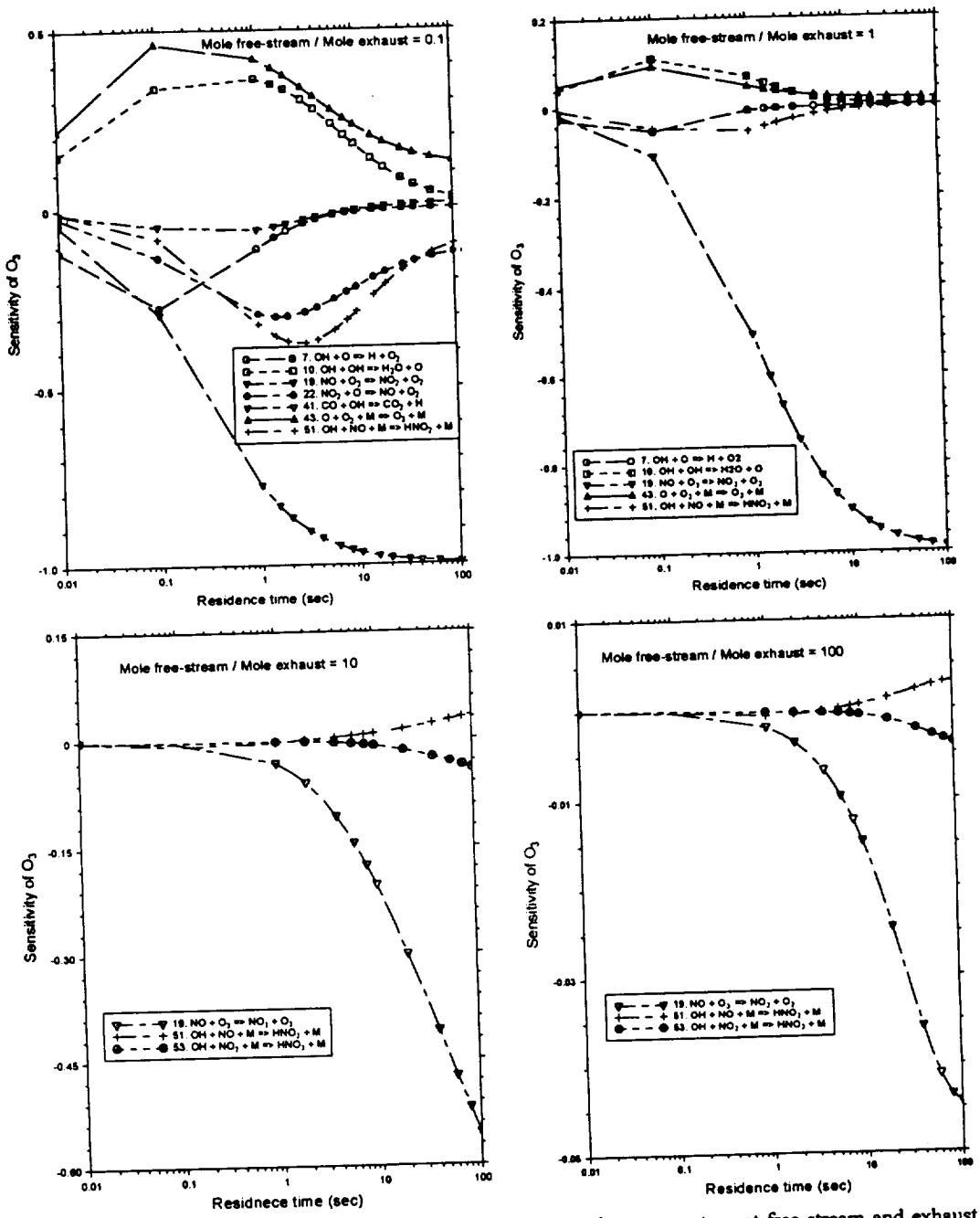

Figure 6. PSR model predictions of sensitivity of O_3 species to elementary steps at free-stream and exhaust mole ratios of 0.1, 1, 10, and 100.

Overall, conversion of NO_x into HNO_3 decreases when more detailed features of mixing processes are included in the model. The WMR model (similar to a Lagrangian box model) gives the largest NO_x conversion into HNO_3 since both macroscale and microscale mixing processes are assumed infinitely fast. When microscale mixing is accounted for in the PaSR, the NO_x response reduces by 3.5%. The PDF jet simulation with well-mixed assumption for each grid cell (similar to the SPF-II code) includes the macroscale mixing process that brings ambient fluids into the jet plume through turbulent convection and stirring. The differences in the NO_x responses between the WMR and the PDF jet model with completely mixed cells are about 25%. When microscale mixing is included by the modified Curl's mixing model, the NO_x response reduces further by 5%. Consequently, the amount of HNO_3 produced is largest when infinitely fast mixing is assumed. The influence of mixing processes at different scales on the predicted O_3 depletion is seen similar to the NO_x response except that the trend is reversed. Within the first 0.05 s, O_3 is produced by $O + O_2 + M \rightarrow O_3 + M$. The

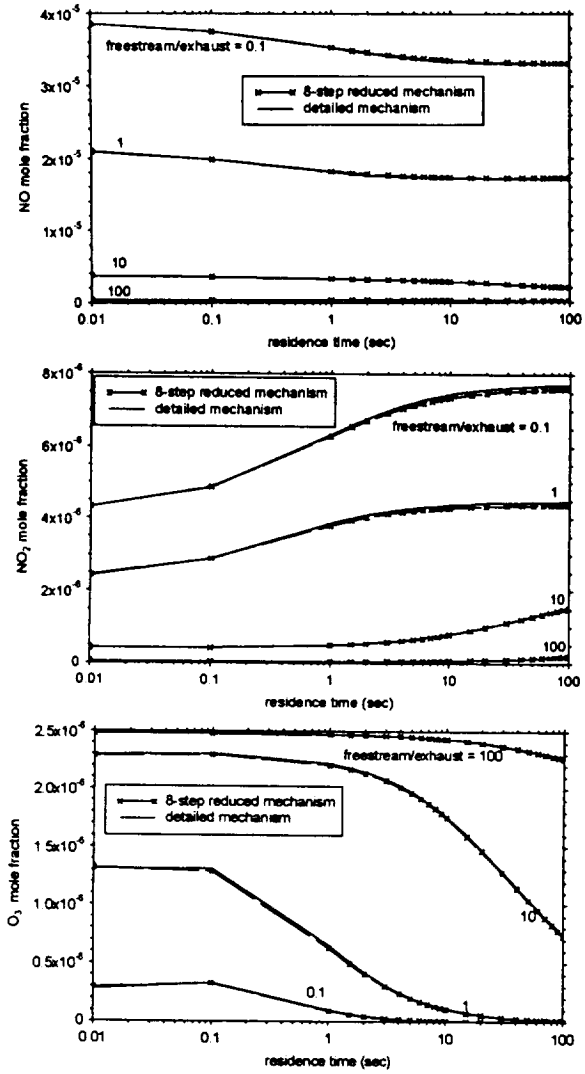

Figure 7. Comparison of PSR model predictions of NO, NO_2, and O_3 mole fractions with detailed and reduced mechanisms, showing good agreement over a wide range of mixtures of exhaust and ambient air as a function of residence time.

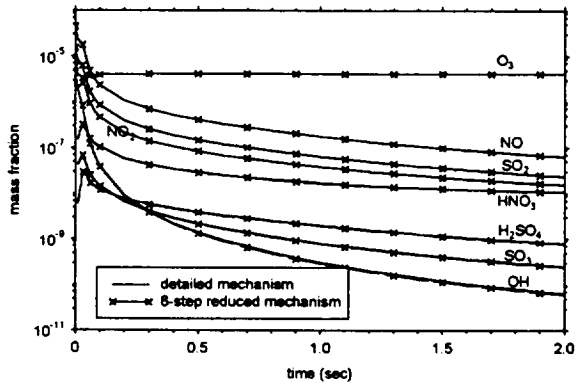

Figure 8. Comparison of WMR predictions of major nitrogen, sulfur, and oxygen species evolution with detailed and reduced mechanisms, showing good agreement.

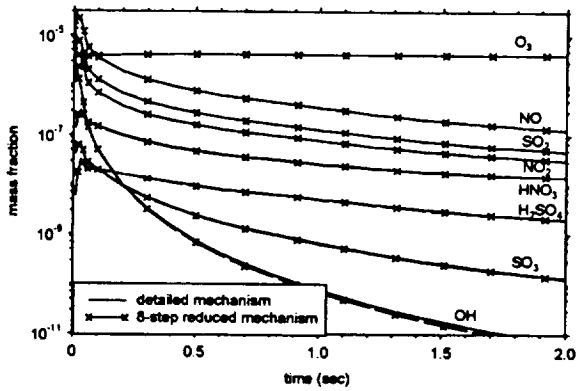

Figure 9. Comparison of partially stirred reactor (PaSR) predictions of major nitrogen, sulfur, and oxygen species evolution with detailed and reduced mechanisms, showing good agreement.

timescale of chemistry for the radical O is comparable with that of microscale mixing. A strong coupling between reaction and mixing is noticed as the amount of O_3 produced increases with mixedness of the jet plume. After about 0.05 s, the destruction reaction $NO_2 + O_3 \rightarrow NO + O_2$ becomes dominant due to fast mixing of jet plume with ambient air. Since the amount of O_3 depleted via this reaction is almost the same, the O_3 response curves for each model evolves in an almost parallel fashion.

A comparison of the predicted centerline mole fractions of major species and the relative differences obtained using the PDF model with/without Curl's mixing model is presented in Figure 13. The comparison shows the influence on chemical kinetics due to microscale mixing only. When the fluids are assumed well mixed at the microscale, the point at which entrainment becomes important starts earlier. The impact of microscale mixing at axis is noticeable after 50 m downstream, where the timescale of chemical reactions for radicals, such as OH and HO_2, is comparable or faster compared with that of microscale mixing. The impact of micromixing on radicals affects concentrations of other species since hydroxyl radical is the driver for major chemical reactions in the near field. Inclusion of microscale mixing increases predicted H_2SO_4 before the axial distance of 500 m and the increase reaches about

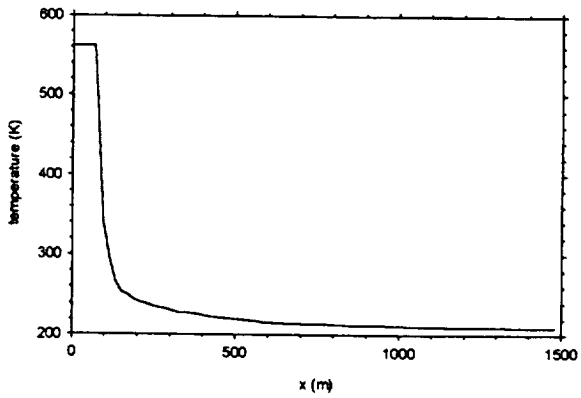

Figure 10. Centerline temperature evolution for probability density function (PDF) jet simulation.

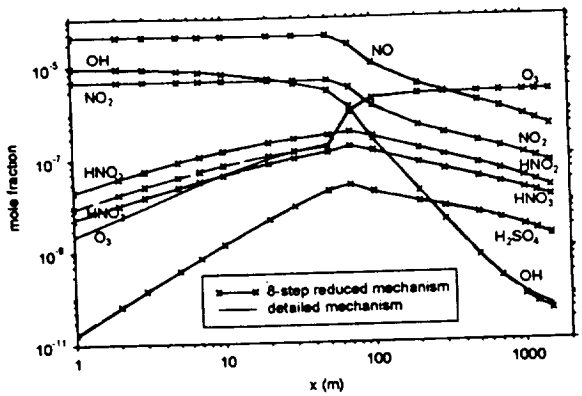

Figure 11. PDF jet simulation of centerline mole fractions of major nitrogen, sulfur, and oxygen species evolution for detailed and reduced mechanisms, showing good agreement.

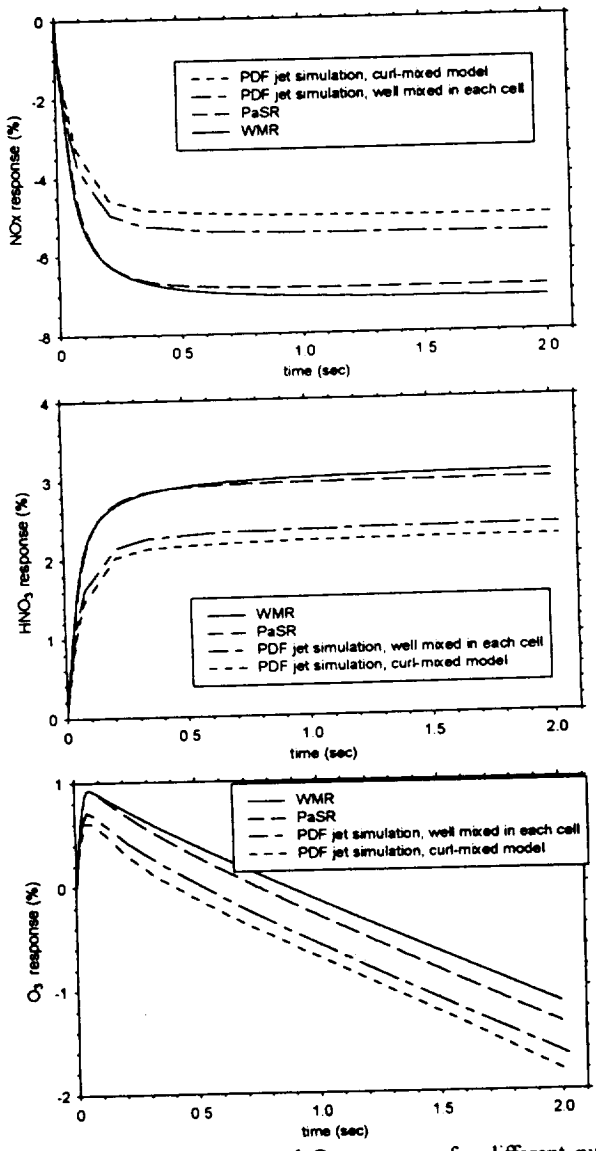

Figure 12. NO_x, HNO_3, and O_3 responses for different numerical models to explore the macromixing and micromixing effects.

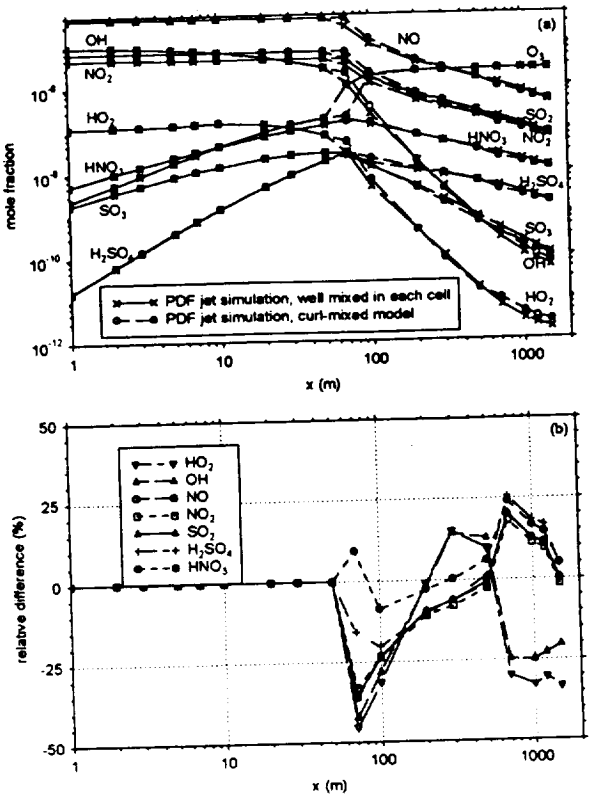

Figure 13. (a) Centerline mole fractions of major nitrogen, sulfur, and oxygen species for PDF jet simulation with different treatment for microscale mixing. (b) Relative difference of major species between the two models. Relative difference = $(X_{mix}-X_{curl})/X_{curl} \times 100$ (%), where X denotes mole fraction, subscript mix means PDF jet simulation with each cell well mixed, and curl means the curl-mixed model.

20% at 100 m. This may have a potential impact on predictions of sulfate aerosol formation which is a subject to be studied in the future.

Conclusions

Using a PSR model with a detailed reaction mechanism, the key reaction steps controlling NO_x, O_3, and OH evolution have been identified in engine exhaust gas mixed with various amounts of ambient air in the stratosphere. On the basis of the detailed mechanism, an eight-step reduced chemistry has been developed and tested extensively using PSR, WMR, PaSR, and the PDF jet simulation. The performances of the reduced chemistry are found quite good over a wide range of mixing conditions.

The relative importance of turbulent mixing at macroscale and microscale on chemistry is investigated by a parametric study using various models for the near-field jet plume. For a typical HSCT flight condition, inclusion of macroscale mixing leads to about 25% lower NO_x conversion to HNO_3 than that predicted by the WMR model (similar to a Lagrangian model). In regions close to nozzle exit, O_3 is produced via the reaction $O + O_2 + M \rightarrow O_3 + M$. The amount of O_3 produced increases with the degree of mixedness inside the exhaust plume. As such, the WMR model yields highest O_3 peak re-

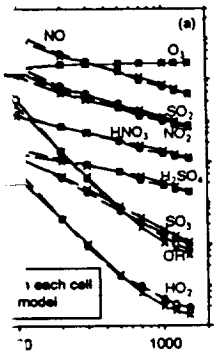

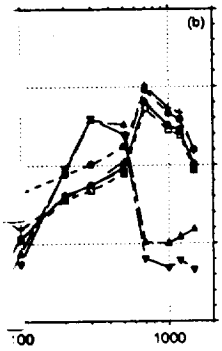

ns of major nitrogen,
simulation with differ-
) Relative difference of
s. Relative difference =
denotes mole fraction,
on with each cell well
model.

tial impact on predic-
ich is a subject to be

d reaction mechanism,
O_3, and OH evolution
as mixed with various
ere. On the basis of the
ced chemistry has been
g PSR, WMR, PaSR,
mances of the reduced
a wide range of mixing

t mixing at macroscale
igated by a parametric
ir-field jet plume. For a
on of macroscale mixing
sion to HNO_3 than that
ular to a Lagrangian
, O_3 is produced via the
amount of O_3 produced
ess inside the exhaust
ds highest O_3 peak re-

sponse in the near field in comparison with other models. The impact of macroscale mixing on chemical kinetics is found most significant in the early development of exhaust plume within 0.2 s. Inclusion of microscale mixing causes a slight delay in the mixing of exhaust species with ambient air. This impact results in about 5% changes in the overall species responses of O_3, NO_x, and HNO_3 across the jet. However, the influence of microscale mixing on local species concentration is found to cause nearly 50% differences for highly reactive radicals in the near field. With the microscale mixing included in the numerical model, the predicted centerline peak H_2SO_4 concentration increases at locations where sulfate aerosol formation could be highly active. The potential impact of microscale mixing on aerosol formation is a subject of future study.

Acknowledgments. This work is supported by National Aeronautics and Space Administration under grant NAG 1-1631. The authors appreciate valuable information and discussions provided by R.C. Miake-Lye.

References

Anderson, M. R., R. C. Miake-Lye, R. C. Brown, and C. E. Kolb, Calculation of exhaust plume structure and emission of the ER2 aircraft in the stratosphere, *J. Geophys. Res., 101*, 4025-4032, 1996.

Arnold, F., J. Scheid, T. Stilp, H. Schlager, and M. E. Reinhardt, Measurements of jet aircraft emissions at cruise altitude, I, The odd-nitrogen gases NO, NO_2, HNO_2, and HNO_3, *Geophys. Res. Lett., 19*, 2421-2424, 1992.

Brown, R. C., R. C. Miake-Lye, M. R. Anderson, C. E Kolb, and T. J. Resch, Aerosol dynamics in near-field aircraft plumes, *J. Geophys. Res., 101*, 22,939-22,953, 1996.

Chen, J.-Y., Stochastic modeling of partially stirred reactors, *Combust. Sci. Technol, 122*, 63-94, 1997.

Chen, J.-Y., W. Kollmann, and R.W. Dibble, Numerical computation of turbulent free-shear flows using a block-tridiagonal solver for a staggered grid system, paper presented at the 18th Annual Conference on Simulation and Modeling, Am. Soc. Mech. Eng., Pittsburgh, Penn., 1987.

Chen, J.-Y., W. Kollmann, and R. W. Dibble, Pdf modeling of turbulent methane-air nonpremixed jet flames, *Combust. Sci. Technol., 64*, 315-346, 1989.

Dash, S. M., H. S. Pergament, D. E. Wolf, N. Sinha, M. W. Taylor, and M. E. Vaughn Jr., The JANNAF standardized plume flowfield code version II (SPF-II), vol. I and II, *TR-CR-RD SS 90-4*, U.S Army Missile Command, Huntsville, Al., 1990.

Fahey, D. W., *et al.*, In situ observations in aircraft exhaust plumes in the lower stratosphere at midlatitudes, *J. Geophys. Res., 100*, 3065-3074, 1995.

Glarborg, P., R. J. Kee, J. F. Grcar, and J. A. Miller, PSR: A FORTRAN program for modeling well-stirred reactors, *Rep SAND86-8209*, Sandia Nat. Lab., Livermore, Calif., 1986.

Herr, C., W.-C. Chang, and J.-Y. Chen, Automatic generation of reduced mechanisms with applications to prediction of NO_x in hydrogen flames, paper presented at the 5th International Conference on Numerical Combustion, Soc. Ind. Appl. Math., Garmisch-Partenkirchen, Germany, Sept. 29 to Oct. 1, 1993.

Janika, J., W. Kolbe, and W. Kollmann, Closure of the transport equation for the pdf of turbulent scalar fields, *J. Nonequil. Thermodyn., 4*, 47-56, 1979.

Karol, I. L., and Y. E. Ozolin, Small- and medium-scale effects of high-flying aircraft exhausts on the atmospheric composition, *Ann Geophys., 12*, 979-985, 1994.

Kärcher, B., Transport of exhaust products in the near trail of a jet engine under atmospheric conditions, *J. Geophys. Res. 99*, 14,509-14,517, 1994.

Kärcher, B., A trajectory model for aircraft exhaust plumes, *J. Geophys. Res., 100*, 18,835-18,844, 1995.

Kärcher, B, M. M. Hirschberg, and P. Fabian, Small-scale chemical evolution of aircraft exhaust species at cruising altitude, *J. Geophys. Res., 101*, 15,169-15,190, 1996.

Miake-Lye, R. C., M. Martinez-Sanchez, R. C. Brown, and C. E. Kolb, Plume and wake dynamics, mixing and chemistry behind a high speed civil transport aircraft, *J. Aircraft, 30*, 467-479, 1993a.

Miake-Lye, R. C., *et al.*, Stratospheric aircraft exhaust plume and wake chemistry, *NASA Contract. Rep. 191495*, Langley Res. Cent., Hampton, Va., 1993b.

Pope, S. B., PDF methods for turbulent reactive flows, *Prog. Energy Combust. Sci., 11*, 119-192, 1985.

Stolarski, R. S., and H. L. Wesoky (Eds.), The atmospheric effects of stratospheric aircraft: A fourth program report, *NASA Ref. Publ. 1359*, 1995.

Tsang, W., and J. T. Herron, Chemical kinetic data base for propellant combustion, I, Reactions invloving NO, NO_2, HNO, HNO_2, HCN, and N_2O, *J. Phys. Chem. Ref. Data, 20*, 609-663, 1991.

J.-Y. Chen and Z. Wang, Department of Mechanical Engineering, 6163 Etcheverry Hall, University of California, Berkeley, CA 94704 (e-mail: jychen@euler.me.berkeley.edu)

(Received February 3, 1996; revised December 16, 1996; accepted March 12, 1997.)

AIAA 98–2902

Numerical Studies of Near-Field Plume-Vortex Interactions

Junxiao Wu and Suresh Menon
School of Aerospace Engineering
Georgia Institute of Technology
Atlanta, Georgia 30332-0150

29th AIAA Fluid Dynamics Conference
June 15–18, 1998 / Albuquerque, NM

Numerical Studies of Near-Field Plume-Vortex Interactions

Junxiao Wu* and Suresh Menon†
School of Aerospace Engineering
Georgia Institute of Technology
Atlanta, Georgia 30332-0150

In this study, fluid mixing and chemical reactions in the near-field wake of an aircraft has been investigated. The plume-vortex regime is studied using a 3D parallel LES code. Simulations of engine plume interaction with the wing-tip vortex of B737 and B747 have been carried out and some comparisons with data have been used to demonstrate the ability of the LES method. Inclusion of detailed gas phase kinetics and simple heterogeneous processes have been carried out to evaluate the effect of turbulent mixing on the chemical processes in the plume-vortex regime. Finally, to determine the impact of temporal assumptions (often used in such flow simulations) comparison with spatial simulations are carried out. Many features of the computed flow field show reasonable agreement with experimental data. The entrainment of the engine plumes into the wing-tip vortex and also the partial detrainment of the plume were numerically captured and analyzed. The impact of fluid mechanics on the chemical process has been estimated. Results indicate that a significant difference between spatial and temporal simulation exists (especially in the predicted SO_3 concentration). This has important implications for the prediction of sulfuric acid aerosols in the wake and may partly explain the discrepancy between past numerical studies and the data. Analysis of the results also show that spatial simulation is more suitable for the near-field interaction process. For example, it was determined that detrainment (observed in the B747 contrail) was only captured using the spatial model.

1 Introduction

The wing-tip vortices shed from an aircraft's wings are known to pose a danger for aircrafts in the wake and are considered a major hazard near airports. Another consequence of the shed vortices that is perhaps less appreciated is their ability to entrain the hot exhaust of the engine during cruise flight in the upper atmosphere. The resulting species-rich and relatively long-lived contrails have been of increasing concern and a focus of research in recent years because the species entrained into the vortex wake can react with the ambient species thereby changing the local chemical balance. These studies have been motivated by the projected increase in future subsonic flights in the upper troposphere by the proposed Advanced Subsonic Transports (AST) operating in the transatlantic and Pacific rim flight corridors and by the possibility of future supersonic flights in the lower stratosphere by the High Speed Civilian Transport (HSCT).

The *near-field* region of the aircraft's wake can be divided roughly into two parts: a *plume* regime and a *plume-vortex* regime. The plume regime is identified as the initial region behind the aircraft where the engine exhaust plume grows and mixes with the ambient air. This regime is typically very short, approximately 1 sec after exhaust or around 200 m downstream of the engine exit plane. Further downstream is the plume-vortex regime where the exhaust plume is entrained into the rolled-up wing tip vortices. This regime is around $1-2$ km long and approximately 10 sec downstream of the exhaust. Due to the relatively high temperature of the engine exhaust and the species content, significant reactions can take place in the plume-vortex regime. The region downstream of the plume-vortex region is the wake region where the vortex wake breaks up due to (Crow) instability and mixes with the ambient air. This region is very large extending over 20 km and the mixing process can take many days depending upon the ambient conditions.

In the present study, the near-field region, especially the plume-vortex regime is of interest. In particular, we are interested in the chemical processes that can occur in this region due to the reaction of the emitted species with the ambient air (in particular, ozone). Key species that are of interest here are nitrogen oxides (NO_x) (generated from the oxidation of molecular nitrogen at high temperature), carbon monoxide(CO) (due to incomplete combustion), methane(CH_4), non-methane hydrocarbons(HC) and soot particles. The role of these trace species in the atmospheric photochemical and radiative processes is not very well understood. For example, the concentration of tropospheric ozone, an important greenhouse gas, is dependent on transport across tropopause and by chemical production and destruction involving reactions of NO_x, non-methane hydrocarbons, carbon monoxide,

*Graduate Research Assistant, AIAA Student Member
†Professor, AIAA Senior Member

and hydrogen oxides (HO_x). Furthermore, the radiative balance of the atmosphere can be affected by the accumulation of carbon dioxide and water (CO_2 and H_2O are the primary species in the engine exhaust) and by the aircraft-induced changes in aerosols and clouds. In addition, the combustion aerosols (soot) and the binary H_2SO_4/H_2O droplets in the plume can be efficient cloud condensation nuclei and serve as sites for heterogeneous reactions.

The ozone balance in the upper troposphere and lower stratosphere can be perturbed by an increase in NO_x and by heterogeneous reactions that take place on the surface of aerosols.[1,2] In the troposphere, NO_x acts as a catalyst to produce O_3 in reactions involving the oxidation of methane and other hydrocarbons. However, in the stratosphere, where O_3 is a barrier to ultraviolet light, NO_x catalytically destroys O_3 in reactions involving O atoms. Thus, the impact of emitted species on ozone is a function of many variables. This can complicate long-term prediction of upper atmosphere chemical balance.

A variety of models have been developed to assess the effect of aircraft flights on the atmosphere. These models generally fall into two categories: "small-scale" and "global" models. "Small-scale" models treat the near-field regime of the exhaust wake by ignoring processes that operate on larger time and space scales. Global models,[3] on the other hand, attempt to represent the large spatial scales and ignore, or represent very crudely, the small scales processes. To obtain some sort of continuity, some of the global models[3] use the engine exhaust conditions or the data at the end of the plume-vortex regime as input to their large-scale models. However, as shown recently,[4–6] the concentration of species (e.g., chemical radicals OH, HO_2 and soot) can undergo very rapid changes in the near-field. This can significantly modify the input conditions for the far field simulations. Thus, to obtain accurate prediction of the global chemical balance due to aircraft emission, the chemical processes in the plume-vortex regime is very important.

Models for the near-field regime have been developed by many researchers. The simplest model, often called the "trajectory box" model,[7,8] ignores flow transport and focuses primarily on the chemical species evolution. This type of model has been very popular since detailed chemical processes can be studied due to its computational efficiency. Models that incorporate both chemical and transport processes have also been developed. However, some approximations were employed to reduce the computational expense. For example, some models[4,9,10] used the well known SPF-II code[11] which is an efficient parabolic Navier-Stokes model. Gas phase kinetics, binary H_2SO_4-H_2O nucleation and aerosol coagulation have been studied using this model. Garnier et al.[12] used an integral model and a two-dimensional direct simulation of convection-diffusion equation to investigate the evolution of the mixing along the wake of a typical large transport aircraft. Menon and Wu[6] developed a new mixing model that included both micro- and macro-scale mixing effects and Wang and Chen[5] used a scalar probability density function model which included the large-scale mixing effect but ignored the micro-scale mixing effects. Comparison of these models was recently carried out[6] and it was demonstrated that inclusion of both macro- and micro-scale mixing results in 30% less O_3 and 15% less NO_2 depletion in the near field regime.[6]

The hydrodynamics of the plume-vortex regime is also quite complex. For example, the competition between the vortex centripetal force and gravitation buoyancy of hot plume can lead to a different final altitude of deposition of emissions.[9] This implies that evolution of the plume occurs in a highly unsteady manner. However, many of the models noted above[4,5] are steady-state models and therefore, are unable to account for the unsteady mixing effects.

To study unsteady jet-vortex interactions, unsteady methods have also been used. For example, direct numerical simulation[13] and large eddy simulation (LES) of trailing vortices[14] showed that there exists strong 3-D instability in vortex wakes with an axial deficit. The vortex instability results in vortex-stretching which may have a substantial effect on the mixing of jet plume with the ambient air. Gerz and Ehret[15] used LES to simulate the vortex roll-up process of the wake of a B-747 one second after exit. They showed that temperature, relative humidity peak at the center of the wingtip vortex, the wing boundary layer turbulence and the ambient turbulence all can affect the plume-vortex interaction process.

Unsteady simulations are computationally very expensive and therefore, most past studies employed some simplifying assumptions. For example, only limited chemical effects have been investigated so far[16] and all simulations reported so far employed periodic boundary conditions in the streamwise directions (i.e. simulated temporal evolution instead of the actual spatial evolution). Temporal approximation is truly justified only far downstream where the interaction between the jet plume and wingtip vortex has been completed. It has not yet been shown what features of the flow and the accompanying chemical processes are different and/or modified by this temporal assumption. This issue is important since it has been shown that the entrainment predicted by temporal and spatial simulations differ markedly due to the asymmetry between the high speed and the low speed sides of the shear layer.[17] The impact of this asymmetric entrainment on the chemical processes in the plume-vortex interaction regime has not been addressed so far.

This paper will address many of these issues and will attempt to quantify the impact of simulation method-

ology (i.e., spatial or temporal) on the prediction of the species distribution. Furthermore, the effect of the fluid dynamic interaction process on the chemical kinetics and on the concentration of species such as NO, SO_3 and O_3 in the plume-vortex regime will be addressed in the presence of both gas and heterogeneous kinetics.

2 Simulation Model

The simulation model used in the present study employs the LES method. In LES, scales smaller than the grid size δx are eliminated by applying an appropriately chosen low-pass filter G to the flow field variables. Any filtered field of a quantity f is given as: $\overline{f} = \int_D G(x - x')f(x')dx'$. A box filter is used since it is appropriate for finite-volume schemes.[18] Using the above definition, the original field f can be decomposed as $f = \overline{f} + f'$. For the compressible flow equations, a Favre-filter is more appropriate.[19] In this case, the Favre-filtered variable is defined as: $\tilde{f} = \frac{\overline{\rho f}}{\overline{\rho}}$. The details of the filtering operation on the Navier-Stokes equations are given in numerous publications[20,21] and therefore, avoided here for brevity. The LES equations for conservation of mass, momentum, energy and species are, respectively:

$$\frac{\partial \overline{\rho}}{\partial t} + \frac{\partial}{\partial x_i}\overline{\rho}\tilde{u}_i = 0 \tag{1}$$

$$\begin{aligned}\frac{\partial \overline{\rho}\tilde{u}_i}{\partial t} + \frac{\partial}{\partial x_j}(\overline{\rho}\tilde{u}_i\tilde{u}_j) &= -\frac{\partial \overline{p}}{\partial x_i} + \frac{\partial \overline{\tau}_{ij}}{\partial x_j} \\ &\quad -\frac{\partial}{\partial x_j}\overline{\rho}(\widetilde{u_i u_j} - \tilde{u}_i\tilde{u}_j)\end{aligned} \tag{2}$$

$$\begin{aligned}\frac{\partial \overline{\rho}\tilde{E}}{\partial t} + \frac{\partial}{\partial x_i}(\overline{\rho}\tilde{E} + \overline{p})\tilde{u}_i &= -\frac{\partial}{\partial x_i}\rho(\widetilde{Eu_i} - \tilde{E}\tilde{u}_i) \\ &\quad -\frac{\partial}{\partial x_i}(\overline{pu_i} - \overline{p}\tilde{u}_i) \\ &\quad +\frac{\partial}{\partial x_i}(\tilde{u}_j\overline{\tau}_{ij}) \\ &\quad +\frac{\partial}{\partial x_i}(\overline{\kappa}\frac{\partial \tilde{T}}{\partial x_i})\end{aligned} \tag{3}$$

$$\begin{aligned}\frac{\partial \overline{\rho}\tilde{Y}_k}{\partial t} + \frac{\partial}{\partial x_j}(\overline{\rho}\tilde{Y}_k\tilde{u}_j) &= \tilde{w}_k - \frac{\partial}{\partial x_j}(\overline{\rho}\tilde{Y}_k\tilde{V}_j^k) \\ &\quad +\frac{\partial}{\partial x_j}(\widetilde{\rho Y_k u_j} - \overline{\rho}\tilde{Y}_k\tilde{u}_j)\end{aligned} \tag{4}$$

In the above equations, ρ is the density, u_i is the velocity component in ith direction, p is pressure, T is temperature and κ is the thermal conductivity. Also, Y_k, ω_k, V_j^k are, respectively, the kth species mass fraction, mass reaction rate and diffusion velocity. The kth species diffusion velocity is determined using Fick's Law of diffusion as: $V_j^k = -D\frac{\partial Y_k}{\partial x_j}/Y_k$, where D is the mixture diffusion coefficient. Also, $\overline{\tau_{ij}}$ is the viscous shear stress determined in terms of the resolved velocity gradients.

The filtered total energy $\tilde{E}$ per unit mass is defined as

$$\tilde{E} = \tilde{e} + \frac{1}{2}\tilde{u}_i\tilde{u}_i + k^{sgs} \tag{5}$$

where the subgrid kinetic energy, k^{sgs}, is defined as

$$k^{sgs} = \frac{1}{2}(\widetilde{u_i u_i} - \tilde{u}_i\tilde{u}_i) \tag{6}$$

Finally, the LES equation of the state equation is

$$\overline{p} = \overline{\rho}R\tilde{T} \tag{7}$$

In the above equation, R is the mixture gas constant given as $\sum_{k=1}^{N} Y_k R_u/W_k$ where R_u and W_k are the universal gas constant and the species molecular weight for kth species respectively, and N is the total number of species.

2.1 Subgrid Closure of the LES Equations

The above LES equations contain many terms that arise due to the filtering process and represent the effect of the unresolved subgrid fluctuation correlations on the resolved motion. Models for these unknown terms must be devised to complete the LES formulation. The key subgrid term that requires determination is the subgrid Reynolds stress term: $\tau_{ij}^{sgs} = \bar{\rho}[\widetilde{u_i u_j} - \tilde{u}_i\tilde{u}_j]$ and the subgrid enthalpy flux $H_i^{sgs} = \bar{\rho}[\widetilde{Hu_i} - \tilde{H}\tilde{u}_i]$. Here, $H = E + p/\rho$ is the stagnation enthalpy per unit mass.

A subgrid eddy viscosity closure is typically chosen for closure of the momentum and energy subgrid fluxes since the small scales primarily provide dissipation for the energy transferred from the large scales. To determine the eddy viscosity, characteristic length and velocity scales must be defined. The grid size is typically chosen as the length scale and the velocity scale in the present study is obtained by solving a transport equation for the subgrid turbulent kinetic energy, k^{sgs}. Without going into the details,[21,22] the final equation for subgrid kinetic energy is given as:

$$\begin{aligned}\frac{\partial \bar{\rho}k^{sgs}}{\partial t} + \frac{\partial}{\partial x_i}(\bar{\rho}\tilde{u}_i k^{sgs}) &= \frac{\partial}{\partial x_i}(\bar{\rho}\nu_t\frac{\partial k^{sgs}}{\partial x_i}) \\ &\quad +P_{ksgs} - D_{ksgs}\end{aligned} \tag{8}$$

In this equation, the three terms on the right-hand-side are respectively, the transport term, the production term, $P_{ksgs} = -\tau_{ij}^{sgs}\partial\tilde{u}_i/\partial x_j$ and the dissipation term $D_{ksgs} = c_\varepsilon\bar{\rho}(k^{sgs})^{3/2}/\Delta$. Here, Δ is a characteristic grid size. Once the subgrid kinetic energy is determined the subgrid stress tensor, τ_{ij}^{sgs} can be obtained as:

$$\tau_{ij}^{sgs} \approx -2\overline{\rho}\nu_t(\tilde{S}_{ij} - \frac{1}{3}\tilde{S}_{kk}\delta_{ij}) + \frac{2}{3}\overline{\rho}k^{sgs}\delta_{ij} \tag{9}$$

where $\tilde{S}_{ij} = \frac{1}{2}(\frac{\partial \tilde{u}_i}{\partial x_j} + \frac{\partial \tilde{u}_j}{\partial x_i})$ is the resolved rate-of-strain tensor and ν_t is the subgrid eddy viscosity which is approximated as $\nu_t \approx c_\nu \sqrt{k^{sgs}}\Delta$, where c_ν is a model coefficient. Similarly, the subgrid enthalpy flux term is modeled as: $\overline{\rho H u_i} - \overline{\rho}\tilde{H}\tilde{u}_i = -c_e \overline{\rho}\sqrt{k^{sgs}}\Delta \frac{\partial \tilde{H}}{\partial x_i}$. Here, c_ν, c_ϵ and c_e are unknown coefficients that must be specified to close the system of equations. Typically, c_e is modeled as c_ν / Pr_t where the turbulent Prandtl number was chosen as 0.9. The method used to evaluate these coefficients is described in the next section.

Closure of the species equation requires closure of the subgrid term: $\overline{\rho Y_k u_j} - \overline{\rho}\tilde{Y}_k\tilde{u}_j$. A subgrid diffusivity model (as the eddy viscosity model given above) is not considered an excellent choice since for combustion to occur species must first mix at the small scales and then, molecularly diffuse. These processes occur at the unresolved scales and therefore, a global eddy diffusivity model for the subgrid species flux that ignores the subgrid processes requires some justifications and can be used only under certain conditions. In the present study, the mixing process is dominated by the large-scale transport of the plume species into the wing-tip vortices. Furthermore, the time-scales for the subsequent chemical reactions are quite large (i.e., slow chemistry). Thus, the fast time small-scale mixing effects can be considered completed before the chemical reactions occur. For these reasons, an eddy diffusivity model for the species subgrid flux is considered a reasonable first-order approximation. With these comments in mind, the subgrid species flux is approximated as:

$$\overline{\rho Y_k u_j} - \overline{\rho}\tilde{Y}_k\tilde{u}_j = -\frac{\overline{\rho}\nu_t}{Sc^T}\frac{\partial \tilde{Y}_k}{\partial x_i} \tag{10}$$

where Sc^T is the turbulent Schmidt number set to unity for the present study.

2.2 Dynamic Evaluation of the Coefficients

The model coefficients c_ν, c_ϵ and c_e are obtained using a dynamic approach. The details of the dynamic approach has been reported elsewhere[21] and therefore, is only briefly summarized here. To obtain the model coefficients, we assume that the subgrid stresses at the grid filter level and the resolved Leonard's stress at the test filter level with a characteristic grid size $\hat{\Delta}$ (at twice the grid filter) are similar. Scale similarity between τ_{ij} and L_{ij} has been observed in some experimental data.[23] Using this similarity, the model coefficients are obtained from the following relations:

$$c_\epsilon = \Delta \frac{(\mu + \nu_t/\overline{\rho})d^{test}}{\langle\overline{\rho}\rangle}(k^{test})^{-3/2} \tag{11}$$

$$c_\nu = \frac{-L_{ij}D_{ij}}{2D_{ij}D_{ij}} \tag{12}$$

$$c_e = \frac{n_i d_i}{d_i d_i} \tag{13}$$

where

$$k^{test} = \frac{1}{2}\left\{\frac{\langle\overline{\rho}\tilde{u}_i\tilde{u}_i\rangle}{\langle\overline{\rho}\rangle} - \frac{\langle\overline{\rho}\tilde{u}_i\rangle}{\langle\overline{\rho}\rangle}\frac{\langle\overline{\rho}\tilde{u}_i\rangle}{\langle\overline{\rho}\rangle}\right\}$$

$$d^{test} = \left\langle\frac{\partial\tilde{u}_i}{\partial x_j}\frac{\partial\tilde{u}_j}{\partial x_i}\right\rangle - \frac{\partial}{\partial x_j}\left(\frac{\langle\overline{\rho}\tilde{u}_i\rangle}{\langle\overline{\rho}\rangle}\right)\frac{\partial}{\partial x_j}\left(\frac{\langle\overline{\rho}\tilde{u}_i\rangle}{\langle\overline{\rho}\rangle}\right)$$

The Leonard stress at the test filter level is

$$L_{ij} = \widehat{\overline{\rho}\tilde{u}_i\tilde{u}_j} - \frac{\widehat{\overline{\rho}\tilde{u}_i}\,\widehat{\overline{\rho}\tilde{u}_j}}{\hat{\overline{\rho}}} - \frac{1}{3}(\widehat{\overline{\rho}\tilde{u}_k\tilde{u}_k} - \frac{\widehat{\overline{\rho}\tilde{u}_k}\,\widehat{\overline{\rho}\tilde{u}_k}}{\hat{\overline{\rho}}})\delta_{ij} \tag{14}$$

and

$$D_{ij} = \hat{\Delta}\hat{\overline{\rho}}(\frac{\widehat{\overline{\rho}\tilde{u}_l\tilde{u}_l}}{2\hat{\overline{\rho}}} - \frac{\widehat{\overline{\rho}\tilde{u}_l}}{2\hat{\overline{\rho}}}\frac{\widehat{\overline{\rho}\tilde{u}_l}}{\hat{\overline{\rho}}})^{\frac{1}{2}}(\widehat{\tilde{S}_{ij}} - \frac{\widehat{\tilde{S}_{kk}}}{3}\delta_{ij}) \tag{15}$$

Finally,

$$n_i = \widehat{\overline{\rho}\tilde{H}\tilde{u}_i} - \hat{\overline{\rho}}\hat{\tilde{H}}\hat{\overline{u_i}} \tag{16}$$

and

$$d_i = \hat{\overline{\rho}}(\frac{\widehat{\overline{\rho}\tilde{u}_l\tilde{u}_l}}{2\hat{\overline{\rho}}} - \frac{\widehat{\overline{\rho}\tilde{u}_l}}{2\hat{\overline{\rho}}}\frac{\widehat{\overline{\rho}\tilde{u}_l}}{\hat{\overline{\rho}}})^{\frac{1}{2}}\Delta\frac{\partial\hat{\tilde{H}}}{\partial x_i} \tag{17}$$

The ability of this type of closure to obtain accurately the LES field for a wide range of test problems in both incompressible and compressible flows has been reported in the past.[20,21] It has also been shown in these earlier studies that predicted subgrid stresses using this model satisfies all the realizability conditions proposed by Schumann.[24] This implies that since τ_{ij}^{sgs} is a positive semi-definite tensor, the modeled term for τ_{ij}^{sgs} should also be positive semi-definite. This requirement results in the following inequalities:

$$\begin{aligned} \tau_{ii}^{sgs} &\geq 0, i \in \{1,2,3\}. \\ |\tau_{ij}^{sgs}|^2 &\leq \tau_{ii}^{sgs}\tau_{jj}^{sgs}, i,j \in \{1,2,3\}. \\ det(\tau_{ij}^{sgs}) &\geq 0. \end{aligned} \tag{18}$$

that must be satisfied. The above inequalities yield certain bounds for c_ν which must be imposed in the simulations. The present implementation of the dynamic model ensures that these requirements are satisfied during the entire simulation. Analysis shows that this criteria is automatically satisfied in over 95% of the grid points during the entire simulation.

3 Numerical Method

An explicit finite-volume scheme that is fourth order accurate in space and second-order accurate in time was used in the present study. The details of the numerical scheme has been reported elsewhere[21,22] and therefore, avoided here for brevity. The current approach is similar to the implementation described by Gamet and Estivalezes[25] except that the fluxes are modified so that a truly fourth-order accuracy in space is obtained at least on an uniform grid. The details of this implementation are given in.[22]

The present code has been parallelized using the standard Message Passing Interface (MPI) library. This allows simulation on a variety of platforms without any changes to the code. Domain decomposition method is employed whereby the computational domain is decomposed into subdomains and assigned to different processors which have an identical copy of the numerical algorithm. For the current scheme, a five point stencil is used and therefore, two rows of variables must be exchanged in either direction. Timings analysis of this code on various parallel machines (e.g., Cray T3E, SGI Origin 2000) shows that the code achieves nearly linear speedup as the number of processors is doubled. However, depending upon the total number of grid points employed there is an optimum number of processors beyond which the message passing overhead overtakes the computing time in each processor's domain.

For a $121 \times 97 \times 97$ computational grid a typical simulation (using 15 reactive species) on the Cray T3E takes around 5000 single processor hours to obtain data sufficient for statistical analysis (5 flow through time). The CPU time per time step per grid point was around 3E-6 sec on 128 processor T3E (or 3.6 sec per time step).

Two types of problems are studied in the present study. Both are in the plume-vortex regime. Figures 1a and 1b show respectively, the plume-vortex domain behind a Boeing 737 and a Boeing 747 aircraft. The primary differences are in the span, the number of engine plumes and the exhaust conditions. These two configurations were chosen primarily because there is some data available for comparison.

For slip or symmetry conditions, values are prescribed for ghost cells such that gradients normal to the face at the bounding face are zero. Periodic boundary conditions are prescribed in the streamwise direction (for the temporal simulations).

For the spatial cases, the inflow and outflow boundaries are more complicated and must be carefully implemented. We employ a method that attempts to provide reasonably accurate inflow turbulence statistics.[22,26] The inflow is critical for the spatial case since it determines the turbulence entering the computational domain. A turbulent inflow field is generated based on a prescribed energy spectrum and turbulence intensity and then superimposed on the mean field. The turbulence spectrum chosen is of the form $E(k) = Ck^4 exp(-2(k/k_p)^2)$ used by Lee *et al*,[27] where constant C is chosen as turbulence intensity level. The turbulence is divergence free and non-periodic in time. The field is stored as 3D array from which a 2-D plane is introduced at the inflow at every time step. At least 10 different arrays of $97 \times 97 \times 97$ are stored and to ensure that the inflow field is not correlated, at randomly chosen instants, the phase in the Fourier modes were randomized. Additional details of the turbulence inflow are given elsewhere.[22]

Table 1 Aircraft parameters for the near field plume-vortex calculations of B747 and B737 data.

type	wing span	maximum circulation	vortex core radius	vortex separation	engines location
B747	60m	$600m^2/s$	4m	54m	9m/18m
B737	30m	$100m^2/s$	2m	26m	5.35m

Table 2 Initial conditions for the near field plume-vortex calculations of B747.

	B747	
	Plume Condition	Ambient Condition
Temperature	500K	217K
velocity(m/sec)	247	0.0
pressure(atm)	0.17	0.17
mole fraction		
CO	2.4×10^{-5}	2.0×10^{-8}
CO_2	3.2×10^{-2}	3.5×10^{-4}
H_2	1.0×10^{-6}	5.2×10^{-7}
O_2	0.159	0.2098
OH	1.0×10^{-5}	2.8×10^{-13}
H_2O	3.0×10^{-2}	4.8×10^{-6}
N_2	0.779	0.789
NO	4.3×10^{-5}	5.9×10^{-11}
NO_2	4.8×10^{-6}	4.3×10^{-10}
N_2O_5	0.0	0.0
HNO_3	0.0	3.3×10^{-9}
$HONO$	0.0	0.0
SO_2	6.9×10^{-6}	0.0
SO_3	0.0	0.0
O_3	0.0	2.5×10^{-7}

The outflow boundary is non-reflecting characteristic boundary conditions.[26] The amplitudes of the outgoing waves are computed based on the interior points and the amplitude of the incoming wave is computed by specifying the background pressure. Details of this type of outflow condition is given elsewhere.

The wing-tip vortex is modeled by the Lamb-Oseen vortex[28] with an axial velocity deficit. This model has been extensively used[12-14,29-31] for earlier studies. The location, core radius, maximum circulation data of the wing-tip vortex and the engine location and exit conditions (Table 1 and 2 summarize these conditions) are chosen according to the aircraft configurations.

4 Results and Discussion

In this section, we summarize the results obtained in the present study. There are three primary objectives of this study. First, comparison with available data is carried out to demonstrate the ability of the simulation model to accurately capture the evolution of the plume-vortex regime. Second, the results obtained using temporal and spatial methods are compared to

identify what features are not predicted accurately using temporal simulations (as noted earlier, nearly all previously reported 3D studies employed periodic conditions in the streamwise direction). The final objective is to determine the impact of turbulence transport on the formation of SO_x and the destruction of ozone.

Before discussing the details of the plume-vortex interaction, the effect of different inflow turbulence on the flow field is briefly summarized. Figure 2 shows the effect of inflow turbulence on the scalar (here SO_2 concentration is used as a scalar marker) decay with increasing plume age in a B747 plume-vortex region. Three different inflow turbulence conditions are used. Two conditions employed the same energy spectrum but with 5% and 10% turbulent intensity, respectively while the third case used the same initial isotropic spectrum as other two but is introduced into the flow field after evolving for certain time with a final turbulent intensity 5%. Thus, in the third case, the inflow has evolved to a more realistic turbulent isotropic state, whereas in the first two cases the field is isotropic but is not realistic turbulence.

It can be seen that the cases with the same turbulent intensity yield almost identical results. This means that the effect of evolving of the inflow turbulent field is small at least for the global measure used here. (Note that such global measures are of interest here). However, it can be seen that turbulent intensity does have an effect on the flow field. This implies that the inflow turbulent intensity must be carefully chosen. The turbulence intensity in the vortex and jet plume varies with flight conditions such as climate, altitude and ambient flow field. A turbulent intensity between 5% and 10% is very common in the typical flight path of interest. Thus, simulations with 5% and 10% inflow turbulence may be used to quantify an upper and lower bound for the species distributions in actual flights. Interestingly, the descending vortex velocity computed from these three cases showed similar results. However, this is understandable because the descending vortex velocity is mainly determined by the overall vortex circulation and small scale turbulence exerts negligible effect on the circulation. The numerical simulation of q-vortex by Ragab and Sreedhar[29] also demonstrated this feature.

4.1 Plume-Vortex Interaction behind a Boeing 737

For quite some time under the Atmospheric Effects of Aviation Program, NASA has been conducting measurements in the wake of actual aircrafts. Some data based on ground based LIDAR measurements in the wake of a Boeing 737 is currently available for comparison. More data is expected in the near future for additional comparison.

Figure 3 shows some typical comparison of the wake LIDAR data with the present calculations. These simulations were performed using 61x101x101 grid points and using the temporal method. The initial conditions and computation domain was chosen to match the data for B737. For comparison, identical location (i.e., plume age), domain size and contour distribution is used in these figures. The chosen location is approximately $1km$ downstream of the engine exhaust (at a plume age of 5 seconds). Some interesting features can be discerned from this comparison. Note that, the numerical study enforced symmetry along the aircraft center-plane primarily to reduce the computational cost (see Figure 1a). As a result, the numerical result shows a symmetric image (obtained by mirror imaging the data) whereas the experimental data shows some asymmetry. In spite of this difference there is quite a bit of similarity in the predicted and the measured vortex structure. These features are discussed below.

First, the scale (size) and the location of the computed structure is in good agreement with data. The separation distance between the vortex pair at this demonstration location is predicted quite accurately even with symmetry boundary condition. Second, the structure of the vortex with its trailing tail (which is the jet plume as it gets entrained) is quite similar. In both the experimental data and in the present simulation, the concentration variation in the core of the vortex is very small. However, there is relatively a large variation in the outer region of the vortex. This implies that the core of the vortex has a stabilizing effect and inhibits the dilution of the passive tracer. The turbulent small-scale structures seen in the experiments are captured by the present study. On the other hand, the earlier comparison reported using the UNIWAKE method[16] did not yield this type of detail on the vortex structure and showed a scalar field that was more concentrated and coherent than the experimental data since the small scale mixing effects are neglected. The more reasonable agreement between the present LES and the data suggest a potential advantage of carrying out full 3D LES where the unsteady mixing effects are explicitly simulated.

We expect to carry out additional comparison with LIDAR data when it becomes available in the near future.

4.2 Plume-Vortex Interaction behind a Boeing 747

The LES model was also used to study the B747 wake. The key differences between the B737 and B747 are in the appropriate scales, flight conditions and the presence of two engine plumes for the B747. These simulations were carried out using both temporal and spatial methods to facilitate direct comparison. The temporal simulation captures a region of plume-vortex evolving in time which corresponds spatially (via a velocity transformation) to a location that moves (with increasing time) in the downstream direction. A grid

resolution of $121 \times 97 \times 97$ is used for both spatial and temporal simulations. For some simulations (of an extended domain) a resolution of $201 \times 111 \times 111$ was employed. The domain size (unless otherwise noted) is $24s$ in streamwise direction and $2.5s$ in other two directions. Here, s is the aircraft's semispan. Only one-half of the wake regime is simulated by employing the symmetry boundary conditions at the wake center plane.

4.2.1 Comparison with experimental data

Figure 4 shows a comparison between present spatial and temporal simulations of the passive tracer concentration on a cross-section of the plume/wake at a distance of 30 semi-spans downstream of the aircraft. The plume age is about 5 seconds. As seen earlier in Figure 3, large-scale structures are seen in both the data and the LES. The wing-tip vortex and entrainment tail of the jet plumes can be clearly seen in the present computation. Again, the concentration variation in the core of the vortex is very small even for the twin plume interaction for the B747. More, turbulent small-scale structures are seen for the B747 due to the interaction between twin plumes with the vortex.

A key difference is seen between the temporal and spatial data in the structure of the plumes as it gets entrained into the vortex. It appears that a large portion of the inboard plume is still very distinctly separated from the vortex for the spatial case whereas in the temporal case the inboard plume is also getting entrained into the vortex. The implication of this difference is discussed in the next section.

The descending vortex velocity is relatively steady within the computational range. The computed descending vortex velocity for spatial simulation and temporal simulation are 0.90 m/s and 0.86 m/s, respectively. From the data by Teske *et al.*,[16] the descending vortex velocity is around 0.93 m/s between about 15 and 40 semi-spans which is in agreement with present simulations.

Figure 5 shows the comparison of the averaged SO_2 scalar concentration decay with increasing plume age. Here, SO_2 is a marker species present initially only in the plume and therefore represents the transport and entrainment of the plume into the vortex. The current result has been normalized by the SO_2 concentration value in Teske *et al.*[16] at plume age 1 second in order to compare the dilution process between the two models. This was required since the present simulation starts with a different initial scalar concentrations when compared with Teske et al.[16] The reason is that there is no experimental data at a plume age of 1 second and the inflow setup in Teske *et al.*[16] and the present LES are not similar. The averaged passive scaler concentration is defined as the volume average of the cells which has at least one percent of the local maximum concentration. This definition was also used by Teske et al.[16]

The decrease in SO_2 concentration is mainly due to mixing with ambient air because the reaction rate for SO_2 destruction is small. The current spatial and temporal simulations are in good agreement, but there is a discrepancy between present study and the result obtained using UNIWAKE.[16] The current result shows a much larger initial decay rate than the UNIWAKE result. The experimental measurements by Arnold *et al.*[32] also showed that a lower value of SO_2 at a distance of 2km downstream of the plane than the prediction by Teske *et al.*[16] The current prediction in that region shows a better agreement with data. As Teske *et al.*[16] noted, the limitation of the turbulence model used in UNIWAKE may be contributing to this discrepancy. In the present LES with the dynamic sub-grid model the turbulent viscosity is dynamicly computed and adjusts to varying strain rate of the mean flow (i.e., different age of the plume). Thus, better comparison with the experimental data is expected and can be observed in this figure. It can also be argued that the more accurate resolution of the turbulent small-scale structures in the LES improves the prediction since turbulent diffusion plays a large role in scalar mixing. In contrast, UNIWAKE predictions ignore the small scale mixing effects. This may contribute to the under-prediction of average scalar concentration decay.

4.2.2 Detrainment of the exhaust plume

Figures 6a, 6b and 6c show respectively, three instantaneous vorticity magnitude contour plots in the x-z plane at y=0 from the spatial simulation. The two jet plumes develop almost independently before the first 4 semi-spans. After 4 semi-spans, the outboard jet plume starts to get entrained into the wing-tip vortex, and the jet plume is deflected towards the wing-tip vortex. Further downstream, the two jet plumes break up into smaller structures. This is characterized by patches of concentrated vorticity which are surrounded by flow with much lower vorticity.

The high level of intermittency seen in the flow field makes Reynolds averaged approach inapplicable since it cannot capture this effect. It can be seen that the broken portions of the outboard jet plume are deflected and entrained into the wing-tip vortex. On the contrary, due to the strong turbulent motion and relatively weak influence of the wing-tip vortex, a portion of the inboard jet plume gets *detrained* from the wing-tip vortex. Observation of contrails from widebody planes such as B747 show that there are two contrails behind the aircraft, one that is the normal vortex core contrail and another that is distinctly separated from it. As Gerz and Ehret[15] pointed out, irregular roll-up of wing-tip vortex, turbulent motion and buoyancy may result in detrainment. Gerz and Ehret[15] failed to capture detrainment in the near field by including

buoyancy effect. Also, the detrainment captured by Quackenbush *at el.*[31] was only in the far field. Present simulation suggests another reason for detrainment. This is the effect of turbulent mixing which breaks up the inboard jet plume before it gets entrained into the vortex. This in turn forms the detrained contrail as seen in Figures 6a-c.

The instantaneous NO mass fraction field corresponding to Figures 6 are shown in figures 7a, 7b and 7c, respectively. In these simulation, the species do not to have a strong effect on the fluid flow because the reactions release almost no heat. As a result, the correlation between the NO mass fraction and the vorticity magnitude is very strong. Since the reaction rate for NO species is relatively small, the NO mass fraction distribution can be used to represent the overall plume mixing process. The entrainment and detrainment of the NO species are thus similar to the vorticity field. It is worthwhile to point out that previous numerical studies[16,31] failed to capture the plume breakup and instead showed a smoothly varying plume species field. This can result in error in entrainment prediction.

Figure 8 shows a 3-D snapshot of the instantaneous vorticity magnitude isosurface with NO mass fraction contour. The sequence of the plume-vortex interaction starts with the break-up of the jet plumes. By the middle point (x=12s), the two jet plumes have broken up completely and part of the outboard jet plume starts to get entrained into the vortex. At the end of the interaction, a major part of jet plumes has been entrained into the wing-tip vortex. However, a portion of the inboard jet plume is detrained from the vortex.

The simulations by Garnier *et al.*[12] showed that the outboard jet plume scalar concentration decays faster than the inboard jet plume. They attributed this phenomenon to the wing-tip vortex effect. However, the current simulations show that both inboard and outboard plumes have almost the same decay rate even though the outboard plume is deflected toward the wing-tip vortex. When the outboard plume interacts with the wing-tip vortex, due to the shear in the flow, strong turbulence is produced. As a result, scalar mixing is enhanced and therefore, faster decay may be expected. However, when part of the plume is entrained into the core of the vortex, due to the inherent stability of the vortex core region, scalar mixing is slowed down. These two contradicting effects result in similar mixing rate for the outboard and the inboard plumes.

Another explanation for the results obtained by Garnier et al.[12] is related to the well-known over prediction by the $k-\epsilon$ turbulence model. The over prediction of the overall SO_2 decay rate by Garnier et al.[12] is also attributed to $k-\epsilon$ turbulence model.

Figures 9a and 9b show respectively, two instantaneous cross-section flow field of the vorticity magnitude contour plots at the downstream location 12s and 24s (s is the semi-span) from the temporal simulation. Figures 10a and 10b show the corresponding vorticity contour from the spatial case. There is great variety in the instantaneous cross section but these figures are very representative. At 6s, the two jet plumes become turbulent and the interaction between the outboard jet plume and wing-tip vortex starts (not shown). At 12s, the two jet plumes begin interact with each other and merge. However, some part of the outboard jet plume gets entrained into the wing-tip vortex. For the spatial case, at 18s (not shown), a large portion of the outboard jet plume is entrained into the wing-tip vortex while a major portion of the inboard jet plume stays separated.

The detrainment of the inboard plume continues as shown at x=24s and is more apparent in the spatial case than in the temporal case. Although there exist highly turbulent structures around the wing-tip vortex, the core of wing-tip vortex remains coherent and laminar. This overall observation of the plume dispersion is quite similar to the results obtained by Sykes and Henn[33] and Sykes et al.,[34] except for the addition of wing-tip vortex in present study.

Comparison of the temporal (Figs. 9) and the spatial (Figs. 10) cases show some significant differences even through the overall entrainment process is qualitatively similar. For example, in the temporal cases, the entrainment process is not very well defined in comparison to the spatial case. The detrained plume for the spatial case is also much more coherent than in the temporal case (also shown in figure 4). The inability of the temporal simulation to capture the detrainment process is due to the fact that detrainment occurs right behind the aircraft where the periodic assumption is not satisfied. This observation suggests that to capture the observed detrainment of the plume, spatial simulations are required.

4.2.3 Comparison between spatial and temporal simulations

Some differences between temporal and spatial simulations have been noted above. Namely, the spatial simulation is able to capture detrainment effects while the temporal case could not. This was attributed to the fact that in the early stages of plume-vortex interaction periodic assumption in the streamwise direction may not be appropriate. Here, to further quantify the results additional entrainment quantities are computed and compared. Figure 11 shows the detrainment ratio from the vortex core. The detrainment ratio is defined as the percentage of representative species NO outside the wing-tip vortex core which has a radius about 4m. The vortex center is located by finding the point where the minimum axial vorticity occurs. Initially, the detrainment rate is 1.0. The spatial and temporal simulations show similar trends however, the spatial simulation data has some oscillations. The os-

cillations of the spatial data could be attributed to the random wandering of wing-tip vortex which has been observed in the experiment by Devenport *et al.*[35] Thus, it would appear that spatial simulation is able to capture this random wandering effect.

As the plume begins to get entrained into the vortex core, the detrainment ratio decreases. This decrease is large in the first $12s$ and then levels off. This indicates that part of the plume has overcome the attraction of the wing-tip vortex after $12s$. This also can be seen in figure 7a, 7b and 7c where there is an apparent separation of jet plumes after $12s$. The detrainment reaches a final value of around 0.87. Therefore, about 13 percent of jet plume is entrained into the core of the wing-tip vortex.

In the vortex core, the temperature is about 8 degree higher than the ambient temperature. Note that without entrainment of the hot jet plumes, the temperature inside the wing-tip core should be a few degree lower than the ambient temperature due to the lower pressure inside the vortex core. Due to entrainment, the temperature of vortex core is increased. The several degrees' increase of temperature is critical when chemical reactions are included. This difference in temperature indicates that the entrained plume undergoes a different chemical reaction path, e.g., via the heterogeneous reactions when compared to the portion that is detrained from the vortex. The previous studies[16,31] showed only a fully entrained plume without any details of the structure inside the vortex.

It is interesting to track the different dilution processes of plume species inside and outside the vortex core since there is a lower pressure zone inside the vortex core and the fluid field is more stable inside the vortex core. It is well known that the conditions for contrail formation are very subtle and a little difference in the thermodynamics and fluid dynamics can result in widely different contrail formation. Figure 12 shows the maximum NO mass fraction inside and outside the vortex core versus downstream distance. Both spatial and temporal results are compared. Inside the vortex core, the maximum NO mass fraction is almost constant after it reaches the maximum. While, outside the vortex core the maximum NO mass fraction drops very fast in the first $12s$. The reason is that turbulent diffusion is very large outside the vortex core due to the enhanced mixing effect due to strong turbulence where jet plume breakdown occurs. On the other hand, the vortex core is relatively stable due to the swirling effect of the wing-tip vortex. After $18s$, when the turbulence begins to die down due to dissipation, the NO concentration begins to level off. Comparisons of the spatial and temporal results show that on the outside maximum NO mass fraction agrees very well. However, inside the vortex core, the temporal simulation shows a higher peak than the spatial simulation (by around 25%).

Figure 13 shows the axial variation of NO mass fraction at vortex center. Although the spatial and temporal simulations show similar trend, the spatial simulation shows a much higher mass fraction than the temporal simulation. From figure 12 and 13, one can conclude that the species distribution inside the vortex core predicted by the temporal simulation is more spread out around the core center than the prediction by the spatial simulation. This implies that the reaction rate in the temporal simulation is slower than that in the spatial simulation.

Figure 14 shows the variation of SO_3 mass fraction at vortex center with downstream distance for both spatial and temporal simulations. In the spatial simulation, SO_3 mass fraction first increases and then levels off near $24s$. On the other hand, in the temporal simulation, SO_3 mass fraction reaches a peak at around $12s$ and then decreases. There are significant difference in the magnitude of peak SO_3. The spatial data shows 10^{-8} where as the temporal data shows 10^{-11}. The wide discrepancy between temporal and spatial results has important implications for heterogeneous reactions and for H_2SO_4 aerosol formulation. This is briefly discussed below.

Note that SO_3 is produced first by the oxidization of SO_2 and then primarily removed by heterogeneous reaction on condensed soot particles. The condensation inside the core may be small due to the lower pressure. As a result, the removal rate of SO_3 is small so that SO_3 mass fraction can keep increasing downstream. The magnitude of the SO_3 mass fraction is thus determined by the rate of SO_2 oxidization reaction which is strongly affected by SO_2 mass fraction. As figures 12 and 13 suggest, the spatial data has a higher species concentration around the vortex center than the temporal data. This explains the higher SO_3 concentration in the spatial simulation. These differences between the spatial and temporal simulations show the necessity for spatial simulation.

The implication of the higher concentration of SO_3 is that it could result in an increase in the H_2SO_4 aerosol formation. Although this feature has not been included here, the present spatial LES prediction appears to partly explain the discrepancy between experimental data and earlier numerical studies. As noted earlier,[36] data suggests a 45 times higher H_2SO_4 aerosols concentration in the vortex-plume than the earlier calculations (using SPF-II type of code). The present prediction of higher SO_3 concentration obtained by doing a spatial simulation (in contrast to temporal or parabolic space marching) seems to suggest that this discrepancy may be partly due to the numerical approach. However, to confirm this we need to carry out these simulation including H_2SO_4 binary nucleation and coagulation aerosol models. This effort is underway and will be reported in the near future.

Some integrated quantities are also analyzed as fol-

lows. The mass of entrained NO into the wing-tip vortex is shown in figure 15. Temporal simulation shows a larger amount of NO is entrained than the spatial simulation. Since the relative reaction rate for NO is small, NO entrainment can be used to represent the entrainment process. The difference between the spatial and temporal simulations can be due to the axial velocity deficit of the jet plume. The deviation between the two types of simulations begins around $x = 12s$, where most of outboard engine plume is entrained into wing-tip vortex and the inboard engine plume splits into two parts. One part eventually gets entrained into the wing-tip vortex while the second part becomes detrained from the wing-tip vortex. The chemical processes that result due to the NO concentration will be different in these two regions.

Other integrated quantities of species also show significant deviation when the two simulations are compared. Figure 16 shows the mass entrainment of SO_3 into the wing-tip vortex. The result of spatial simulation shows a higher peak than the temporal simulation and shows an overall larger entrainment. This leads to the conclusion that the temporal simulation is not suitable for the early plume-vortex interaction region because there exists no periodicity in the interaction region. The discrepancy in the SO_3 concentration in the vortex is particularly bothersome as noted earlier. The increased number of aerosol measured in the wake[36] and the potential increase in the condensed sulfuric acid (due to the reaction between SO_3 and condensed water) forming on these particles have been identified as one process that could impact long term global atmosphere chemical balance.

5 Conclusions

In this study, fluid mixing and chemical reactions in the near-field wake of an aircraft has been investigated. The plume-vortex regime is studied using a 3D parallel LES code. Simulations of engine plume interaction with the wing-tip vortex of B737 and B747 have been carried out and some comparison with data have been used to demonstrate the ability of the LES method. Inclusion of detailed gas phase kinetics and simple heterogeneous processes have been carried out to evaluate the effect of turbulent mixing on the chemical processes in the plume-vortex regime. Finally, to determine the impact of temporal assumptions (often used in such flow simulations) comparison with spatial simulations were carried out.

Many features of the computed flow field show reasonable agreement with experimental data. The entrainment and detrainment of engine plumes into the wing-tip vortex were numerically captured in the spatial simulation and analyzed. The impact of fluid mechanics on the chemical process has been estimated. Results indicate that a significant difference between spatial and temporal simulation exists (especially in the predicted SO_3 concentration). This has important implication for the prediction of sulfuric acid aerosols in the wake and may partly explain the discrepancy between past numerical studies and the data. Analysis of the results also show that spatial simulation is more suitable for the near field interaction process. For example, it was determined that detrainment (observed in the B747 contrail) was only captured using the spatial model.

6 Acknowledgments

This work was supported in part by NASA Langley Research Center and the Air Force Office of Scientific Research under the Focused Research Initiative (monitored by General Electric Aircraft Engine Company, Cincinnati, Ohio). Computations were carried out at the DoD HPC center at MSRC NAVO, Stennis Space Center and ARC, Huntsville.

References

[1] Johnston, H., Kinnison, D., and Wuebbles, D., "Nitrogen oxides from high altitude aircraft: An update of potential effects on ozone," *J. Geophys. Res.*, Vol. 94, 1989, pp. 16351–16363.

[2] Beck, J., Reeves, C., de Leeuw, F., and Penkett, S., "The effect of aircraft emissions on tropospheric ozone in the northern hemisphere," *Atm. Env.*, Vol. 26, 1992, pp. 17–19.

[3] Schumann, U., "Pollution from aircraft emissions in the north Atlantic flight corridor(POLINAT)," Tech. Rep. EUR 16978 EN, Office for official publication of the European Communities Luxembourg, 1996.

[4] Brown, R., Miake-Lye, R., Anderson, M., and Kolb, C., "Aerosol dynamics in near-field aircraft plumes," *J. Geophys. Res.*, Vol. 101, 1996, pp. 22939–22953.

[5] Wang, Z. and Chen, J.-Y., "Numerical modeling of mixing and chemistry in near-field engine exhaust plumes," *J. Geophys. Res.*, Vol. 102, 1997, pp. 12871–12883.

[6] Menon, S. and Wu, J., "Effects of Micro- and Macro-scale turbulent mixing on the chemical processes in engine exhaust plumes," *J. Appl. Meteorology*, Vol. 37, 1998, pp. 639–654.

[7] Karcher, B., "A trajectory box model for aircraft trailing vortices," *J. Geophys. Res.*, Vol. 100, 1995, pp. 18835–18844.

[8] Karcher, B., Peter, T., Biermann, U., and Schumann, U., "The initial composition of jet condensation trails," *J. Atm. Sci.*, Vol. 53, 1996, pp. 3066–3083.

[9] Miake-Lye, R., Martinez-Sanchez, M., Brown, R., and Kolb, C., "Plume and wake dynamics, mixing, and chemistry behind a high speed civil transport aircraft," *J. of Aircraft*, Vol. 30, 1993, pp. 467–479.

[10] Miake-Lye, R., Martinez-Sanchez, M., Brown, R., and Kolb, C., "Calculations of condensation and chemistry in an aircraft contrail," *Impact of emissions from aircraft and spacecraft upon the atmosphere*, 1994, pp. 106–112.

[11] Dash, S., Pergament, H., Wolf, D., Sinha, N., Taylor, M., and Vaughn Jr., M., *The JANNAF standardized plume flow field code version II(SPF-II), Vol. I and II, TR-CR-RD SS 90-4*, U.S. Army Missile Command, Huntsville, AL, 1990.

[12] Garnier, F., Jacquin, L., and Laverdant, A., "Engine jet entrainment in the near field of an aircraft," *Proceedings on the impact of Aircraft Emissions upon the Atmosphere.(II)*, 1996.

[13] Risso, F., Corjon, A., and Stoessel, A., "Direct numerical simulation of trailing vortices in homogeneous turbulence," *AIAA-96-0802*, 1996.

[14] Ragab, S. and Sreedhar, M., "Large-scale structures in a trailing vortex," *AIAA-94-2316*, 1994.

[15] Gerz, T. and Ehret, T., "Wake dynamics and exhaust distribution behind cruising aircraft," *AGARD-CP-584*, 1996.

[16] Teske, M., Quackenbush, T., Sykes, R., and Bilanin, A., "Long-time aircraft vortex wake predictions and plume evolution consequences," *AIAA-97-1843*, 1997.

[17] Dimotakis, P., "Two-dimensional shear laryer entrainment," *AIAA J.*, Vol. 24, 1986, pp. 1791–1796.

[18] Schumann, U., "Subgrid Scale Model for Finite Difference Simulations of turbulent Flows in Plane Channels and Annuli," *Journal of Computational Physics*, Vol. 18, 1975, pp. 376–404.

[19] Erlebacher, G., Hussaini, M. Y., Speziale, C. G., and Zang, T. A., "Toward the Large-Eddy Simulation of Compressible Turbulent Flows," *Journal of Fluid Mechanics*, Vol. 238, 1992, pp. 155–185.

[20] Kim, W.-W. and Menon, S., "A New Dynamic One-Equation Subgrid-Scale Model for Large-Eddy Simulations," *AIAA-95-0356*, 1995.

[21] Nelson, C. C. and Menon, S., "Unsteady Simulations of Compressible Spatial Mixing Layers," *AIAA-98-0786*, 1998.

[22] Nelson, C. C., *Simulations of Spatially Evolving Compressible Turbulence Using a Local Dynamic Subgrid Model*, Ph.D. thesis, Georgia Institute of Technology, Atlanta, Georgia, 1997.

[23] Liu, S., Meneveau, C., and Katz, J., "On the properties of similarity subgrid-scale models as deduced from measurements in a turbulent jet," *J. of Fluid Mech.*, Vol. 275, 1994, pp. 83–119.

[24] Schumann, U., "Realizability of Reynolds-Stress Turbulence Models," *The Physics of Fluids*, Vol. 20, No. 5, 1976, pp. 721–725.

[25] Gamet, L. and Estivalezes, J. L., "Non-reflective boundary conditions applied to jet aeroacoustics," *AIAA-95-0159*, 1995.

[26] Poinsot, T. and Lele, S., "Boundary conditions for direct simulations of compressible viscous flow," *Journal of Computational Physics*, Vol. 101, 1992, pp. 104–129.

[27] Lee, S., Lele, S., and Moin, P., "Eddy shocklets in decaying compressible turbulence," *Physics of Fluids, A*, Vol. 3, 1991, pp. 657–664.

[28] Saffman, P., "Structure of turbulent line vortices," *Phys. of Fluids*, Vol. 16, 1973, pp. 1181–1188.

[29] Ragab, S. and Sreedhar, M., "Numerical simulation of vortices with axial velocity deficits," *Phys. Fluids*, Vol. 7, 1994, pp. 549–558.

[30] Quackenbush, T., Teske, M., and Bilanin, A., "Computation of Wake/Exhaust mixing downstream of advanced transport aircraft," *AIAA-93-2944*, 1993.

[31] Quackenbush, T., Teske, M., and Bilanin, A., "Dynamics of Exhaust Plume Entrainment in Aircraft Vortex Wakes," *AIAA-96-0747*, 1996.

[32] Arnold, F., Scheneider, J., Gollinger, K., Schlager, H., Schulte, P., Hagen, D., Whitefield, P., and van Velthoven, "Observation of upper tropospheric sulfur dioxide- and acetone-pollution: potential implications for hydroxyl radical and aerosol formation," *Geophys. Res. Lett.*, Vol. 24, 1997, pp. 57–60.

[33] Sykes, R. I. and Henn, D. S., "Large-eddy simulation of concentration fluctuations in a dispersing plume," *Atm. Env.*, Vol. 26, 1992, pp. 3127–3144.

[34] Sykes, R. I., Henn, D. S., Parker, S., and Lewellen, W. S., "Large-eddy simulation of turbulent reacting plume," *Atm. Env.*, Vol. 26, 1992, pp. 2565–2574.

[35] Devenport, W., Rife, M., Liapis, S., and Follin, G., "The structure and development of a wing-tip vortex," *J. Fluid Mech.*, Vol. 312, 1996, pp. 67–106.

[36] Fahey, D., Keim, E., and Woodbridge, R. *et al.*, "*In situ* observations in aircraft exhaust plumes in the lower stratosphere at mid-latitudes," *J. Geophys. Res.*, Vol. 100, 1995, pp. 3065–3074.

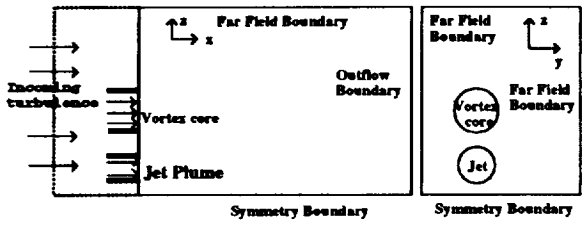

a) Computational domain for the B737 wing-tip vortex and jet plume.

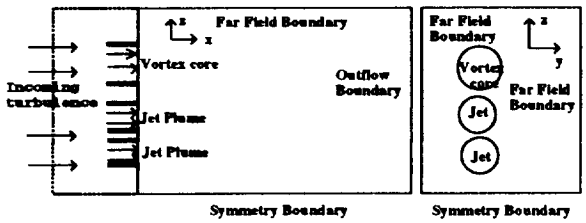

b) Computational domain for the B747 wing-tip vortex and jet plumes.

Fig. 1 Setup of the numerical simulations for the spatial LES simulations.

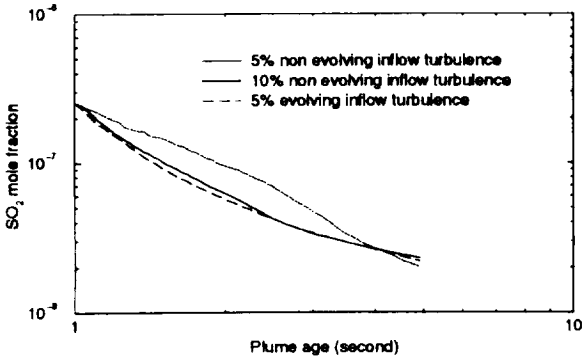

Fig. 2 Comparison of averaged SO_2 mole fraction decay for different turbulence inflow conditions.

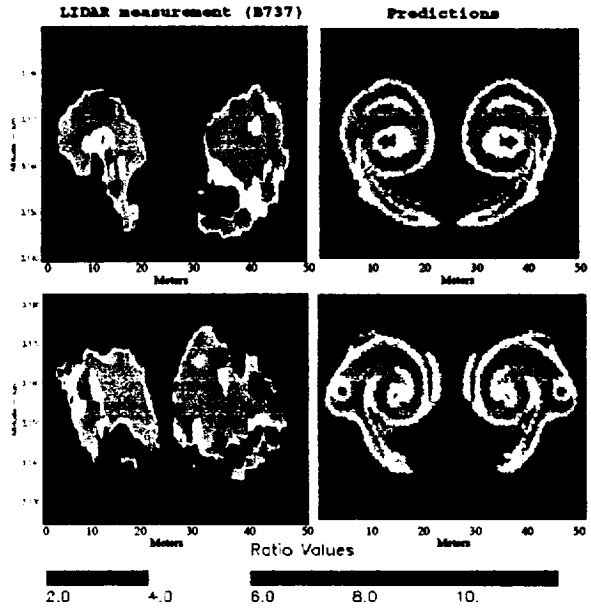

Fig. 3 Comparison of B737 scalar concentration with LIDAR measurement

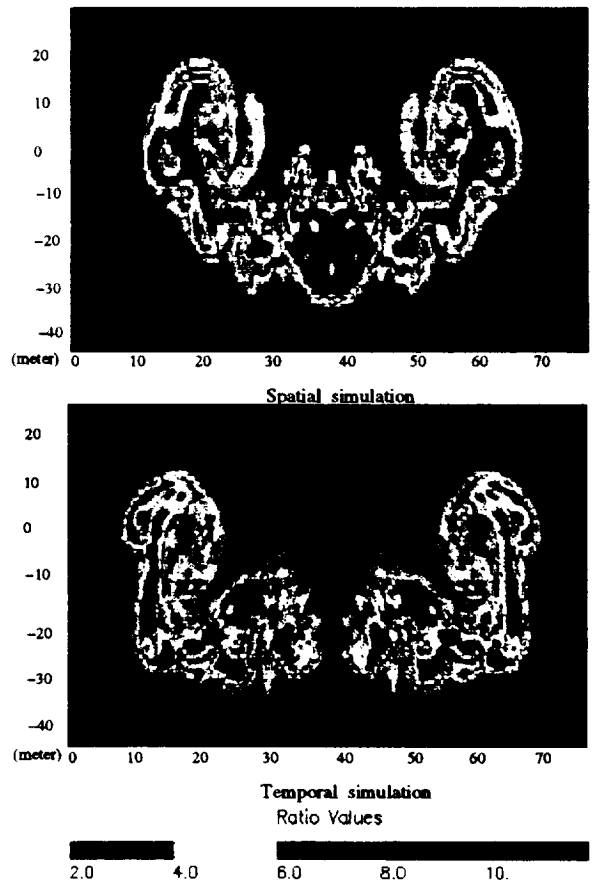

Fig. 4 Comparison of scalar concentration between spatial and temporal simulations

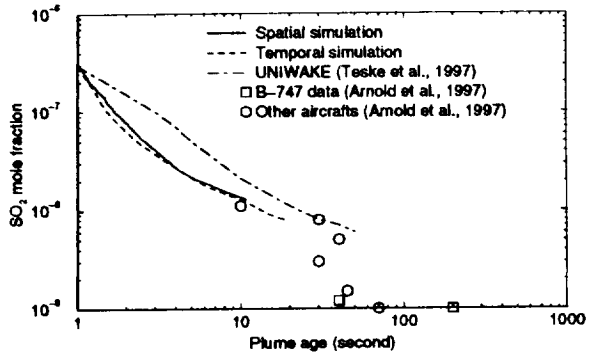

Fig. 5 Comparison of averaged SO_2 mole fraction decay with experimental data.

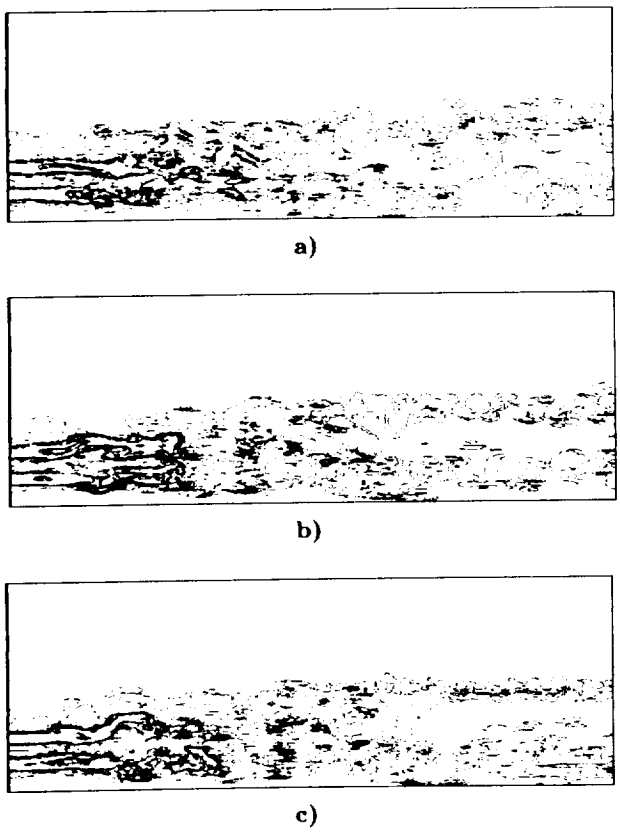

a)

b)

c)

Fig. 6 Instantaneous vorticity magnitude contours at different times for the spatial B747 case.

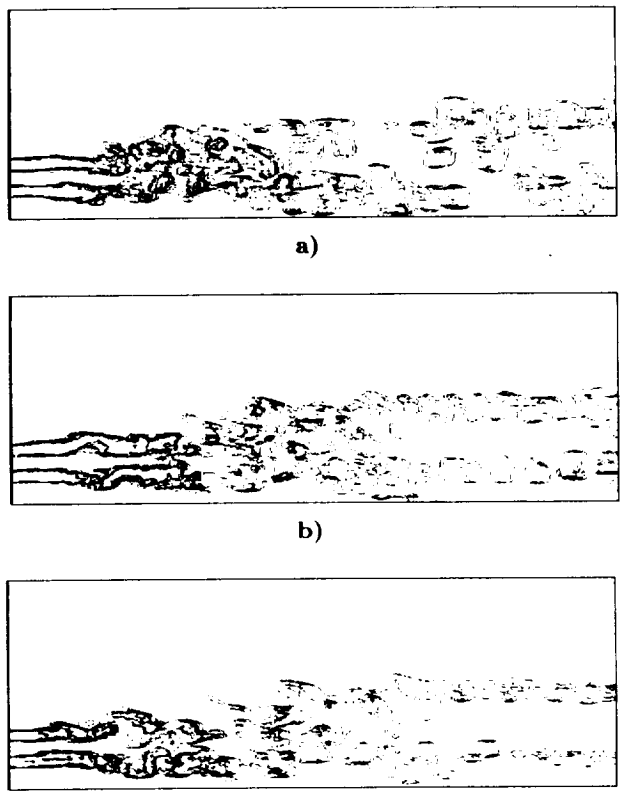

a)

b)

c)

Fig. 7 Instantaneous NO mass fraction contours at different times for the spatial B747 case.

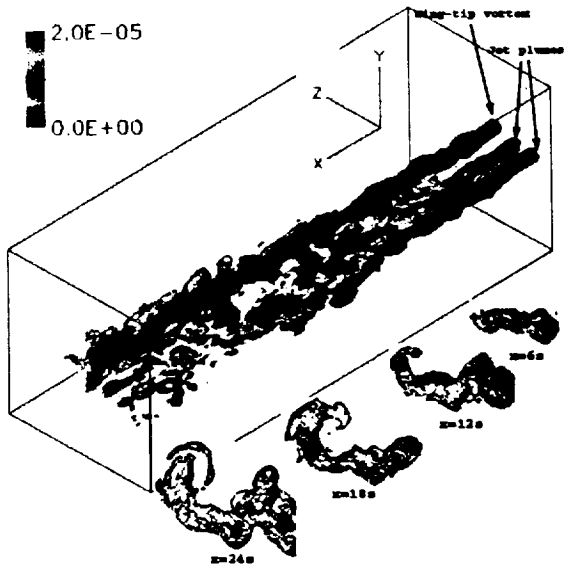

Fig. 8 3D instantaneous vorticity magnitude iso-surface for the B747 plume-vortex interaction.

a) x=12s b) x=24s

Fig. 9 Vorticity magnitude contours at different locations in the temporal simulation.

a) x=12s b) x=24s

Fig. 10 Vorticity magnitude contours at different locations in the spatial simulation.

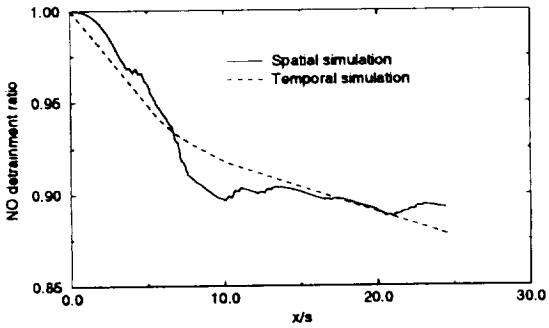

Fig. 11 Variation of the detrainment ratio of *NO* species with the downstream distance for B747.

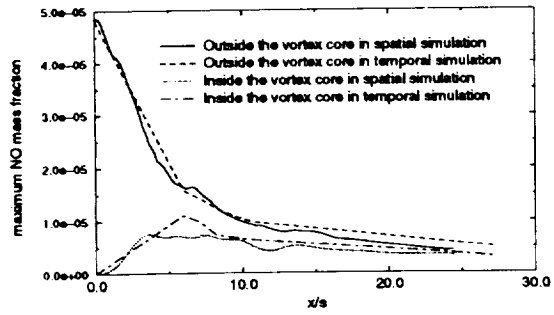

Fig. 12 Maximum *NO* mass fraction inside and outside the vortex core (vortex core has a radius of 4m).

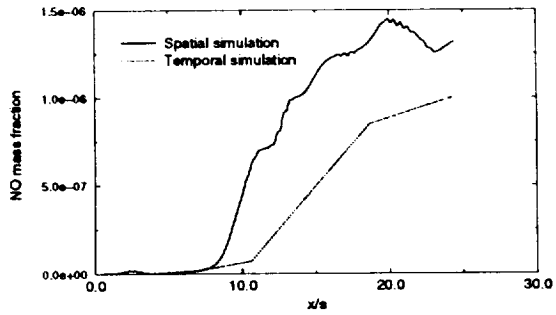

Fig. 13 *NO* mass fraction at the vortex core center.

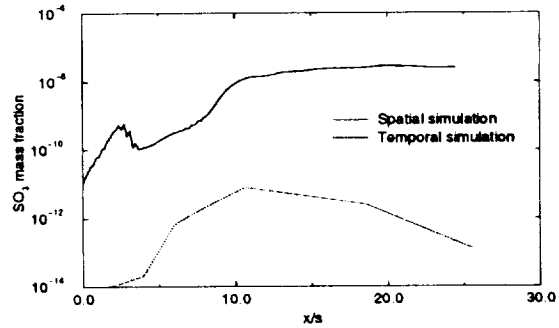

Fig. 14 SO_3 mass fraction at the vortex center.

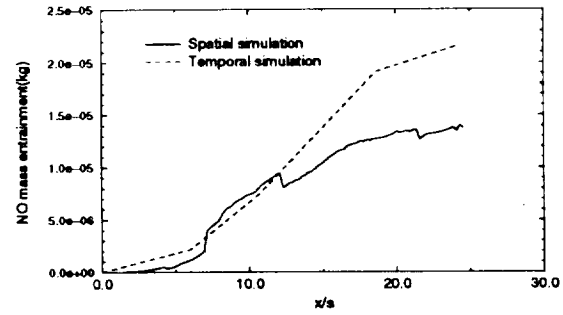

Fig. 15 *NO* mass entrainment into the vortex core.

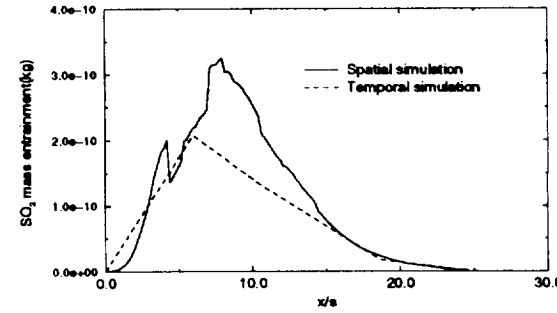

Fig. 16 SO_3 mass entrainment into the vortex core.

Large-Eddy Simulations of Near-Field Plume-Vortex Interactions

Junxiao Wu and Suresh Menon
Georgia Institute of Technology, Atlanta, Georgia

Short title: PLUME-VORTEX INTERACTION

Submitted to *Journal of Geophysics Research* on Oct. 23, 1998

Abstract. Species mixing and chemical reactions in the near-field wake of an aircraft have been investigated using a large eddy simulation (LES) model. Simulations of the interaction between engine plumes and the wing-tip vortices of B737 and B747 have been carried out and comparisons with available data have been used to demonstrate the ability of the LES method. The effect of turbulent mixing on the chemical processes in the plume-vortex regime has been studied using detailed gas phase and simple heterogeneous kinetics. Finally, to determine the impact of temporal assumptions (often used in such flow simulations) comparisons with spatial simulations were carried out.

Many features of the computed flow field show reasonable agreement with experimental data. Analysis of the results also shows that spatial simulation is more suitable for the near field interaction process. The entrainment of engine plumes into the wing-tip vortex were numerically captured in the spatial simulation and analyzed. However, detrainment (observed in the B747 contrail) was only captured using the spatial model. Results indicate that a significant difference between spatial and temporal simulation exists, especially in the predicted SO_3 concentration. This has important implication for the prediction of sulfuric acid aerosols in the wake and may partly explain the discrepancy between past numerical studies and measured data.

1. Introduction

The wing-tip vortices shed from an aircraft's wings are known to pose a danger for aircrafts in the wake and are considered a major hazard near airports. Another consequence that is perhaps less appreciated is their ability to entrain the hot exhaust of the engine during cruise flight in the upper atmosphere. The resulting species-rich and relatively long-lived contrails have been of increasing concern and a focus of research in recent years because the species entrained into the vortex wake can react with the ambient species, thereby, changing the local chemical balance. These studies have been motivated by the projected increase in future subsonic flights in the upper troposphere by the proposed Advanced Subsonic Transports (AST) operating in the transatlantic and Pacific rim flight corridors and by the possibility of future supersonic flights in the lower stratosphere by the High Speed Civilian Transport (HSCT).

The *near-field* region of the aircraft's wake can be divided roughly into two parts: a *plume* regime and a *plume-vortex* regime. The plume regime is identified as the initial region behind the aircraft where the engine exhaust plume grows and mixes with the ambient air. This regime is typically very short, approximately 1 sec after exhaust or around 200 m downstream of the engine exit plane. Further downstream is the plume-vortex regime where the exhaust plume is entrained into the rolled-up wing tip vortices. This regime is around $1-2$ km long and approximately 10 sec downstream of the exhaust. Due to the relatively high temperature of the engine exhaust and the species content, significant reactions can take place in the plume-vortex regime. The region downstream of the plume-vortex region is the wake region where the vortex wake breaks up due to the Crow instability and mixes with the ambient air. This region is very large extending over 20 km and the mixing process can take many days depending upon the ambient conditions.

The near-field region, especially the plume-vortex regime, is of interest here. In particular, we are interested in the chemical processes that occur in this region. Key

species of interest are nitrogen oxides (NO_x), carbon monoxide (CO), methane (CH_4), non-methane hydrocarbons (HC) and soot particles. These trace species play an important role in the atmospheric photochemical and radiative processes. For example, the concentration of tropospheric ozone, an important greenhouse gas, is dependent on transport across tropopause and by chemical production and destruction involving reactions of NO_x, non-methane hydrocarbons, carbon monoxide, and hydrogen oxides (HO_x). Furthermore, the radiative balance of the atmosphere can be affected by the accumulation of carbon dioxide and water and by the aircraft-induced changes in aerosols and clouds. In addition, the combustion aerosols (soot) and the binary H_2SO_4/H_2O droplets in the plume can be efficient cloud condensation nuclei and serve as sites for heterogeneous reactions.

A variety of models have been developed to assess the effect of aircraft flights on the atmosphere. These models generally fall into two categories: "small-scale" and "global" models. "Small-scale" models treat the near-field regime of the exhaust wake by ignoring processes that operate on larger time and space scales. Global models [*Schumann*, 1996], on the other hand, attempt to represent the large spatial scales and ignore, or represent very crudely, the small scales processes. To obtain some sort of continuity, some of the global models [*Schumann*, 1996] use the engine exhaust conditions or the data at the end of the plume-vortex regime as input to their large-scale models. However, as shown recently [*Brown et al.*, 1996; *Wang and Chen*, 1997; *Menon and Wu*, 1998], the concentration of species (e.g., chemical radicals OH, HO_2 and soot) can undergo very rapid changes in the near-field. This can significantly modify the input conditions for the far field simulations. Thus, to obtain accurate prediction of the global chemical balance due to aircraft emission, the chemical processes in the plume-vortex regime are very important.

The hydrodynamics of the plume-vortex regime is also quite complex. For example, the competition between the vortex centripetal force and gravitation buoyancy of

hot plume can lead to a different final altitude of deposition of emissions [*Miake-Lye et al.*, 1993]. This implies that evolution of the plume occurs in a highly unsteady manner. However, many of the models [*Brown et al.*, 1996; *Wang and Chen*, 1997] are steady-state models and therefore, are unable to account for the unsteady mixing effects.

To study unsteady jet-vortex interactions, unsteady methods have also been used. For example, direct numerical simulation [*Risso et al.*, 1996] and large eddy simulation (LES) of trailing vortices [*Ragab and Sreedhar*, 1994a] showed that there exists strong 3-D instability in vortex wakes with an axial deficit. The vortex instability results in vortex-stretching which may have a substantial effect on the mixing of jet plume with the ambient air. *Gerz and Ehret* [1996] used LES to simulate the vortex roll-up process of the wake of a B-747 one second after exit. They showed that temperature, relative humidity peak at the center of the wingtip vortex; the wing boundary layer turbulence and the ambient turbulence all can affect the plume-vortex interaction process.

Unsteady simulations are computationally expensive and therefore, most past studies employed some simplifying assumptions. For example, only limited chemical effects have been investigated so far [*Teske et al.*, 1997] and all simulations reported so far employed periodic boundary conditions in the streamwise directions (i.e, simulated temporal evolution instead of the actual spatial evolution). Temporal approximation is truly justified only far downstream where the interaction between the jet plume and wingtip vortex has been completed [*Lewellen et al.*, 1998]. It has not yet been shown what features of the flow and the accompanying chemical processes are different and/or modified by this temporal assumption in the near field. This issue is important since it has been shown that the entrainment predicted by temporal and spatial simulations differ markedly due to the asymmetry between the high speed and the low speed sides of the shear layer [*Dimotakis*, 1986]. This asymmetry cannot be captured in a temporal simulation. The impact of this asymmetric entrainment on the chemical processes in the plume-vortex interaction regime has not been addressed so far.

This paper will address many of these issues and will attempt to quantify the impact of simulation methodology (i.e., spatial or temporal) on the prediction of the species distribution. Furthermore, the effect of the fluid dynamic interaction process on the chemical kinetics and on the concentration of species such as NO, SO_3 and O_3 in the plume-vortex regime will be addressed in the presence of both gas and heterogeneous kinetics.

2. Simulation Model

The formulation of the simulation model is briefly summarized below. More details are given elsewhere [*Menon et al.*, 1996; *Kim and Menon*, 1995; *Nelson and Menon*, 1998] and, therefore, avoided here for brevity.

The fluid dynamic LES equations are obtained by spatially filtering the compressible Navier Stokes equations. The resulting equations contain unknown subgrid terms such as the stress in the momentum equations, $\tau_{ij}^{sgs} = \bar{\rho}[\widetilde{u_i u_j} - \tilde{u}_i \tilde{u}_j]$, the enthalpy flux and the viscous terms in the energy equation, $H_i^{sgs} = \bar{\rho}[\widetilde{H u_i} - \tilde{H}\tilde{u}_i]$, $\sigma_i^{sgs} = [\widetilde{u_j \tau_{ij}} - \tilde{u}_j \bar{\tau}_{ij}]$; and the scalar correlations, $\omega_k^{sgs} = \widetilde{TY_k} - \tilde{T}\tilde{Y}_k$ in the equation of state. Here, tilde and bar indicate filtered variables. $\tilde{u}_i$, $\bar{\rho}$, $\bar{\tau}_{ij}$ and $\tilde{H}$ are, respectively, the resolved velocity components, the density, the viscous stresses and the total enthalpy per unit volume. To close these subgrid terms, a model equation for the subgrid kinetic energy $k^{sgs} = \widetilde{u_i u_i} - \tilde{u}_i \tilde{u}_i$:

$$\begin{aligned} \frac{\partial \bar{\rho} k^{sgs}}{\partial t} + \frac{\partial}{\partial x_i}(\bar{\rho}\tilde{u}_i k^{sgs}) \;=\; & \frac{\partial}{\partial x_i}(\bar{\rho}\nu_t \frac{\partial k^{sgs}}{\partial x_i}) \\ & -\tau_{ij}^{sgs}\partial \tilde{u}_i/\partial x_j \\ & -c_\epsilon \bar{\rho}(k^{sgs})^{3/2}/\Delta \end{aligned} \qquad (1)$$

is also solved along with the LES equations. Here, $\nu_t = c_\nu \sqrt{k^{sgs}}\Delta$ is the subgrid eddy viscosity and Δ is the grid size. The coefficients c_ν and c_ϵ are computed locally (in space and time) during the simulation. With k^{sgs} known, the subgrid terms are approximated

as $\tau_{ij}^{sgs} \approx -2\overline{\rho}\nu_t(\tilde{S}_{ij} - \frac{1}{3}\tilde{S}_{kk}\delta_{ij}) + \frac{2}{3}\overline{\rho}k^{sgs}\delta_{ij}$, $H_i^{sgs} = -\overline{\rho}\nu_t\sqrt{k^{sgs}}\Delta\frac{\partial\tilde{H}}{\partial x_i}/Pr_t$ and $\sigma_i^{sgs} = \tilde{u}_j\tau_{ij}^{sgs}$. Here, $Pr_t \approx 1$ is the turbulent Prandtl number and $\tilde{S}_{ij}$ is the resolved rate-of-strain tensor, $\tilde{S}_{ij} = \frac{1}{2}(\frac{\partial\tilde{u}_i}{\partial x_j} + \frac{\partial\tilde{u}_j}{\partial x_i})$. All third-order subgrid correlations are neglected in this closure for simplicity.

Closure of the species equation requires closure of the subgrid species transport term $\overline{\rho Y_k u_j} - \overline{\rho}\tilde{Y}_k\tilde{u}_j$. A subgrid diffusivity model (as the eddy viscosity model given above) is not considered an excellent choice since for combustion to occur, species must first mix at the small scales and then molecularly diffuse. These processes occur at the unresolved scales and therefore, a global eddy diffusivity model for the subgrid species flux that ignores the subgrid processes, requires some justifications and can be used only under certain conditions. In the present study, the mixing process is dominated by the large-scale transport of the plume species into the wing-tip vortices. Furthermore, the time-scales for the subsequent chemical reactions are quite large (i.e., slow chemistry). Thus, the fast time small-scale mixing effects can be considered completed before the chemical reactions occur. For these reasons, an eddy diffusivity model for the species subgrid flux is considered a reasonable first-order approximation. With these comments in mind, the subgrid species flux is approximated as:

$$\overline{\rho Y_k u_j} - \overline{\rho}\tilde{Y}_k\tilde{u}_j = -\frac{\overline{\rho}\nu_t}{Sc^T}\frac{\partial\tilde{Y}_k}{\partial x_i} \tag{2}$$

where Sc^T is the turbulent Schmidt number set to unity for the present study.

3. Numerical Method

An explicit finite-volume scheme that is fourth order accurate in space and second order accurate in time was used in the present study. The details of the numerical scheme has been reported elsewhere [*Nelson*, 1997; *Nelson and Menon*, 1998] and therefore, avoided here for brevity. The current approach is similar to the implementation described by *Gamet and Estivalezes* [1995] except that the fluxes are modified so that a

truly fourth-order accuracy in space is obtained at least on an uniform grid.

The present code has been parallelized using the standard Message Passing Interface (MPI) library. The computational domain is decomposed into subdomains and assigned to different processors which have an identical copy of the numerical algorithm. For the current scheme, a five point stencil is used and therefore, two rows of variables must be exchanged in either direction. Timings analysis of this code on various parallel machines (e.g., Cray T3E, SGI Origin 2000) show that the code achieves nearly linear speedup as the number of processors is doubled. However, depending upon the total number of grid points employed there is an optimum number of processors beyond which the message passing overhead overtakes the computing time in each processor's domain.

For a $121 \times 97 \times 97$ computational grid a typical simulation (using 15 reactive species) on the Cray T3E takes around 5000 single processor hours to obtain data sufficient for statistical analysis (5 flow through time). The CPU time per time step per grid point was around 3E-6 sec on 128 processor T3E (or 3.6 sec per time step).

Two types of problems are studied in the present study. Figures 1a and 1b show, respectively, the plume-vortex domain behind a Boeing 737 and a Boeing 747 aircraft. The primary differences are in the span, the number of engine plumes and the exhaust conditions. These two configurations were chosen primarily because there is some data available for comparison.

Figure 1.

For slip or symmetry conditions, values are prescribed for ghost-cells such that gradients normal to the face at the bounding face are zero. Periodic boundary conditions are prescribed in the streamwise direction for the temporal simulations.

For the spatial cases, the inflow and outflow boundaries are more complicated and must be carefully implemented. We employ a method that attempts to provide reasonably accurate inflow turbulence statistics [*Nelson*, 1997; *Poinsot and Lele*, 1992]. The inflow is critical for the spatial case since it determines the turbulence entering the computational domain. A turbulent inflow field is generated based on a prescribed

energy spectrum and turbulence intensity and then superimposed on the mean field. The turbulence spectrum chosen is of the form $E(k) = Ck^4 exp(-2(k/k_p)^2)$ used by *Lee et al.* [1991], where constant C is chosen as turbulence intensity level. The turbulence is divergence free and non-periodic in time. The field is stored as 3D array from which a 2-D plane is introduced at the inflow at every time step. At least 10 different arrays of $97 \times 97 \times 97$ are stored and to ensure that the inflow field is not correlated, at randomly chosen instants, the phase in the Fourier modes is randomized.

The outflow boundary is non-reflecting characteristic boundary conditions [*Poinsot and Lele*, 1992]. The amplitudes of the outgoing waves are computed from the interior points and the amplitude of the incoming wave is computed by specifying the background pressure. Details of this type of outflow condition are given in [*Poinsot and Lele*, 1992].

The wing-tip vortex is modeled by the Lamb-Oseen vortex [*Saffman*, 1973] with an axial velocity deficit. This model has been extensively used [*Ragab and Sreedhar*, 1994a, b; *Quackenbush et al.*, 1993, 1996; *Risso et al.*, 1996; *Garnier et al.*, 1996] for earlier studies. The location, core radius, maximum circulation data of the wing-tip vortex and the engine location and exit conditions (Table 1 and 2 summarize these conditions) are chosen according to the aircraft configurations. Table 1. Table 2.

The gas phase chemical kinetics studied in the present paper are identical to the chemical mechanism in [*Brown et al.*, 1996] except that in the present case, we employ a reduced reaction mechanism that shows an excellent agreement with the full mechanism [*Wang and Chen*, 1997; *Menon and Wu*, 1998]. A total of 15 species were simulated in the present study. The heterogeneous kinetics studied are very simplistic and consist of condensation of nitric and sulfuric acid on the soot particles. The details of this model are given in [*Wang and Chen*, 1997; *Menon and Wu*, 1998] and avoided here for brevity.

4. Results and Discussion

In this section, we summarize the results obtained in the present study. There are three primary objectives of this study. First, comparison with available data is carried out to demonstrate the ability of the simulation model to accurately capture the evolution of the plume-vortex regime. Second, the results obtained using temporal and spatial methods are compared to identify what features are not predicted accurately using temporal simulations (as noted earlier, nearly all previously reported 3D studies employed periodic conditions in the streamwise direction). The final objective is to determine the impact of turbulence transport on the formation of SO_x and the destruction of ozone.

Before discussing the details of the plume-vortex interaction, the effect of different inflow turbulence on the flow field is briefly summarized. Figure 2 shows the effect of inflow turbulence on the scalar (here SO_2 concentration is used as a scalar marker) decay with increasing plume age in a B747 plume-vortex region. Three different inflow turbulence conditions are used. Two conditions employed the same energy spectrum but with a 5% and 10% turbulent intensity, respectively, while the third case used the same initial isotropic spectrum as the other two but was introduced into the flow field after evolving for a certain length of time with a final turbulent intensity of 5%. Thus, in the third case, the inflow evolved to a more realistic turbulent isotropic state whereas in the first two cases, the field is isotropic but is not realistic turbulence.

Figure 2.

It can be seen that the cases with the same turbulent intensity yield almost identical results. This means that the effect of evolving of the inflow turbulent field is small, at least for the global measure used here. (Note that such global measures are of interest here). However, it can be seen that turbulent intensity does have an effect on the flow field. This implies that the inflow turbulent intensity must be carefully chosen. The turbulence intensity in the vortex and jet plume varies with flight conditions such as climate, altitude and ambient flow field. A turbulent intensity between 5% and 10% is

very common in the typical flight path of interest [*Ragab and Sreedhar*, 1994b]. Thus, simulations with 5% and 10% inflow turbulence may be used to quantify an upper and lower bound for the species distributions in actual flights.

Interestingly, the descending vortex velocity computed from these three cases showed similar results. However, this is understandable because the descending vortex velocity is mainly determined by the overall vortex circulation and small scale turbulence exerts negligible effects on the circulation. The numerical simulation of q-vortex by *Ragab and Sreedhar* [1994b] also demonstrated this feature.

4.1. The Boeing 737 wake

Figure 3 shows some typical comparison of the wake LIDAR data [*Poole et al.*, 1996] with the present calculations. These simulations were performed using 61x101x101 grid points and using the temporal method. The initial conditions and computation domain was chosen to match the data for B737. For comparison, identical location (i.e., plume age), domain size and contour distribution is used in these figures. The chosen location is approximately $1km$ downstream of the engine exhaust (at a plume age of 5 seconds). Note that the numerical study enforced symmetry along the aircraft center-plane primarily to reduce the computational cost (see Figure 1a). As a result, the numerical result shows a symmetric image (obtained by mirror imaging the data) whereas the experimental data shows some asymmetry. In spite of this difference there is quite a bit of similarity in the predicted and the measured vortex structure. These features are discussed below.

Figure 3.

First, the scale (size) and the location of the computed structure is in good agreement with data. The separation distance between the vortex pair is also predicted quite accurately even with symmetry boundary condition. Second, the structure of the vortex with its trailing tail (which is the jet plume as it gets entrained) is quite similar. In both the experimental data and in the present simulation, the concentration

variation in the core of the vortex is very small. However, there is relatively a large variation in the outer region of the vortex. This implies that the core of the vortex has a stabilizing effect and inhibits the dilution of the passive tracer. The turbulent small-scale structures seen in the experiments are qualitatively captured by the LES. On the other hand, the earlier comparison reported using the UNIWAKE method [*Teske et al.*, 1997] did not yield this type of detail on the vortex structure and showed a scalar field that was more concentrated and coherent than the experimental data since the small scale mixing effects were neglected. The more reasonable agreement between the present LES and the data suggest a potential advantage of carrying out full 3D LES.

We expect to carry out additional comparison with the LIDAR data when it becomes available in the near future.

4.2. The Boeing 747 wake

The LES model was used extensively to study the B747 wake. The key differences between the B737 and B747 are in the appropriate scales, flight conditions and the presence of two engine plumes for the B747. These simulations were carried out using both temporal and spatial methods to facilitate direct comparison. The temporal simulation captures a region of plume-vortex evolving in time which corresponds spatially (via a velocity transformation) to a location that moves (with increasing time) in the downstream direction. A grid resolution of $121 \times 97 \times 97$ is used for both spatial and temporal simulations. For some simulations (of an extended domain) a resolution of $201 \times 111 \times 111$ was employed. The calculation begins from $6s$ and domain size of $24s$ in the streamwise direction was simulated. In the other two directions, the domain size is $2.5s$. Here, s is the aircraft's semispan. Only one-half of the wake regime is simulated by employing the symmetry boundary conditions at the wake center plane.

4.2.1. Plume evolution Figure 4 shows a comparison between present spatial and temporal simulations of the passive tracer concentration on a cross-section of the

plume/wake at a distance of 30 semi-spans downstream of the aircraft. The plume age is about 5 seconds. As seen earlier in Figure 3 (for the B737), large-scale structures are seen in the present LES. The wing-tip vortex and the tail of the jet plumes can be clearly seen in the present computation. Again, the concentration variation in the core of the vortex is very small even for the twin plume interaction for the B747. More turbulent small-scale structures are seen for the B747 due to the interaction between twin plumes with the vortex.

Figure 4.

A key difference is seen between the temporal and spatial data in the structure of the plumes as it gets entrained into the vortex. It appears that a large portion of the inboard plume is still very distinctly separated from the vortex for the spatial case, whereas in the temporal case the inboard plume is also getting entrained into the vortex. The implication of this difference is discussed in the next section.

The descending vortex velocity is relatively steady within the computational range. The computed descending vortex velocity for spatial simulation and temporal simulation are 0.90 m/s and 0.86 m/s, respectively. From the data by *Teske et al.* [1997], the descending vortex velocity is around 0.93 m/s between about 15 and 40 semi-spans which is in agreement with present simulations.

Figure 5 shows the comparison of the averaged SO_2 scalar concentration decay with increasing plume age (These simulations were carried out for large domain using $201 \times 111 \times 111$ grid). Here, SO_2 is a marker species present initially only in the plume and therefore, represents the transport and entrainment of the plume into the vortex. The averaged concentration is defined as the volume average of the cells which has at least one percent of the local maximum concentration. This definition was also used by *Teske et al.* [1997]. This was required since the present simulation begins with a different initial scalar concentration when compared with *Teske et al.* [1997]. Since the inflow in *Teske et al.* [1997] and the present LES are not similar, the current result has been normalized by the SO_2 concentration value in *Teske et al.* [1997] at plume age 1

second in order to compare the dilution process between the two models. **Figure 5.**

The decrease in SO_2 concentration is mainly due to mixing with ambient air because the reaction rate for SO_2 destruction is small. The current spatial and temporal simulations are in good agreement, but there is a discrepancy between present study and the result obtained using UNIWAKE [*Teske et al.*, 1997]. The current results show a much larger initial decay rate than the UNIWAKE result. The experimental measurements by *Arnold et al.* [1997] also showed a lower value of SO_2 at a distance of 2km downstream of the plane than the prediction by *Teske et al.* [1997]. The current predictions in this region show a better agreement with data. As *Teske et al.* [1997] noted, the limitation of the turbulence model used in UNIWAKE may be contributing to this discrepancy. In the present LES with the dynamic sub-grid model the turbulent viscosity is dynamicly computed and adjusted to varying strain rate of the mean flow (i.e., different age of the plume). Thus, better comparison with the experimental data is expected and can be observed in this figure. It can also be argued that the more accurate resolution of the turbulent small-scale structures in the LES improves the prediction since turbulent diffusion plays a large role in scalar mixing. In contrast, UNIWAKE predictions ignore the small scale mixing effects. This may contribute to the under-prediction of average scalar concentration decay.

4.2.2. Detrainment of the exhaust plume Figures 6a and 6b show, respectively, two instantaneous vorticity magnitude contour plots in the x-z plane at y=0 from the spatial simulation. The two jet plumes develop almost independently in the first 4 semi-spans. After 4 semi-spans, the outboard jet plume starts to get entrained into the wing-tip vortex, and the jet plume is deflected towards the wing-tip vortex. Further downstream, the two jet plumes break up into smaller structures. This is characterized by patches of concentrated vorticity which are surrounded by flow with much lower vorticity. **Figure 6.**

The high level of intermittency seen in the flow field makes Reynolds averaged

approach inapplicable since it cannot capture this effect. It can be seen that the broken portions of the outboard jet plume are deflected and entrained into the wing-tip vortex. On the contrary, due to the strong turbulent motion and relatively weak influence of the wing-tip vortex, a portion of the inboard jet plume gets *detrained* from the wing-tip vortex. Observation of contrails from widebody planes such as the B747, show that there are two contrails behind the aircraft; one that is the normal vortex core contrail and another that is distinctly separated from it. As *Gerz and Ehret* [1996] pointed out, irregular roll-up of the wing-tip vortex, turbulent motion and buoyancy may result in detrainment. *Gerz and Ehret* [1996] failed to capture detrainment in the near field by including buoyancy effect (Note that, buoyancy is also included here). Also, the detrainment captured by *Quackenbush et al.* [1996] was only in the far field. Present simulation suggests another reason for detrainment. This is the effect of turbulent mixing which breaks up the inboard jet plume before it gets entrained into the vortex. This, in turn, forms the detrained contrail as seen in Figures 6a-b.

Figures 7a and 7b show, respectively, two instantaneous cross-section flow fields of the vorticity magnitude contour plots at the downstream location 12s and 24s (s is the semi-span) from the temporal simulation. The downstream distance for temporal simulation is estimated from the temporal time by using the Taylor's hypothesis. Figures 8a and 8b show the corresponding vorticity contours from the spatial case. There is great variety in the instantaneous data but these figures are very representative. At 6s, the two jet plumes become turbulent and the interaction between the outboard jet plume and the wing-tip vortex starts (not shown). At 12s, the two jet plumes begin to interact with each other and then merge. However, some part of the outboard jet plume gets entrained into the wing-tip vortex. For the spatial case, at 18s (not shown), a portion of the outboard jet plume is entrained into the wing-tip vortex while a major portion of the inboard jet plume stays separated.

Figure 7.

The detrainment of the inboard plume continues as shown at x=24s and is more

apparent in the spatial case than in the temporal case. Although there exist highly turbulent structures around the wing-tip vortex, the core of the wing-tip vortex remains coherent and laminar. This overall observation of the plume dispersion is quite similar to the results obtained by *Sykes and Henn* [1992] and *Sykes et al.* [1992], except for the addition of the wing-tip vortex in the present study.

Comparison of the temporal (Figs. 7) and the spatial (Figs. 8) cases show some significant differences even through the overall entrainment process is qualitatively similar. For example, the detrained plume for the spatial case is also much more coherent than in the temporal case (also shown in Fig. 4). The inability of the temporal simulation to clearly capture the detrainment process is due to the fact that detrainment occurs right behind the aircraft where the periodic assumption is not satisfied. This observation suggests that to capture detrainment of the plume, spatial simulations may be more appropriate.

Figure 8.

4.2.3. Spatial versus temporal entrainment effects Some differences between temporal and spatial simulations have been noted above. Namely, the spatial simulation is able to capture detrainment effects while the temporal case could not. This was attributed to the fact that in the early stages of plume-vortex interaction periodic assumption in the streamwise direction may not be appropriate. Here, additional entrainment quantities are computed and compared to quantify the impact of simulation methodology.

Figure 9 shows the detrainment ratio from the vortex core. The detrainment ratio is defined as the percentage of representative species NO outside the wing-tip vortex core which has a radius of about 4m. The vortex center is located by finding the point where the minimum axial vorticity occurs. Initially, the detrainment ratio is 1.0. The spatial and temporal simulations show similar trends, however, the spatial simulation data has some variations which may be attributed to the random wandering of the wing-tip vortex. This wandering has been observed in experiments by *Devenport et al.*

[1996]. Thus, it would appear that spatial simulation is able to qualitatively capture this random wandering effect.

Figure 9.

As the plume begins to get entrained into the vortex core, the detrainment ratio decreases. This decrease is large in the first 12*s* and then begins to level off. This indicates that part of the plume has overcome the attraction of the wing-tip vortex after 12*s*. This was also seen in Figures 6a and 6b where there is an apparent separation of jet plumes after 12*s*. The detrainment ratio reaches a final value of around 0.87. Therefore, about 13 percent of jet plume is entrained into the core of the wing-tip vortex.

In the vortex core, the temperature is about 8 degree higher than the ambient temperature. Note that without entrainment of the hot jet plumes, the temperature inside the wing-tip core should be a few degrees lower than the ambient temperature due to the lower pressure inside the vortex core. However, due to entrainment, the temperature in the vortex core is increased. The several degrees' increase of temperature is critical when chemical reactions are included. This difference in temperature indicates that the entrained plume undergoes a different chemical reaction path, e.g., via the heterogeneous reactions (if included) when compared to the portion that is detrained from the vortex. The previous studies [*Quackenbush et al.*, 1996; *Teske et al.*, 1997] showed only a fully entrained plume without any details of the structure inside the vortex.

It is interesting to track the different dilution processes of plume species inside and outside the vortex core since there is a lower pressure zone inside the vortex core and the flow field is more stable inside the vortex core. It is well known that the conditions for contrail formation are very subtle and a little difference in the thermodynamics and fluid dynamics can result in widely different contrail formation. Figure 10 shows the maximum NO mass fraction inside and outside the vortex core versus downstream distance. Both spatial and temporal results are compared. Inside the vortex core, the maximum NO mass fraction is almost constant after it reaches the maximum. However,

outside the vortex core the maximum NO mass fraction drops very fast in the first $12s$. The reason is that turbulent diffusion is very large outside the vortex core due to the enhanced mixing by the strong turbulence near jet plume breakdown. On the other hand, the vortex core is relatively stable due to the swirling effect of the wing-tip vortex. After $18s$, when the turbulence begins to die down due to viscous dissipation, the NO concentration begins to level off. Comparisons of the spatial and temporal results show that on the outside maximum NO mass fraction agrees very well. However, inside the vortex core, the temporal simulation shows a higher peak than the spatial simulation (by around 25%). **Figure 10**

Figure 11 shows the axial variation of NO and SO_3 mass fractions at vortex center. Although the spatial and the temporal simulations show similar trend, the spatial simulation shows a much higher mass fraction than the temporal simulation. From Figures 10 and 11, one can conclude that the species distribution inside the vortex core predicted by the temporal simulation is more spread out around the core center than the prediction by the spatial simulation. This implies that the reaction rate in the temporal simulation is slower than that in the spatial simulation. **Figure 11**

In both the spatial and the temporal simulations, SO_3 mass fraction first increases and then peaks near $10s$. However, there are significant difference in the magnitude of peak SO_3. The spatial data shows a peak twice as much as the temporal data. The wide discrepancy between temporal and spatial results has important implications for heterogeneous reactions and for H_2SO_4 aerosol formulation. This is briefly discussed below.

Note that SO_3 is produced by the oxidization of SO_2 and then primarily removed by heterogeneous reaction on condensed soot particles. As a result, there is an SO_3 mass fraction peak at around $10s$. Since the heterogeneous reaction rate is mainly related to the thermodynamic condition at the core and almost the same for both spatial and temporal simulations, the peak of the SO_3 mass fraction is determined by

the rate of SO_2 oxidization reaction which is strongly affected by SO_2 mass fraction. As Figure 10 and 11 suggest, the spatial data has a higher species concentration around the vortex center and thus, a higher production rate of SO_3 than the temporal data. These differences between the spatial and temporal simulations imply a necessity for spatial simulation in the near field regime.

The implication of the higher concentration of SO_3 (in the spatial LES) is that it could result in an increase in the H_2SO_4 aerosol formation. Although this feature has not been included here, the spatial LES prediction appears to partly explain the discrepancy between experimental data and earlier numerical studies. As noted earlier [*Fahey et al.*, 1995], data suggests a 45 times higher H_2SO_4 aerosols concentration in the vortex-plume than the earlier calculations [*Brown et al.*, 1996]. The present prediction of higher SO_3 concentration in a spatial LES (in contrast to temporal or parabolic space marching) seems to suggest that this discrepancy may be partly due to the numerical approach. However, to confirm this we need to carry out these simulations, including H_2SO_4 binary nucleation and coagulation aerosol models. This effort is underway and will be reported in the near future.

Some integrated quantities are also analyzed. The mass of entrained NO and SO_3, into the wing-tip vortex are shown in Figure 12. Temporal simulation shows that a larger amount of NO and SO_3 is entrained than the spatial simulation does. Since the relative reaction rate for NO is small, NO entrainment can be used to represent the entrainment process. The difference between the spatial and the temporal simulations may be due to the axial velocity deficit of the jet plume. The deviation between the two types of simulations begins around $x = 12s$, where most of outboard engine plume is entrained into the wing-tip vortex and the inboard engine plume splits into two parts. One part eventually gets entrained into the wing-tip vortex while the second part becomes detrained from the wing-tip vortex. The chemical processes that result due to the NO concentration will be different in these two regions. **Figure 12**

The mass entrainment of SO_3 into the wing-tip vortex shows a higher peak for the spatial case. The discrepancy in the SO_3 concentration in the vortex is particularly bothersome as noted earlier. The increased number of aerosol measured in the wake [*Fahey et al.*, 1995] and the potential increase in the condensed sulfuric acid (due to the reaction between SO_3 and condensed water) forming on these particles have been identified as one process that could impact long term global atmosphere chemical balance. The high peak for the spatial case again suggests that simulation boundary conditions can affect the predictions especially in the near-field plume. **Figure 13**

In order to study the effect of heterogeneous reactions of HNO_3 and H_2SO_4 on plume evolution, temporal and spatial simulations without heterogeneous reactions were also carried out. Since the heterogeneous reactions have negligible effect on NO and SO_2 concentrations, only SO_3 data is analyzed. Figure 13 shows the comparison of SO_3 mass fraction at vortex core and entrainment into the vortex core between spatial and temporal simulations. Both simulations show much higher SO_3 concentration than the simulations with heterogeneous reactions. Also, the concentration keeps increasing in the downstream direction. The reason is that without heterogeneous reactions (which converts SO_3 into H_2SO_4), SO_3 concentration keeps increasing due to the production through SO_2 oxidization mechanism. Both simulations also show a much higher SO_3 entrainment than the simulation with heterogeneous reactions. This is as expected. The spatial and temporal results differ much more without heterogeneous kinetics. This implies that the spatial simulation yields a higher removal rate of gas phase SO_3 inside the wing-tip vortex when heterogeneous reactions are included. Furthermore, the result suggests that more condensed H_2SO_4 is formed in the spatial case than the temporal simulation.

5. Conclusions

In this study, fluid mixing and chemical reactions in the near-field wake of B737 and B747 aircrafts have been investigated. The plume-vortex regime is studied using a 3D parallel LES code. Simulations of engine plume interaction with the wing-tip vortex of the B737 and B747 have been carried out and comparisons with available data have been used to demonstrate the ability of the LES method. Detailed gas phase kinetics and simple heterogeneous processes have been included to evaluate the effect of turbulent mixing on the chemical processes in the plume-vortex regime. Finally, to determine the impact of temporal assumptions (often used in such flow simulations) comparisons with spatial simulations were carried out.

Many features of the computed flow field show reasonable agreement with experimental data. The plume-vortex simulation for the B737 shows qualitative agreement with LIDAR data and the variation of average SO_2 concentration with axial distance for the B747 shows reasonable quantitative agreement with available data. The entrainment and detrainment of engine plumes into the wing-tip vortex were numerically captured in the spatial simulation (for the B747) and analyzed. The impact of fluid mechanics on the chemical process has been estimated. Results indicate that a significant difference between spatial and temporal simulation exists (especially in the predicted SO_3 concentration). This difference has an important implication for the prediction of sulfuric acid aerosols in the wake and may partly explain the discrepancy between past numerical studies and the data. Analysis of the results also shows that spatial simulation is more suitable for the near field interaction process. For example, it was determined that detrainment (observed in the B747 contrail) was only captured using the spatial model.

Acknowledgments. This work was supported in part by NASA Langley Research Center and the Air Force Office of Scientific Research under the Focused Research Initiative

(monitored by General Electric Aircraft Engine Company, Cincinnati, Ohio). Computations were carried out at the DoD HPC center at MSRC NAVO, Stennis Space Center and ARC, Huntsville.

References

Arnold, F., J. Scheneider, K. Gollinger, H. Schlager, P. Schulte, D. Hagen, P. Whitefield, and van Velthoven, Observation of upper tropospheric sulfur dioxide- and acetone-pollution: potential implications for hydroxyl radical and aerosol formation, *Geophys. Res. Lett.*, *24*, 57–60, 1997.

Brown, R., R. Miake-Lye, M. Anderson, and C. Kolb, Aerosol dynamics in near-field aircraft plumes, *J. Geophys. Res.*, *101*, 22,939–22,953, 1996.

Devenport, W., M. Rife, S. Liapis, and G. Follin, The structure and development of a wing-tip vortex, *J. Fluid Mech.*, *312*, 67–106, 1996.

Dimotakis, P., Two-dimensional shear laryer entrainment, *AIAA J.*, *24*, 1791–1796, 1986.

Fahey, D., E. Keim, and R. *et al.* Woodbridge, *In situ* observations in aircraft exhaust plumes in the lower stratosphere at mid-latitudes, *J. Geophys. Res.*, *100*, 3065–3074, 1995.

Gamet, L., and J. L. Estivalezes, Non-reflective boundary conditions applied to jet aeroacoustics, *AIAA-95-0159*, 1995.

Garnier, F., L. Jacquin, and A. Laverdant, Engine jet entrainment in the near field of an aircraft, in *Proceedings on the impact of Aircraft Emissions upon the Atmosphere.(II)*, 1996.

Gerz, T., and T. Ehret, Wake dynamics and exhaust distribution behind cruising aircraft, *AGARD-CP-584*, 1996.

Kim, W.-W., and S. Menon, A new dynamic one-equation subgrid-scale model for large-eddy simulations, *AIAA-95-0356*, 1995.

Lee, S., S. Lele, and P. Moin, Eddy shocklets in decaying compressible turbulence, *Physics of Fluids, A*, *3*, 657–664, 1991.

Lewellen, D., W. Lewellen, L. Poole, R. DeCoursey, G. Hansen, C. Hostetler, and G. Kent, Large-eddy simulations and lidar measurement of vortex-pair breakup in aircraft wakes, *AIAA Journal*, *36*, 1439–1445, 1998.

Menon, S., and J. Wu, Effects of micro- and macro-scale turbulent mixing on the chemical processes in engine exhaust plumes, *J. Appl. Meteorology*, *37*, 639–654, 1998.

Menon, S., P.-K. Yeung, and W.-W. Kim, Effect of subgrid models on the computed interscale energy transfer in isotropic turbulence, *Computers and Fluids*, *25*, 165–180, 1996.

Miake-Lye, R., M. Martinez-Sanchez, R. Brown, and C. Kolb, Plume and wake dynamics, mixing, and chemistry behind a high speed civil transport aircraft, *J. of Aircraft*, *30*, 467–479, 1993.

Nelson, C. C., Simulations of spatially evolving compressible turbulence using a local dynamic subgrid model, Ph.D. thesis, Georgia Institute of Technology, Atlanta, Georgia, 1997.

Nelson, C. C., and S. Menon, Unsteady simulations of compressible spatial mixing layers, *AIAA-98-0786*, 1998.

Poinsot, T., and S. Lele, Boundary conditions for direct simulations of compressible viscous flow, *Journal of Computational Physics*, *101*, 104–129, 1992.

Poole, L., J. Alvarez, C. Hostetler, R. DeCoursey, G. Kent, G. Hansen, and S. Sylvan, Ground-based lidar observations of boeing 737 exhaust particulates in near-field regime, *Tech. Rep. EOS 77, Supplement No. S58*, 1996.

Quackenbush, T., M. Teske, and A. Bilanin, Computation of wake/exhaust mixing downstream of advanced transport aircraft, *AIAA-93-2944*, 1993.

Quackenbush, T., M. Teske, and A. Bilanin, Dynamics of exhaust plume entrainment in aircraft vortex wakes, *AIAA-96-0747*, 1996.

Ragab, S., and M. Sreedhar, Large-scale structures in a trailing vortex, *AIAA-94-2316*, 1994a.

Ragab, S., and M. Sreedhar, Numerical simulation of vortices with axial velocity deficits, *Phys. Fluids*, *7*, 549–558, 1994b.

Risso, F., A. Corjon, and A. Stoessel, Direct numerical simulation of trailing vortices in homogeneous turbulence, *AIAA-96-0802*, 1996.

Saffman, P., Structure of turbulent line vortices, *Phys. of Fluids*, *16*, 1181–1188, 1973.

Schumann, U., Pollution from aircraft emissions in the north atlantic flight corridor(polinat). *Tech. Rep. EUR 16978 EN*, Office for official publication of the European Communities Luxembourg, 1996.

Sykes, R. I., and D. S. Henn, Large-eddy simulation of concentration fluctuations in a dispersing plume, *Atm. Env.*, *26*, 3127–3144, 1992.

Sykes, R. I., D. S. Henn, S. Parker, and W. S. Lewellen, Large-eddy simulation of turbulent reacting plume, *Atm. Env.*, *26*, 2565–2574, 1992.

Teske, M., T. Quackenbush, R. Sykes, and A. Bilanin, Long-time aircraft vortex wake predictions and plume evolution consequences, *AIAA-97-1843*, 1997.

Wang, Z., and J.-Y. Chen, Numerical modeling of mixing and chemistry in near-field engine exhaust plumes, *J. Geophys. Res.*, *102*, 12,871–12,883, 1997.

Junxiao Wu and Suresh Menon, School of Aerospace Engineering, Georgia Institute of Technology, Atlanta, Georgia 30332-0150. (e-mail:menon@condor.ae.gatech.edu)

Received _____

Figure Captions

Figure 1. Setup of the numerical simulations for the spatial LES simulations.

Figure 2. Comparison of averaged SO_2 mole fraction decay for different turbulence inflow conditions.

Figure 3. Comparison of B737 scalar concentration with LIDAR measurement (data from *Poole et al.* [1996]).

Figure 4. Comparison of scalar concentration predicted by spatial and temporal simulations at a plume age of 5 seconds (30 semispans).

Figure 5. Comparison of averaged SO_2 mole fraction decay with experimental data.

Figure 6. Instantaneous vorticity magnitude contours at different times for the spatial LES of the B747 wake. The contour interval is 2 sec^{-1}.

Figure 7. Vorticity magnitude contours at different locations in the temporal simulation. The contour interval is 2 sec^{-1}.

Figure 8. Vorticity magnitude contours at different locations in the spatial simulation. The contour interval is 2 sec^{-1}.

Figure 9. Variation of the detrainment ratio of NO species with the downstream distance for B747.

Figure 10. Maximum NO mass fraction inside and outside the vortex core (vortex core has a radius of 4m).

Figure 11. NO and SO_3 mass fraction at the vortex core center.

Figure 12. NO and SO_3 mass entrainment into the vortex core.

Figure 13. SO_3 mass fraction at the vortex center and entrainment into the vortex core with only gas phase chemistry.

Tables

Table 1. Data for B737 and B747.

type	wing span	maximum circulation	vortex core radius	vortex separation
B737	30m	$100m^2/s$	2m	26m
B747	60m	$600m^2/s$	4m	54m

Table 2. Initial conditions for the plume-vortex calculations of B747.

	B747	
	Plume	Ambient condition
Temperature	500K	217K
velocity(m/sec)	247	0.0
pressure(atm)	0.17	0.17
mole fraction		
CO	$2.4\text{x}10^{-5}$	$2.0\text{x}10^{-8}$
CO_2	$3.2\text{x}10^{-2}$	$3.5\text{x}10^{-4}$
H_2	$1.0\text{x}10^{-6}$	$5.2\text{x}10^{-7}$
O_2	0.159	0.2098
OH	$1.0\text{x}10^{-5}$	$2.8\text{x}10^{-13}$
H_2O	$3.0\text{x}10^{-2}$	$4.8\text{x}10^{-6}$
N_2	0.779	0.789
NO	$4.3\text{x}10^{-5}$	$5.9\text{x}10^{-11}$
NO_2	$4.8\text{x}10^{-6}$	$4.3\text{x}10^{-10}$
N_2O_5	0.0	0.0
HNO_3	0.0	$3.3\text{x}10^{-9}$
$HONO$	0.0	0.0
SO_2	$6.9\text{x}10^{-6}$	0.0
SO_3	0.0	0.0
O_3	0.0	$2.5\text{x}10^{-7}$

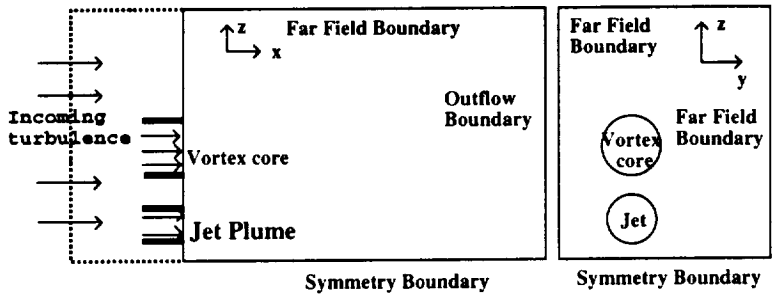

(a) Computational domain for the B737 wing-tip vortex and jet plume.

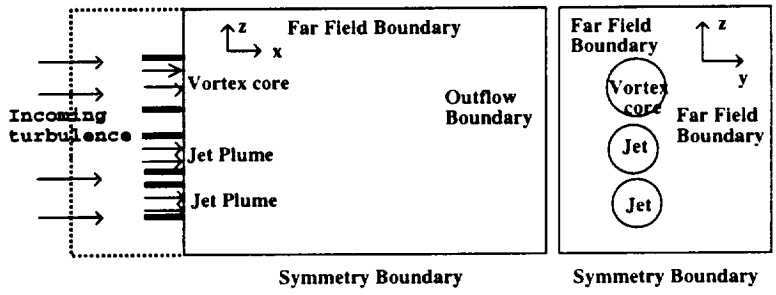

(b) Computational domain for the B747 wing-tip vortex and jet plumes.

Figure 1: Setup of the numerical simulations for the spatial LES simulations.

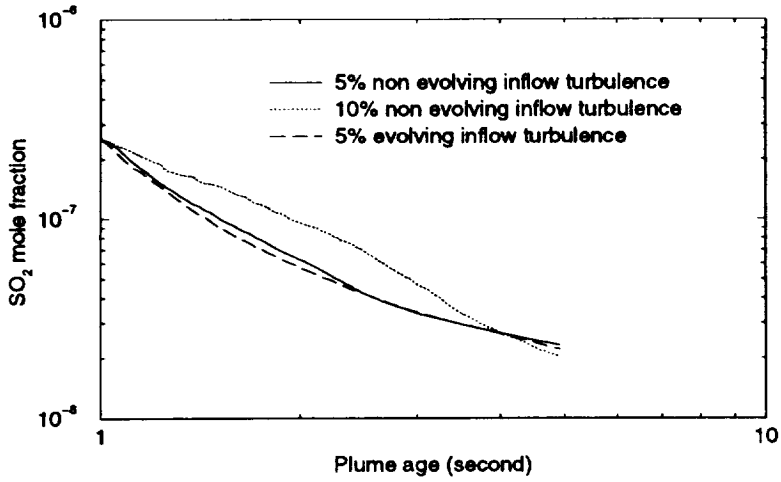

Figure 2: Comparison of averaged SO_2 mole fraction decay for different turbulence inflow conditions.

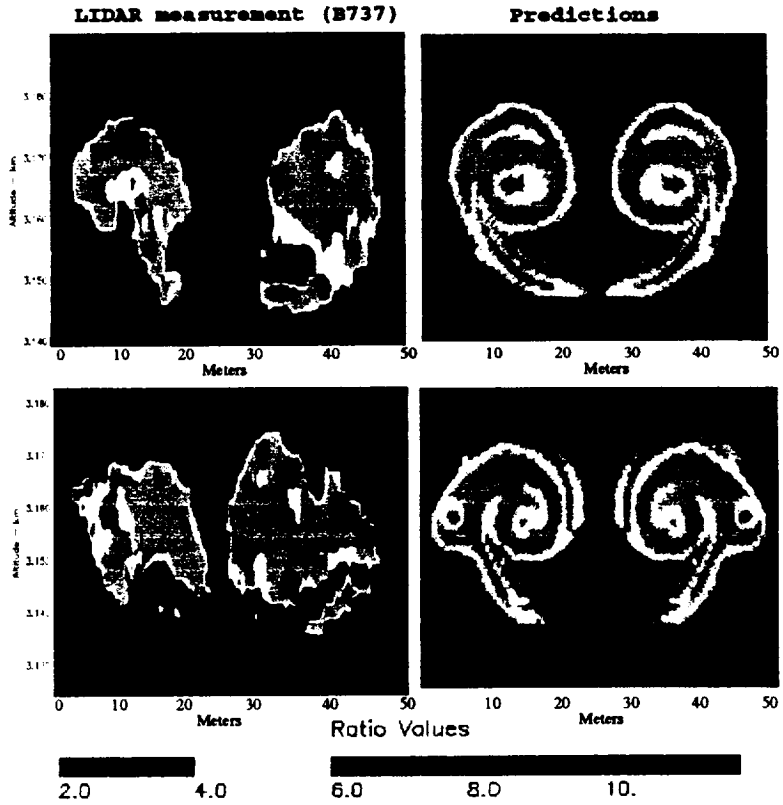

Figure 3: Comparison of B737 scalar concentration with LIDAR measurement (data from *Poole et al.* [1996]).

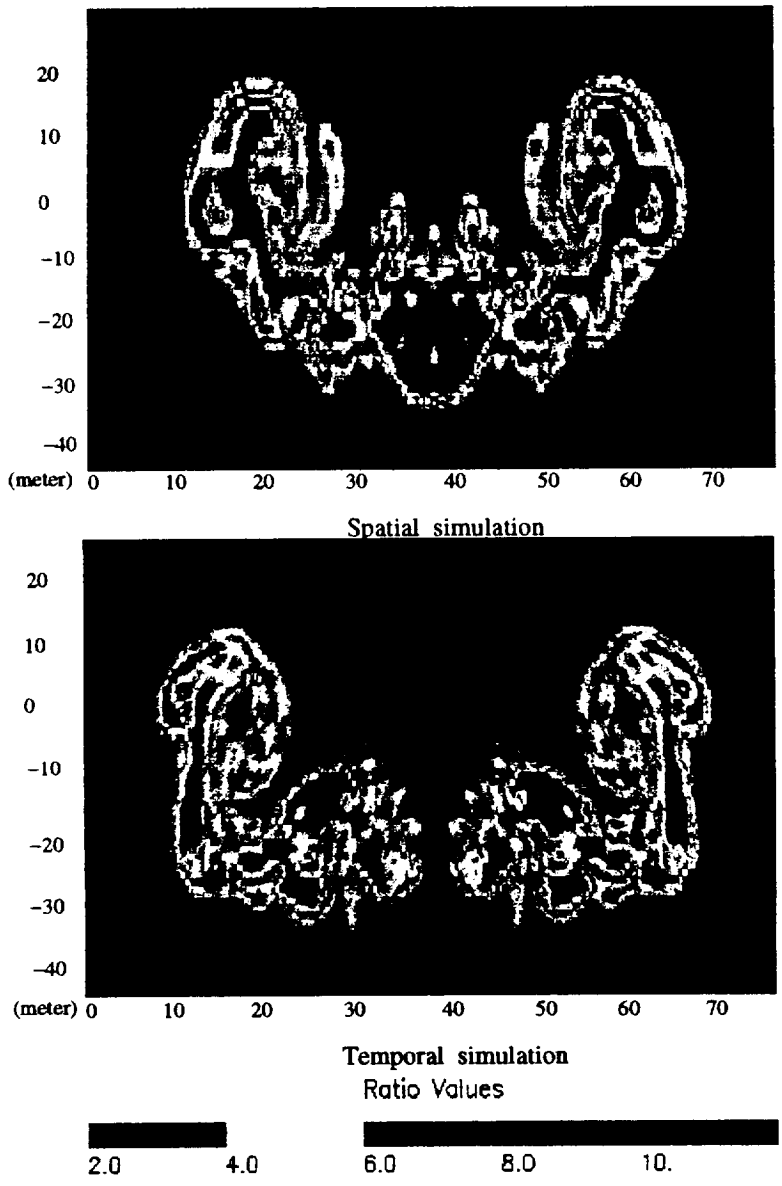

Figure 4: Comparison of scalar concentration predicted by spatial and temporal simulations at a plume age of 5 seconds (30 semispans).

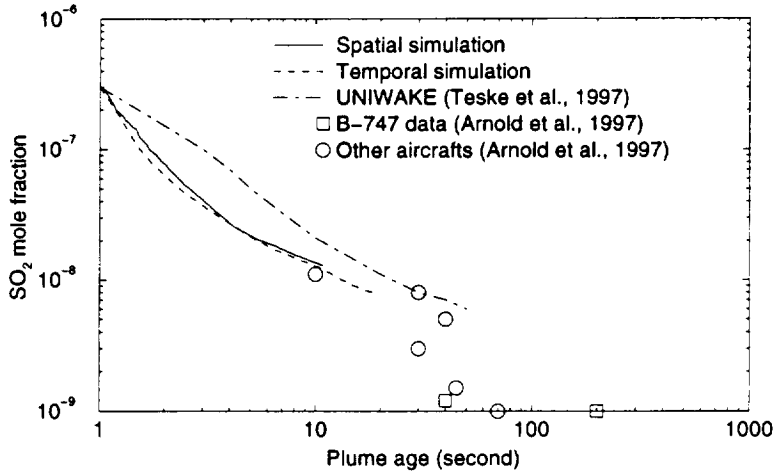

Figure 5: Comparison of averaged SO_2 mole fraction decay with experimental data.

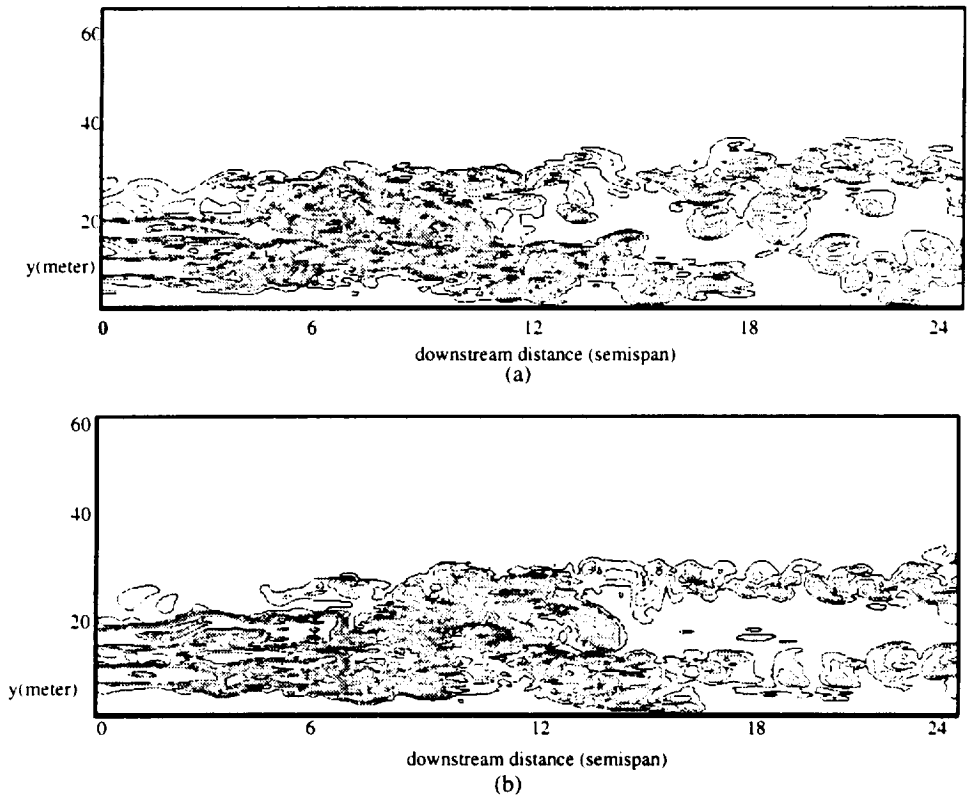

Figure 6: Instantaneous vorticity magnitude contours at different times for the spatial LES of the B747 wake. The contour interval is $2sec^{-1}$.

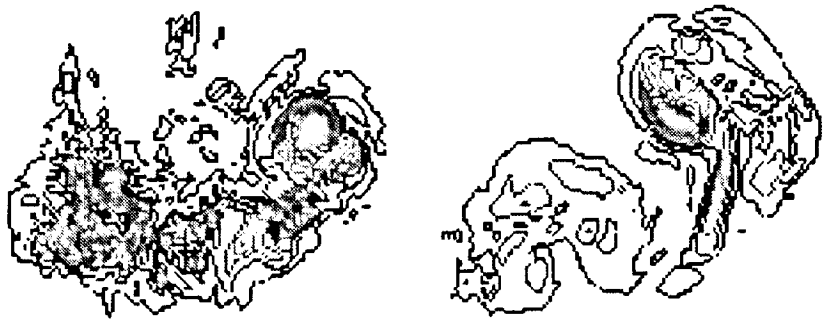

(a) x=12s (b) x=24s

Figure 7: Vorticity magnitude contours at different locations in the temporal simulation. The contour interval is $2sec^{-1}$.

(a) x=12s (b) x=24s

Figure 8: Vorticity magnitude contours at different locations in the spatial simulation. The contour interval is $2sec^{-1}$.

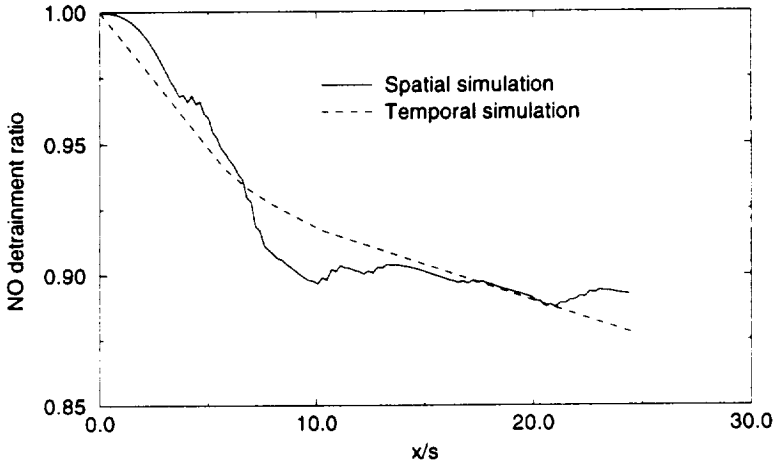

Figure 9: Variation of the detrainment ratio of NO species with the downstream distance for B747.

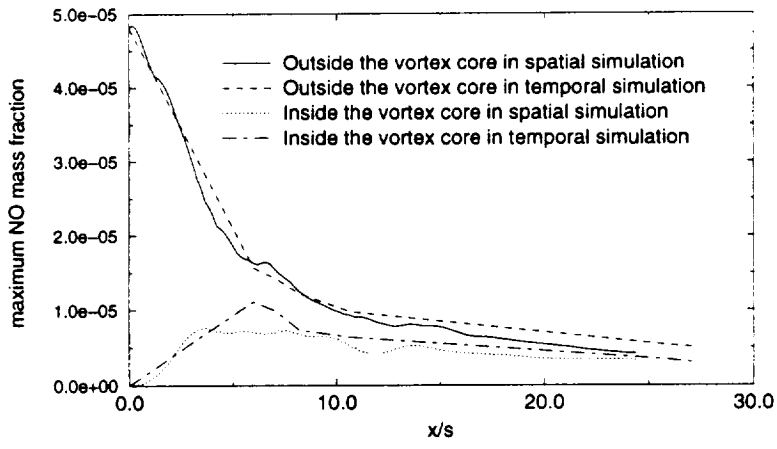

Figure 10: Maximum NO mass fraction inside and outside the vortex core (vortex core has a radius of 4m).

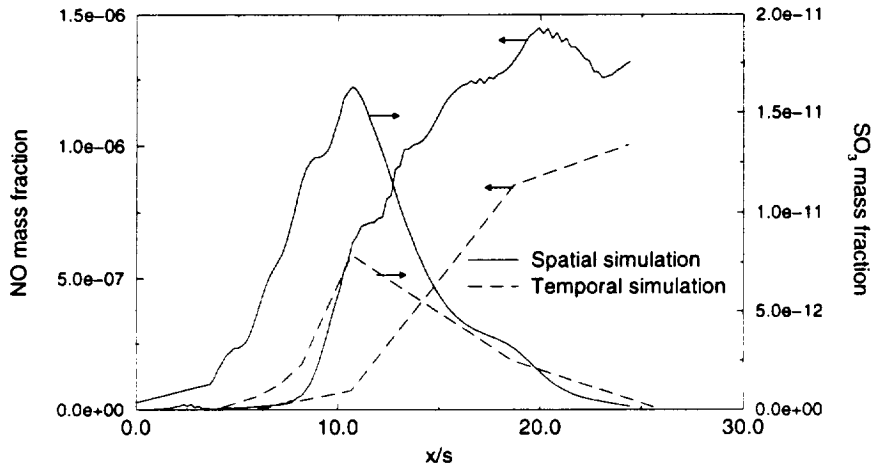

Figure 11: NO and SO_3 mass fraction at the vortex core center.

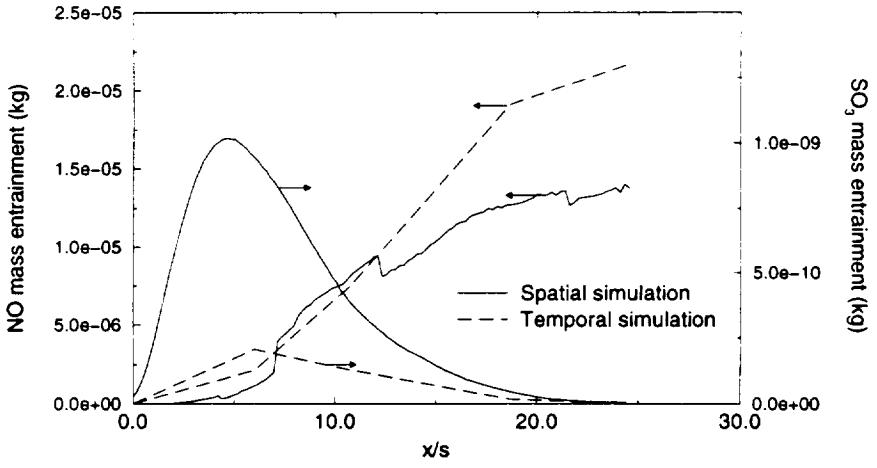

Figure 12: NO and SO_3 mass entrainment into the vortex core.

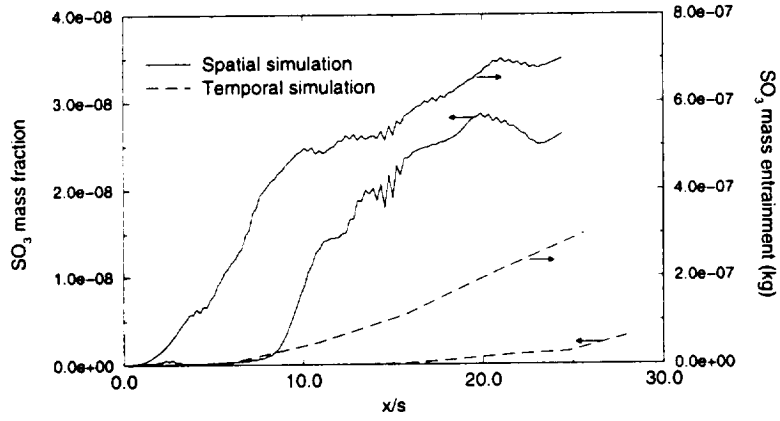

Figure 13: SO_3 mass fraction at the vortex center and SO_3 entrainment into the vortex core with only gas phase chemistry.

Numerical Modeling of Chemistry, Turbulent Mixing and Aerosol Dynamics in Near-Field Aircraft Plumes

Z. Wang and J.-Y. Chen

Department of Mechanical Engineering

University of California

Berkeley, CA 94720

A detailed mechanism including gas phase HO_x, NO_x, and SO_x chemistry between the aircraft exhaust and the ambient air in near-field aircraft plumes is compiled. A reduced mechanism capturing the major chemical pathways is developed. Predictions by the reduced mechanism are found to be in good agreement with those by the detailed mechanism. With the reduced chemistry, the computer CPU time is saved by a factor of more than 3.5 for the near-field plume modeling. Distributions of major chemical species are obtained and analyzed. The computed sensitivities of major species with respect to reaction step are deduced for identification of the dominant gas phase kinetic reaction pathways in the jet plume. The potential interaction of subgrid turbulent mixing with chemistry is investigated and found to have

minor impact on the major species evolution.

A comprehensive aerosol model is developed and it is coupled with chemical kinetics and the axisymmetric turbulent jet flow models. The integrated model is used to simulate microphysical processes in the near-field jet plume, including sulfuric acid and water binary homogeneous nucleation, coagulation, non-equilibrium heteromolecular condensation, and sulfur-induced soot activation.

The formation and evolution of aerosols are computed and analyzed. The computed results show that a large number of ultrafine (0.3–0.6 nm in radius) volatile H_2SO_4-H_2O embryos are generated in the near-field plume. These embryos further grow in size by self coagulation and condensation. Soot particles can be activated by both heterogeneous nucleation and scavenging of H_2SO_4-H_2O aerosols. These activated soot particles can serve as water condensation nuclei for contrail formation. Conditions under which ice contrails can form behind aircrafts are studied. The sensitivities of the threshold temperature for contrail formation with respect to aircraft propulsion efficiency, relative humidity, and ambient pressure are evaluated. The computed aerosol properties for different extent of fuel sulfur conversion to S(VI) (SO_3 and H_2SO_4) in engine are examined and the results are found to be sensitive to this conversion fraction.

Contents

List of Figures

List of Tables

Chapter 1

Introduction and Literature Review

Research on the impact of aircraft emission on the atmosphere was initiated due to interest in commercial supersonic fleet for trans-Atlantic and Pacific rim [Stolarski and Wesoky, 1995; WMO, 1995]. Research effort was later extended to subsonic aircraft emission impact due to their annual growth rate of 5–7% and environmental concern by communities [Schumann, 1995a; Friedl, 1997]. Aircraft emissions in heavily traversed air corridors may have major atmospheric perturbation. Main concern is the effect on O_3 distribution and climate effects. Since there is considerable uncertainty about aviation's impact on the atmosphere, NASA launched the Atmospheric Effects of Aviation Project (AEAP), which includes elements of Subsonic Assessment (SASS) and Atmospheric Effects of Supersonic Aviation (AESA). The goal of NASA's SASS

project is to develop scientific basis for assessment of atmospheric effects caused by engine exhaust emissions, to assist international ozone and climate assessment. The assessments serve as necessary recommendations for regulatory agencies, i.e., EPA and FAA, as a basis for possible emission standards, and as a guide for technology development.

The emphasis in the assessments of the aviation impact has long been put on the emission of nitrogen oxides (NO_x) and their potential impact on ozone. Recent in-situ emission measurements [Fahey et al., 1995; Schumann et al., 1996; Petzold et al., 1997] have demonstrated that a large amount of volatile aerosols and a small amount of nonvolatile particles are produced in nascent exhaust plumes of subsonic and supersonic aircrafts. Researchers are now especially concerned about the presently largely unknown global chemical effects of aircraft-produced particles and soot [Weisensten et al., 1996; Bekki, 1997] and how these particles could affect cirrus cloud formation [Jenson and Toon, 1997] and thus radiative balance, which in turn could affect the climate.

For simulation purpose, an aircraft wake is divided into three parts: the near-field jet plume regime, the vortex interaction regime, and the vortex break-up regime. The relationship between different numerical models is displayed schematically in Figure 1.1. Plume models are used for tracking chemistry and microphysical processes in the near field, while global atmospheric models are intended for estimating the potential effects of aviation on the atmosphere. Results from the atmospheric models

[Bekki and Pyle, 1992; Xue et al. 1994; Weisenstein et al., 1996] indicate potential significant atmospheric effects depending, to some extent, on the chemical kinetics and microphysical processes in the exhaust plume. The two dimensional global modeling study of Weisenstein et al. [1996], for example, predicts a two-fold increase in the stratospheric aerosol surface area (under non-volcanic ambient conditions) due to sulfuric acid nucleation in supersonic High Speed Civil Transport (HSCT) plumes if 10% of the emitted SO_2 is converted to H_2SO_4 shortly after emission. Near-field plume studies will similarly be important for subsonic assessments.

The present work is focusing on the simulation of near-field jet plume, which extends from the engine nozzle exit plane to the location where the plume begins to interact with the vortex shed downstream from the wing tip. Near-field modeling results serve as an input to the later larger-scale modeling. In the near field, major chemical oxidation of gas phase HO_x, SO_x, NO_x by hydroxyl radical OH takes place, and volatile sulfate aerosols are generated through binary homogeneous nucleation. Chemical activation of soot into condensation nuclei (CN) also occurs in this near-field regime.

A study of near field jet plume with detailed chemical kinetics was previously conducted by Miake-Lye et al.[1993]. The flow field was modeled by the JANNAF Standard Plume Flowfield model (SPF-II) [Dash et al., 1990] which is an axisymmetric parabolic Navier Stokes flow code with a two-equation turbulence model. Kärcher et al. [1996a] further studied in detail the specific features that may result from

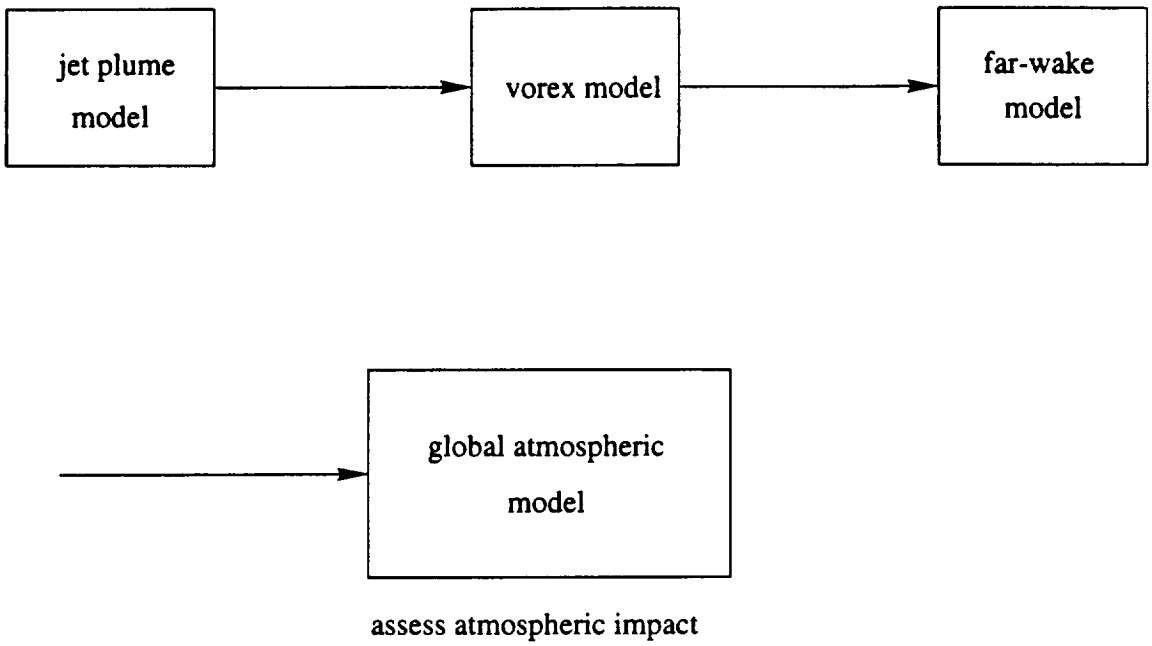

Figure 1.1: Schematic of relationship among different numerical models in simulating aircraft emission impact.

the coupling between chemistry and turbulent diffusion. More recently, Brown et al. [1996a] and Kärcher [1996b] investigated the potential importance of microphysical processes in the near field. The interaction of subgrid turbulent mixing with chemistry was not included in any of the previous simulations. A trajectory model was used to study aerosol dynamics by Kärcher [1996b] and by Yu and Turco [1996, 1997]. Therefore, the flow field is not coupled to the chemistry and microphysical processes and no radial resolution is offered. In addition, Yu and Turco's [1996, 1997] work did not include chemical kinetics.

In the wake-vortex regime, the flow is highly three-dimensional. Large-eddy simulation (LES) is believed necessary to accurately resolve the complicated fluid dynam-

ics. However, LES is computationally expensive and it is not feasible to incorporate detailed chemistry. A reduced chemistry is therefore required to alleviate the computational burden.

The objectives of the present work are: 1) to compile a detailed chemical mechanism for modeling reactions between engine exhaust and ambient air; 2) to develop a reduced chemistry for LES in the wake-vortex regime; 3) to study chemical transformation in the near field and to predict distribution of key species; 4) to explore the interaction between turbulence and chemistry using the probability density function (pdf) approach; 5) to develop a comprehensive aerosol model for studying microphysical processes of aerosols in the near field plume; 6) to investigate the sensitivity of particle properties to less-known parameters; and 7) to study the threshold condition for contrail formation behind aircrafts and to access its sensitivity. The present modeling provides detailed predictions of gas phase species as well as aerosol particles, which serve as an input for the follow-on model.

Chapter 2

Model Formulation

2.1 Model Structure

Figure 2.1 shows schematically the chemical and microphysical transformation processes of aerosols modeled in the present work. SOx and soot particles are emitted from the nozzle exits of jet engines at high temperatures (500 K - 600 K). Sulfuric acid H_2SO_4 is generated through gas phase chemical reactions of SOx with OH and H_2O. Soot particles can be chemically activated by adsorption of SO_3 and H_2SO_4, leading to the formation of a partial or full liquid H_2SO_4-H_2O coating. As the plume cools by the entrainment of the cold ambient air, volatile liquid H_2SO_4-H_2O aerosols are formed through binary homogeneous nucleation. These volatile aerosols grow in size through either condensation of gaseous H_2SO_4 and H_2O or by self coagulation. The volatile aerosols can interact with soot particles through coagulation, which provides

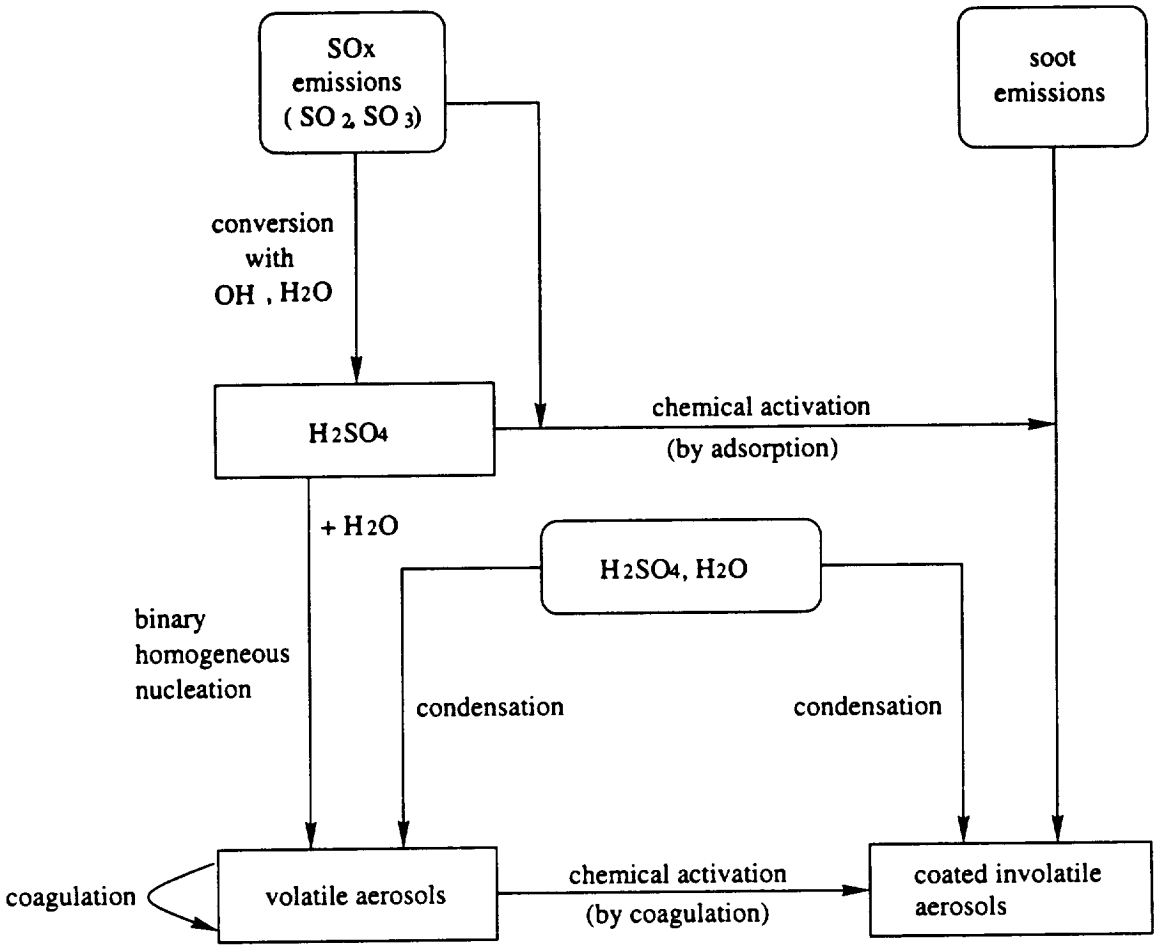

Figure 2.1: Schematic of particle microphysical processes in near-field aircraft plumes as simulated by the aerosol model.

another pathway for the sulfur induced soot activation. H_2SO_4 and H_2O can condense onto the coated part of soot particles.

2.2 Model Input

To initialize our numerical calculations and to convert emission indices of primary exhaust products into mole fractions, we need engine exit-plane properties of aircrafts.

Table 2.1: Exit plane parameters for B747 engine

	Exhaust Core Flow	Bypass Air Flow	Ambient
Fuel flow rate $\dot{m}_F$, kg/s	0.795		
Exit radius, m	0.44	0.435	
Velocity, m/s	475.7	316.3	237
Temperature, K	547.3	253.4	219.2
Pressure, atm	0.2361	0.2361	0.2361

We will concentrate on the CF6-80 C2B1F engine used by the Boeing 747 aircrafts. The formation and evolution of chemical species and particles are expected to develop similarly behind other engines, with slight changes in the length scales due to different nozzle geometry and axial exhaust velocity. The results of this work are considered to be representative of other types of aircrafts qualitatively.

Recently, Schumann [1995b] has estimated the relevant nozzle exit plane parameters for the B747 engine in such a way that they are consistent with the integral mass, momentum, and energy balances of the jet core and bypass flows. Table 2.1 lists the parameters adapted from Schumann [1995b] for a B747 at the cruising condition of $P_a = 0.2361$ atm and $T_a = 219.2$ K with airspeed $u_a = 237$ m/s.

Given the emission indices EI_k of the exhaust product k in gram per kilogram of fuel burnt, the species volume mixing ratios (mole fractions) at the nozzle exit plane can be derived from the following relation based on mass conservation

$$x_{k,0} = \frac{EI_k}{m_k} \cdot \frac{\dot{m}_F}{\dot{V}} \cdot \frac{1}{N_a}, \tag{2.1}$$

where m_k is the molecular mass of species k, $\dot{m}_F$ is the engine fuel flow rate, $\dot{V} =$

$A_{core,0}u_{core,0}$ is the volumetric flow rate of the core flow at the exit plane. The subscript 0 denotes the engine exit plane, and $N_a = P_a/(k_B T_{core,0})$ is the air number density at engine exit plane. With the data in Table 2.1, we find for a B747,

$$x_{k,0} = 5.27 \times 10^{-4} \cdot \frac{EI_k \text{ [g/kg]}}{M_k \text{ [g/mol]}}, \tag{2.2}$$

where M_k is the molar mass of species k.

In Table 2.2, we present the initial mole fractions at the exhaust core based on equation (2.2). The mole fractions in the ambient air are prescribed as the boundary conditions in the numerical model. These ambient compositions are extracted from a mesoscale chemical transport model based on the RADM mechanism [Chang et al., 1987; Petry et al., 1994] and represent a region with dense air traffic, e.g., at northern midlatitude (50°N) summer conditions at noon. The choice of the boundary values is not crucial since we only focus on the short-term evolution of the near-field jet regime. The ambient water mole fraction listed in Table 2.2 corresponds to a relative humidity of $RH = \frac{x_{H_2O,a} P_a}{P^{\infty}_{sat,H_2O}(T_a)} \approx 50\%$, where the subscript a denotes the ambient condition and the superscript ∞ denotes a flat surface.

The emission indices of water vapor and carbon dioxide can be estimated relatively accurately assuming stoichiometric jet fuel combustion. Jet fuel sulfur contents (FSC) typically vary from 0.1 to 1 g/kg [Busen and Schumann, 1995], with a broad average around 0.4g/kg (400ppmm) and a maximum specification limit of 3 g/kg [American Society for Testing and Materials (ASTM), 1994]. Assuming that fuel sulfur is totally oxidized to sulfur dioxide during combustion in the engine, the SO_2 emission index

Table 2.2: Initial and boundary conditions of gas species for B747

	Exhaust Core Flow	Ambient Air
Mole Fraction		
O	0	1.1×10^{-14}
O_2	0.135	0.21
O_3	0	3.0×10^{-7}
H	0	0
H_2	0	9.0×10^{-7}
OH	6.2×10^{-6}	2.8×10^{-13}
HO_2	0	3.6×10^{-12}
H_2O	3.6×10^{-2}	8.8×10^{-5}
H_2O_2	0	2.4×10^{-11}
NO	1.3×10^{-4}	8.1×10^{-11}
NO_2	6.9×10^{-6}	6.5×10^{-11}
NO_3	0	8.9×10^{-15}
N_2O_5	0	1.0×10^{-11}
HNO_2	0	3.4×10^{-13}
HNO_3	0	2.0×10^{-9}
CO	9.4×10^{-5}	4.0×10^{-8}
CO_2	3.8×10^{-2}	3.3×10^{-4}
SO	0	0
SO_2	5.8×10^{-6}	9.1×10^{-12}
SO_3	0	0
HSO_3	0	0
H_2SO_4	0	0

can be directly calculated with $EI_{SO_2} = FSC \cdot M_{SO_2}/M_S$. In this work, we use $EI_{SO_2} = 0.7g/kg$. A sensitivity study with different levels of SO_3 emission will be presented in Chapter 4. The emission indices of the other two major air pollutants resulting from combustion, CO and NO_x (= NO + NO_2), are also less well known because they depend on several factors including combustion temperature, fuel-air ratio, hydrocarbon oxidation process, and fuel nitrogen content. In the present work, we employ $EI_{CO} = 5g/kg$ and EI_{NOx} equivalent to 12 g of NO_x per kg fuel burnt. NO_x emission is assumed to consist of 95% NO and 5% NO_2 on a molar basis.

The hydroxyl radical OH is a key gaseous species driving major radical chemical reactions in the cooling jet plume. Unfortunately its emission index is currently only known with considerable uncertainties from simulations of the internal engine flow and combustion [Miake-Lye et al., 1993; Stolarski and Wesoky, 1995]. Kärcher [1996] showed that EI_{OH} = 0.2 g/kg fuel, corresponding to 6.2 ppmv from equation (2.2), can be used as a reasonable reference case. The abundances of all other radicals at the exit plane are set to zero mainly because their emission indices are likely to be insignificant or simply unknown.

Typical size distributions of nascent soot particles are assumed to be log-normal, with mean radii in the range of 15–30 nm, modal widths of 1.4–1.6, and number densities of 10^6–10^7 cm^{-3} [Hagen et al., 1992; Petzold and Schroder, 1997]. In this work, we take the median radius as 20nm, the modal width as 1.4, and the total

number density as 1.6×10^6 cm^{-3}. Since the number density can be expressed as

$$N_{soot} = \frac{EI_{soot}\dot{m}_F}{\dot{V}m_{soot}}, \tag{2.3}$$

where the mass of a soot can be approximated as $m_{soot} = \rho_{soot} \cdot 4/3\pi\bar{r}^3$ with $\rho_{soot} \approx 2$ g/cm^3 for graphitic carbon. The soot emission index is estimated to be 0.04 g of soot per kg of fuel. This corresponds to an emission index of $EI_{soot}/(\rho_{soot} \cdot 4/3\pi\bar{r}^3) = 0.6 \times 10^{15}$ soot particles per kg of fuel.

2.3 Solution Method

To simulate the near-field jet plume, we assume the flow field is axisymmetric, steady-state, and parabolic. Isobaric expansion at a prescribed ambient pressure P_a is assumed. The turbulent mean velocity field is modeled by the Reynolds average Navier Stokes equations with a second moment turbulence closure model, which directly solves the modeled transport equations for the Reynolds stresses. A marching downstream algorithm is used and the details can be found in Chen et al. [1987, 1989]. When the turbulence interaction with chemistry in a subgrid is neglected, the mean concentrations and temperature can be solved by the conservation equations of mean species and energy. The mean chemical reaction rate can be expressed in terms of mean temperature and mean concentrations $\bar{\omega}_k = f(\bar{T}, \bar{C}_i)$. To account for the subgrid interaction of turbulence with chemistry, an additional term of subgrid molecular mixing is needed, and the mean chemical reaction rate cannot be expressed

in general as a function of mean temperature and mean species concentrations. An efficient way to resolve this problem is by using the probability density function (pdf) approach. In general, the instantaneous composition of a reacting mixture of gases can be determined from the set of $kk+1$ scalars comprising mass fractions and enthalpy $\bar{\phi}(\vec{x},t) = \phi_1, \phi_2, \cdots, \phi_{kk}, \phi_{kk+1}$, where kk is the total number of gaseous species. With $\bar{\psi} = \psi_1, \psi_2, \cdots, \psi_{kk+1}$ being the composition space corresponding to $\bar{\phi}$, the mean value of any quantity $\langle Q(\bar{\phi})\rangle$ can be determined from the probability density function of joint scalar $\bar{\phi}$, $P_{\bar{\phi}}(\bar{\psi};\vec{x},t)$, by $\langle Q(\bar{\phi})\rangle = \int P_{\bar{\phi}}(\bar{\psi})Q(\bar{\psi})d\bar{\psi}$, where $P_{\bar{\phi}}(\bar{\psi};\vec{x},t)$ is defined as $P_{\bar{\phi}}(\bar{\psi};\vec{x},t)d\bar{\psi} = \text{Probability}\{\bar{\psi} \le \bar{\phi} \le \bar{\psi} + d\bar{\psi}\}$. In variable-density turbulent flows, the density-weighted average of a function Q is defined as $\widetilde{Q} \equiv \langle \rho Q\rangle / \langle \rho\rangle = \int P_{\bar{\phi}}(\bar{\psi})\rho(\bar{\psi})Q(\bar{\psi})d\bar{\psi} / \langle \rho\rangle = \int \widetilde{P}_{\bar{\phi}}(\bar{\psi})Q(\bar{\psi})d\bar{\psi}$. Therefore, the density-averaged reaction rate can be expressed as $\tilde{\omega}_k = \int \widetilde{P}_{\bar{\phi}}(\bar{\psi})\omega_k(\bar{\psi})d\bar{\psi}$.

The density-weighted joint scalar pdf can be solved by the following transport equation [Pope, 1985]:

$$\begin{aligned}\langle\rho\rangle\tilde{u}_k\frac{\partial\widetilde{P}_{\bar{\phi}}(\bar{\psi};\vec{x})}{\partial x_k} = &-\sum_{\alpha=1}^{kk+1}\frac{\partial}{\partial\psi_\alpha}\left[\langle\rho\rangle S_\alpha(\bar{\psi})\widetilde{P}_{\bar{\phi}}(\bar{\psi};\vec{x})\right]\\ &-\frac{\partial}{\partial x_k}\left[\langle\rho\rangle\langle u_k''|\bar{\phi}=\bar{\psi}\rangle\widetilde{P}_{\bar{\phi}}(\bar{\psi};\vec{x})\right]\\ &-\sum_{\alpha=1,\beta=1}^{kk+1}\frac{\partial^2}{\partial\psi_\alpha\partial\psi_\beta}\left[\langle\rho\rangle\langle\varepsilon_{\alpha\beta}|\bar{\phi}=\bar{\psi}\rangle\widetilde{P}_{\bar{\phi}}(\bar{\psi};\vec{x})\right],\end{aligned} \tag{2.4}$$

where $\langle\rangle$ denotes the mean value, $\varepsilon_{\alpha\beta}$ is the scalar dissipation rate given by $\varepsilon_{\alpha\beta} = \Gamma\frac{\partial\phi_\alpha}{\partial x_k}\frac{\partial\phi_\beta}{\partial x_k}$ where Γ is the molecular diffusivity, $\langle\varepsilon_{\alpha\beta}|\bar{\phi}=\bar{\psi}\rangle$ represents the average

scalar dissipation rate conditioned on a certain set of scalars, and S_α is the chemical source term for scalar ψ_α. The first two terms on the right hand side represent the effects of chemical reaction and turbulent transport on the joint scalar pdf, respectively. Both of these terms can be calculated directly with no need for modeling. The last term stands for the effect of microscale mixing on the pdf which requires closure approximations. In this study, the effect of microscale mixing on the pdf is modeled by the modified Curl's mixing model [Janika et al., 1979],

$$\begin{aligned} &-\sum_{\alpha=1,\beta=1}^{k} \frac{\partial^2}{\partial\psi_\alpha \partial\psi_\beta}\left[\langle \varepsilon_{\alpha\beta}|\bar{\phi}=\bar{\psi}\rangle \widetilde{P}_{\bar{\phi}}(\bar{\psi};\vec{x})\right] \\ =&\frac{1}{\tau_{mix}}\left\{\int_{\psi'}\int_{\psi''} \widetilde{P}_{\bar{\phi}}(\psi';\vec{x})\widetilde{P}_{\bar{\phi}}(\psi'';\vec{x})H(\psi',\psi''|\psi)d\psi' d\psi'' - \widetilde{P}_{\bar{\phi}}(\bar{\psi};\vec{x})\right\}, \end{aligned} \tag{2.5}$$

where H is the transitional probability defined as

$$\begin{aligned} H(\psi',\psi''|\psi) &= \frac{1}{|\psi''-\psi'|} \quad \text{for } \psi \in [\psi',\psi''] \\ &= 0 \quad \text{elsewise.} \end{aligned} \tag{2.6}$$

The amount of mixing is modeled through a characteristic mixing time which is related to the turbulence time scale for micromixing, $\tau = \tilde{k}/\tilde{\varepsilon}$, where $\tilde{k} = 0.5\langle u_k'' u_k''\rangle$ is the turbulence kinetic energy and $\tilde{\varepsilon} = \nu\langle \frac{\partial u_i''}{\partial x_k}\frac{\partial u_i''}{\partial x_k}\rangle$ is the turbulence dissipation rate with ν being the kinematic viscosity. Reactive flows of practical interest usually involve many species, leading to a large dimensionality of $P(\psi_1,\psi_2,\cdots,\psi_{kk+1})$. The computational expense of finite difference method is found to rise exponentially with the dimensionality and it is impractical to solve a variable with dimensionality greater than three. However, the computational expense of the Monte Carlo technique rises

only linearly with the dimensionality, which is the best that can be achieved by any algorithm. Therefore, the Monte Carlo technique is employed to solve the pdf evolution equation (2.4).

The turbulent transport term can be modeled by a gradient diffusion model using turbulence time and fluctuating velocities from the Reynolds stress model,

$$\langle u_k'' | \bar{\phi} = \bar{\psi} \rangle \widetilde{P}_{\bar{\phi}}(\bar{\psi}; \vec{x}) = -C_s \frac{\tilde{k}}{\tilde{\varepsilon}} \widetilde{u_\alpha'' u_\beta''} \frac{\partial \widetilde{P}_{\bar{\phi}}(\bar{\psi}; \vec{x})}{\partial x_\beta}, \tag{2.7}$$

where C_s is an adjustable constant (= 0.25 in jet flows), $u_k'' = u_k - \tilde{u}_k$ is the density-weighted velocity fluctuation and $\langle u_k'' | \bar{\phi} = \bar{\psi} \rangle$ is the average fluctuation conditioned on a certain set of scalars.

Chapter 3

Gas Phase Chemistry

3.1 Detailed Chemistry

3.1.1 Compilation of Detailed Chemical Reaction Mechanism

Table 3.1 and 3.2 list the bimolecular and termolecular gas phase reactions employed in our model, which include 60 chemical reactions and 24 species. The reaction kinetic parameters are selected to cover the temperature range from 1000 K to 200 K as required by the jet plume temperature history. Photochemical reactions are excluded as the time scale of the fastest photolytic reaction, $NO_2 + h\nu \rightarrow NO + O$, is about 2 minutes which is larger than the plume age of just a few seconds. Hydrocarbon reactions are also excluded because the oxidation potential of the young exhaust plume is too small to affect the emitted hydrocarbons. We also do not attempt to model ion chemistry that may influence the radical balance in the very early

jet regime.

Most of the reaction rate parameters are extracted from the chemical kinetics database collected by the National Institute of Standards and Technology (NIST) [Mallard et al., 1994]. Rate constants for the reaction of HNO_2 with H and O (reactions (R28) and (R29)) are taken from data by Tsang et al. [1991]. JPL database [Demore et al., 1992] on chemical reaction rate constants provides accurate rate data only for common atmospheric temperature below $\sim$ 300 K. To model the kinetics of the reactive jet flow properly, however, we need to employ rate constants which are also valid at higher temperatures. In some cases, a simple extrapolation of the JPL rates would give similar answers, but this may not hold for all reactions.

3.1.2 Chemical Kinetics Package

The Chemkin package [Kee et al., 1989] is a software tool designed to facilitate simulations of elementary chemical kinetics. An important advantage of the general-purpose and problem-independent structure of Chemkin is that it allows us to work with the same chemical input for different application codes. As indicated in Figure 3.1, this package consists of two major FORTRAN codes, the Interpreter and the Gas-Phase Subroutine Library, along with the Thermodynamic Database. When the Interpreter is executed, it reads in the user's symbolic description of the reaction mechanism and then extracts the appropriate thermodynamic information for the species involved from the Thermodynamic Database. The major output of the

Table 3.1: Gas Phase Chemical Reaction Mechanism: Binary Reactions

	Reaction	Rate Constant (cm^3 $molecule^{-1}$ sec^{-1})
R1	$O + O_3 \longrightarrow 2O_2$	$1.21 \times 10^{-11}exp(-2125/T)$
R2	$H + O_3 \longrightarrow OH + O_2$	$1.15 \times 10^{-10}exp(-436/T)$
R3	$H + OH \longrightarrow O + H_2$	$8.10 \times 10^{-21}T^{2.8}exp(-1950/T)$
R4	$H + HO_2 \longrightarrow OH + OH$	$2.8 \times 10^{-10}exp(-440/T)$
R5	$H + HO_2 \longrightarrow H_2 + O_2$	$6.9 \times 10^{-11}exp(-636.9/T)$
R6	$H + HO_2 \longrightarrow H_2O + O$	$2.8 \times 10^{-12}T^{0.46}exp(-677.9/T)$
R7	$OH + O \longrightarrow H + O_2$	$1.83 \times 10^{-11}exp(173.3/T)$
R8	$OH + O_3 \longrightarrow HO_2 + O_2$	$1.9 \times 10^{-12}exp(-1000/T)$
R9	$OH + H_2 \longrightarrow H_2O + H$	$1.11 \times 10^{-16}T^{1.64}exp(-1589/T)$
R10	$OH + OH \longrightarrow H_2O + O$	$8.34 \times 10^{-17}T^{1.54}exp(355/T)$
R11	$OH + HO_2 \longrightarrow H_2O + O_2$	$5.09 \times 10^{-11}exp(72.6/T)$
R12	$OH + H_2O_2 \longrightarrow H_2O + HO_2$	$2.13 \times 10^{-13}T^{0.47}exp(-179.8/T)$
R13	$HO_2 + O \longrightarrow OH + O_2$	$2.71 \times 10^{-11}exp(-224/T)$
R14	$HO_2 + O_3 \longrightarrow OH + 2O_2$	$1.4 \times 10^{-14}exp(-600/T)$
R15	$HO_2 + HO_2 \longrightarrow H_2O_2 + O_2$	$2.2 \times 10^{-13}exp(600/T)$
R16	$H_2O_2 + O \longrightarrow OH + HO_2$	$2.33 \times 10^{-11}exp(-2814/T)$
R17	$H_2O_2 + H \longrightarrow OH + H_2O$	$1.7 \times 10^{-11}exp(-1800/T)$
R18	$H_2O_2 + H \longrightarrow HO_2 + H_2$	$1.77 \times 10^{-11}exp(-2890/T)$
R19	$NO + O_3 \longrightarrow NO_2 + O_2$	$2.14 \times 10^{-12}exp(-1408/T)$
R20	$NO + HO_2 \longrightarrow NO_2 + OH$	$3.7 \times 10^{-12}exp(240/T)$
R21	$NO + NO_3 \longrightarrow NO_2 + NO_2$	$1.8 \times 10^{-11}exp(110/T)$
R22	$NO_2 + O \longrightarrow NO + O_2$	$6.5 \times 10^{-12}exp(120/T)$
R23	$NO_2 + O_3 \longrightarrow NO_3 + O_2$	$1.2 \times 10^{-13}exp(-2450/T)$
R24	$H + NO_2 \longrightarrow OH + NO$	1.4×10^{-10}
R25	$NO_2 + NO_3 \longrightarrow NO + NO_2 + O_2$	$1.91 \times 10^{-13}exp(-1696/T)$
R26	$NO_3 + O \longrightarrow NO_2 + O_2$	1.0×10^{-11}
R27	$OH + NO_3 \longrightarrow HO_2 + NO_2$	2.3×10^{-11}
R28	$HNO_2 + O \longrightarrow OH + NO_2$	$2.0 \times 10^{-11}exp(-3000/T)$
R29	$HNO_2 + H \longrightarrow NO_2 + H_2$	$2.0 \times 10^{-11}exp(-3700/T)$
R30	$HNO_2 + OH \longrightarrow H_2O + NO_2$	$1.8 \times 10^{-11}\,exp(-390/T)$
R31	$HNO_3 + O \longrightarrow OH + NO_3$	3.0×10^{-17}
R32	$HNO_3 + OH \longrightarrow H_2O + NO_3$	$4.02 \times 10^{-14}exp(317.7/T)$
R33	$SO + O_2 \longrightarrow SO_2 + O$	$1.55 \times 10^{-13}exp(-2288/T)$
R34	$SO + O_3 \longrightarrow SO_2 + O_2$	$4.3 \times 10^{-12}exp(-1148/T)$
R35	$SO + OH \longrightarrow SO_2 + H$	8.59×10^{-11}
R36	$SO + NO_2 \longrightarrow SO_2 + NO$	1.4×10^{-11}
R37	$SO_2 + O_3 \longrightarrow O_2 + SO_3$	$3.0 \times 10^{-12}exp(-7000/T)$
R38	$SO_3 + O \longrightarrow O_2 + SO_2$	$3.17 \times 10^{-11}exp(-4455/T)$
R39	$SO_3 + H_2O \longrightarrow H_2SO_4$	1.2×10^{-15}
R40	$HSO_3 + O_2 \longrightarrow HO_2 + SO_3$	$1.23 \times 10^{-12}exp(-316.8/T)$
R41	$CO + OH \longrightarrow CO_2 + H$	$4.44 \times 10^{-16}T^{0.98}exp(94/T)$

Table 3.2: Gas Phase Chemical Reaction mechanism: Three-Body Combination and Thermal Decombination Reactions

	Reaction	Low-Pressure Limit k_0	High-Pressure Limit k_∞
R42	$O + O \xrightarrow{M} O_2$	$5.2 \times 10^{-35}\exp(900/T)$	... ...
R43	$O + O_2 \xrightarrow{M} O_3$	$5.51 \times 10^{-31}T^{-1.3}\exp(152.6/T)$	$4.2 \times 10^{-12}\exp(-183/T)$
R44	$H + O \xrightarrow{M} OH$	$1.30 \times 10^{-29}T^{-1}$	... ...
R45	$H + O_2 \xrightarrow{M} HO_2$	$1.05 \times 10^{-30}T^{-0.7}\exp(144.2/T)$	7.5×10^{-11}
R46	$H + H \xrightarrow{M} H_2$	$1.28\times10^{-29}T^{-1.13}\exp(-100.6/T)$	$2.9 \times 10^{-10}\exp(5821/T)$
R47	$H + OH \xrightarrow{M} H_2O$	$1.538\times10^{-28}T^{-1.21}\exp(295.3/T)$	$2.69 \times 10^{-10}\exp(-75/T)$
R48	$OH + OH \xrightarrow{M} H_2O_2 + O_2$	$6.58 \times 10^{-29}T^{-0.8}$	1.5×10^{-11}
R49	$HO_2 + HO_2 \xrightarrow{M} H_2O_2$	$1.9 \times 10^{-33}\exp(980/T)$	$2.2 \times 10^{-13}\exp(600/T)$
R50	$NO + O \xrightarrow{M} NO_2$	$9.09 \times 10^{-28}T^{-1.6}$	$5.43 \times 10^{-12}T^{0.3}$
R51	$OH + NO \xrightarrow{M} HNO_2$	$1.91 \times 10^{-26}T^{-1.9}\exp(164.8/T)$	$5.1 \times 10^{-12}\exp(159.8/T)$
R52	$NO_2 + O \xrightarrow{M} NO_3$	$6.21\times10^{-23}T^{-3.22}\exp(-570.5/T)$	$2.65 \times 10^{-11}\exp(-25.78/T)$
R53	$OH + NO_2 \xrightarrow{M} HNO_3$	$3.50 \times 10^{-16}T^{-5.2}\exp(-840/T)$	$1.84 \times 10^{-12}\exp(587.2/T)$
R54	$NO_2 + NO_3 \xrightarrow{M} N_2O_5$	$6.98 \times 10^{-22}T^{-3.4}$	$6.40 \times 10^{-13}T^{0.2}$
R55	$N_2O_5 \xrightarrow{M} NO_2 + NO_3$	$1.5 \times 10^{-6}\exp(-9104/T)$	$5.9 \times 10^{11}\exp(-9370/T)$
R56	$HNO_2 \xrightarrow{M} OH + NO$	$5.0 \times 10^{6}\ T^{-3.8}\exp(-25340/T)$	$1.20\times10^{19}T^{-1.23}\exp(-25010/T)$
R57	$HNO_3 \xrightarrow{M} OH + NO_2$	$1.2 \times 10^{-6}\exp(-22270/T)$	$2.14 \times 10^{15}\exp(-24270/T)$
R58	$SO_2 + O \xrightarrow{M} SO_3$	$1.49 \times 10^{-32}\exp(-601/T)$	1.19×10^{-9}
R59	$SO_2 + OH \xrightarrow{M} HSO_3$	$1.97 \times 10^{-32}\exp(867.3/T)$	2.0×10^{-12}
R60	$CO + O \xrightarrow{M} CO_2$	$2.49 \times 10^{-33}\exp(-1550/T)$	$2.66 \times 10^{-14}\exp(-1459/T)$

The effective second-order reaction rate constant is [Demore et al., 1992]:

$$k(M,T) = \left(\frac{k_0(T)[M]}{1 + (k_0(T)[M]/k_\infty(T))}\right) 0.6^{\{1+[\log_{10}(k_0(T)[M]/k_\infty(T))]^2\}^{-1}}$$

For third-order low and second-order high pressure limits, the units are $cm^6molecule^{-2}sec^{-1}$ and $cm^3molecule^{-1}sec^{-1}$, respectively. For second-order low and first-order high pressure limits, the units are cm^3sec^{-1} and sec^{-1}, respectively.

Interpreter is a linking file, which contains all the pertinent information on the elements, species, and reactions of the specific mechanism. The Gas-Phase Subroutine Library is a collection of more than 100 subroutines that return information on elements, species, reactions, equations of state, thermodynamic properties, and chemical reaction rates.

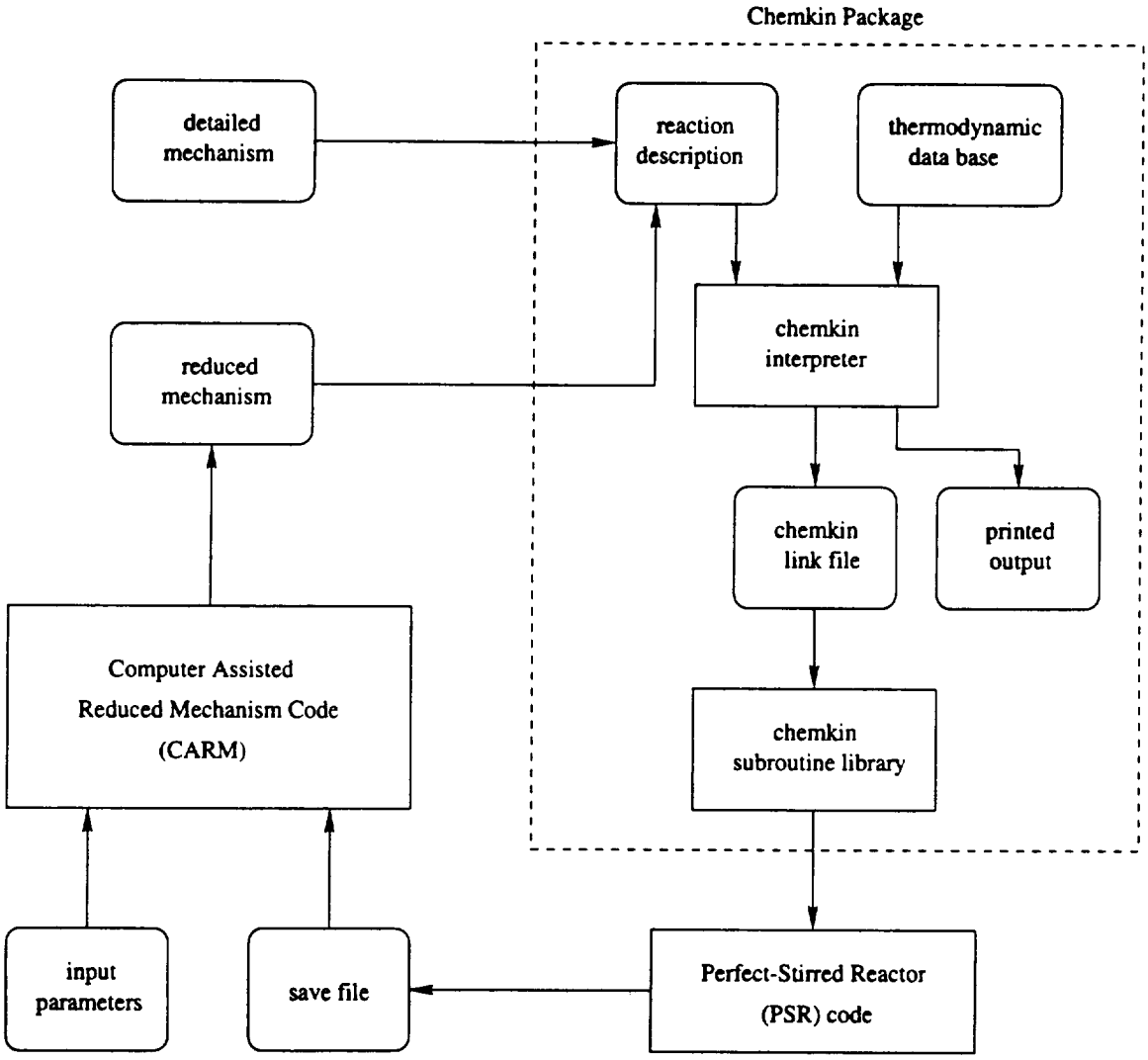

Figure 3.1: Flow chart of using the CARM code with Chemkin and PSR code to develop reduced mechanisms.

3.2 Reduced Chemistry

In the intermediate regime of the wake, the jet plume will be entrained into the wing tip vortex. To model the impact of the wing tip vortex on chemistry in this regime, large eddy simulation (LES) may be required in order to model the three-dimensional vortex properly. Solving the flow field by LES would demand significant computer time, making it impossible to incorporate a detailed chemical mechanism. A reduced mechanism capable of describing the key reactions is necessary.

3.2.1 Perfectly-Stirred Reactor (PSR) Model

Perfectly-Stirred Reactor (PSR) model will be used in the current study to develop reduced chemistry. PSR is an idealized reactor which is assumed to be homogeneous (spatially uniform) and well-mixed at the molecular scale. As shown in Figure 3.2, there is a continuous mass flow in and out of the reactor as shown in Figure 3.2. When the incoming fluids enter the reactor, it is assumed that the fluids are perfectly mixed with the fluids existed in the reactor immediately. This assumption is justified when the characteristic time of turbulent mixing at both macroscale and microscale is much smaller than that of chemistry. Consequently, the rate of chemical process is controlled solely by chemical kinetics. Turbulent effects are not accounted for in this model because of the assumption of infinitely fast mixing.

The conservation equations for reactive species at the steady state PSR is given

by

$$\dot{m}(Y_k - Y_k^*) - \dot{\omega}_k M_k V = 0, \tag{3.1}$$

and the energy conservation equation is described by

$$\dot{m} \sum_{k=1}^{KK} (Y_k h_k - Y_k^* h_k^*) + Q = 0. \tag{3.2}$$

In these two equations, Y_k is the mass fraction of the kth species (there are a total of KK species), M_k is the molecular weight of the kth species, V is the reactor volume, $\dot{m}$ is the mass flow rate through the reactor, $\dot{\omega}_k$ is the molar production rate of kth species per unit volume by chemical reactions, h_k is the specific enthalpy of the kth species, and Q is the reactor heat loss. The superscript asterisk indicates the inlet conditions. The characteristic flow time is residence time $\tau = \rho V/\dot{m}$. A hybrid Newton/time-integration algorithm is used to solve for the solution and details are described by Glarborg et al. [1986].

3.2.2 Derivation of reduced chemistry

A reduced chemistry is feasible if certain intermediate species reach the quasi-steady state when their production rates are nearly equal to their consumption rates. To identify a species in the quasi-steady state, we apply the criterion:

$$X_k \cdot \frac{|\dot{\omega}_k^p - \dot{\omega}_k^c|}{\max(|\dot{\omega}_k^p|, |\dot{\omega}_k^c|)} \ll 1, \tag{3.3}$$

where $\dot{\omega}_k^p$ and $\dot{\omega}_k^c$ are the production and consumption rate of species k,respectively, and X_k is the mole fraction of species k. It is noteworthy that due to the rapid

temperature changes in the near field of jet plume, a species that does not satisfy the quasi-steady state criterion in the near field may reach it in the far field, such as radicals OH and SO_3 in the present case. One may construct different reduced mechanisms suitable for different wake regimes.

The present development of reduced chemistry has been carried out using the PSR with an interactive Computer-Assisted Reduced Mechanism (CARM) code [Chang, 1995] for the near field jet plume. Figure 3.1 shows the flow chart of using CARM with Chemkin and PSR codes to develop a reduced mechanism.

Assuming the quasi-steady state for O, H, H_2, H_2O_2, HO_2, SO, HSO_3, NO_3, and N_2O_5 (9 species out of a total of 24 species), we obtain the following eight-step reduced mechanism:

(G-R1) $2O_3 = 3O_2$

(G-R2) $O_2 + 2OH = H_2O + O_3$

(G-R3) $NO + O_3 = O_2 + NO_2$

(G-R3) $2O_2 + NO + HNO_3 = OH + 2NO_2 + O_3$

(G-R6) $2O_2 + HNO_2 = OH + NO_2 + O_3$

(G-R5) $O_3 + SO_2 = O_2 + SO_3$

(G-R7) $H_2O + SO_3 = H_2SO_4$

(G-R8) $O_3 + CO = O_2 + CO_2$

The rates for the global reactions are expressed in terms of elementary reaction rates as:

$$\omega_{G-R1} = \omega_3 - \omega_4 + \omega_8 + \omega_{10} - \omega_{13} - \omega_{16} - \omega_{17} - \omega_{20} + \omega_{25} + \omega_{27} + \omega_{29} + \omega_{30} + \omega_{32} - \omega_{42} - \omega_{43} - \omega_{44} + \omega_{48} - \omega_{50} - \omega_{51} - \omega_{52} - \omega_{53} + \omega_{56} + \omega_{57} - \omega_{58} - \omega_{60}$$

$$\omega_{G-R2} = \omega_6 + \omega_9 + \omega_{10} - \omega_{11} + \omega_{12} + \omega_{17} + \omega_{30} - \omega_{32} + \omega_{47}$$

$$\omega_{G-R3} = \omega_{19}+\omega_{20}-\omega_{22}+\omega_{23}-\omega_{24}-2\omega_{25}-\omega_{26}-\omega_{27}-\omega_{36}+\omega_{50}+\omega_{51}+\omega_{52}+\omega_{53}-\omega_{56}-\omega_{57}$$

$$\omega_{G-R4} = \omega_{21} - \omega_{23} + \omega_{25} + \omega_{26} + \omega_{27} - \omega_{52} - \omega_{53} + \omega_{57}$$

$$\omega_{G-R5} = \omega_{28} + \omega_{29} + \omega_{30} - \omega_{51} + \omega_{56}$$

$$\omega_{G-R6} = \omega_{37} - \omega_{38} + \omega_{40} + \omega_{58}$$

$$\omega_{G-R7} = \omega_{39}$$

$$\omega_{G-R8} = \omega_{41} + \omega_{60}$$

Although the species in the quasi-steady state do not appear explicitly in the global reactions, their species concentrations are needed in computing the elementary reaction rates which contribute to the global reaction rates as shown above. The concentrations of quasi-steady state species are computed using the following expressions:

$$[HSO_3] = \frac{k_{59}[OH][SO_2]}{k_{40}[O_2]}$$

$$[NO_3] = \frac{k_{31}[O][HNO_3] + k_{55}[N_2O_5] + k_{52}[O][NO_2] + k_{23}[NO_2][O_3] + k_{32}[OH][HNO_3]}{k_{26}[O] + k_{25}[NO_2] + k_{27}[OH] + k_{54}[NO_2] + k_{21}[NO]}$$

$$[H] = \frac{k_{35}[OH][SO] + k_7[OH][O] + k_9[OH][H_2] + k_{41}[OH][CO]}{A}$$

$$A = k_{46}[H] + k_3[OH] + k_{44}[O][M] + k_{18}[H_2O_2] + k_{29}[HNO_2] + k_{17}[H_2O_2] + k_6[HO_2] + k_5[HO_2] + k_{47}[OH] + k_4[HO_2] + k_2[O_3] + k_{24}[NO_2] + k_{45}[O_2]$$

$$[O] = \frac{k_{33}[O_2][SO] + k_3[H][OH] + k_6[H][HO_2] + k_{10}[OH][OH]}{B}$$

$$B = k_{b,33}[SO_2] + k_{38}[SO_3] + k_{44}[H][M] + k_{42}[O][M] + k_{16}[H_2O_2] + k_{60}[CO] + k_{31}[HNO_3]$$
$$+ k_{28}[HNO_2] + k_{26}[NO_3] + k_{13}[HO_2] + k_{58}[SO_2] + k_1[O_3] + k_7[OH] + k_{52}[NO_2]$$
$$+ k_{50}[NO] + k_{22}[NO_2] + k_{43}[O_2]$$

$$[SO] = \frac{k_{b,33}[O][SO_2]}{k_{34}[O_3] + k_{35}[OH] + k_{36}[NO_2] + k_{33}[O_2]}$$

$$[H_2] = \frac{k_{31}[O][HNO_3] + k_{31}[O][HNO_3] + k_{31}[O][HNO_3] + k_{31}[O][HNO_3]}{k_9[OH]}$$

$$[H_2O_2] = \frac{k_{49}[HO_2][HO_2] + k_{15}[HO_2][HO_2] + k_{48}[OH][OH]}{k_{18}[H] + k_{16}[O] + k_{17}[H] + k_{12}[OH]}$$

$$[HO_2] = \frac{A}{B}$$

$$A = k_{18}[H][H_2O_2] + k_{16}[O][H_2O_2] + k_{27}[OH][NO_3] + k_{12}[OH][H_2O_2] + k_8[OH][O_3]$$
$$+ k_{40}[O_2][HSO_3] + k_{45}[H][O_2]$$

$$B = k_6[H] + k_5[H] + k_4[H] + k_{13}[O] + k_{49}[HO_2] + k_{15}[HO_2] + k_{14}[O_3] + k_{11}[OH]$$
$$+ k_{20}[NO]$$

$$[N_2O_5] = \frac{k_{54}[NO_2][NO_3]}{k_{55}}$$

Consequently, the concentrations of the quasi-steady state species can be expressed in terms of major species by a set of algebraic equations. This saves computing time as there is no need to solve ordinary differential equations (ODE) for these species. In addition, the stiffness of the ODEs with the global chemistry derived is reduced since the species in the quasi-steady state are often fast-reacting. The Newton iteration

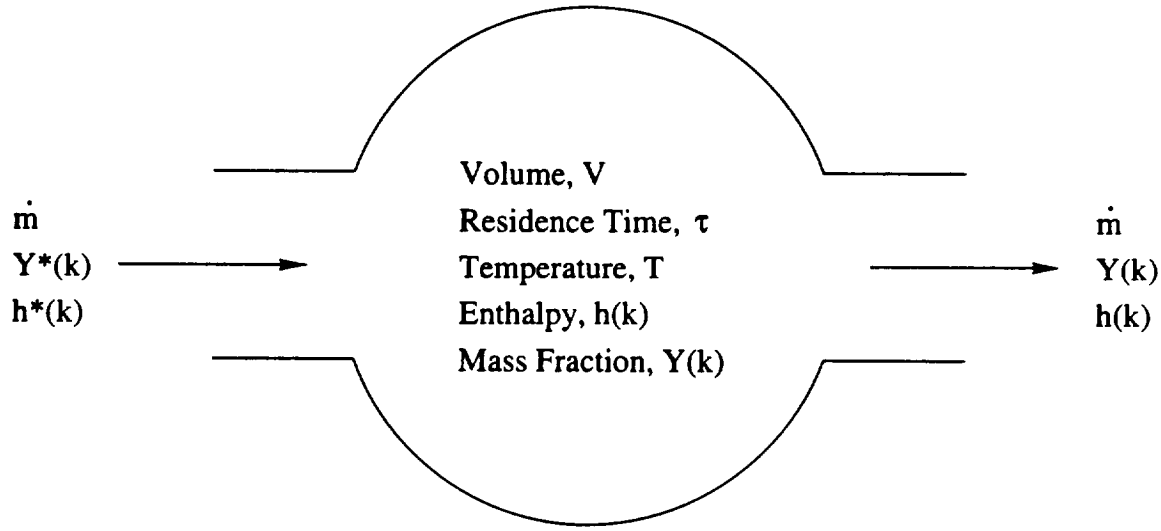

Figure 3.2: Schematic of a Perfectly-Stirred Reactor (PSR). The characteristics of the reactor is shown, where $\dot{m}$ is the mass flow rate, k denotes species k, and superscript * indicates the inlet condition. The key parameter is the residence time, $\tau = \rho V/\dot{m}$.

is used to solve the coupled nonlinear algebraic equations for concentrations of the quasi-steady state species.

3.3 Sensitivity Analysis

Sensitivity information is useful for identifying the controlling chemical steps that have strong influence on the creation/destruction of a certain species. The sensitivity coefficients are displayed as

$$\beta_{i,k} = \frac{\partial X_k}{\partial A_i}, \tag{3.4}$$

where $\beta_{i,k}$ is the sensitivity of change in the mole fraction of the kth species, X_k, due to a small change in temperature-independent pre-factor, A_i, of the i-th reaction rate $k_i = A_i T^n \exp(-E_a/T)$.

The transient well-mixed reactor (WMR) model enables one to study the time evolution of chemical kinetics of the engine exhaust gas subject to injection of ambient air. A WMR model is employed here to investigate the sensitivity of species with respect to reaction step. A schematic diagram for the WMR is sketched in Figure 3.3. Similar to the PSR, a global residence time can be defined as

$$\tau_R = \frac{m_R}{\dot{m}_a}, \tag{3.5}$$

where m_R is the mass of gas inside the reactor and $\dot{m}_a$ is the mass entrainment rate. Using τ_R as a parameter, conservation equations of mass, species, and energy can be written as

$$\frac{dm_R}{dt} = \frac{m_R}{\tau_R} \tag{3.6}$$

$$\frac{dY_{Rj}}{dt} = \frac{1}{\tau_R}(Y_{a,j} - Y_{R,j}) + \frac{\dot{\omega}_{Rj}}{\rho_R} \cdot M_j, \quad j = 1, \cdots, K \tag{3.7}$$

$$\frac{dT_R}{dt} = \frac{1}{\bar{c}_{pR}\tau_R} \sum_{j=1}^{N} [(h_{a,j} - h_{R,j})Y_{a,j}] - \sum_{j=1}^{K} \frac{\dot{\omega}_{Rj} h_{Rj} M_j}{\rho_R \bar{c}_{PR}} - \frac{\dot{Q}_{loss}}{\bar{c}_{pR} m_R}, \tag{3.8}$$

where the subscript R represents quantities inside the reactor and those entrained are denoted by the subscript a. If the temperature is fixed, the WMR model is similar to the Lagrangian box model [Miake-Lye et al., 1993b; Karol et al., 1994; Kärcher, 1995] when the following relation is used to bridge the two models

$$\frac{\dot{m}_a}{m_R} = \frac{K(t)}{A}. \tag{3.9}$$

A is the cross-section area of a plume and K(t) is the growth rate of the plume

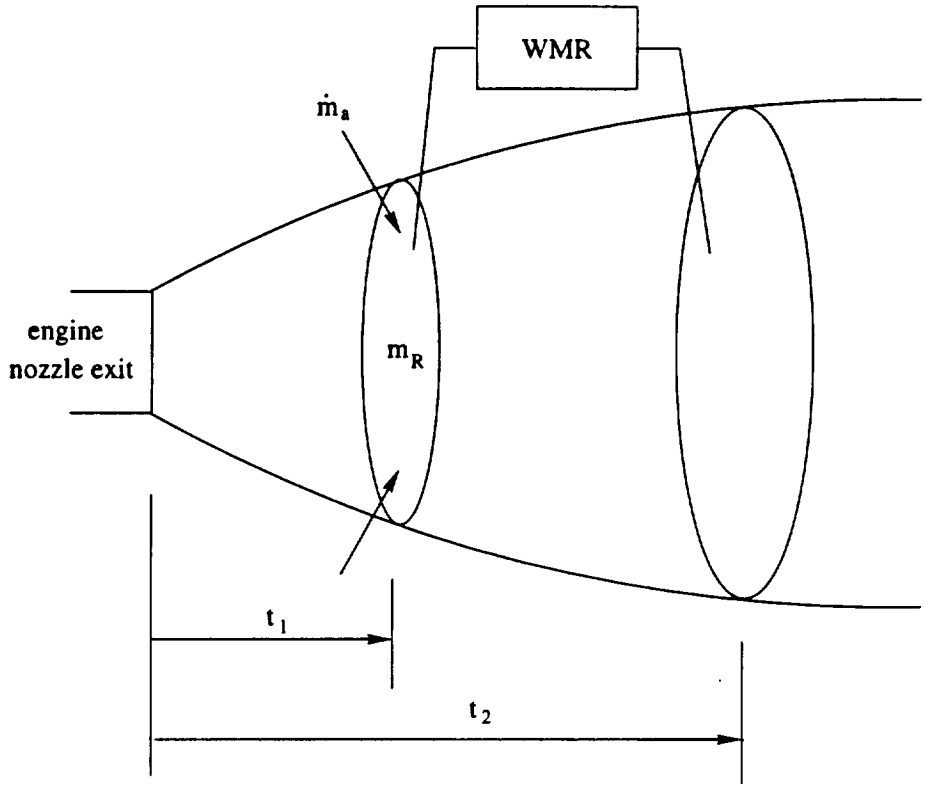

Figure 3.3: Schematic diagram of a transient well-stirred reactor (WMR) showing ambient air entrained into the reactor with a rate of $\dot{m}_a$. m_R is the mass of gas in the reactor, and it increases with time.

cross-section area in Lagrangian box model equation

$$\frac{dC_i}{dt} = P_i - L_i - \frac{K(t)}{A}(C_i - C_i^a) + R_i, \tag{3.10}$$

where C_i and C_i^a are the ith species concentrations inside the box and in the air, respectively, P_i and L_i are the production and destruction rate by chemical reactions, and R_i is the source or sink due to other mechanisms.

3.4 Results and Discussions

The WMR model is used to provide sensitivity information of a certain species with respect to various reactions. The entrainment rate of ambient air is prescribed from centerline mass increment rate predicted by the pdf jet plume model. Therefore, the sensitivity information is informative for understanding qualitatively the centerline species distribution in a jet plume. Figure 3.4 shows the computed sensitivities of hydroxyl radical, OH, with respect to various reaction steps. The most important chemistry for the OH radical is its reaction with NO via the three-body step (R51) $OH + NO + M \rightarrow HNO_2 + M$. The generated HNO_2 then further reacts with OH to produce NO_2 by step (R30) $HNO_2 + OH \rightarrow H_2O + NO_2$. The self combination reaction step (R10) $OH + OH \rightarrow H_2O + O$ is the next important pathway contributing to the OH consumption in the early jet regime when the OH level is high. (R41) $CO + OH \rightarrow CO_2 + H$ and (R48) $OH + OH + M \rightarrow H_2O_2 + M$ also play important roles in this early stage. The magnitudes of the OH sensitivity coefficient start to decline when the OH abundance begins to decrease dramatically. They become very small when OH decreases to a very low level. Compared to the major OH consumption pathways mentioned above, a very small amount of OH is consumed by SO_2 via step (R59) $SO_2 + OH + M \rightarrow H_2SO_3 + M$, which has a very small magnitude of OH sensitivity. This explains why the conversion rate of SO_2 to H_2SO_4 is less than 1-2 % as will be shown later in this section. A small amount of OH can be generated through (R20) $NO + HO_2 \rightarrow NO_2 + OH$ with minor contributions from (R24)

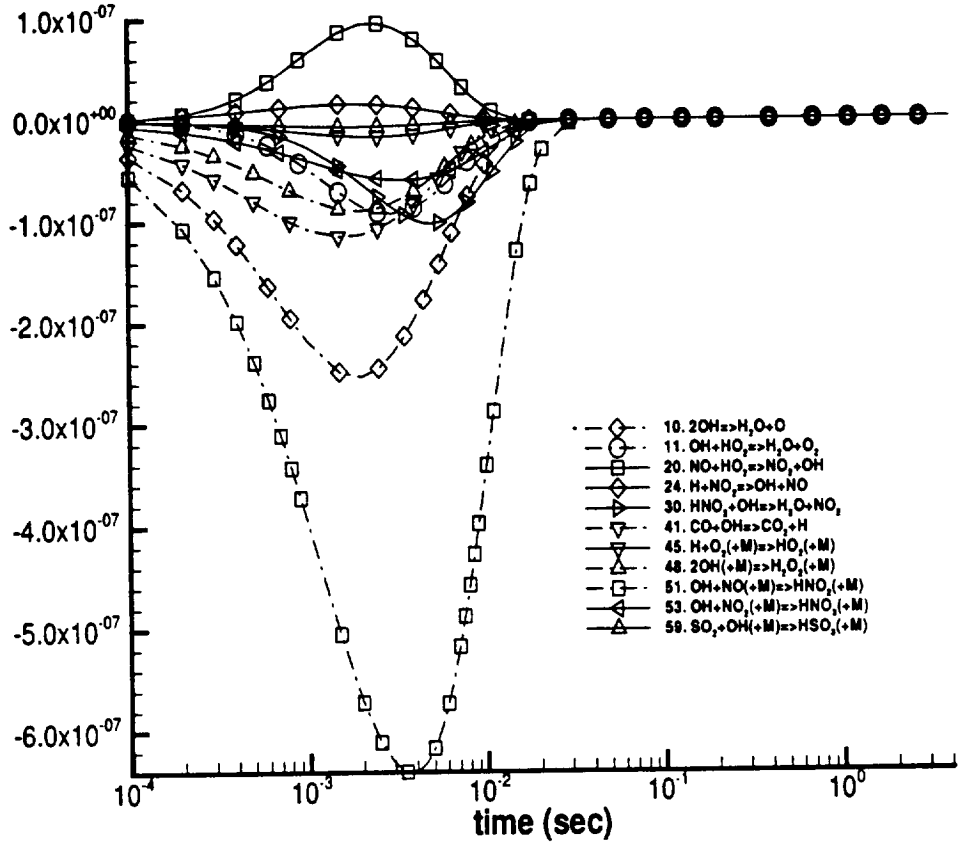

Figure 3.4: Sensitivities of OH to reaction steps predicted by WMR model.

$H + NO_2 \rightarrow OH + NO$.

Figure 3.5 shows the sensitivities of NO with respect to different steps. As revealed in the figure, NO is consumed mainly by its conversion to HNO_3 via the three-body reaction step (R51) $OH + NO + M \rightarrow HNO_2 + M$. The next important reaction chain influencing NO consumption is step (R41) $CO + OH \rightarrow CO_2 + H$ followed by step (R45) $H + O_2 + M \rightarrow HO_2 + M$. These two steps generate HO_2 which reacts with NO via step (R20) $HO_2 + NO \rightarrow NO_2 + OH$. Reaction (R43) $O + O_2 \rightarrow O_3$ and the

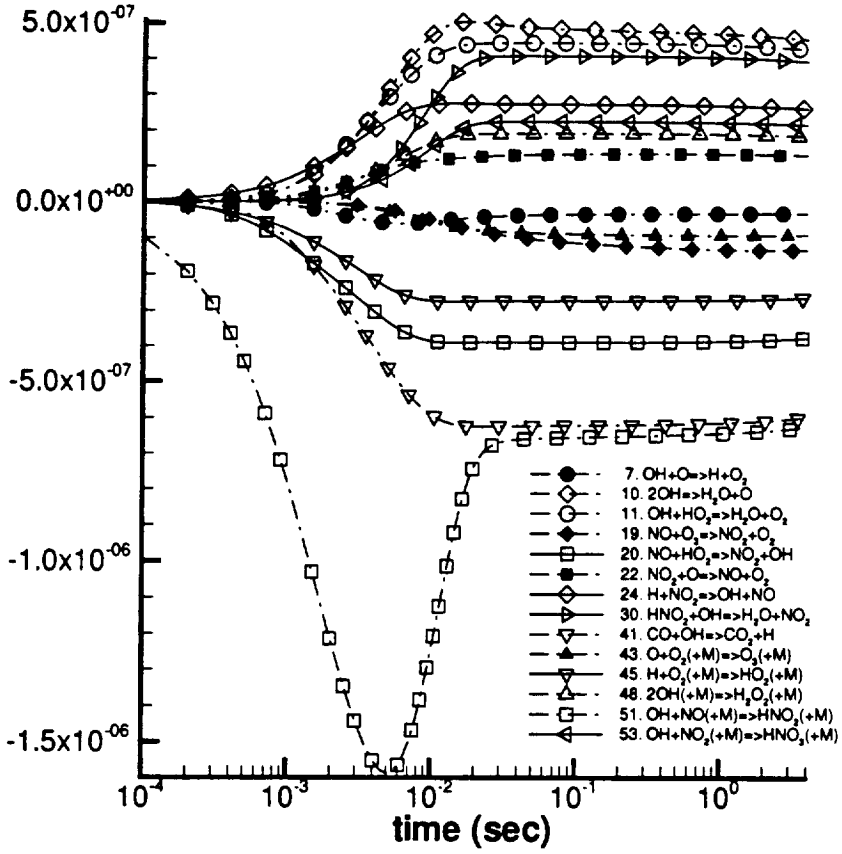

Figure 3.5: Sensitivities of NO to reaction steps predicted by WMR model.

further reaction of O_3 with NO via (R19) $NO + O_3 \rightarrow NO_2 + O_2$ also contribute to NO reduction. Steps (R10) $OH + OH \rightarrow H_2O + O$, (R11) $OH + HO_2 \rightarrow H_2O + O_2$, and (R30) $HNO_2 + OH \rightarrow H_2O + NO_2$ are the most important reactions for NO production. These reactions compete with the most dominant NO destruction step (R51) for OH.

Figure 3.6 shows the computed sensitivity results of NO_2. The most dominant reaction path for NO_2 production is through step (R41) $CO + OH \rightarrow CO_2 + H$, with

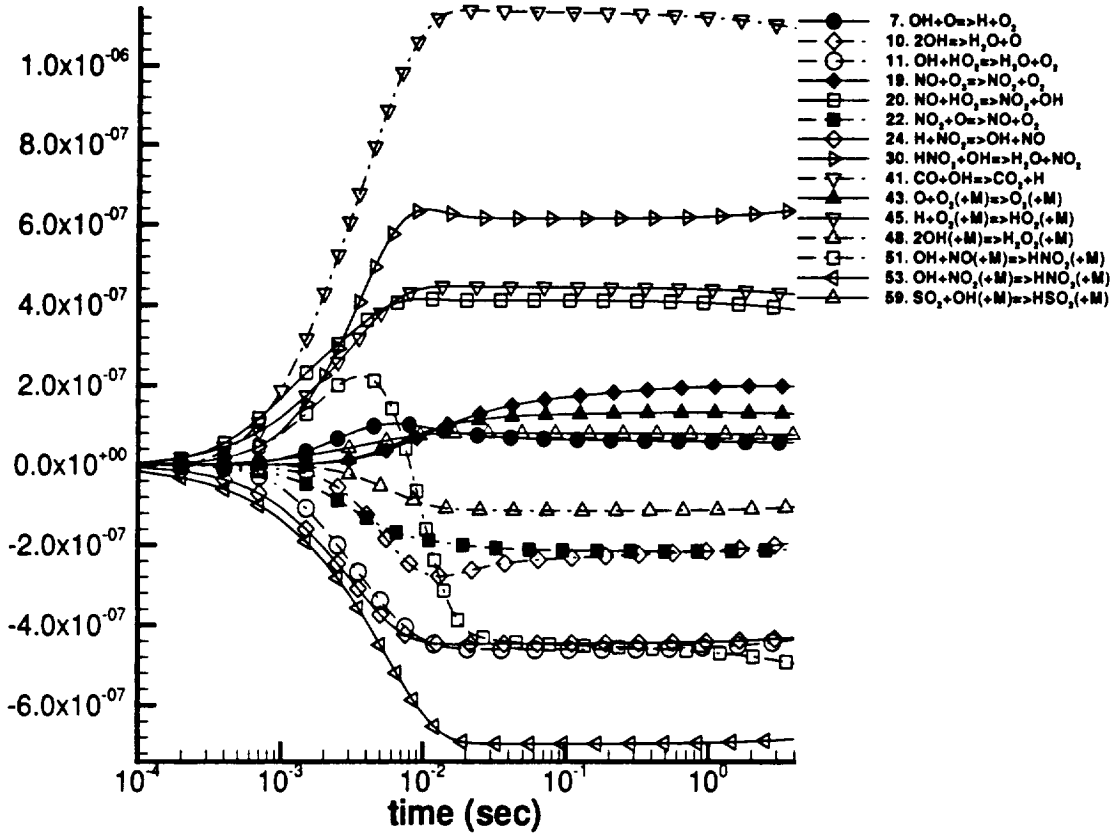

Figure 3.6: Sensitivities of NO_2 to reaction steps predicted by WMR model.

subsequent reaction (R45) $H + O_2 + M \rightarrow HO_2 + M$ and further reaction (R20) $NO + HO_2 \rightarrow NO_2 + OH$. NO_2 is consumed mainly by the three-body reaction (R53) $NO_2 + OH + M \rightarrow HNO_3 + M$.

Figure 3.7 shows the sensitivity of ozone, O_3, with respect to various reaction steps. O_3 is mainly produced by step (R43) $O + O_2 + M \rightarrow O_3 + M$ and the O atom is supplied via reaction (R10) $OH + OH \rightarrow H_2O + O$. As OH is depleted mainly due to its reactions with NO, these two reactions become less important. O_3 is consumed

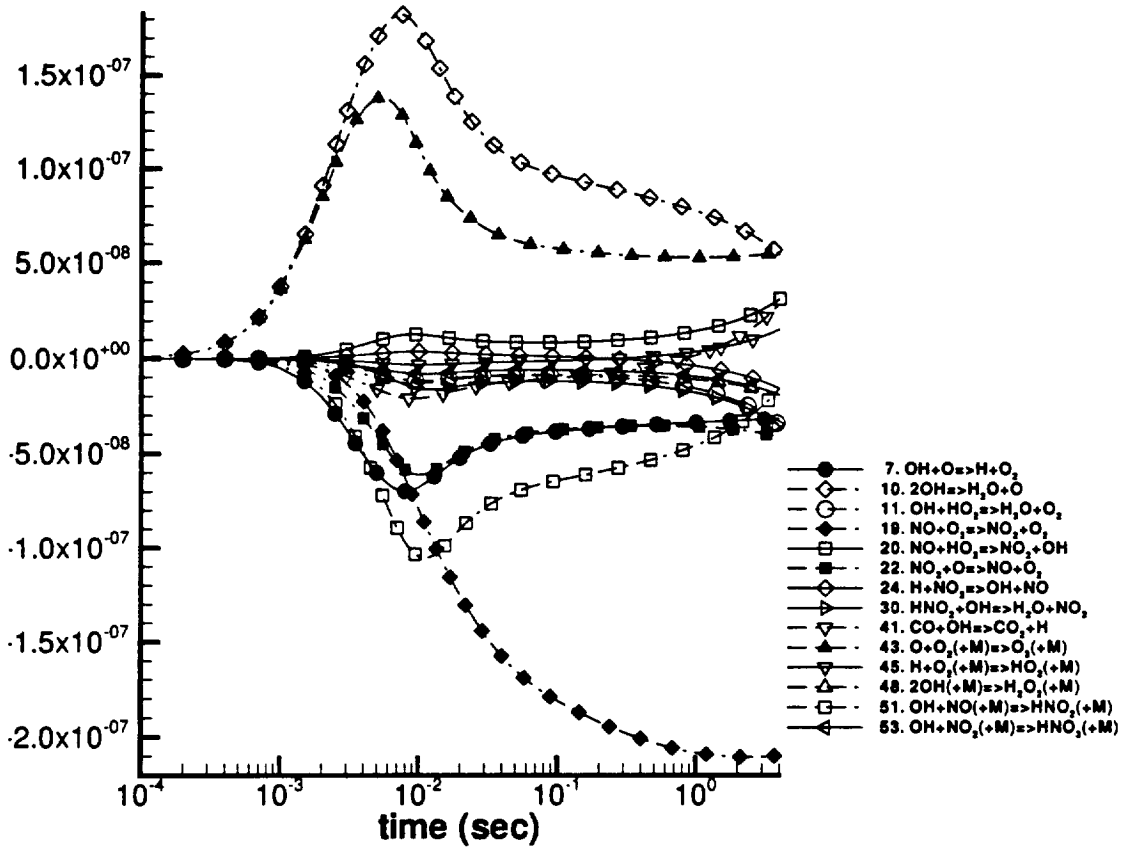

Figure 3.7: Sensitivities of O_3 to reaction steps predicted by WMR model.

mainly by (R19) NO + O_3 → NO_2 + O_2. As more O_3 is entrained into the plume with time, reaction (R19) becomes increasingly important.

Figure 3.8 shows the sensitivity of H_2SO_4 with respect to different steps. The buildup of H_2SO_4 is initiated by (R59) SO_2 + OH + M → H_2SO_3 + M, and the product HSO_3 further reacts with O_2 via fast reaction (R40) HSO_3 + O_2 → HO_2 + SO_3 (not shown on the plot due to the small H_2SO_4 sensitivity to this reaction). Finally H_2SO_4 is generated through (R39) SO_3 + H_2O → H_2SO_4. Since OH is consumed

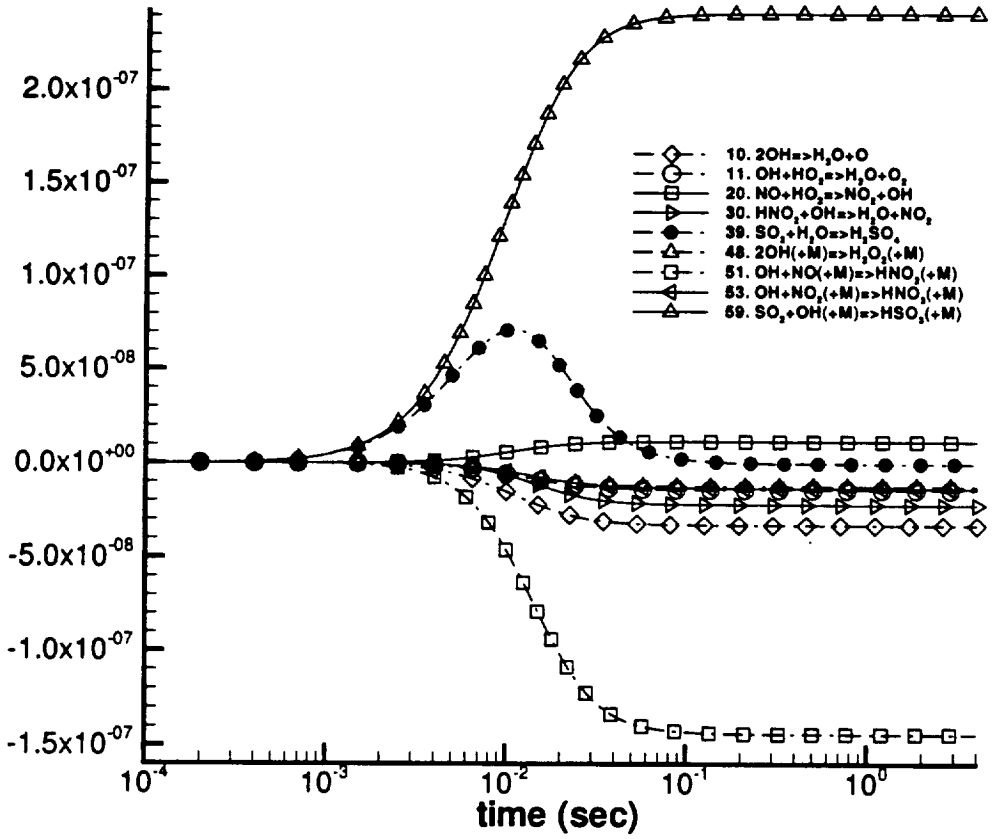

Figure 3.8: Sensitivities of H_2SO_4 to reaction steps predicted by WMR model.

mainly by NO and NO_2 via three-body reactions (R51) and (R53) and by self consumption reactions (R10) and (R48) as depicted in Figure 3.4, the conversion of SO_2 to H_2SO_4 is expected to be low. This low conversion fraction will be demonstrated later in this section from the distribution of major sulfur species.

Figure 3.9 to 3.11 depict the major species evolution along the plume axis. A second x-axis is also plotted on the top of these figures to show the corresponding plume age. The centerline evolution of major nitrogen species is shown in Figure 3.9.

At about 5 m past the nozzle exit plane, the turbulent stirring (macroscale mixing) becomes important and the corresponding plume age is about 3 ms. The primary exhaust products NO and NO_2 stay nearly constant up to this point and then decrease slowly. In the early jet regime, small amounts of NO and NO_2 are oxidized by OH (not discernible on this logarithmic scale) via three-body reactions (R51) and (R53). However, these reactions lead to significant amounts of nitrous acid, HNO_2, and nitric acid, HNO_3, as compared to their background abundances. A small fraction of HNO_2 is consumed through (R30) when the OH level is high. After OH becomes depleted (compare Figure 3.11), the chemical buildup of HNO_2 and HNO_3 ceases and these secondary exhaust products are diluted like tracers, similar to the fate of NO_x in the late jet regime. At later stages of plume dispersion these acids may either become photolyzed under daytime conditions, or depleted by heterogeneous removal processes.

In the early jet regime, the nitrate radicals, NO_3, are generated via (R52) $NO_2 + O + M \rightarrow NO_3 + M$ and (R32) $HNO_3 + OH \rightarrow H_2O + NO_3$. The chemical production of NO_3 ceases as soon as O and OH become depleted and its further evolution is governed by plume dilution. In the early jet phase, dinitrogen pentoxide, N_2O_5, is produced via (R54) $NO_2 + NO_3 + M \rightarrow N_2O_5 + M$ in contrast to the strong thermal decay reaction (R55) $N_2O_5 + M \rightarrow NO_2 + NO_3 + M$. Hereafter the N_2O_5 abundance increases quickly by entrainment, and at the end of jet regime, N_2O_5 already attains its ambient level. The NO_3 level at the end of the jet regime is much lower compared

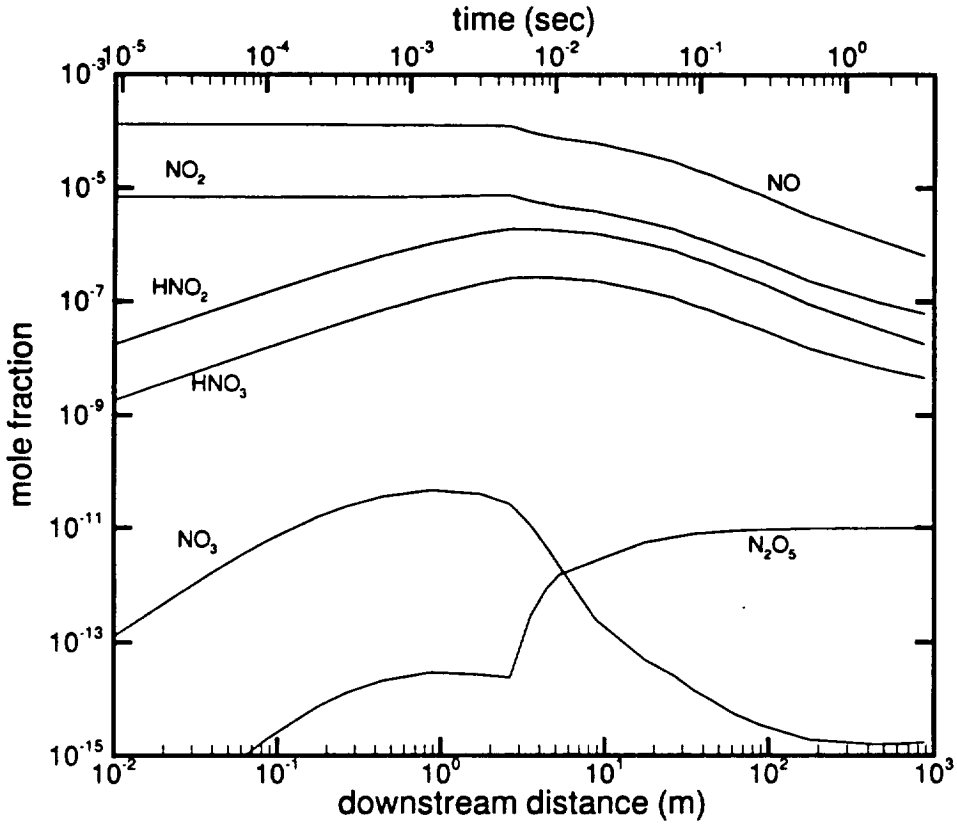

Figure 3.9: Centerline evolution of mole fractions of major nitrogen species.

to its background abundance due to step (R54).

In the the jet plume, the ratio of NO_x (= NO + NO_2) to NO_y (= NO_x + HNO_2 + HNO_3 + $2N_2O_5$), assumed to be unity at the nozzle exit plane, decreases slightly as NO_y is built up. $[NO_x]/[NO_y]$ is found to be approximately 0.975 at the end of jet regime.

Figure 3.10 shows the centerline evolution of major sulfur species. The sulfur reaction chain is initiated by oxidation of the exhaust SO_2 by OH via (R59)

$SO_2 + OH + M \rightarrow HSO_3 + M$ which immediately builds up HSO_3. This is followed by fast reaction (R40) $HSO_3 + O_2 \rightarrow HO_2 + SO_3$, in which SO_3 is generated. Sulfuric acid, H_2SO_4, is then generated through (R39) $SO_3 + H_2O \rightarrow H_2SO_4$. Reaction (R59) is the rate-limiting step in this three-reaction sequence in producing H_2SO_4. Consequently, SO_2 oxidation is indirectly coupled with NO_y, CO, and HO_x reactions that compete for OH. The maximum conversion of SO_2 to H_2SO_4, $\frac{(X_{H_2SO_4})_{max}}{(X_{SO_2})_0}$ is less than 1%. After OH is depleted, the SO_3 concentration reaches its maximum and then decreases due to plume dilution. H_2SO_4 exhibits a similar evolution as SO_3, except that it is shifted to slightly downstream distance. H_2SO_4 losses due to binary H_2SO_4-H_2O nucleation is not considered at this time. It will be discussed in detail later in Chapter 4.

Figure 3.11 depicts the evolution of major oxygen and hydrogen species along the plume axis versus downstream distance. Hydroxyl radical OH, being the most abundant primary HO_x exhaust product, is responsible for the rapid production of other radicals. In the early jet regime, O is produced via (R10) $OH + OH \rightarrow O + H_2O$, which further produces ozone through the three body reaction (R43) $O + O_2 + M \rightarrow O_3 + M$. In the late jet regime, mixing becomes important and the further increase of the O_3 concentration is due to the entrainment of ambient ozone. However, as long as the NO level stays high, ozone is continuously consumed due to its reaction with NO via (R19) $NO + O_3 \rightarrow NO_2 + O_2$ and stays below its ambient level within the jet plume. The self-reaction (R48) $OH + OH + M \rightarrow H_2O_2 + M$ is

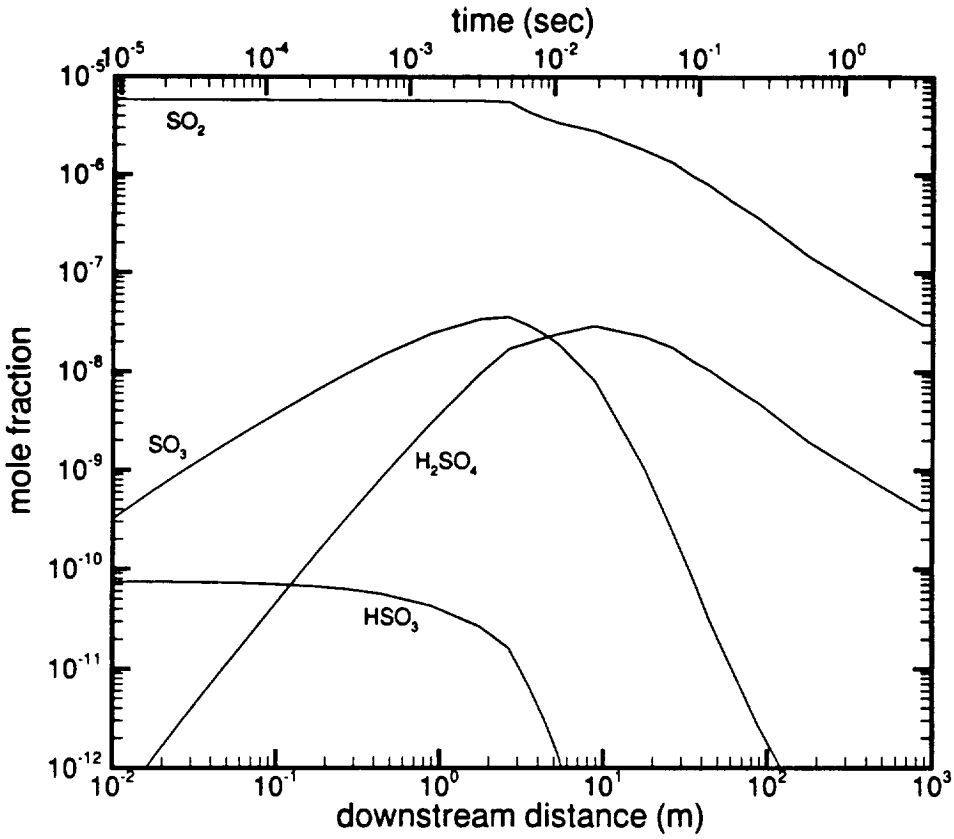

Figure 3.10: Centerline evolution of mole fractions of major sulfur species.

the most important pathway for the production of hydrogen peroxide, H_2O_2, leading to a maximum abundance around the point of the strongest mixing. In the late jet regime, H_2O_2 decreases due to plume dilution. On longer timescales H_2O_2 may either act as a HO_x sink through heterogeneous removal or as a slow source for regeneration of OH by photolysis.

The buildup of hydrogen atoms H in the early jet regime is initiated by reaction (R41) $CO + OH \rightarrow H + CO_2$. H further reacts with O_2 via (R45) $H + O_2 + M \rightarrow$

HO_2 + M which is the major production pathway of the hydroperoxy radical, HO_2. Hydrogen molecules H_2 are subsequently produced via (R3) H + OH $\rightarrow$ O + H_2 and (R5) HO_2 + H $\rightarrow$ H_2 + O_2, and by (R46) H + H + M $\rightarrow$ H_2 + M when the H level is high.

It is observed in Figure 3.11 that the OH concentration dramatically decreases in the intermediate stage of jet mixing between 1 and 10 m past the nozzle exit. As depicted from the OH sensitivity coefficients in Figure 3.4, the rapid removal of OH is mainly due to its reaction with NO and NO_2 via (R51) and (R53)and partially due to self reactions (R10) and (R48). The reactions that sustain the O and H concentrations in the isothermal jet core are quickly reduced due to the depletion of OH radical. Hence the O and H atoms quickly decrease to negligible levels and only slowly recover in later stages of plume dispersion due to OH regeneration through photolysis. OH and HO_2 abundances sharply bend in the decaying jet flow field, which is due to the entrainment of HO_2 from the ambient air and its quick conversion to OH by reaction with NO through (R20) NO + HO_2 $\rightarrow$ NO_2 + OH.

Figure 3.12 shows the centerline temperature and major species distributions obtained with the detailed and the eight-step reduced mechanisms. It is assumed that the fluids in each computational grid are well-mixed. The centerline temperature stays nearly constant up to the point where the ambient air begins to mix with the centerline gaseous species. Temperature decreases rapidly and reaches near ambient level at the end of jet plume. Predictions of the temperature and major species evo-

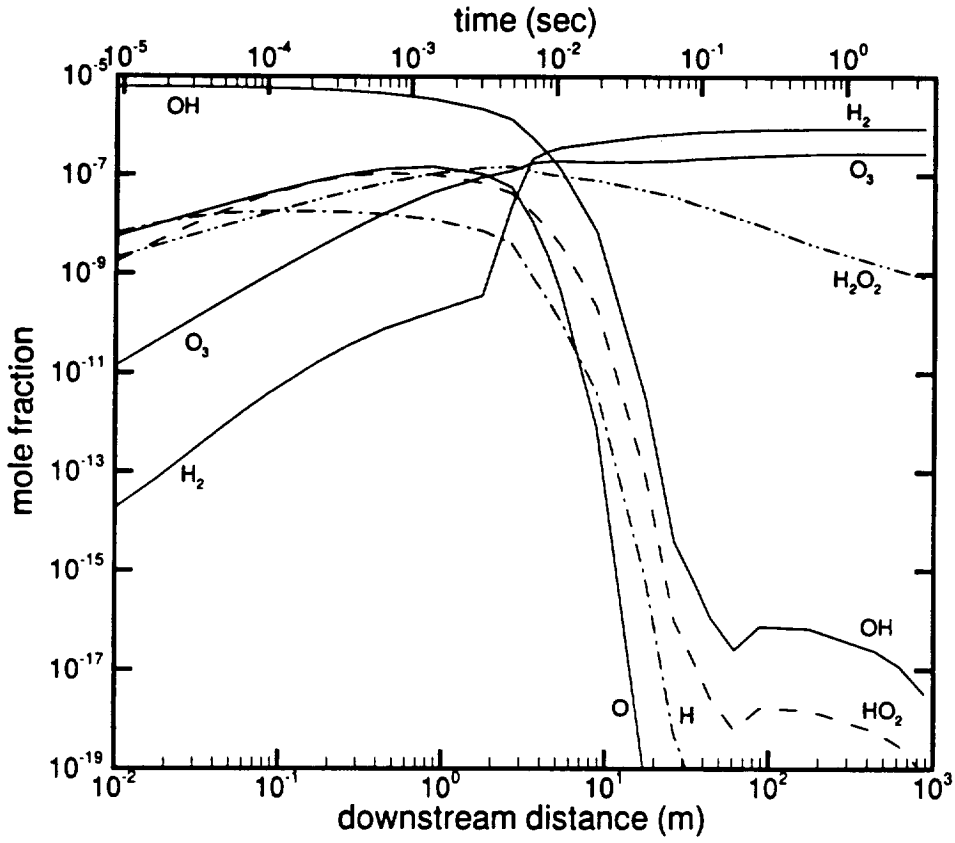

Figure 3.11: Centerline evolution of mole fractions of major hydrogen and oxygen species.

lutions by the eight-step reduced mechanism is shown to be in excellent agreement with those by the detailed mechanism.

Figure 3.13 shows the results obtained under the same conditions as in Figure 3.12 but with the subgrid mixing accounted for by the modified Curl's mixing model. When the interaction of subgrid mixing with chemistry is considered, the eight-step reduced mechanism still gives results that are in good agreement with those predicted by the detailed mechanism. Simulation with the reduced mechanism is about 3.4 times

faster in computer CPU time compared to the computation with the detailed one for the near-field jet plume.

Figure 3.14 compares the centerline major species distributions with and without the interaction of subgrid turbulent mixing and chemistry. The differences between these two profiles are relatively minor. The predicted results with the subgrid mixing modeled by the modified Curl's mixing model show slightly lower levels of species concentration compared to the results with the subgrid well-mixed.

There have been no measurements of major species concentrations carried out in the jet plume regime. Fahey et al. [1995] carried the in-situ measurement with an ER 2 research aircraft flying in the lower stratosphere during the NASA Stratospheric Photochemistry, Aerosol and Dynamics Expedition (SPADE) program. To compare our model predictions with their measured values, we perform calculations for an ER 2 aircraft with flight conditions and initial exhaust properties given by Anderson et al.[1996]. Figure 3.15 compares the ratios of various chemical species concentrations above the ambient background levels for an ER 2 aircraft from the present predictions at 1 km to UNIWAKE results at 20.2 km by Anderson et al. [1996] and to the measured values at 126.0 km by Fahey et al. [1995]. The present calculations present results at a much smaller distance downstream compared to the UNIWAKE results and the SPADE data. However, since chemical kinetics is negligible after 100 m downstream and the evolution of species concentration is due almost entirely to mixing, the ratios of $\Delta NO_2/\Delta NO$, $\Delta NO_x/\Delta NO_y$, and $\Delta NO_y/\Delta CO_2$ are gen-

erally independent of the dilution level and thus tend to stay constant downstream. The comparison shows good agreement among different predictions and the SPADE measurements.

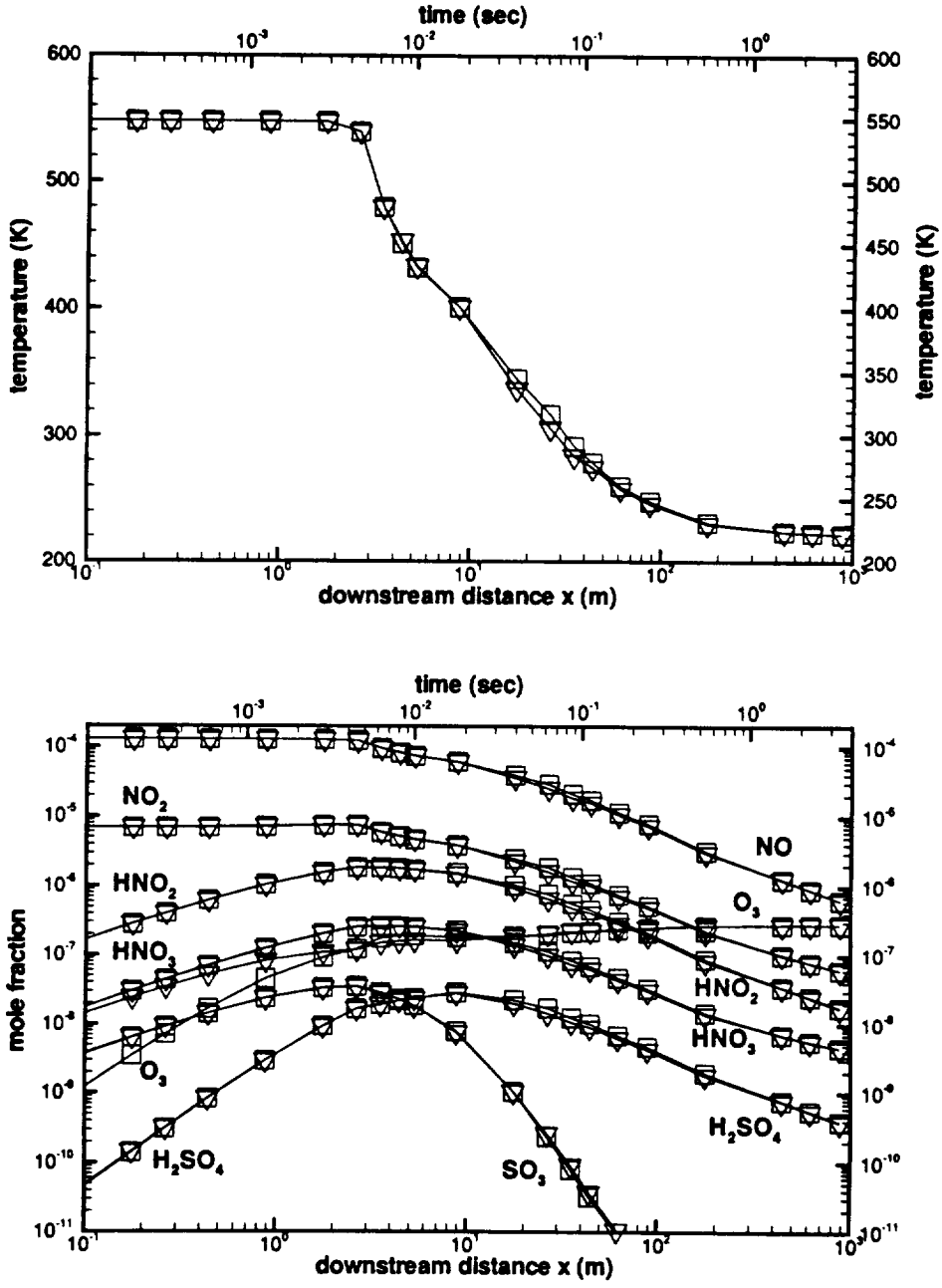

Figure 3.12: Centerline temperature and major species distributions with the detailed (lines with squares) and the reduced (lines with reversed triangles) mechanisms. Subgrid is assumed to be well-mixed.

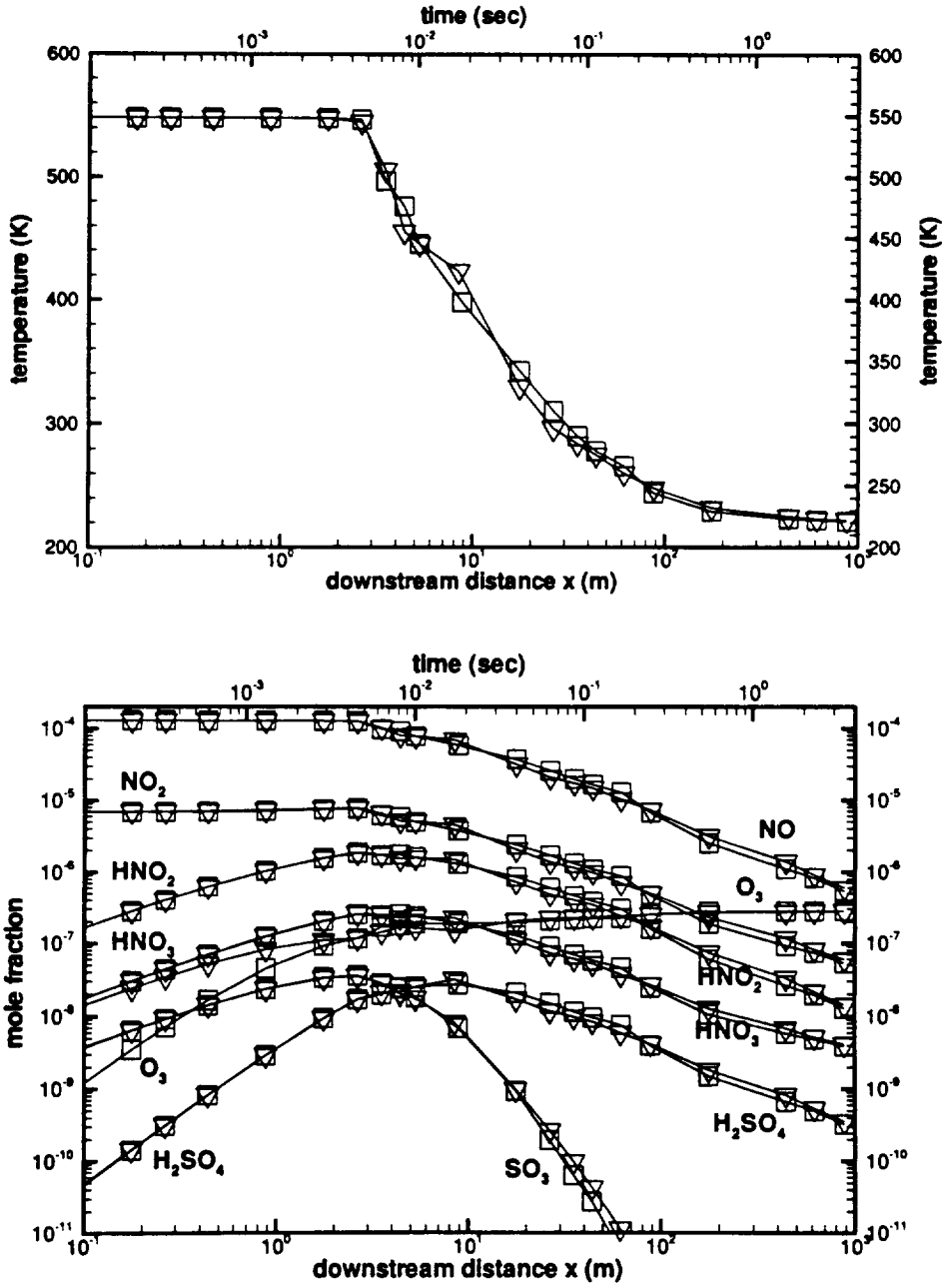

Figure 3.13: Centerline temperature and major species distributions with the detailed (lines with squares) and the reduced (lines with reversed triangles) mechanisms. Subgrid mixing is modeled by modified Curl's mixing model.

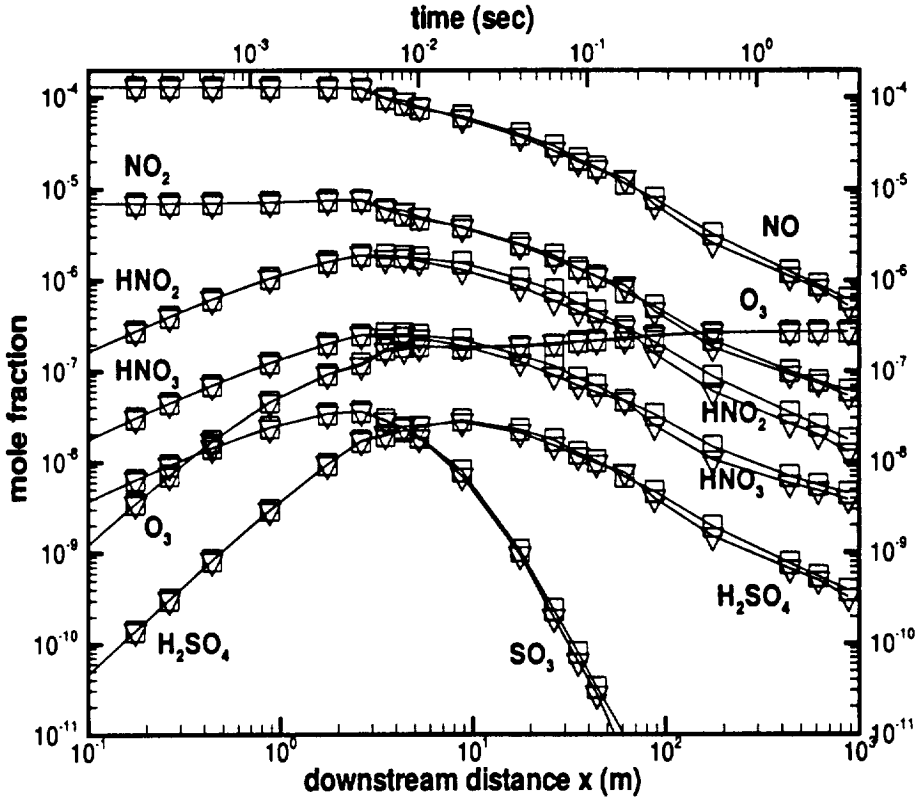

Figure 3.14: Centerline major species distribution by pdf jet simulation, with different treatment of subgrid mixing model. Lines with squares are results with subgrid mixing well-mixed, and lines with reversed triangles are results with subgrid mixing modeled by modified Curl's mixing model.

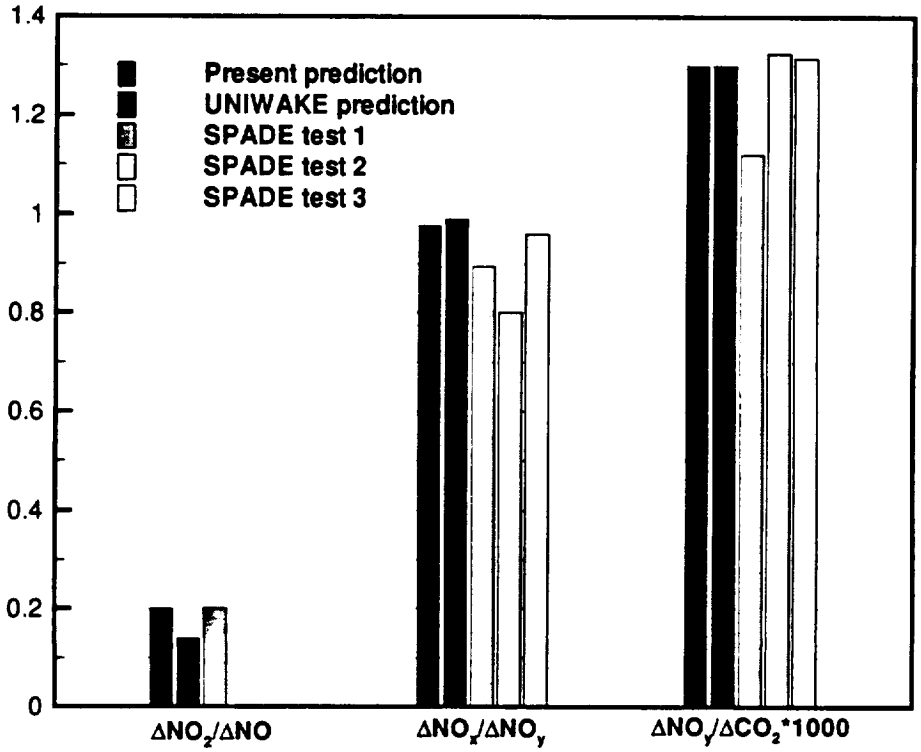

Figure 3.15: Comparison of the ratios of various chemical species concentrations over the ambient background levels from the present predictions at 1 km to UNIWAKE results at 20.2 km and to measured values at 126.0 km.

Chapter 4

Aerosol Dynamics

4.1 Introduction

The emission and formation of new aerosols caused by subsonic aircrafts and their subsequent evolution in the upper troposphere and lower stratosphere have become an important research issue. Global impact of fleets of aircraft depend on how much H_2SO_4-H_2O aerosols are generated in the near-field aircraft exhaust [Weisenstein, 1996]. In this regime, not only major gas-phase chemical reactions take place, but also a large number of small-sized volatile H_2SO_4-H_2O aerosols are generated due to binary homogeneous nucleation. Soot activation as water condensation nuclei also occurs in this regime. Preliminary analysis of data collected under the SUCCESS (SUbsonic Aircraft: Contrail and Cloud Effects Special Studies) program [NASA, 1996] has indicated a high level of small volatile aerosols whose number density varies

with the mass loading of fuel sulfur [Ballenthin et al., 1996].

In-flight field measurements of aerosols by the instrumentation aboard the ER2 aircraft in plume encounters of the Concorde wake [Fahey et al., 1995] have reported between 12% and 45% conversion of fuel sulfur to sulfuric acid (assuming the diameter of sulfuric acid aerosols is 10 nm) after approximately 16 minutes at 16.2 km from the nozzle exit plane. Ground-based measurement indicates sulfur oxidation greater than 0.4% at the early plume stage [Frenzel and Arnold, 1994]. Modeling studies of aircraft plume chemistry have predicted that the conversion of fuel sulfur to sulfuric acid is limited to 0.5%–2% [Kärcher et al., 1996a, Brown et al., 1996a, Wang and Chen, 1997]. These numerical estimates are based on the assumption that fuel sulfur is emitted from the engine as SO_2 which is subsequently converted to sulfuric acid by gas phase reactions in the exhaust plume. The discrepancy seen between the experimental estimate by Fahey et al. [1995] and the numerical results raises concern on the validity of the above assumption. Hence, field measurements of sulfur speciation at the nozzle exit plane are suggested to resolve the disagreement.

Using numerical modeling, Brown et al. [1996b] have recently estimated the extent of fuel sulfur converted to volatile aerosol precursors during combustion and the subsequent turbine flow for the subsonic ATTAS and the supersonic Concord aircraft engines. The results of their analysis suggested that the conversion rate of fuel sulfur to S(VI)(SO_3 and H_2SO_4) is between 2% and 10% in the engine. The large uncertainty in the estimated values is due to the limitations of the models used in

that study to characterize the oxidative pyrolysis of typical jet engine fuels and the three-dimensional fluid dynamics for real combustors and turbines. The lack of high temperature kinetic data for important sulfur oxidation reactions also contributes to the uncertainty.

The laboratory studies by Wyslouzil et al. [1994] with samples of carbon black have indicated that carbon is hydrophobic. This result suggests that soot particulates emitted in aircraft exhausts may be poor condensation nuclei in the absence of activating precursors. Both Wyslouzil et al. [1994] and Rogaski et al. [1996] have observed in their experiments a substantial increase in water uptake on carbon in the presence of sulfuric acid. Therefore, the potential role of sulfuric acid formed through sulfur oxidation is currently of particular interest to soot activation.

In this chapter, we will consider the microphysical processes including binary homogeneous nucleation, aerosol coagulation, adsorption, and heteromolecular condensation. These processes are coupled with gas phase chemical reactions and turbulent mixing in an axisymmetric flow. Compared to the modeling work of Brown et al.'s [1996a; 1996c], the present work assesses the impact of SO_3 emissions on the formation and evolution of aerosols and studies the condensation processes with a kinetic model. Kärcher [1997] studied the near-field microphysical processes with a box model, in which the aerosol processes were not coupled to the flow field and no spatial resolution was offered. The mixing and cooling rates along the plume trajectory were chosen to represent the evolution of the bulk of the exhaust. Currently, there are only few

aerosol modules implemented in global chemistry models [Bekki and Pyle, 1992; Tie et al., 1994; Weisenstein et al., 1997]. However, the formulations of aerosol microphysics used in global models are too simplified to be applied to near-field aircraft-related aerosol simulations.

4.2 Aerosol Model Structure

The time evolution of number density due to homogeneous nucleation, coagulation, and condensation can be described by the following equations

$$\frac{dN_{v,i}}{dt} = J_{hom} + (\frac{dN_{v,i}}{dt})_{coag} + (\frac{dN_{v,i}}{dt})_{cond} \tag{4.1}$$

$$\frac{dN_{c,i}}{dt} = (\frac{dN_{c,i}}{dt})_{coag} + (\frac{dN_{c,i}}{dt})_{cond}, \tag{4.2}$$

where N_i is particle number density representing particle number in size bin i per cm^3 of air with the unit of $\#/cm^3$, and J denotes the nucleation rate. The subscript v indicates volatile H_2SO_4-H_2O aerosols, and the subscript c indicates either initially emitted bare soot particles or later evolved soot-cored droplets. It is computationally efficient to combine the number density of bare soot and that of soot coated with H_2SO_4-H_2O as one variable, which will be justified in section 4.5. Given the number density N, the mixing ratio x can be computed by $x = N/N_a$, where N_a is the number density of air ($N_a = P/(k_BT)$ where k_B is Boltzmann's constant). Details of each term in equations (4.1) and (4.2) will be described in the next section.

4.3 Aerosol Model Formulation

The size range of particles is discretized into a number of j_{max} radial size bins. Each set of size bins is based on a geometrically increasing particle volume. The bins are centered at volume

$$V_j = V_{RAT} V_{j-1} \tag{4.3}$$

with $V_{RAT} \geq 2$. Correspondingly, the particle radius r_j is located at

$$r_j = (V_{RAT})^{1/3} r_{j-1}. \tag{4.4}$$

The bin widths increase according to

$$\Delta V_j = 2V_j \frac{V_{RAT} - 1}{V_{RAT} + 1} \tag{4.5}$$

$$\Delta r_j = \left(\frac{2}{V_{RAT} + 1}\right)^{1/3} (V_{RAT}^{1/3} - 1) r_j. \tag{4.6}$$

The upper and lower limits of each particle size bin in terms of radius are

$$r_{j,up} = \left(\frac{2V_{RAT}}{V_{RAT} + 1}\right)^{1/3} r_j \tag{4.7}$$

$$r_{j,low} = \left(\frac{2}{V_{RAT} + 1}\right)^{1/3} r_j. \tag{4.8}$$

The total number of bins covering the particle size range from r_1 to r_j is

$$j_{max} = 1 + \frac{\ln(r_j/r_1)^3}{\ln V_{RAT}}. \tag{4.9}$$

In this study, we use $r_1 = 0.3$ nm which is about the size of the sulfuric acid embryo, $V_{RAT} = 2$, and $j_{max} = 45$ which leads to $r_{j_{max}} \approx 8$ μm by doubling the volume for consecutive bins.

The typical size distributions of nascent primary soot particles are assumed to be log-normal, with median radii of 15–30 nm, modal widths of 1.4–1.6, and number densities of 10^6–10^7 cm^{-3} [Hagen et al., 1992; Petzold and Schröder, 1998]. The log-normal distribution for the size of soot particles can be expressed as

$$n(\ln r) = \frac{N_t}{\sqrt{2\pi}\ln\sigma_g}\exp\left[-\frac{(\ln r - \ln\bar{r}_g)^2}{2\ln^2\sigma_g}\right], \tag{4.10}$$

where $n(\ln r)d\ln r$ is the number of particles per cm^3 of air in the size range from $\ln r$ to $\ln r + d\ln r$, N_t is the total number of particles of all sizes per cm^3 of air, $\bar{r}_g$ is the median radius, and σ_g is the geometric standard deviation. The number density of particles in the jth size bin centered around the radius r_j is given by

$$\begin{aligned} dN = n(\ln r)d\ln r &= \frac{n(\ln r)}{r}dr \\ &= \frac{N_t}{\sqrt{2\pi}r\ln\sigma_g}\exp\left[-\frac{(\ln r - \ln\bar{r}_g)^2}{2\ln^2\sigma_g}\right]dr. \end{aligned} \tag{4.11}$$

4.3.1 Homogeneous Nucleation

The classical nucleation theory is based on the equilibrium state of critical-sized liquid droplets, or embryos, in contact with their parent vapors. The theory gives the nucleation rate in the form of

$$J = A\exp\left(-\Delta G^*/(R_u T)\right), \tag{4.12}$$

where J is the nucleation rate with the unit of embryos/(cm^3-sec), A is the kinetic prefactor, ΔG^* is the change of the Gibbs free energy during the phase change for the formation of an embryo, and R_u is the universal constant. The exponential dependence of J on ΔG^* implies that ΔG^* must be accurately calculated.

The change of the Gibbs free energy for the formation of a liquid embryo in contact with a binary vapor mixture can be written as [Flood, 1934; Reiss, 1950; Doyle, 1961]

$$\Delta G = n_1(\mu_1^l - \mu_1^g) + n_2(\mu_2^l - \mu_2^g) + 4\pi r^{*2}\sigma, \tag{4.13}$$

where n_i is the number of moles of component i in the embryo, μ_i^l is the chemical potential of the ith component in the liquid solution with the unit of J/mole, μ_i^g is the chemical potential of the ith component in the gas phase, σ is the surface tension with the unit of J/cm^2, and r^* is the radius of an embryo. The first two terms on the right side represent the energy that is gained by forming the liquid phase and the last term is the energy required to create the surface of the liquid droplet. The change of chemical potential in transforming from gas to liquid phase for each component is

$$\mu_i^l - \mu_i^g = -R_u T \ln\left(\frac{P_i}{P_{i,sol}^{\infty}}\right), \tag{4.14}$$

where P_i represents the partial pressure of gas-phase species i and $P_{i,sol}^{\infty}$ is the equilibrium vapor pressure of species i over a flat surface of the mixed solution.

The critical free energy ΔG^* is determined as the value of ΔG at the saddle point in the two dimensional energy surface. The conventional way is to solve iteratively a pair of generalized Kelvin equations [Mirabel and Katz, 1974] representing the derivatives of ΔG with respect to n_1 and n_2:

$$\left(\frac{\partial \Delta G}{\partial n_1}\right)_{n_2} = 0, \qquad \left(\frac{\partial \Delta G}{\partial n_2}\right)_{n_1} = 0. \tag{4.15}$$

However, this method involves tedious calculations in a two-dimensional parameter space. Recently, Zhao and Turco [1995] have devised an efficient method for locating

the saddle point (critical Gibbs free energy) that reduces the search for the roots of the generalized Kelvin equations in a two-dimensional space (n_1, n_2) to a search in two one-dimensional spaces. They transformed the coordinate system from (n_1, n_2) to (ω, V), that is, the weight fraction of sulfuric acid and the volume of a solution droplet. They are defined as

$$\omega = \frac{M_2 n_2}{M_1 n_1 + M_2 n_2} \tag{4.16}$$

and

$$V = \frac{M_1 n_1 + M_2 n_2}{\rho}, \tag{4.17}$$

where M_i is the molar weight of species i and ρ is the density of the solution. Then a revised version of the generalized Kelvin equations is derived from the derivatives of ΔG with respect to V and ω for a binary system as

$$\frac{dV}{dA} = \frac{\sigma}{Y}, \tag{4.18}$$

$$\Delta\mu_2 \left[1 + \frac{d\ln\rho}{d\omega}\omega\right] - \frac{M_2}{M_1}\Delta\mu_1 \left[1 - \frac{d\ln\rho}{d\omega}(1-\omega)\right] = 0, \tag{4.19}$$

where

$$Y = -\rho\left[\frac{\omega}{M_2}\Delta\mu_2 + \frac{1-\omega}{M_1}\Delta\mu_1\right], \tag{4.20}$$

and $A = 4\pi r^2$ is the surface area of an aerosol.

The advantage of the transformation is that equation (4.19) is independent of radius so that ω^* can be obtained iteratively by solving this equation alone. Equa-

tion (4.18) can be simplified as

$$r^* = \frac{2\sigma(\omega^*)}{Y(\omega^*)}. \tag{4.21}$$

Hence, once ω^* is determined, r^* can be obtained immediately with equation (4.21).

Using equation (4.13), the Gibbs free energy at the saddle point is

$$\Delta G^*_{hom} = \frac{4}{3}\pi\sigma(\omega^*)r^{*2}. \tag{4.22}$$

The homogeneous nucleation rate with the unit of embryos/(cm^3-sec) is

$$J_{hom} = 4\pi r^{*2}\beta_2 N_1 \exp\left(\frac{-\Delta G^*}{R_u T}\right), \tag{4.23}$$

where β_2 is the gas kinetic impingement rate of H_2SO_4 molecules towards the embryo surface, $\beta_2 = N_2(k_B T/2\pi m_2)^{1/2}$ with the unit of molecules/(cm^2-sec), and N_1 is the number density of water molecules in the gas phase. The prefactor, $A = 4\pi r^{*2}\beta_2 N_1$, is valid for the usual situation when $N_1 >> N_2$.

Finally, the critical numbers of H_2SO_4 and H_2O molecules in an embryo are then computed from

$$N_1^* = \rho(\omega^*, T)V^*(1-\omega^*)/m_1 \tag{4.24}$$

$$N_2^* = \rho(\omega^*, T)V^*\omega^*/m_2, \tag{4.25}$$

where the volume of the embryo is $V^* = 4\pi r^{*3}/3$, m_1 and m_2 are the molecular masses of H_2O and H_2SO_4, and ρ is the mass density of the liquid solution droplet.

4.3.2 Coagulation

Coagulation model is based on Toon's [1988] approach which conserves particle number and volume. The change of number density of volatile H_2SO_4-H_2O particles due to coagulation can be described by

$$\begin{aligned}(\frac{dN_{v,i}}{dt})_{coag} &= \frac{1}{2}K_{i-1,i-1}N_{v,i-1}^2 + N_{v,i}\sum_{j<i}(1-\frac{V_j}{V_i})K_{ij}N_{v,j} \\ &+N_{v,i-1}\sum_{j<i-1}(1-\frac{V_j}{V_{i-1}})K_{i-1,j}N_{v,j} - N_{v,i}\sum_{j\neq i}K_{ij}N_{v,j}, \\ &-N_{v,i}\sum_{j}K_{ij}N_{c,j} \end{aligned} \tag{4.26}$$

where $K_{ij} = K_{ji}$ is the Brownian coagulation coefficient between particles with size indices i and j. The subscript v denotes the volatile H_2SO_4-H_2O particles and c denotes the soot or the soot coated with H_2SO_4-H_2O.

Because bin i has twice the volume of bin $i-1$, collisions between bin i and bin j, where j is less than i, result in particles of volume intermediate between bin i and bin $i+1$. The volume ratio V_j/V_i is the fraction added to the larger bin by this collision.

Boundary conditions in coagulation are imposed to conserve mass. Instead of allowing particles to leave the largest size bin due to coagulation, those particles are kept in the largest size bin. Special conditions also apply to the production terms in the first size bin. It is assumed that there is no particles of size smaller than the first size bin so that coagulation cannot produce particle of size $j = 1$.

The Brownian diffusion kernel is calculated using the interpolation formula by

Fuchs [1964]

$$K_{i,j} = \frac{4\pi(r_i + r_j)(D_i + D_j)}{\dfrac{r_i + r_j}{r_i + r_j + (\delta_i^2 + \delta_j^2)^{1/2}} + \dfrac{4(D_i + D_j)}{(v_{p,i}^2 + v_{p,j}^2)^{1/2}(r_i + r_j)} \cdot \dfrac{1}{\beta}}, \tag{4.27}$$

where r_i and r_j are the radii of particles in the ith and jth size bins and β is the sticking coefficient which is assumed to be unity in the present work. D_i and D_j are the particle diffusion coefficient that can be calculated from the Einstein relation

$$D_i = k_B B_i T, \tag{4.28}$$

where k_B is the Boltzmann constant. T is the absolute temperature and B is the mobility given by

$$B_i = \frac{1}{6\pi\eta r_i}\left[1 + 1.246Kn_i + 0.42\exp\left(-\frac{0.87}{Kn_i}\right)\right], \tag{4.29}$$

where η is the viscosity of air and Kn is the Knudsen number defined as the ratio of mean free path of air and particle radius

$$Kn_i = \frac{\lambda_a}{r_i}. \tag{4.30}$$

$v_{p,i}$ is the mean thermal velocity of a particle

$$v_{p,i} = \left(\frac{8k_B T}{\pi m_i}\right)^{1/2}, \tag{4.31}$$

where m_i is the mass of the particle. δ_i is a correction factor given by

$$\delta_i = \frac{(2r_i + \lambda_{p,i})^3 - (4r_i^2 + \lambda_{p,i}^2)^{3/2}}{6r_i\lambda_{p,i}} - 2r_i, \tag{4.32}$$

with the mean free path of a particle in size bin i being

$$\lambda_{p,i} = \frac{8D_i}{\pi v_{p,i}}. \tag{4.33}$$

It can be shown that the coagulation coefficient increases with the difference between r_1 and r_2 and it reaches minimum for coagulation between particles with the same size. Coagulation between the soot particles is not important due to their low amount compared to the large amount of H_2SO_4-H_2O particles, and therefore is neglected in the wake-regime studies. This is because the time scale required to introduce a significant change in the distribution function for these aerosols is longer than the time available in the near-field plume. The characteristic time for coagulation is estimated as [Flagan and Seinfeld, 1988]

$$t_{coag} = \frac{1}{nH},$$

where n is the number density of particles and the typical value for the coagulation constant is $H = 10^{-9}$ cm^3/sec. This implies that the number density must lie between 10^8 and 10^{10} cm^{-3} in order for coagulation to be important in the near-field exhaust flow. The number density of H_2SO_4-H_2O embryos formed through binary homogeneous nucleation is sufficiently large for embryo-embryo and embryo-soot interactions to be important on a timescale of a few seconds. However, the soot particulates emitted in the exhaust flow are typically present at much lower levels.

Scavenging of H_2SO_4-H_2O aerosols by the soot particles is an important soot surface chemical activation pathway. Wetting the soot particles by this mechanism

is assumed to have no effect on the size of the soot because it can only lead to a monolayer coverage. However, the heterogeneous condensation on the liquid coating of soot is coupled to radial growth and might cause a shift in the size distribution.

4.3.3 Soot Activation

Soot particles can be activated as water condensation nuclei by adsorption of oxidized sulfur species (H_2SO_4 and SO_3) and by scavenging (coagulation) of volatile sulfate aerosols. The fraction of soot surface that is covered by oxidized sulfur species is defined as $\theta_i = A(SO_3 + H_2SO_4)/A_{s,i}$, where $A_{s,i}$ is the surface area density of soot in size bin i, which is $4\pi r_{s,i}^2 N_{c,i}$. The surface coverage due to the above two activation pathways is $\theta_i = \theta_{ads,i} + \theta_{sca,i}$.

Kärcher [1998] presented a kinetic formulation which gives the maximum sulfur adsorption on soot. Since $r_{s,i} < 100$ nm, vapor adsorption on fresh soot takes place in the gas kinetic regime. Therefore, the corresponding rate of change of θ is given by

$$\frac{\theta_{ads,i}}{dt} = \alpha \frac{\bar{v}}{4}(C_{SO_3} + C_{H_2SO_4}) \times 6.02 \times 10^{23} \frac{1 - \theta_i}{\sigma_0}, \tag{4.34}$$

where α is the sticking probability which is set to zero for $T > 420$ K and equal to unity for $T \leq 420$ K, $\bar{v}$ is the thermal speed for the SO_3 and H_2SO_4 molecules evaluated at their reduced mass, C is the molar density of gas phase species, and $\sigma_0 \approx 5 \times 10^{14}$ cm^{-2} is the approximate number of active sites available on the soot surface. This kinetic formulation gives the maximum adsorbed sulfur mass and it

represents the upper bound to the binary H_2SO_4-H_2O heterogeneous nucleation rate on the soot surface.

The change of surface coverage for a soot particle in size bin i by scavenging volatile droplets is determined by

$$\frac{d\theta_{sca,i}}{dt} = \sum_{j=1}^{j_{max}} K(r_{s,i}, r_{v,j}) N_{v,j} \pi r_{v,j}^2 \times \frac{1-\theta_i}{4\pi r_{s,i}^2}, \tag{4.35}$$

where K is the coagulation coefficient and N_v is the number density of volatile droplet. The gas phase losses of SO_3 and H_2SO_4 due to adsorption is $\propto (1-\theta)$, i.e., they are proportional to the available "dry" soot surface area

$$\left(\frac{dC_m}{dt}\right)_{ads} = -\alpha \frac{\bar{v}}{4} C_m \sum_{i=1}^{i_{max}} 4\pi r_{s,i}^2 N_{c,i} (1-\theta_i), \tag{4.36}$$

where m denotes H_2SO_4 or SO_3. This model also accounts for the condensation of H_2SO_4 and H_2O on the part of the soot surface that has already acquired the liquid coating. Consequently, condensation rates on soot and related gas phase losses scale with θ.

4.3.4 Condensation

Condensation can occur on the liquid volatile aerosols and on the partial liquid coating on the soot surface. The equilibrium vapor pressure of H_2SO_4 over the solution is so small that once H_2SO_4 molecules are condensed they can not re-evaporate. In contrast, droplets may take up or evaporate H_2O, depending of the evolution of temperature and the partial pressure of H_2O in the plume.

The condensation formulation follows the derivation by Fukuta and Walter [1970], which was based on the idea of Fuchs [1959]. The space outside of a particle is divided into two zones, the layer $r \leq R \leq r+\delta$ and the region beyond $R \geq r+\delta$ where $\delta \approx \lambda_a$, the molecular mean free path of air. The conventional diffusion equation, which is based on the assumption that vapor density in air is continuous, is valid for $R \geq r+\delta$, while gas kinetic theory is applied within the layer. The condition of continuity of vapor flux across the surface $R = r + \delta$ is invoked to complete the description. Consequently, the change in moles of gaseous species m due to condensation on or evaporation from an aerosol with radius r_i is

$$\frac{dn_{m,i}}{dt} = 4\pi r_i D^*_{v,i} \left(\frac{P_m - P_{m,i,sat}}{R_u T} \right), \tag{4.37}$$

where the modified diffusivity is

$$D^*_{v,i} = \frac{D_v}{\dfrac{r_i}{r_i + \delta} + \dfrac{4D_v}{r_i \alpha \bar{v}_m}} \tag{4.38}$$

with α being the mass accomodation coefficient. For condensation onto liquid surfaces considered in the present model, α is taken as unity. The mean thermal velocity of gaseous species m is given by

$$\bar{v}_m = \sqrt{\frac{8R_u T}{\pi M_m}}. \tag{4.39}$$

Without the diffusivity modification, equation (4.37) is in the conventional Maxwell's form, which would strongly overestimate the growth rate for submicron particles. For soot particles, since condensation can only take place on the activated fraction θ of

the surface, the right hand side of equation (4.37) needs to be multiplied by θ when calculating condensation on soot particles.

The saturation pressure is obtained by the Kelvin equation

$$\frac{P_{m,i,sat}}{P_{m,\infty,sat}} = \exp\left(\frac{2\sigma\bar{v}_m}{R_u T r_i}\right), \tag{4.40}$$

where $P_{m,i,sat}$ is the saturation vapor pressure of gaseous species m over a spherical droplet of radius r_i, and $P_{m,\infty,sat}$ is the saturation vapor pressure of species m over a flat surface of a liquid with the same composition as the droplet. The Kelvin equation (4.40) states that the saturation vapor pressure over the surface of a droplet is greater than that over a flat surface. The smaller the droplet, the larger is the saturation vapor pressure. Consequently smaller droplets tend to evaporate, while larger ones tend to grow. The effect of curvature is important for droplets less than 0.1 μm.

Denoting the total radial growth rate of a particle (volatile droplet or soot coated with H_2SO_4-H_2O) in size bin j due to condensation by dr_j/dt, the flux of particles growing from r_j to $r_j + \Delta r_j$ per unit time and per cubic centimeter of air is

$$G_j = \frac{N_j}{\Delta r_j}\frac{dr_j}{dt}, \tag{4.41}$$

where the expression of $\frac{dr_j}{dt}$ will be given later in this section. The rate of change of particle abundances due to condensation ($G_j > 0$) and evaporation ($G_j < 0$) will not affect the total number of each particle type. Therefore, the net rate of change of each particle type in size bin j over a time step can be expressed as [Kärcher, 1998]

$$\Delta G_j = \max\{0, G_{j-1}\} + |\min\{G_{j+1}, 0\}| - |G_j|. \tag{4.42}$$

The first term on the right hand side represents the possible gain of particles in size bin j from size bin $j-1$ upon condensation. The second term denotes the gain of particles from size bin $j+1$ due to evaporation. The last term is the loss of particles in size bin j by growth or evaporation. To conserve the total particle numbers in each type, boundary conditions at size bin $j=1$ and $j=j_{max}$ are set so that particles are kept within the size range $[r_{min}, r_{max}]$.

Using equation (4.42), the term $(dN/dt)_{cond}$ in equations (4.1) and (4.2) can be expressed as

$$\left(\frac{dN_j}{dt}\right)_{cond} = \frac{\Delta G_j}{N_a} = \frac{\Delta G_j}{(P_a/k_B T)}. \tag{4.43}$$

The change of radius due to condensation or evaporation is

$$\frac{dr_j}{dt} = \sum_m \left(\frac{\partial r_j}{\partial n_{m,j}}\right) \frac{dn_{m,j}}{dt}, \qquad m = H_2O, H_2SO_4, \tag{4.44}$$

where the partial derivative can be obtained from mass conservation in the liquid

$$\frac{\partial r_j}{\partial n_{m,j}} = \frac{M_m}{4\pi \rho_{sol} r_j^2}. \tag{4.45}$$

The condensation and evaporation processes control the weight fraction of H_2SO_4 in the liquid solution, $W_{H_2SO_4}$, on which the thermodynamic quantities depend. This especially holds for the saturation vapor pressure which in turn determines the condensation rate $\frac{dn_{m,j}}{dt}$. Therefore it is necessary to determine $W_{H_2SO_4}$. From the definition

$$W_{H_2SO_4,j} = \frac{M_{H_2SO_4} N_{H_2SO_4}}{\sum_m M_m N_{m,j}}, \qquad m = H_2SO_4, H_2O, \tag{4.46}$$

where

$$\sum_m M_m N_{m,j} = 4\pi\rho_{sol} r_j^3/3, \tag{4.47}$$

and taking derivative of equation (4.46) with respect to time and combining equations (4.44) and (4.45), we get

$$\frac{dW_j}{dt} = \frac{3}{r_j}\left[\left(\frac{dr_j}{dn_{m,j}}\right)\frac{dn_{m,j}}{dt} - W_j\frac{dr_j}{dt}\right], \qquad m = H_2O, H_2SO_4. \tag{4.48}$$

4.3.5 Summary of Coupling between Chemistry and Aerosol Dynamics

The evolution equations of gas-phase H_2SO_4 and H_2O will have additional sources or sinks due to the microphysical processes mentioned in the previous sections. The rate equations for H_2O and H_2SO_4 are modified as follows

$$\frac{dC_1}{dt} = \dot{\omega}_1 - J_{hom} n_1^* - \sum_i \frac{dn_{1,i}}{dt} N_{v,i} - \sum_i \frac{dn_{1,i}}{dt} N_{cv,i} - \sum_i \alpha\frac{\bar{v}}{4} C_m \sum_{i=1}^{i_{max}} 4\pi r_{s,i}^2 N_{c,i}(1-\theta_i), \tag{4.49}$$

$$\frac{dC_2}{dt} = \dot{\omega}_2 - J_{hom} n_2^* - \sum_i \frac{dn_{2,i}}{dt} N_{v,i} - \sum_i \frac{dn_{2,i}}{dt} N_{cv,i} - \sum_i \alpha\frac{\bar{v}}{4} C_m \sum_{i=1}^{i_{max}} 4\pi r_{s,i}^2 N_{c,i}(1-\theta_i), \tag{4.50}$$

where the subscript 1 denotes H_2O, and 2 denotes H_2SO_4, C is the species gas-phase concentration with unit of mole/cm^3, and $\dot{\omega}$ is the gas-phase chemical reaction rate. J_{hom} is the homogeneous nucleation rate given by equation (4.23), n_m^* is the moles of

gaseous species m in a H_2SO_4-H_2O aerosol of critical size, and N_i is number density of particles in size bin i with the subscript v as volatile H_2SO_4-H_2O aerosol and the subscript c as soot coated with H_2SO_4-H_2O. Terms due to condensation, $\frac{dn_{1,i}}{dt}$ and $\frac{dn_{2,i}}{dt}$, can be obtained from equation (4.37). The last term accounts for soot activation. Equations (4.49) and (4.50) reveal the coupling of microphysical processes with chemistry kinetics through concentrations of H_2SO_4 and H_2O. Microphysical processes also couple with turbulent flow field from mixing of the exhaust plume with the ambient air.

4.3.6 Thermodynamic Properties

Various thermodynamic quantities are needed for simulation of the aerosol dynamics. Described in this section are details of methods used to calculate or estimate these properties.

Mean free path:

At the standard condition, $P_0 = 1.013 \times 10^5$ Pa and $T_0 = 293.15$ K, the molecular mean free path of air is $\lambda_{a,0} = 6.6 \times 10^{-6}$ cm. Since $\lambda_a = \frac{k_B T}{\sqrt{2} P \pi d_m^2} \propto \frac{T}{P}$, for other levels of P and T,

$$\lambda_a = \lambda_{a,0} \frac{P_0}{P} \frac{T}{T_0}. \tag{4.51}$$

Diffusivity:

The diffusivity of water vapor D_v in air is obtained from the extrapolation by Pruppacher and Klett [1997] with the following best-estimated relation for temperatures between -40°C and 40°C

$$D_{v,H_2O} = 0.211 \left(\frac{T}{T_0}\right)^{1.94} \left(\frac{P_0}{P}\right) \tag{4.52}$$

with $T_0 = 273.15$ K, $P_0 = 1013.25$ mbar, and D_v in cm^2/sec. As $D_v \propto v\lambda_a$ and $v \propto 1/\sqrt{M_v}$, we get $D_v \propto 1/\sqrt{M_v}$. Therefore, D_{v,H_2SO_4} can be obtained through

$$D_{v,H_2SO_4} = D_{v,H_2O} \frac{\sqrt{M_{H_2O}}}{\sqrt{M_{H_2SO_4}}}. \tag{4.53}$$

Surface tension:

The surface tension of H_2SO_4-H_2O solutions has been reported by Sabinina and Terpugow [1935] for 15 levels of H_2SO_4 content. Data were reported for temperatures between 10°C and 50°C in 10°C intervals. The reported data are fitted with an eighth-order polynomial at each temperature. The surface tension at temperatures between tabulated values is then determined by the linear interpolation.

Solution density:

The solution density is obtained from tabulated values [Perry, 1963]. Tabulated data were given for temperatures between 0°C and 100°C and for H_2SO_4 weight percent between 0 and 100. The tabulated data at each temperature are fitted with

an eighth-order polynomial. The density at temperatures between tabulated data is also computed by the linear interpolation.

Equilibrium partial vapor pressure:

The equilibrium partial vapor pressure over the binary solution H_2SO_4-H_2O is presented by Taleb et al. [1996] in a very simple form, which is valid over the entire range of concentrations for temperatures in the range 190–298 K. In terms of a Van Laar type equation, the activity coefficients γ_1 and γ_2 of components 1 and 2 in a binary system can be expressed as [Taleb et al., 1996]

$$\begin{aligned} T \log \gamma_1 &= \frac{A_1 X_2^2}{[X_2 + B_1 X_1]^2} \\ T \log \gamma_2 &= \frac{A_2 X_1^2}{[X_1 + B_2 X_2]^2}, \end{aligned} \tag{4.54}$$

where T is the temperature in degree K, X is the mole fraction, and A_i and B_i are coefficients for a given binary solution. Based on the data of Zeleznik [1991], the following expressions are used in equation (4.54)

$$\begin{aligned} A_1 &= 2.989 \times 10^3 - \frac{2.147 \times 10^6}{T} + \frac{2.33 \times 10^8}{T^2} \\ A_2 &= 5.672 \times 10^3 - \frac{4.074 \times 10^6}{T} + \frac{4.421 \times 10^8}{T^2} \\ B_1 &= \frac{1}{B_2} = 0.527, \end{aligned} \tag{4.55}$$

where A_1 and B_1 are for water, and A_2 and B_2 are for sulfuric acid.

The definitions of the activity coefficient γ_i and the activity a_i are given by

$$a_i = \frac{P_{sol,i}}{P_{0,i}} \tag{4.56}$$

$$\gamma_i = \frac{a_i}{X_i} = \frac{P_{sol,i}}{X_i P_{0,i}}, \tag{4.57}$$

where $P_{sol,i}$ is the equilibrium partial pressure of component i over a solution containing i and $P_{0,i}$ is the equilibrium pressure of pure i. It is straightforward to compute $P_{sol,i}$ provided that $P_{0,i}$ is known, which is generally the case, through

$$P_{sol,i} = \gamma_i X_i P_{0,i}. \tag{4.58}$$

The equilibrium vapor pressure of pure water expressed in millibars for the temperature range between 220 and 320 K is taken from the compilation of Tabata [1973]

$$\log P_{0,H_2O}(\text{mbars}) = 8.42926609 - \frac{1827.17834}{T} - \frac{71208.271}{T^2}. \tag{4.59}$$

And the equilibrium vapor pressure of the pure sulfuric acid is given by Ayers et al. [1980]

$$\ln P_{0,H_2SO_4}(\text{atm}) = -10156/T + 16.259. \tag{4.60}$$

Mixture molar volume:

The molar volume of a two-component solution is given by

$$\bar{v} = \frac{M}{\rho} = \frac{(1 - x_2)M_1 + x_2 M_2}{\rho}, \tag{4.61}$$

where x_2 is the mole fraction of component 2. For a two-component mixture, the partial molar volume of component 1 or 2 in a solution can be obtained through the tangent line at a given mixture composition on the composition curve $\bar{v}$ versus x_2 (can

be obtained experimentally) at the intercept $x_2 = 0$ or $x_2 = 1$ as shown in Figure 4.1. Mathematically, the partial molar volumes are expressed as

$$\bar{v}_1 = \bar{v} - \frac{d\bar{v}}{dx_2} x_2 \tag{4.62}$$

and

$$\bar{v}_2 = \bar{v} - \frac{d\bar{v}}{dx_2}(x_2 - 1), \tag{4.63}$$

such that $(1 - x_2)\bar{v}_1 + x_2\bar{v}_2 = \bar{v}$.

4.4 Threshold Condition for Contrail Formation from Aircraft Exhaust

Contrails (condensation trails) are observed behind an aircraft only under certain conditions depending on various factors. The threshold criterion for contrail formation was first developed by Appleman [1953]. He explained that contrails are expected to form in the engine exhaust plumes when isobaric mixing between the hot and humid exhaust gases and cold ambient air results in a mixture reaching saturation with respect to water. However, Busen and Schumann [1995] observed contrails at ambient temperatures well above the Appleman's threshold temperature. They explained this discrepancy by considering a fraction of combustion heat transformed to the trailing vortex system in the form of kinetic energy. They identified this fraction with the overall propulsion efficiency of the aircraft, i.e., the fraction of combustion heat that

is converted into work to propel the aircraft

$$\eta = FV/(Q\dot{m}_F), \tag{4.64}$$

where F is the thrust, V is the airspeed, Q is the specific combustion heat, and $\dot{m}_F$ is the fuel flow rate. Hence, the exhaust gases contain only $(1-\eta)Q$ of heat per mass of fuel instead of all the heat assumed by Appleman [1953]. Consequently, the threshold temperature for contrail formation is higher than that if the exhaust gases are assumed to receive all the combustion heat directly. The overall propulsion efficiencies, η, for modern bypass turbofan engines is usually higher than those for older turbojet engines or turbofan engines with low bypass ratio. The kinetic energy of the jet plume is shown by Schumann [1996] to have very little impact on the threshold temperature although the kinetic energy of the trailing vortex system induced by the aircraft is important. Hence it is justified to assume a stagnant plume when calculating the threshold criterion for contrail formation.

Figure 4.2 illustrates schematically how the threshold ambient temperature can be determined in a partial water pressure versus temperature diagram. Saturated states corresponding to liquid water and ice are denoted by $P_{sat,liq}$ and $P_{sat,ice}$, respectively. Mixing of the aircraft exhaust with ambient air follows along the line connecting the state of the exhaust gas at engine exit and that in the ambient air. The coordinate corresponding to the condition at the engine nozzle exit is $(T_{exit}, x_{H_2O,exit}P_a)$ where P_a is the ambient total pressure, which is on the far right upper corner outside the range plotted. The ambient condition corresponds to the point $(T_a, RH_a \cdot P_{sat}(T_a))$ where

RH stands for relative humidity and the subsript a denotes the ambient condition. Visible contrails form when the the plume reaches supersaturation with respect to water [Jenson et al., 1998]. In Figure 4.2, this corresponds to the conditions when the mixing line crosses the saturation curve with respect to liquid water, $P_{sat,liq}$ (given by equation (4.59)). Thus the threshold condition is defined as the situation when the mixing line is tangent to the liquid saturation curve. Also plotted in the figure is the saturation vapor pressure with respect to ice, $P_{sat,ice}(T)$ which is given by $\ln P_{sat,ice} = 24.313 - 6146.8/T$ [Tabazadeh et al., 1997].

The gradient of the mixing line is approximated by [Schumann, 1996]

$$G = \frac{EI_{H_2O}c_pP_a}{\varepsilon Q(1-\eta)}, \tag{4.65}$$

where $\varepsilon = M_{H_2O}/M_{air} = 0.622$. The temperature at the tangent point T_{LM} can be calculated through

$$\frac{dP_{sat}(T_{LM})}{dT} = G. \tag{4.66}$$

Equation (4.66) is nonlinear and it can be solved for T_{LM} through Newton's iteration. A good guess to initiate the iteration is given by [Schumann, 1996]

$$T_{LM} = -46.46 + 9.43\ln(G - 0.053) + 0.720[\ln(G - 0.053)]^2 + 273.15, \tag{4.67}$$

where T is in unit K and G in is unit Pa/K. From the definition of the ambient relative humidity RH_a and that of the gradient of the mixing line, the threshold ambient temperature for contrail formation is determined by

$$T_{LC} = T_{LM} - [P_{sat}(T_{LM}) - RH_a \cdot P_{sat}(T_{LC})]/G. \tag{4.68}$$

Equation (4.68) is also an implicit equation which requires Newton's iteration. T_{LM} is a good initial guess to start the iteration. Contrails are expected to form when the ambient temperature is less than T_{LC}, for example, the temperature at point A as illustrated in Figure 4.2. The threshold ambient temperature can also be determined by the ice saturation state as denoted by T_{IC}. As the specific volume increases when liquid water freezes, the saturation pressure of ice is higher than that of liquid water; consequently, $T_{IC} > T_{LC}$.

In-situ measurements of the ambient temperature and humidity made by Schumann et al. [1996] and by Jensen et al. [1998] during the SUCCESS experiment suggest that liquid saturation in the plume is required for visible contrail formation. The fact that the ambient temperature needs to be below T_{LC} may indicate that liquid water droplets must be activated and subsequently freeze in order to generate a sufficient number of ice crystals for a visible contrail. According to the above in-situ observations, visible contrails do not form when $T_{LC} < T < T_{IC}$. In this temperature range, the number of ice crystals nucleated may be too low to form ice contrails that are visible.

In this thesis work, the formation of ice particles by freezing and their subsequent evolution are not modeled. This is justified for situations when contrails are not formed, i.e., when ambient temperature is above the threshold ambient temperature. The present analysis also sets a stage for further research on ice particles when contrails are formed.

4.5 Results and Discussion

4.5.1 Aerosol evolution

Figure 4.3 depicts the predicted temperature profile as a function of the axial distance x and the jet radius r. The initial distribution is characterized by a hot, isothermal core and a somewhat colder bypass region. At the nozzle exit plane the initial values over the core and the bypass cross sections are assumed to be uniform. The inner bypass zone is heated up due to mixing of heat out of the core in the very near field. The plume temperature decays within the mixing region as the ambient air is entrained into the plume.

Figure 4.4 presents the profile of soot emitted by the engine and transported as a passive tracer in the jet flow field. We assume that there is no soot present in the ambient air. The initial profile of the exhaust particulates decays, similar to the trend of the temperature, but a strong perturbation of the background atmosphere with respect to soot is observed, even at the simulated plume length of $x = 1$ km.

Figure 4.5 shows the homogeneous nucleation rate along the plume axis. The present modeling results reveal that the typical germ radii are 0.3nm with 1.5 sulfuric acid and 3 water molecules per germ on average. The freshly nucleated acid aerosols have H_2SO_4 weight fractions ranging from 0.7–0.8 depending on germ radius. The nucleation rate reaches its maximum by 100 m from the exit plane , and then it plummets as gaseous H_2SO_4 is depleted.

Figure 4.6 depicts the evolution of number densities of H_2SO_4-H_2O aerosols, soot particles, and soot coated with H_2SO_4-H_2O along the plume axis with and without coagulation effects. High levels of volatile H_2SO_4-H_2O droplets are predicted by 100 m past the nozzle exit. After reaching its maximum, the amount of volatile droplets decreases due to both dilution and coagulation as manifested in the figure. The predicted number densities of bare soot and soot coated with H_2SO_4-H_2O coincide with those of mixed soot without coagulation effects. This suggests that we can combine the bare soot and those coated with H_2SO_4-H_2O into one parameter to save computing time. Here the generation path of H_2SO_4-H_2O coated soot particles through adsorption is neglected.

Figure 4.7 shows the mixing ratio of gaseous sulfur species and H_2SO_4-H_2O aerosols. It clearly shows that the binary homogeneous nucleation effectively removes H_2SO_4 species from the gas phase. By the time of 1 second (c.f. Figure 3.10), the gas-phase H_2SO_4 species is almost depleted. It indicates that any SO_2 that is oxidized to SO_3 and subsequently to sulfuric acid (H_2SO_4) would form new small aerosols in the first second after emission. This estimate is comparable with the simulation results by Miake-Lye et al. [1994] and Kärcher [1996], and is also consistent with the prediction of < 1.6 sec by Arnold et al.'s [1998] measurements.

4.5.2 Soot Activation

Figure 4.8 shows the time evolution of the average surface coverage of sulfur species on soot particles along the plume axis. Prior to the onset of homogeneous binary nucleation, adsorption dominates. This process can be viewed as prompt binary heterogeneous nucleation of H_2SO_4 and H_2O on the surface. After homogeneous binary nucleation, gaseous H_2SO_4 is depleted and the scavenging dominates the surface activation.

4.5.3 Effects of sulfur emission from engine

To explore the effect of SO_x emissions at the exhaust exit on the formation, growth, and chemical processing of near field aerosols, parametric studies are performed. Since direct measurements of the level of S(VI) (SO_3 and H_2SO_4) at the exhaust exit have not been reported, the percentage conversion of fuel sulfur into SO_3 in the engine was varied between 2% and 20%. This range encompasses both Brown et al's [1996b] model estimates for the Concord and a smaller subsonic engine as well as experimental measurements of gas turbine exhausts [Hunter, 1982; Harris, 1990].

Figure 4.9 presents the maximum conversion efficiency of emitted SO_x to H_2SO_4 along the plume axis versus percentage conversion of fuel sulfur to SO_3 in the engine. $[SO_3]_0/[SO_x]_0$ is used as a free parameter since direct measurements of SO_3 at the engine exit are not available. The subscript 0 indicates initial plume concentration at the nozzle exit plane. For low levels of SO_3 emission with $[SO_3]_0/[SO_x]_0 < 1\%$,

$[H_2SO_4]_{max}/[SO_x]_0$ depends strongly on $[OH]_0$, because SO_3 levels produced via SO_2 + OH are greater than or at least similar to $[SO_3]_0$. Limited by the SO_2 + OH reaction rate, $[H_2SO_4]_{max}/[SO_x]_0$ is bounded between 0.1% and 2% for $[OH]_0$ levels between 0.1ppmv and 10ppmv. Direct emission of H_2SO_4 could enhance this limit. However, when $[SO_3]_0/[SO_x]_0 > 1\%$, $[H_2SO_4]_{max}/[SO_x]_0$ increases dramatically because the fast SO_3 + H_2O reaction produces H_2SO_4 directly, bypassing the slower SO_2 + OH reaction pathway and eliminating the $[OH]_0$ dependence. Direct emission of H_2SO_4 and possible heterogeneous losses of SO_3 and H_2SO_4 due to adsorption on soot particles were not considered here. The computed conversion range is consistent with the estimated value of > 0.4% based on measurements by Frenzel and Arnold [1994].

Figure 4.10 shows the accumulative number densities (as would be detected by a condensation nucleus counter) of volatile H_2SO_4-H_2O aerosols with radius greater than 3.5 nm along the jet plume axis. Profiles are shown assuming that 2%, 5%, 10%, and 20% of the fuel sulfur is converted to SO_3 in the engine. The predicted cumulative number density of volatile aerosols is shown to increase with the SO_3 emission. As more SO_3 is emitted from the nozzle exit, more gas-phase H_2SO_4 is produced as shown in Figure 4.9. This leads to higher peak homogeneous binary nucleation rates and therefore more volatile H_2SO_4-H_2O embryos are generated in the early jet regime. Elevated levels of gaseous H_2SO_4 also promote the condensation process which causes volatile acid droplets to grow into larger size. This is reflected in the earlier and

sharper rise of the average aerosol radius for higher SO_3 emission as depicted in Figure 4.11. The average radius of aerosols is defined as $r_{v,ave} = \sqrt{A_{v,tot}/(N_{v,tot} \cdot 4\pi)}$, where $A_{v,tot}$ and $N_{v,tot}$ are the total surface area and number density of volatile particles in a grid, respectively. When all the SOx emitted from nozzle are in the form of SO_2, the cumulative number densities are too small to be shown in Figure 4.10. In the late stage of the jet plume the evolution of number densities are shown to be dominated by dilution.

In Figure 4.12, the evolution of relative humidity (RH) along the plume axis is illustrated. The relative humidity first increases due to rapid temperature decrease caused by the entrainment of cold ambient air. The water vapor reaches supersaturation at about 100 m after exit. The level of water vapor supersaturation achieves its maximum by 250 m, then it falls off due to condensation of water vapor onto aerosols until $RH \approx 100\%$. Hereafter, particles begin to evaporate water due to entrainment. The net effect is that RH decreases slightly. With higher conversion of fuel sulfur to oxidized sulfur in the engine, more and larger volatile aerosols are generated leading to higher levels of surface area density to be presented in Figure 4.13. Hence enhanced condensation due to larger surface area available causes RH to decrease to 100% sooner as depicted in Figure 4.12.

A natural and important consequence of the generation of high number density of volatile H_2SO_4-H_2O aerosols is a significant increase in aerosol surface area density. Figure 4.13 presents the volatile aerosol surface area density along the plume axis

for the conditions with 0, 2 %, 5%, 10%, and 20% emission of SO_x as SO_3 at the exhaust exit. Homogeneous binary nucleation first causes a marked increase of surface area density of volatile acid aerosols. After reaching its maximum at about 50 m, nucleation is slowed down, and surface area density is decreased by coagulation. Once the plume becomes supersaturated with respect to water, the surface area increases due to rapid water condensation on droplets with radii larger than nanometer size. After the plume relative humidity decreases to about 100 %, condensation ceases and the surface area density decreases which is dominated by plume dilution and aerosol coagulation. When SO_3 emission is zero at the nozzle exit, the limited amount of H_2SO_4 is depleted by adsorption and homogeneous binary nucleation before the plume becomes saturated. The sizes of volatile aerosols stay small and water uptake will not be important due to the Kelvin barrier. Hence the surface area does not exhibit a second increase period which is caused by water condensation. For higher percentage emission of SOx as SO_3, more H_2SO_4 is generated, which leads to higher homogeneous binary nucleation rate and thus generates more volatile acid aerosols. This results in larger increase in surface area early in the plume. Higher levels of gas phase H_2SO_4 also enhance H_2SO_4 condensation and accordingly induce more H_2O uptake, which makes particles grow into larger size as manifested in Figure 4.11. Therefore a second increase period becomes more profound with higher levels of SO_3 emission from the nozzle exit. The computed surface area density levels are in the range of $O(10^3)$–$O(10^5)$ $\mu m^2 cm^{-3}$ which are consistent with the predictions by Kärcher [1996].

As shown in Figure 4.14, the level of chemical activation of soot particles increases as fuel sulfur conversion to SO_3 in the engine increases. When the exhaust from the nozzle exit contains no SO_3, θ is about 0.3 at the end of jet plume regime. If 2% of fuel sulfur is converted to SO_3 in the engine, θ would get to nearly 0.8 at the end of jet. When the conversion fraction is $\geq$ 5%, θ reaches nearly 1.

In the near-field jet plume, the computed results indicate that only 1%–5% of exhaust SO_3 is adsorbed on soot during the time required for chemical buildup of maximum H_2SO_4 (10 ms) in the gas phase for the range of SO_3 emission studied here. Hence the adsorption of SO_3 is not a limit to its gas-phase chemical conversion to H_2SO_4. The H_2SO_4 generated in the gas phase is adsorbed by soot until the depletion of available H_2SO_4 by homogeneous binary nucleation and condensation around a plume age of 0.1 sec. The model results show that approximately 3%–25% of the chemically produced H_2SO_4 is adsorbed by soots. Hence we can conclude that H_2SO_4 is the major species adsorbed on soot particles compared to the adsorption of SO_3 on soot. However, the amount of H_2SO_4 adsorbed on soot particles is still relatively small and it will not limit the H_2SO_4-H_2O binary homogeneous nucleation and H_2SO_4 condensation.

Based on simulation of combustion chemistry, Brown et al. [1996b] concluded that the conversion fraction of fuel sulfur to S(VI) (SO_3+H_2SO_4) does not scale linearly with fuel sulfur content (FSC). The conversion is lower for higher FSC.

4.5.4 Threshold temperature for contrail formation

Jet-A1 fuel is a standard aviation kerosene with hydrogen mass fraction of m_H=0.14 and specific combustion heat of $Q = 43 \times 10^6$ J/kg [Schumann, 1996]. For a B747 aircraft burning kerosene with a thrust $F = 31.1 \times 10^3$ N per engine [Schumann, 1996], a fuel flow rate $\dot{m} = 0.785$ kg/s, and the air velocity $V = 237$ m/s, the propulsion efficiency and the H_2O emission index are estimated to be $\eta = 0.216$ and $EI_{H_2O} = 1.25$, respectively. With the ambient pressure $P_a = 0.2361$ atm and relative humidity $RH_a = 30\%$, we compute the threshold ambient temperature T_{LC} to be 221.51 K. For a higher ambient relative humidity $RH_a = 50\%$, T_{LC}=222.48 K. As expected, ambient air with higher relative humidity facilitates contrail formation. For $\eta = 0$ and $RH = 50\%$, T_{LC} is 220.19 K which is about 2 K smaller than the situation with $\eta = 0.216$. Hence, the Appleman's criterion would give lower threshold temperatures since it did not consider the conversion of combustion heat into kinetic energy in the wake vortex regime.

Given the overall propulsion efficiency of an aircraft and the type of fuel burnt, the threshold temperature turns out to be a function of ambient relative humidity and pressure (altitude), as seen from equations (4.65), (4.66), and (4.68). In Figure 4.15, the computed threshold temperature for contrail formation is plotted versus ambient pressure for ambient relative humidities of 0, 50, and 100%. The propulsion efficiency η is specified to be 0.3, which is the approximate value for modern commercial jet engines. It clearly indicates that contrails tend to form at higher ambient pressure or

higher relative humidity. The threshold temperature is seen sensitive to the aircraft propulsion efficiency, and contrails tend to form at a higher propulsion efficiency.

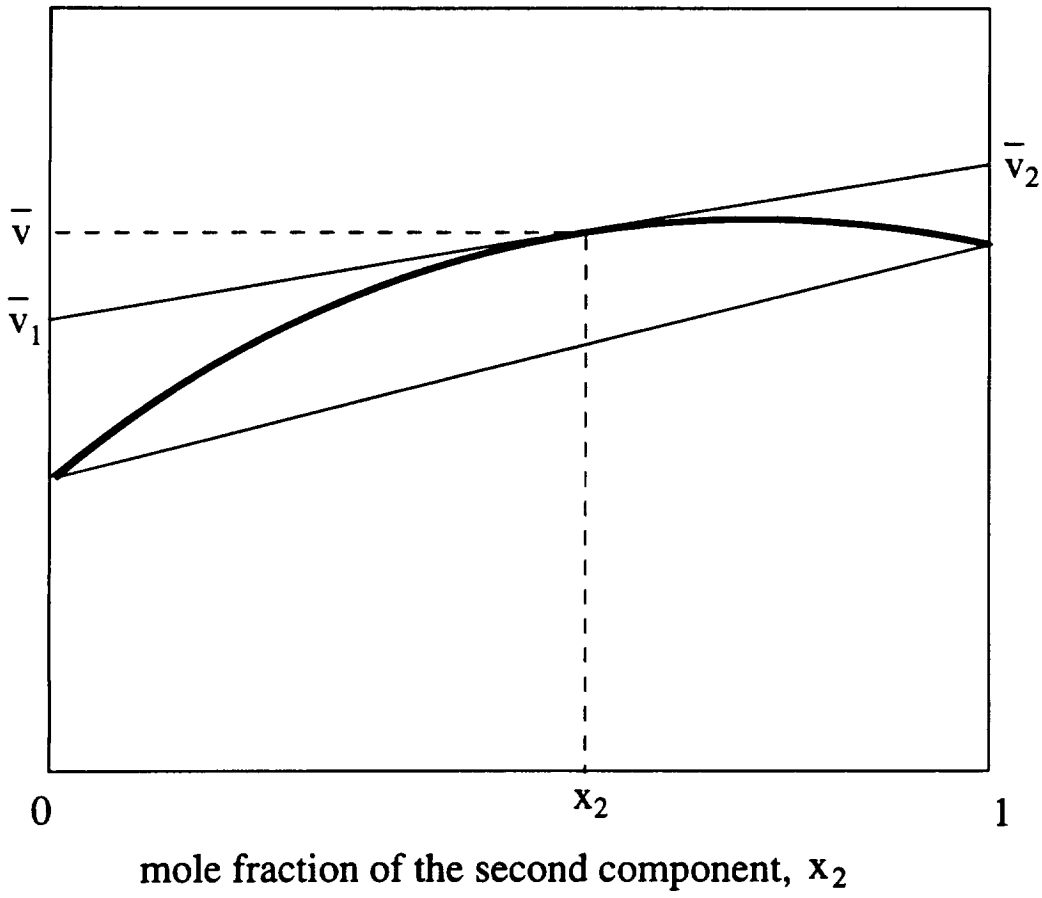

Figure 4.1: Schematic of the partial molar volume, $\bar{v}$, of a two-component mixture. $\bar{v}_1$ and $\bar{v}_2$ are the partial molar volume of component 1 and 2, respectively.

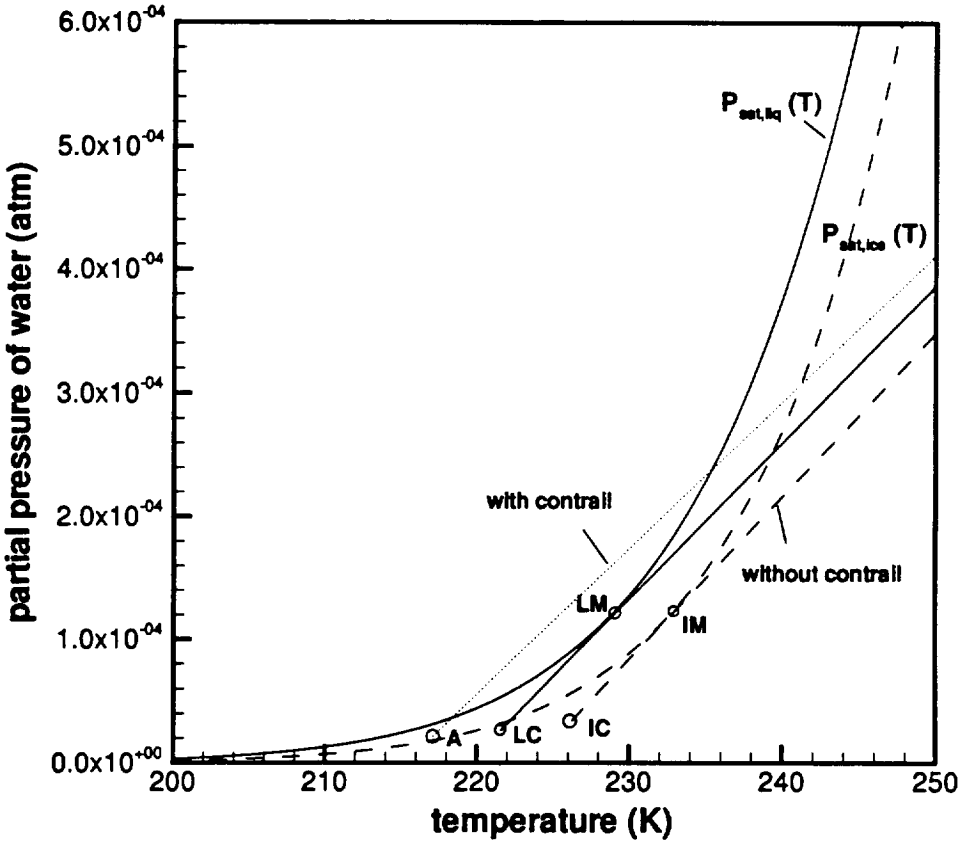

Figure 4.2: Schematic showing threshold condition for contrail formation. It shows the curve of the liquid water saturation pressure $P_{sat,liq}(T)$ and ice saturation pressure $P_{sat,ice}(T)$ versus temperature and the mixing lines. T_{LC} is the threshold ambient temperature for contrail formation.

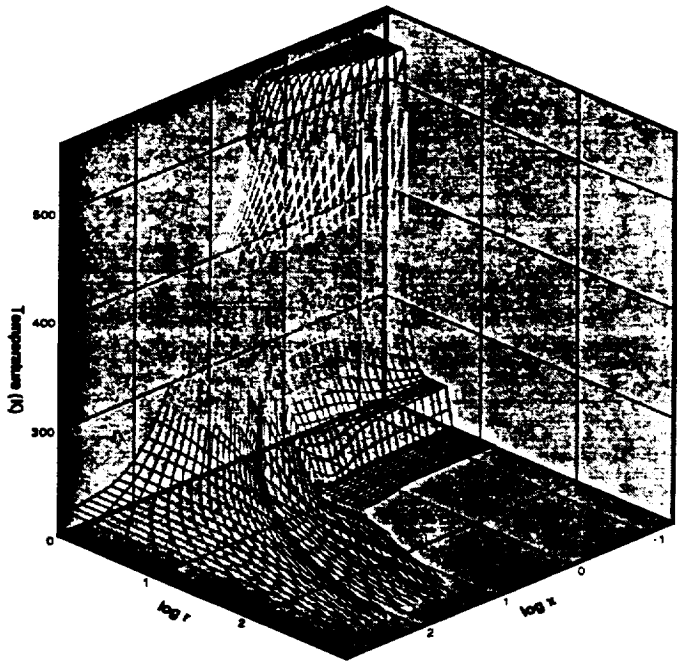

Figure 4.3: Spatial distribution of temperature in the flow field of a B747 jet engine. The radial distance, r, and the downstream distance, x, are in unit m.

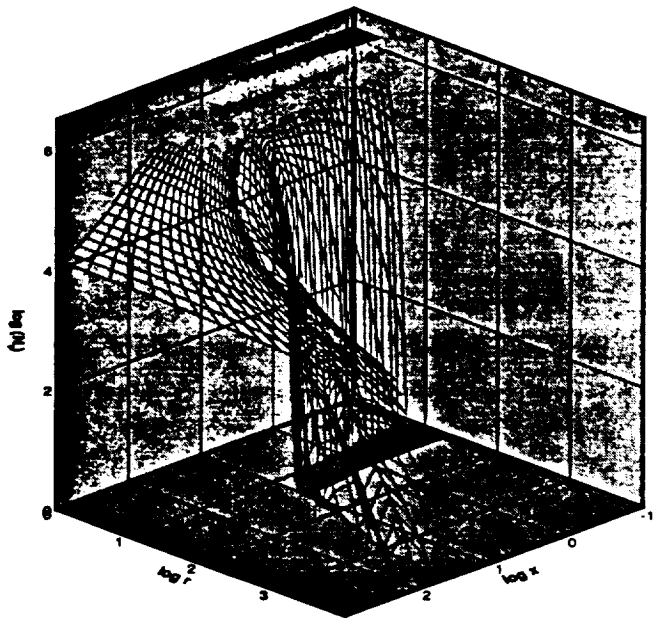

Figure 4.4: Spatial distribution of the total number density of soot particles in the flow field of a B747 jet engine. The radial distance, r, and the downstream distance, x, are in unit m.

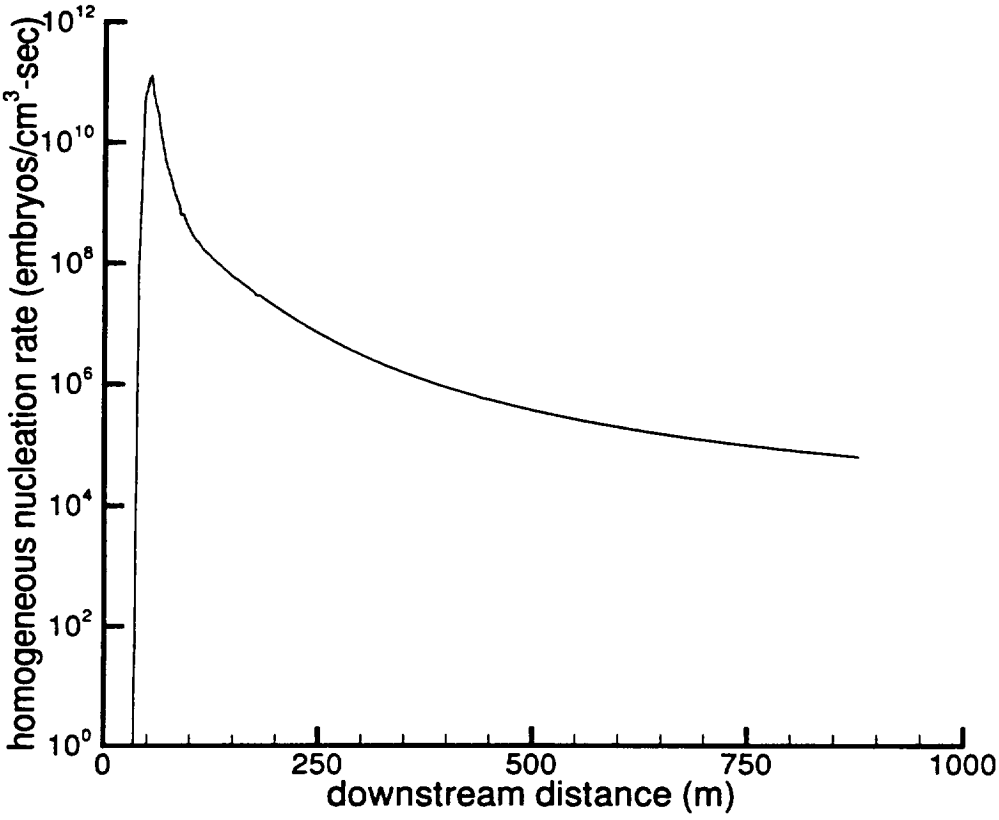

Figure 4.5: Homogeneous H_2SO_4-H_2O nucleation rates along the jet plume axis.

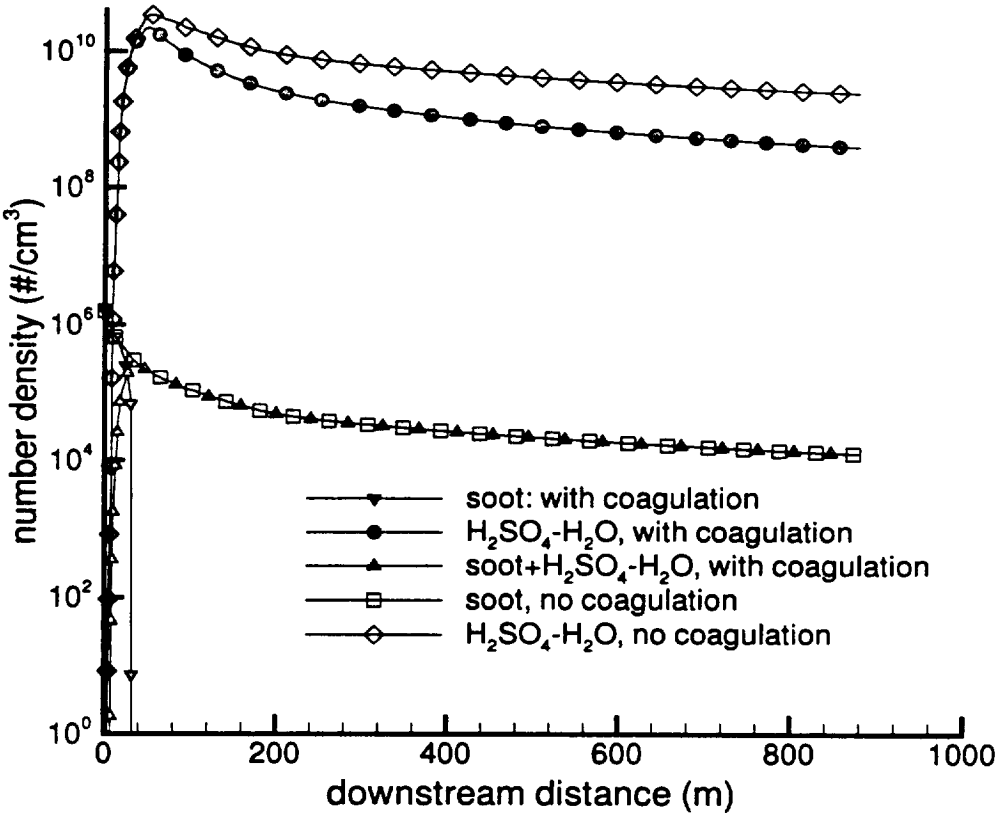

Figure 4.6: Number densities of volatile H_2SO_4-H_2O droplets, soot particles, and soot coated with H_2SO_4-H_2O versus downstream distance with and without coagulation effects.

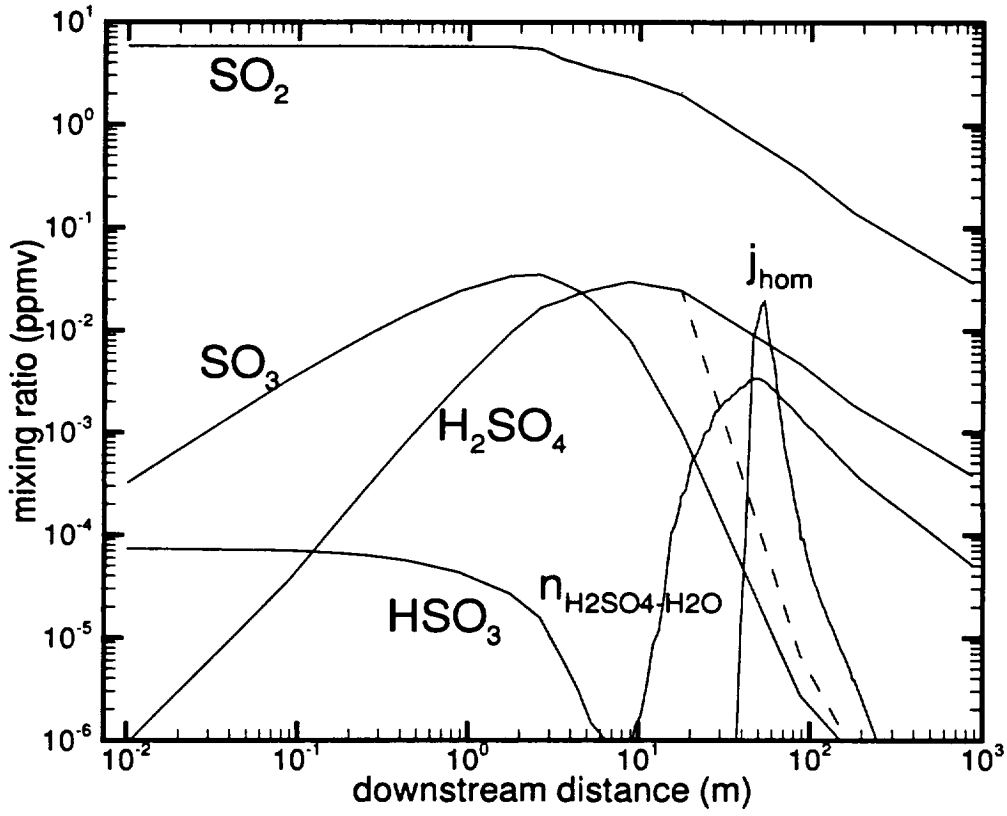

Figure 4.7: Mixing ratio of gaseous sulfur species and sulfate aerosols versus downstream distance. The homogeneous nucleation rate J_{hom} in unit of ppmv/sec is also shown. Dashed line represents the evolution of gaseous H_2SO_4 species when nucleation is included as compared to the pure dilution (solid line).

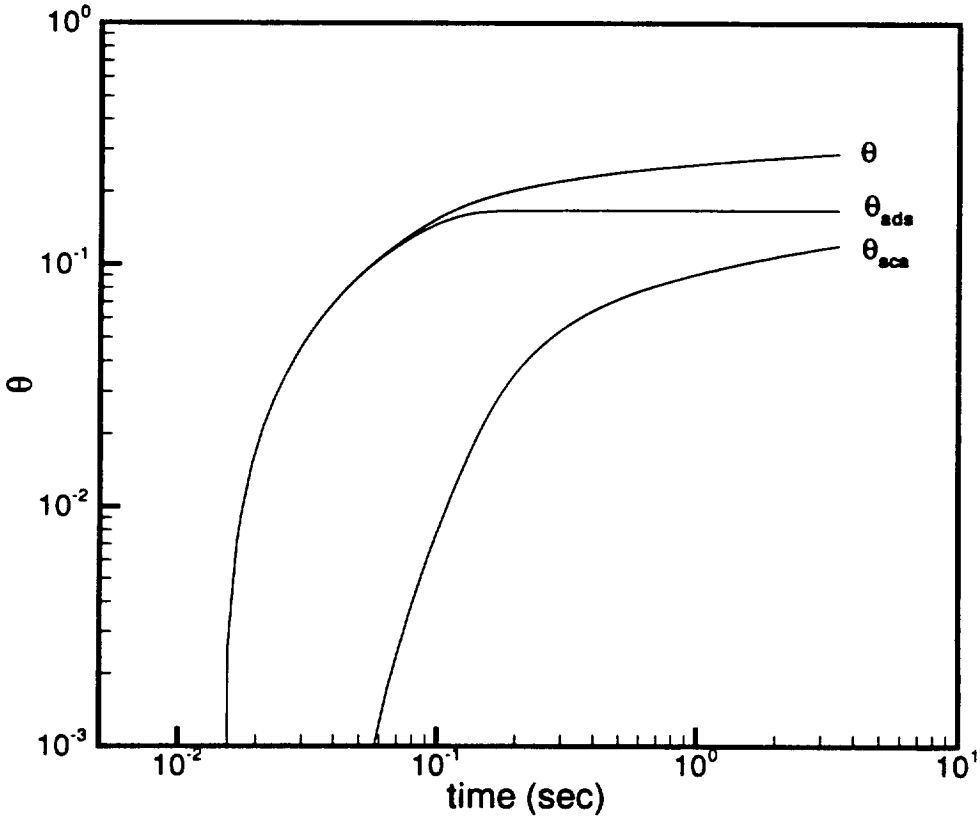

Figure 4.8: Average surface coverage of oxidized sulfur species for a soot versus plume age. It is composed of coverage by adsorption of gaseous H_2SO_4 and by scavenging of volatile H_2SO_4-H_2O aerosols.

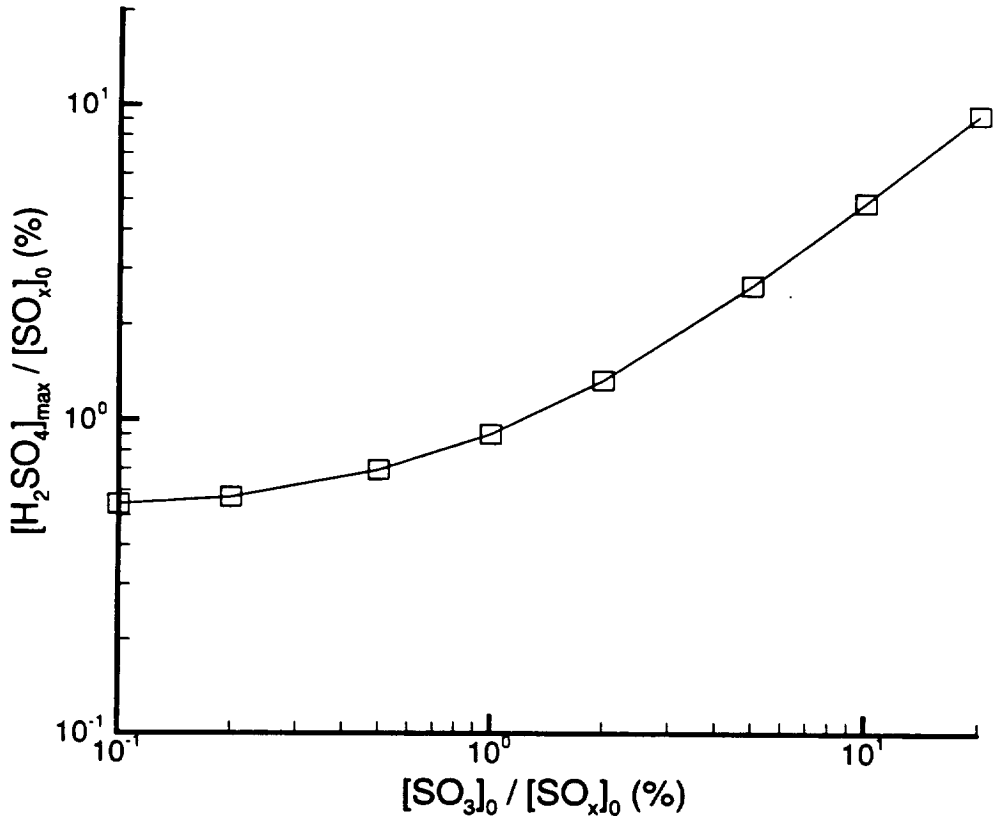

Figure 4.9: Maximum conversion efficiency of emitted SO_x to H_2SO_4 at axis versus percentage of fuel sulfur conversion to SO_3 in the engine. Subscript 0 indicates initial plume concentration.

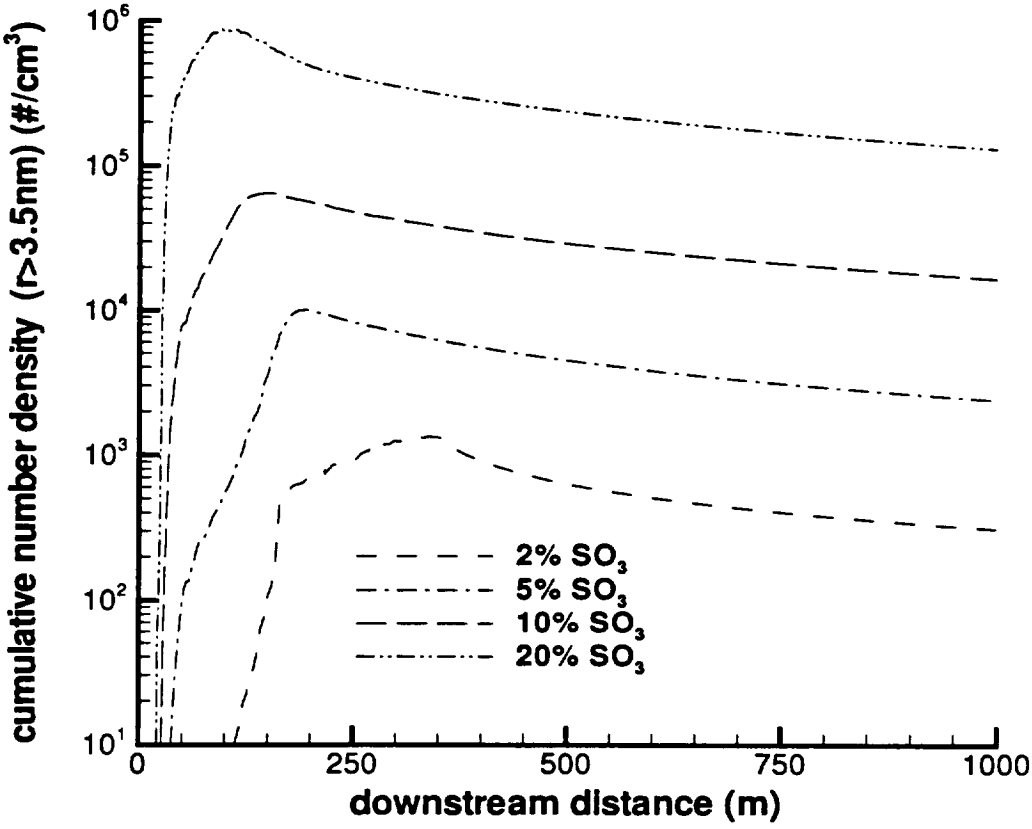

Figure 4.10: Cumulative number densities of volatile H_2SO_4-H_2O aerosols with radius greater than 3.5 nm along the jet plume axis, assuming that 2%, 5%, 10%, and 20% of the fuel sulfur is converted to SO_3 in the engine.

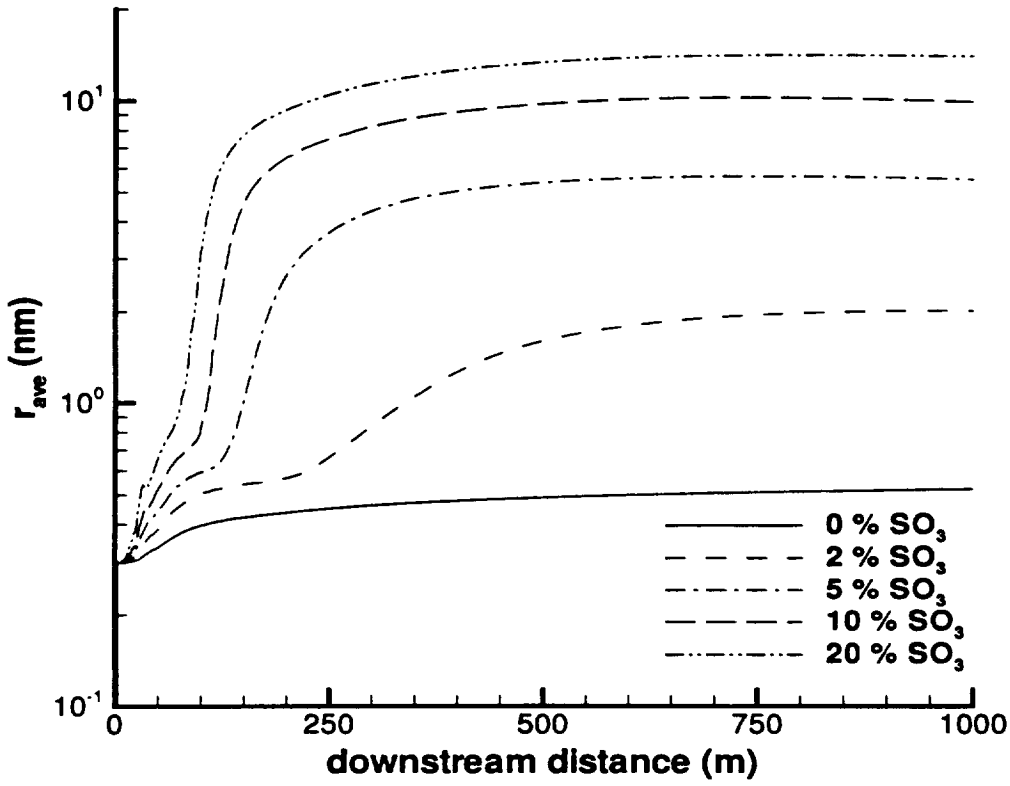

Figure 4.11: Average radius of volatile acid aerosols along the jet plume axis with 0, 2%, 5%, 10%, and 20% of the fuel sulfur converted to SO_3 in the engine.

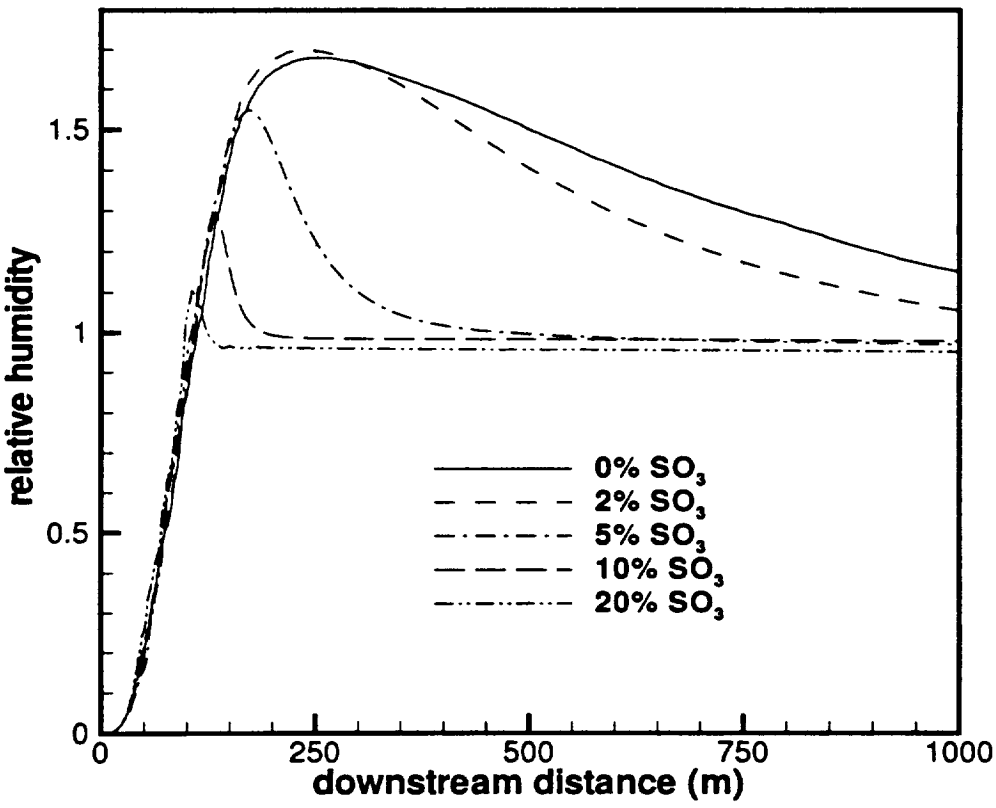

Figure 4.12: The evolution of relative humidity along the plume axis. Profiles are shown assuming 0, 2%, 5%, 10%, and 20% of the fuel sulfur is converted to SO_3 in the engine.

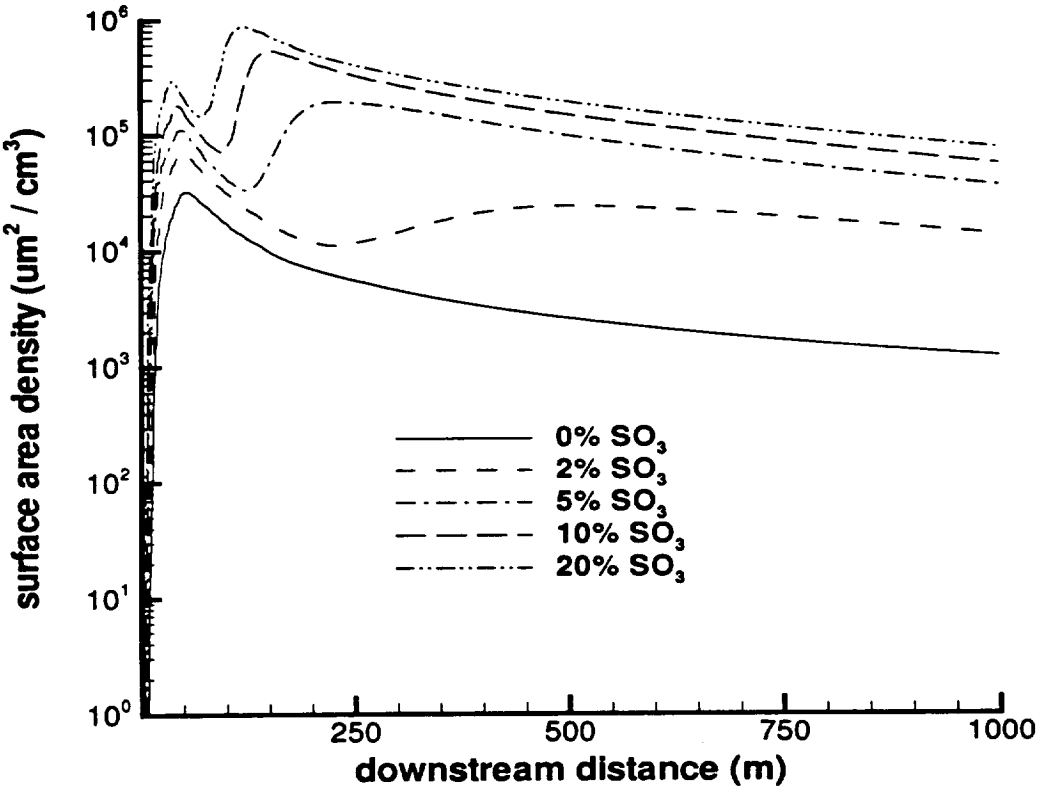

Figure 4.13: Volatile H_2SO_4-H_2O aerosol total surface area density along the jet plume axis. Profiles are shown assuming 0, 2%, 5%, 10%, and 20% of the fuel sulfur is converted to SO_3 in the engine.

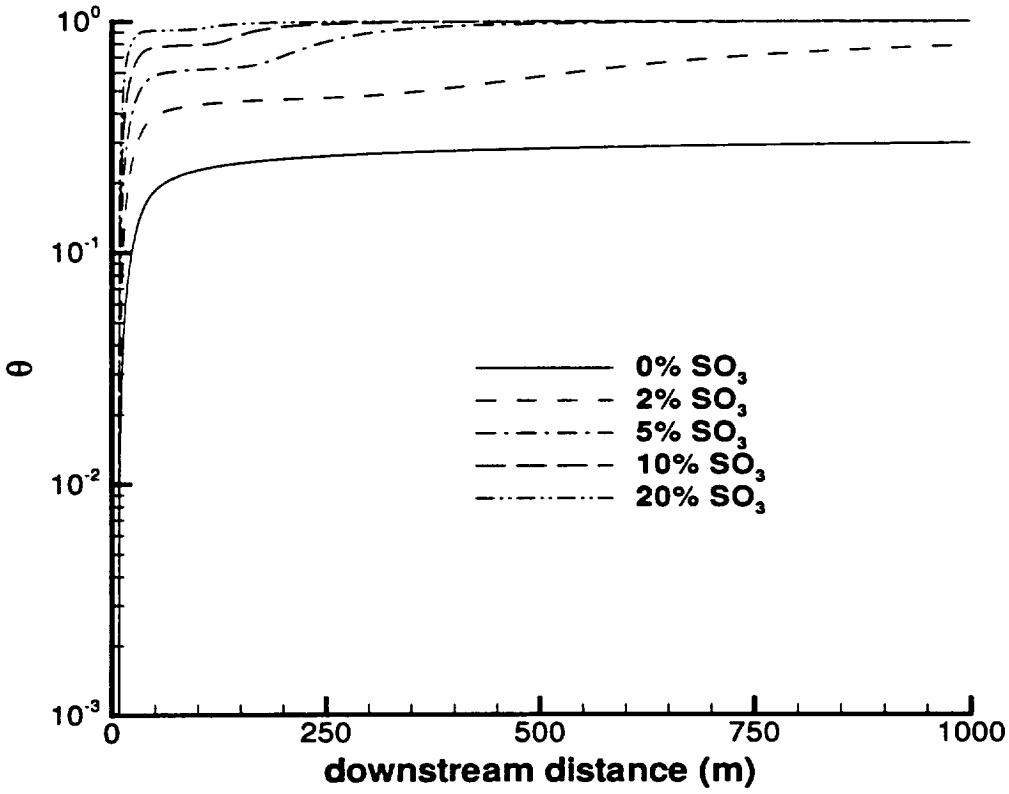

Figure 4.14: Surface average coverage of a soot particle along the plume axis with 0, 2%, 5%, 10%, and 20% of the fuel sulfur converted to SO_3 in the engine.

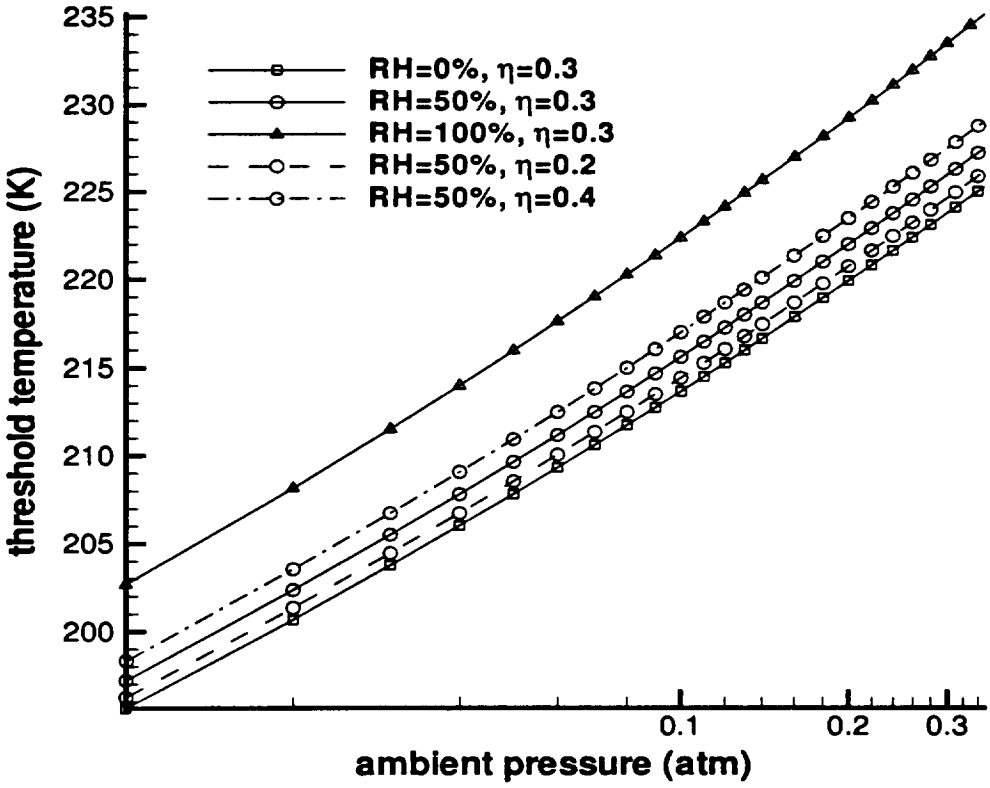

Figure 4.15: Threshold temperature for contrail formation versus ambient pressure for ambient relative humidities (RH) of 0, 50, and 100%. Contrails are predicted to form when the ambient temperature is below the curve. Threshold temperatures are also shown for an engine propulsion efficiency of 0.2 and 0.4.

Chapter 5

Conclusions

A detailed chemical mechanism between aircraft exhaust and ambient air in near-field jet plumes is compiled. The dominant oxidation kinetic pathways are identified through sensitivity analysis of major species with respect to gas phase reaction steps. The spatial distributions of major chemical species in the near-field jet plume are computed and analyzed. The potential impact of subgrid turbulent mixing on chemistry is investigated and found to be of negligible importance.

In the vortex regime of the wake, large eddy simulations (LES) may be required to track the highly three-dimensional fluid dynamics. The expensive computation on fluid dynamics makes it impossible to incorporate detailed chemistry. A reduced mechanism is therefore required. An eight-step reduced mechanism is developed which captures the major chemical pathways in the near-field jet plume. Results obtained with the reduced chemistry show good agreement with those predicted by the detailed

chemistry. However, using the eight-step reduced chemistry has cut down computer CPU time by a factor of more than 3.5 for the near-field simulation.

A comprehensive aerosol model is developed to simulate microphysical processes including sulfuric acid and water binary homogeneous nucleation, aerosol coagulation, non-equilibrium heteromolecular condensation, and sulfur-induced soot activation as water condensation nuclei. These microphysical processes are coupled with gas-phase chemistry and axisymmetric turbulent jet flow.

The modeling results indicate that a large number of subnanometer-sized volatile H_2SO_4-H_2O embryos are generated in the near-field plume. These embryos grow in size by condensation in the early jet regime and by self coagulation later. Soot particles can be activated into water condensation nuclei in the jet plume for possible contrail formation through both heterogeneous nucleation and scavenging of volatile H_2SO_4-H_2O aerosols.

The gas phase conversion of SO_2 to H_2SO_4 is controlled by OH driven oxidation and it is limited to less than 1%. However, the amount of H_2SO_4 produced will increase via fast reaction of SO_3 with H_2O directly if SO_3 emission due to fuel sulfur oxidation to SO_3 in the engine is considered. Higher levels of H_2SO_4 in turn result in more sulfate aerosol embryos formed in the early jet stage, and also enhance condensation of H_2SO_4 and H_2O onto the sulfate aerosols in this regime. Consequently, SO_3 emission from the engine nozzle exit increases the cumulative number density and surface area density of volatile sulfate aerosols. SO_3 emission also promotes chemical

activation of soot particles with enhanced acid coating. This suggests the need for measurements of the partitioning of sulfur species (SO_2 and SO_3) at the exhaust exit.

The threshold condition for ice contrail formation behind an aircraft depends on the ambient pressure, the ambient relative humidity, the overall propulsion efficiency of the aircraft, and the fuel properties such as the fuel hydrogen mass fraction and the specific combustion heat. Higher values of ambient relative humidity or pressure facilitate contrail formation. The threshold temperature is found sensitive to the overall propulsion efficiency of the aircraft.

The prediction of particle and species distribution in the near-field plume can serve as input for the follow-on larger-scale model. The present work also provides an estimate of the aerosol surface area density for subsequent evaluation of heterogeneous oxidation mechanisms in the wake.

References

American Society for Testing and Materials (ASTM) *Standard specification for aviation fuels, D 1655-93a*, Annual Book of ASTM Standards, Philadelphia, Pa., 555-563, 1994.

Anderson, M.R., Miake-Lye, R.C., Brown, R.C., and Kolb, C.E., *Calculation of exhaust plume structure and emission of the ER2 aircraft in the stratosphere*, J. Geophys. Res., **101**, 4025–4032, 1996.

Appleman, H., *The formation of exhaust condensation trails by jet aircraft*, Bull. Amer. Meterol. Soc., **34**, 14–20, 1953.

Arnold, F., Scheid, J., Stilp, T., Schlager, H., and Reinhardt, M.E., *Measurements of jet aircraft emissions at cruise altitude, I. the odd-nitrogen gases NO, NO_2, HNO_2, and HNO_3*, Geophys. Res. Lett., **19**, 2421–2424, 1992.

Arnold, F., Wohlfrom, K.-H., Klemm, M.W., Schneider, J., and Gollinger, K., *First gaseous ion composition measurements in the exhaust plume of a jet aircraft in*

flight: Implications for gaseous sulfuric acid, aerosols, and chemiions, Geophys. Res. Lett., **25**, 2137–2140, 1998.

Ayers, G.P., Gillett, R.W., and Gras, J.L., *On the vapor pressure of sulfuric acid*, Geophys. Res. Lett., **7**, 433–436, 1980.

Ballenthin, J.O., Miller, T.M., Knighton, W.B., Trzcinski, E., Borghetti, J.F., and Federico, G.S., *In-situ mass spectrometric sampling of jet aircraft exhaust wakes*, American Geophysical Union, Spring Meeting, Baltimore, MA, 1996.

Bekki, S. and Pyle, J.A., *Two-dimensional assessment of the impact of aircraft sulphur emissions on the stratospheric sulphate aerosol layer*, J. Geophys. Res., **97**, 15839–15847, 1992.

Bekki, S., *On the possible role of aircraft generated soot in the middle latitude ozone depletion*, J. Geophys. Res., **102**, 10751–10758, 1997.

Brown, R.C., Miake-Lye, R.C., Anderson, M.R., Kolb, C.E., and Resch, T.J., *Aerosol dynamics in near-field plumes*, J. Geophys. Res., **101**, 22939–22953, 1996a.

Brown, R.C., Anderson, M.R., Miake-Lye, R.C., Kolb, C.E., Sorokin, A.A., and Buriko, Y.I., *Aircraft exhaust sulfur emissions*, Geophys. Res. Lett., **23**, 3603–3606, 1996b.

Brown, R.C., Miake-Lye, R.C., Anderson, M.R., and Kolb, C.E., *Effect of aircraft*

exhaust sulfur emissions of near field plume aerosols, Geophys. Res. Lett., **23**, 3607–3610, 1996c.

Brown, R.C., Miake-Lye, R.C., Anderson, M.R., and Kolb, C.E., *Aircraft sulfur emissions and the formation of visible contrails*, Geophys. Res. Lett., **24**, 385–388, 1997.

Chang, W.C., *Modeling of NO_x formation in turbulent flames: development of reduced mechanisms and mixing models*, Ph. D. thesis, Department of Mechanical Engineering, University of California, Berkeley, 1995.

Chang, J.S., Brost, R.A., Isaaksen, S.A., Madronich, S., Middleton, P., Stockwell, W.R., and Walcek, C.J., *A three-dimensional Eulerian acid deposition contents*, J. Geophys. Res., **92**, 14681–14700, 1987.

Chen, J.-Y., Kollmann, W., and Dibble, R.W., *A two-dimensional model of sulfur species and aerosols*, Combust. Sci. Technol., **64**, 315–346, 1989.

Chen, J.-Y., Kollmann, W., and Dibble, R.W., *Pdf modeling of turbulent methane-air nonpremixed jet flames*, Proceedings of the 18th Annual Pittsburgh Conference, 1833–1837, 1987.

Danilin, M.Y., Ebel, A., Elbern, H., and Petry, H., *Evolution of concentrations of trace species in an aircraft plume: trajectory study*, J. Gerophys. Res., **99**, 18951–18972, 1994.

Dash, S.M., Pergament, H.S., Wolf, D.E., Sinha, N., Taylor, M.W., and Vaughn, M.E., Jr., *The JANNAF standardized plume flowfield code Version II (SPF-II), Volume II*, SAIC/PR-TR-18-11, July,1990.

Demore, W.B., Sander, S.P., Golden, D.M., Hampson, R.F., Kurylo, M.J., Howard, C.J., Ravishankara, A.R., Kolb, C.E., and Molina, M.J., *Chemical kinetics and photochemical data for use in stratospheric modeling*, Jet Propulsion Lab, JPL Publication 90-1, Pasadena, CA, Aug., 1992.

Doyle, J.G., *Self nucleation in the sulfuric acid-water system*, J. Chem. Phys., **35**, 795–799, 1961.

Fahey, D.W., Keim, E.R., Woodbridge, E.L., Gao, R.S., Boering, K.A., Daube, B.C., Wofsy, S.C., Lohmann, R.P., Hintsa, E.J., Dessler, A.E., Webster, C.R., May, R.D., Brock, C.A., Wilson, J.C., Miake-Lye, R.C., Brown, R.C., Rodriguez, J.M., Loewenstein, M., Proffitt, M.H., Stimpfle, R.M., Bowen, S.W., and Chan, K.R. *In situ observations in aircraft exhaust plumes in the lower stratosphere at midlatitudes*, J. Geophys. Res., **100**, 3065–3074, 1995a.

Fahey, D.W., Keim, E.R., Boering, K.A., Brock, C.A., Wilson, J.C., Anthony, S., Hanisco, T.F., Wennberg, P.O., Mikae-Lye, R.C., Salawitch, R.J., Louisnard, N., Gao, R.S., Donelly, S.G., Wamsley, R., DelNegro, L.A., Daube, B.C., Wofsy, S.C., Webster, C.R., May, R.D., Kelly, K.K., Loewenstein, M., Podolske, J.R., and Chan,

K.R. *Emission measurements of the Concorde supersonic aircraft in the lower stratosphere*, Science, **270**, 70–74, 1995b.

Flood, H., *Tröpfchenbildung in Übersättigten Äthylalkohol - Wasserdampfgemischen*, Z. Phys. Chem., **A170**, 286–294, 1934.

Friedl, R.R., Editor, *Atmospheric Effects of Subsonic Aircraft: Interim Assessment Report of the Advanced Subsonic Technology Program*, NASA Reference Publication 1400, 1997.

Fuchs, N., *Evaporation and Droplet Growth in Gaseous Media*, Pergamon Press, New York, 1959.

Fuchs, N., *The Mechanics of Aerosols* Pergamon Press, New York, 1964.

Fukuta, N. and Walter, L.A., *Kinetics of hydrometeor growth from a vapor-spherical model*, J. Atmos. Sci., **27**, 1160–1172, 1970.

Glarborg, P., Kee, R.J., Grcar, J.F., and Miller, J.A., *PSR: A FORTRAN program for modeling well-stirred reactors*, Sandia National Labotories Report SAND86–8209, 1986.

Hagen, D.E., Trueblood, M.B., and Whitefield, P.D., *A field sampling of jet exhaust aerosols*, Part. Sci. Technol., **10**, 53–63, 1992.

Harris, B.W., *Conversion of SO_2 to SO_3 in gas turbine exhaust*, J. Eng. Gas Turb. Power, **112**, 585–589, 1990.

Hunter, S.C., *Formation of SO_3 in gas turbines*, J. Eng. Power, **104**, 44–51, 1982.

Jacker-Voirol, A., Ponche, J.L., and Mirabel P., *Vapor pressures in the ternary system water nitric acid sulfuric acid at low temperatures*, J. Geophys. Res., **95**, 11857–11863, 1990.

Janika, J., Kolbe, W., and Kollmann, W., *Closure of the transport equation for the pdf of turbulent scalar fields*, J. Nonequil. Thermodyn., **4**, 47–56, 1979.

Jensen, E.J. and Toon, O.B., *The potential impact of soot particles from aircraft exhaust on cirrus clouds*, Geophys. Res. Lett., **24**, 249–252, 1997.

Jensen, E.J., Toon, O.B., Kinne, S., Sachse, G.W., Anderson, B.E., Chan, K.R., Twohy, C.H., Gandrud, B., Heymsfield, A., and Miake-Lye, R.C., *Environmental conditions required for contrail formation and persistence*, J. Geophys. Res., **103**, 3929–3936, 1998.

Kärcher, B., Peter, T., and Ottmann, R., *Contrail formation - homogeneous nucleation of H_2SO_4/H_2O droplets*, Geophys. Res. Lett., **22**, 1501–1504, 1995.

Kärcher, B. , *Aircraft-generated aerosols and visible contrails*, Geophys. Res. Lett., **23**, 1933–1936, 1996a.

Kärcher, B., Peter, T., Biermann, U.M., and Schumann, U., *The initial composition of jet condensation trails*, J. Atmos. Sci., **53**, 3066–3083, 1996b.

Kärcher, B., Hirschberg, M.M., and Fabian, P., *Small-scale chemical evolution of aircraft exhaust species at cruising altitude*, J. Geophys. Res., **101**, 15169–15190, 1996c.

Kärcher, B., *On the potential importance of sulfur-induced activation of soot particles in nascent jet aircraft exhaust plumes*, Atmos. Res., **46**, 293–305, 1998.

Karol, I.L. and Ozolin, Y.E., *Small- and medium-scale effects of high-flying aircraft exhausts on the atmospheric composition*, Ann. Geophys., **12**, 979–985, 1994.

Kee, R.J., Rupley, F.M., and Miller, J.A., *Chemkin-II: A FORTRAN chemical kinetics package for the analysis of gas-phase chemical kinetics*, Sandia Report SAND 89-8009, 1989.

Miake-Lye, R.C., Martinez-Sanchez, M., Brown, R.C., and Kolb, C.E., *Plume and wake dynamics, mixing and chemistry behind a high speed civil transport aircraft*, J. Aircraft, **30**, 467–479, 1993a.

Miake-Lye, R.C., Martinez-Sanchez, M., Brown, R.C., Kolb, C.E., Worsnop, D.R., Zahniser, M.S., Robinson, G.N., Rodriguez, J.M., Ko, M.K.W., Shia, R.-L., Sze, N.D., Heisey, C.W., Fox, L., Wofsy, S.C., and Davidovits, P., *Stratospheric aircraft exhaust plume and wake chemistry*, Langley Research Center, Hampton, VA, July, 1993b.

Miake-Lye, R.C., Anderson, M.R., Brown, R.C., and Colb, C.E., *Calculations of*

condensation and chemistry in an aircraft contrail, in DLR-Mitteilung, 94-06, p.274–279, DLR, D-51140, Köln, 1994. Edited by U. Schumann and D. Wurzel.

Mallard, W.G., Westley, F., Herron, J.T., Hampson, R.F., Fizzel, D.H., *NIST Chemical Kinetics Database: Version 6.0*, Natl. Inst. of Stand. and Technol., Gaithersburg, Md., 1994.

Mirabel, P. and Katz, J.L., *Binary homogeneous nucleation as a mechanism for the formation of aerosols*, J. Chem. Phys., **60**, 1138–1144, 1974.

Mirabel, P. and Ponche, J.L., *Studies of gas-phase clustering of water on sulphuric acid molecules*, Chem. Phys. Lett., **183**, 21–24, 1991.

NASA, *Subsonic Aircraft: Contrail and Cloud Effects Special Study:, Project Report*, Ames Research Center, National Aeronautics and Space Administration, March, 1996.

Perry, J.H. (Ed.), *Chemical Engineers' Handbook*, McGraw-Hill, New York, 1963.

Petry, H., Elbern, H., Lippert, E., and Ebel, A., *Three-dimensional mesoscale simulations of airplane exhaust impact in a flight corridor*, DLR-Mitt, 94-06, 329–335, Dtsch. Forschungs. für Luft- and Raumfahrt, Cologne, Germany, 1994.

Petzold, A., Busen, R., Schröder, F.P., Baumann, R., Kuhn, M., Ström, J., Hagen, D., Whitefield, P., Baumgardner, D., Arnold, F., Borrmann, S., and Schumann,

U., *Near field measurements on contrail properties from fuels with different sulfur content*, J. Geophys. Res., **102**, 29867–29880, 1997.

Petzold, A. and Schröder, F.P., *Jet engine exhaust aerosol characterization*, Aerosol Sci. Technol., **28**, 62–76, 1998.

Pope, S. B., *PDF methods for turbulent reactive flows* Prog. Energy Combust. Sci., **11**, 119–192, 1985.

Pruppacher H.R. and Klett, J.D., *Microphysics of clouds and precipitation*, Kluwer Academic Publ., Dordrecht, Holland, 1997.

Reiss, H. *The kinetics of phase transitions in binary systerms*, J. Chem. Phys., **18**, 840–848, 1950.

Rogaski, C.A., Golden, D.M., and Williams, L.R., *Reactive uptake and hydration experiments on amorphous carbon treated with NO_2, SO_2, O_3, HNO_3, and H_2SO_4*, Geophys. Res. Lett., **24**, 381–384, 1997.

Sabinina, L. and Terpugow, L., *Die Oberflachenspannung des Systems Schwefelsäure-Wasser*, Z. Phys. Chem., A173, 237–241, 1935.

Schumann, U., Editor, *AERONOX - The impact of NOx emissions from aircraft upon the atomosphere at flight altitude 8–15 km*, Report EUR 16209 EN, European Commisiion DG XXII and DLR Cologne, 1995a.

Schumann, U., *Jet engine exit conditions derived from budget analysis for the ATTAS-M45H and other engines*, Internal Report, IB-553-3/95, DLR, Ist. für Phys. der Atmos., Oberpfoffenhofen, Germany, 1995b.

Schumann, U., *On condistions for contrail formation from aircraft exhausts*, Meteorol. Zeitschrift, **5**, 4–23, 1996.

Schumann, U., Ström, J., Busen, R., Baumann, R., Gierens, K., Krautstrunk, M., Schröder, F.P., and Stingl, J., *In-situ observations of particles in jet aircraft exhausts and contrails for different sulfur containing fuels*, J. Geophys. Res., **101**, 6853–6869, 1996.

Flagan, R.C. and Seinfeld, J.H. *Fundamentals of air pollution engineering* Prentice Hall Publ., New Jersey, 1988.

Stolarski, R.S. and Wesoky, H.L., Editors, *The atmospheric effects of stratospheric aircraft: A fourth program report*, NASA Ref. Publ. RP–1359, 1995.

Tabata, S., *A simple but accurate formula for the saturation vapor pressure over liquid water*, J. Appl. Meterorol., **12**, 1410–1412, 1973.

Tabazadeh, A., Jensen, E.J., Toon, Owen, B.T. *A model description for cirrus cloud nucleation from homogeneous freezing of sulfate aerosols*, J. Geophys. Res., **102**, 23845–23850, 1997.

Tie, X., Lin, X., and Brasseur, G., *Two-dimensional coupled dynamic/chemical /microphysical simulations of global distribution of El Chichon volcanic aerosols*, J. Geophys. Res., **99**, 16779–16792, 1994.

Toon, O.B., Turco, R.P., Westphal, D., Malone, R. and Liu, M.S., *A multidimensional Model for Aerosols: Description of Computational Analogs*, J. Atmos. Sci., **45**, 2123–2143, 1988.

Tsang, W., and Herron, J.T., *Chemical kinetic data base for propellant combustion, I, Reactions invloving NO, NO_2, HNO, HNO_2, HCN and N_2O*, J. Phys. Chem. Ref. Data, **20**, 609–663, 1991.

Turco, R.P. and Yu, F.Q., *Aerosol invariance in expanding coagulating plumes*, Geophys. Res. Lett., **24**, 1223–1226, 1997.

Wang, Z. and Chen, J.-Y., *Modeling of microscale turbulence and chemistry interaction in near-field aircraft plumes*, J. Geophys. Res., **102**, 12871–12883, 1997.

Weisenstein, G.K., Ko, M.K.W., Sze, N.-D., and Rodriguez, J.M., *Potential impact of SO_2 emissions from stratospheric aircraft on ozone*, Geophys. Res. Lett., **23**, 161–164, 1996.

Weisenstein, D.K., Yue, G.K., Ko, M.K.W., Sze, N.D., Rodriguez, J.M., and Scott, C.J., *A two-dimensional model of sulfur species and aerosols*, J. Geophys. Res., **102**, 13019–13035, 1997.

WMO, *Scientific Assessment of Ozone Depletion, Global Ozone Research and Monitoring Project*, Report 37, World Meterological Organization, Geneva, Switzerland, February, 1995.

Wyslouzil, B.E., Carleton, K.L, Sonnenfroh, D.M., Rawlins, W.T., and Arnold, S., *Observation of hydration of single, modified carbon aerosols*, Geophys. Res. Lett., **21**, 2107–2110, 1994.

Xue, X.T., Brasseur, G., Lin, X., Friedlingstein, P., Granier, C., and Rasch, P., *The impact of high altitude aircraft on the ozone layer in the stratosphere*, J. Atmos. Chem., **18**, 103–128, 1994.

Yu, F. and Turco, R.P., *The role of ions in the formation and evolution of particles in aircraft plumes*, Geophys. Res. Lett, **24**, 1927–1930, 1997.

Zeleznik, F.J., *Thermodynamic properties of the aqueous sulfuric acid system to 350K*, J. Phys. Chem. Ref. Data, **20**, 1157–1200, 1991.

Zhao, J. and Turco, R.P., *Nucleation simulations in the wake of a jet aircraft in stratospheric flight*, J. Aero. Sci., **26**, 779–795, 1995.